On a Comprehensive Evaluation of Mössbauer Hyperfine Spectra Measured on Different Types of Magnetic Nanoparticles

Von der Fakultät für Elektrotechnik, Informationstechnik, Physik
der Technischen Universität Carolo-Wilhelmina zu Braunschweig

zur Erlangung des Grades eines Doktors

der Naturwissenschaften (Dr. rer. nat.)

genehmigte Dissertation

von Mathias Kraken

aus Iserlohn

eingereicht am: 11.02.2014

Disputation am: 29.04.2014

1. Referent: Prof. Dr. F. J. Litterst

2. Referent: Prof. Dr. M. Schilling

Druckjahr: 2014

Zusammenfassung

Die Eigenschaften magnetischer Partikel hängen sehr stark von ihrer Größe ab. Unterhalb eines kritischen Wertes (typischerweise im Nanometer-Bereich) bildet sich in den Partikeln jeweils nur eine magnetische Domäne. Man kann sich eine Vielzahl solcher Partikel als Ansammlung riesiger magnetischer Momente, die ggf. miteinander magnetisch wechselwirken können, vorstellen. Ohne Wechselwirkung untereinander, sind zwischen der Curie- bzw. Néel-Temperatur des Systems und der sog. Blocking-Temperatur T_{B}, die magnetischen Momente im Inneren der Partikel zueinander ausgerichtet, können aber kollektiv fluktuieren. Magnetische Anisotropien sind in diesem Temperaturbereich nicht stark genug, um diese Fluktuationen zu unterbinden. In Analogie zu einem Paramagneten, nennt man diesen Zustand Superparamagnetismus. Erst unterhalb der Blocking-Temperatur ist die Anisotropie so stark, dass die Momente der Partikel einfrieren. Bei magnetischer Wechselwirkung zwischen den Partikeln, können die Momente schon oberhalb der Blocking-Temperatur einfrieren und sich unterschiedliche Grundzustände ausbilden.

Die Mössbauerspektroskopie ist eine der Standardmethoden bei der Untersuchung eisenhaltiger Nanopartikel. Sie ist eine lokale Messmethode; mit ihr lassen sich Eigenschaften, wie z.B. die Valenz der verwendeten Sondenatome, deren lokale Symmetrie oder die Kationenverteilung bestimmen. Die Form der magnetischen Hyperfeinspektren hängt bei Nanopartikeln außerdem stark vom Relaxationsverhalten der Partikel ab, wie z.B. vom Einfrierprozess, von der Wechselwirkung zwischen den Partikeln etc. Durch eine adäquate Auswertung der Spektren, lässt sich dieses Verhalten genauer untersuchen. Zwar existieren Modelle für die Beschreibung von Mössbauerspektren an Nanopartikeln, jedoch sind diese entweder stark vereinfacht oder sehr komplex, weshalb die in der Literatur berichteten Auswerteverfahren häufig nur qualitativer Art sind, bzw. auf unzutreffenden Modellannahmen beruhen, so dass ein Großteil der dynamischen Informationen nicht erfasst wird. Die vorliegende Arbeit beschäftigt sich mit der eingehenden Auswertung der magnetischen Hyperfeinspektren von Partikeln, die von Anwendungsinteresse sind und daher wissenschaftlich vielfältig untersucht werden.

Im ersten Teil, wird eine Einführung in die physikalischen Eigenschaften von Nanopartikeln und die häufig verwendeten Messmethoden gegeben.

Bei einem Überblick über die unterschiedlichen Modelle zur Beschreibung der Mössbauerspektren zeigt sich, dass das sog. multi-level relaxation model (MLR) und das super-ferromagnetism / super-spin glass model (SFM/SSG), die beiden vielversprechendsten Modelle für eine Analyse der Mössbauerspektren sind.

Zum Test dieser beiden Modelle, werden als Erstes Messungen an $ZnFe_2O_4$-Nanopartikeln mit einem Durchmesser von ca. 10 nm betrachtet. Da diese Partikel als Pulver vorliegen, kann man von einer starken magnetischen Wechselwirkung zwischen ihnen ausgehen, die bei der Auswertung berücksichtigt werden muss. Es zeigt sich, dass das MLR keine korrekte Beschreibung der Mössbauerspektren ermöglicht. Der Grund ist, dass die Wechselwirkung der Partikel in diesem Modell nicht implementiert ist. Erst nach einer Modifikation, gelingt die erste Anwendung des MLRs auf ein System aus magnetisch wechselwirkenden Nanoteilchen. Das SFM/SSG Modell ist auf wechselwirkende Partikel ausgelegt. Auch dessen Anwendung gibt wertvolle Informationen, ist aber nicht so ergiebig wie die des MLRs.

Diese Erkenntnisse werden in einem weiteren experimentellen Teil zur detaillierten Untersuchung der Entstehung von Eisenoxid Partikeln, während ihrer Herstellung mit der nicht-wässerigen Sol-Gel Methode, angewendet. Dazu wird Probenmaterial durch ein Ventil des zur Herstellung verwendeten Ofens während unterschiedlicher Stufen der Synthese entnommen. Mit Röntgendiffraktionsmessungen und Transmissionselektronenmikroskopie wird zunächst eine Charakterisierung der Partikel hinsichtlich ihrer Größe und der strukturellen Eigenschaften durchgeführt. Im Anschluss, werden die magnetischen Eigenschaften durch eine Untersuchung der Mössbauerspektren der Partikel, unter Verwendung der Ergebnisse aus dem vorherigen Abschnitt, untersucht. Es zeigt sich, dass die Anwendung des MLRs eine nahezu vollständige Charakterisierung der magnetischen Eigenschaften erlaubt. Durch die Messungen kann die Entwicklung der strukturellen und magnetischen Eigenschaften der Partikel während des gesamten Herstellungsprozesses nachvollzogen und Ansätze zur Optimierung des Prozesses entwickelt werden.

Nach der erfolgreichen Beschreibung der Mössbauerspektren von magnetischen Eisenoxid Nanoteilchen, die entweder getrocknet oder in Lösung vorlagen, wird im letzten Abschnitt dieser Arbeit untersucht, wie sich die Spektren eines völlig anderen Typs magnetischer Nanoteilchen auswerten lassen. Es handelt sich dabei um dünne Filme, bei denen Cluster metallischen Eisens in eine nicht-magnetische Matrix (Ag oder Yb) eingebettet sind. Sie wurden durch Codeposition der verdampften Ausgangsmaterialien hergestellt. Durch eine genaue Einstellung der Verdampfungsrate, lassen sich unterschiedliche Eisenkonzentrationen in den Filmen realisieren. Frühere Messungen hatten gezeigt, dass dabei unterschiedliche Clustertypen, sowie RKKY-Wechselwirkung zwischen den Clustern auftritt. Daher unterscheidet nicht nur der metallische Charakter der Cluster, sondern auch deren Einbettung in die Matrix und

die unterschiedliche Art der Wechselwirkung dieses System stark von den bisher Untersuchten.

Zunächst werden die Ag(Fe) Filme untersucht. Zur Auswertung der Tieftemperaturspektren wird ein spezielles Modell entwickelt, was exakt auf die Eigenschaften dieser Cluster abgestimmt ist. Es wird sich zeigen, dass dieses Modell die Spektren sehr gut nachbilden kann. Zum Vergleich wird auch das MLR angewendet. Die Spektren, die an Eisenclustern in einer Ytterbiummatrix gemessen wurden, können mit keinem der Modelle gefittet werden. Der Grund ist der gleichzeitige Einfluss von dynamischer und inhomogener Verbreiterung auf die Mössbauer Linien. Allerdings gibt auch schon eine qualitative Analyse Informationen über die Wechselwirkungsstärke zwischen den Clustern und ihre Position in den Filmen. Zusätzliche AC-Suszeptibilitätsmessungen unterstreichen die Ergebnisse.

Diese Arbeit verdeutlicht, dass eine eingehende Auswertung der Mössbauerspektren von magnetischen Nanopartikeln sehr lohnend ist und gibt Beispiele für eine erfolgreiche Anwendung verschiedener Modelle. Es wird über die erste erfolgreiche Beschreibung der Mössbauerspektren von magnetisch wechselwirkenden Nanopartikeln mit einem MLR berichtet. Durch dessen Anwendung lassen sich neben den lokalen Eigenschaften, auch Informationen über das Relaxationsverhalten der Partikel gewinnen. Weitere Messungen mit anderen Methoden werden dadurch überflüssig. Darüber hinaus, werden durch die Anwendung der Modelle bei einer genauen Untersuchung der Entstehung von Nanopartikeln während ihrer Synthese mit der nicht-wässerigen Sol-Gel Methode, wichtige Informationen über den Herstellungsprozess gewonnen und die magnetischen Eigenschaften von Eisenclustern in eine Silber- bzw. Ytterbiummatrix genauer bestimmt.

Abstract

The properties of magnetic particles depend strongly on their size. Below a critical value (typically in the nanometer range), only one magnetic domain forms inside the particles. A multiplicity of those particles can be understood as a conglomerate of huge magnetic moments, that may interact with each other. Between the Curie- resp. Néel-temperature of the system and the so-called blocking temperature, T_B, the magnetic moments within the particles are aligned with each other but fluctuate collectively in case of vanishing interparticle interactions. Magnetic anisotropies are not strong enough to suppress these fluctuations in this temperature range. Inspired by a paramagnet, this scenario is called "superparamagnetism". Only below T_B, the strength of the magnetic anisotropies is sufficient to allow a freezing of the particle magnetic moments. In the presence of interparticle interactions, a freezing of the moments may happen above T_B and different magnetic groundstates may develop.

Mössbauer spectroscopy is one of the key methods when examining nanoparticles that contain iron. Since it is a local probe method, properties like e.g. the valence and the local symmetry of the probe atoms or the cation distribution can be studied. The shape of the magnetic hyperfine spectra depends furthermore strongly on the dynamic behavior of the particles, e.g. the freezing process, interparticle interactions, etc. An adequate evaluation of the spectra allows a detailed examination of these properties. However, the existing models are either too simplified or too complex, wherefore the evaluation of Mössbauer spectra on this type of samples are typically only qualitative or not using appropriate assumptions. Hence, most of the informations about the dynamic behavior of the particles is not determined. The present work is focused on the detailed examination of magnetic hyperfine spectra measured on particles, that are commercially interesting and therefore frequently discussed in scientific literature.

The first part of this work gives an introduction to the physical properties of nanoparticles and the frequently used measurement techniques.

An overview over the different models for the description of the hyperfine spectra of magnetic nanoparticles identifies the so-called multi-level relaxation model (MLR) and the super-ferromagnetism / super-spin glass model (SFM/SSG) as the

most promising candidates for a successful application to the spectra.

In order to prove their usability, they are applied to measurements on a sample of $ZnFe_2O_4$-nanoparticles with a size of approximately 10 nm. Since these particles are dried, strong interparticle interactions are supposed to be present. The MLR is not able to give a correct description of the Mössbauer spectra. This is due to the interparticle interactions, which are not implemented. A slight modification is necessary, to allow the correct description of the spectra. This is the first successful application of a MLR to a series of measurements on strongly interacting magnetic nanoparticles. The SFM/SSG is designed for particles that experience interparticle interaction. Its application reveals valuable informations, but is however not as fruitful as the application of the MLR.

The findings from the application of the MLR are used in a further experimental section for a detailed study on the development of iron oxide nanoparticles during their preparation using the non-aqueous sol-gel method. Sample material is extracted through a valve in the preparation apparatus at different stages of the synthesis. For a characterization of the size and the structural properties of the particles, x-ray diffraction measurements and transmission electron microscopy is used. The magnetic properties are examined by a detailed analysis of Mössbauer spectra measured on different samples at different temperatures, using the results of the previous section. The application of the MLR allows an almost complete characterization of the magnetic properties. With the measurements discussed in this chapter, a detailed reconstruction of the structural and magnetic properties during the entire preparation process and the development of approaches to improve the properties of the particles from this reaction is possible.

After the successful application of the Mössbauer models on measurements on magnetic iron oxide nanoparticles, dried or dispersed in a solution, the following section of this work is focused on the evaluation of Mössbauer spectra measured on a whole different type of magnetic nanoparticles. It deals with thin films of silver or ytterbium that contain clusters of metallic iron. They were prepared using vapor codeposition with different iron concentrations. Earlier measurements revealed the presence of different cluster types as well as RKKY interactions between them. The difference of this system to the ones discussed in the earlier chapters, is therefore not only the metallic character of the clusters, but also their embedding in the Ag or Yb matrix and the RKKY interaction.

Initially, the Ag(Fe) films are examined. For the analysis of their low temperature Mössbauer spectra, a model designed specifically on the basis of the properties of this system, is developed. It is able to reproduce the spectra very well. For comparison, the MLR is applied as well. The spectra measured on iron clusters in an ytterbium matrix cannot be reproduced with these models, due to the simulta-

neous presence of dynamic and inhomogeneous broadening of the Mössbauer lines. However, a qualitative analysis already gives informations about the intercluster interaction strength and about the positions of the clusters within the film. Additional AC-susceptibility measurements support these findings.

This work emphasizes the importance of a careful analysis of the Mössbauer spectra of magnetic nanoparticles, and gives examples for a successful application of different models, amongst other the first application of a MLR to a set of interacting magnetic nanoparticles. This allows not only the examination of local properties of the particles, but of the dynamic behavior as well. Additional measurements with other techniques are therefore not necessary. Furthermore, detailed informations about the preparation of particles with the non-aqueous sol-gel method are gained through the application of the models on samples extracted during the synthesis, as well as details about the magnetic properties of iron clusters in a silver or ytterbium matrix.

Contents

Introduction

Nanoparticles affect the life of people already for a long time. One of the first examples of the (accidental) utilization of nanoparticles is the Lycurgus cup, an artifact being dated to the 4th century AD, whose color changes whether it is illuminated from the outside or from the inside [1]. This is due to gold nanoparticles with a size of roughly 40 nm, which are dispersed in the glass. When light is transmitted through the cup, surface plasmons on the metal nanoparticles are excited, which results in an increased absorption of certain wavelengths [2]. In the subsequent decades, nanoparticles could e.g. be found in stained glass windows in churches. The first scientific approach to nanoparticles can be dated to the 1850s, when Michael Faraday discussed the formation of gold nanoparticles (although not yet called nanoparticles at that time, but "exceedingly fine particles") [3]. However, the attention was drawn on the nanoparticles predominately because of their optical properties, at that time.

In the subsequent decades, the interest on nanoparticles grew not only because of their optical properties. In addition, the magnetic properties of nanoparticles were found to differ significantly from the bulk properties of the same material. The first correct explanation of this effect was given by Frenkel and Dorfmann in 1930 [4], who predicted that ferromagnetic particles below a critical size form only one magnetic domain. This results in a superparamagnetic state below the Curie-/Néel-temperature of the material, where the spins within the particles are already in a (anti-)ferro- / ferrimagnetic state, but the collective of the spins in one particle still undergoes magnetic relaxation. Below a certain temperature, the blocking temperature T_B, the magnetic moment of the particles "freezes".

Nowadays, nanoparticles are an important and growing topic in scientific research, as it can be observed from figure 1. Therein, the number of publications with the term "nanoparticles" in the title in five year steps as found in Google scholar is plotted. In the years 2005 - 2010, more the 40000 publications on nanoparticles can be found. The articles do not only have a pure physical background, they also cover different branches like material science, chemistry, medicine and pharmacology, amongst others. This shows, that nanoparticles are not only interesting for the purely scientific research, but also offer the possibility of different applications.

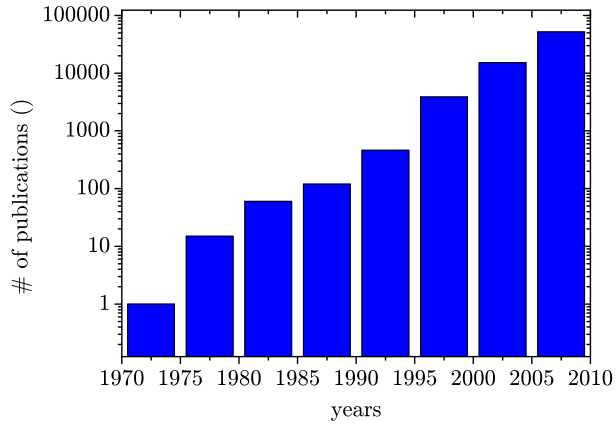

Figure 1: Number of articles with the term "nanoparticles" in the title as listed in Google scholar within time intervals of five years.

A very important example of the applications of magnetic nanoparticles is their utilization for medical purposes, especially in cancer therapy. The large surface to volume ration allows an effective coating of the nanoparticles with selected materials, e.g. molecules that allow a targeting of the nanoparticles to special (cancer) cells within the body. When the nanoparticles arrive at the tumor, imaging techniques like magnetic resonance imaging (MRI) can be applied or the region can be exposed to electromagnetic waves, resulting in a heating of the area around the particles and the destruction of the surrounding (cancer) cells. For recent reviews on the actual progress of this topic, see e.g. [5, 6].

Heating of magnetic nanoparticles by an electromagnetic wave can also be used for non-medical application, e.g. for a rapid hardening of glue at a certain position. This subject is one application of the nanoparticles prepared at the Institut für Partikeltechnik (iPAT) at the TU Braunschweig. Two sections of this work are based on a collaboration with the iPAT and dealing with particles prepared in this institute.

However, all the applications discussed above require nanoparticles with well defined and reproducible properties. An accurate characterization of the nanoparticles is therefore essential in order to allow their application. One outstanding method for the characterization of magnetic nanoparticles, which is frequently used in scientific publications, is Mössbauer spectroscopy. Despite its frequent application to this type of materials and although different models that describe the Mössbauer spectra of magnetic nanoparticles can be found in literature, the evaluation of the Mössbauer spectra in publications is often performed only qualitatively or even with inaccurate approaches. The most prominent example is the description of the data

with a distribution of static magnetic hyperfine fields even at temperatures around T_B and higher, where the magnetic moments of the nanoparticles are undoubtedly fluctuating (see e.g. [7, 8, 9]). The reason for this frequently occurring inaccurate description is, that the applicable models are rather complex and that they are developed only for an ideal particle system. Characteristic features that influence the Mössbauer spectrum and can be found in almost every nanoparticle system, like interparticle interactions, surface spin canting, particle size distributions etc. are commonly not implemented. This makes the application of the models complicated.

The main topic of this work, is the application of the most promising Mössbauer relaxation models to different types of magnetic nanoparticles and, if necessary, a modification of the models in order to allow a valuable usage of them. In order to get access to nanoparticles of different types, samples obtained from two different synthesis methods are discussed in this work. On the one hand, a detailed examination of the formation of magnetic nanoparticles during the preparation process with the so-called solvothermal synthesis was performed, while on the other hand, the low temperature properties of small iron clusters in metallic, nonmagnetic matrices prepared by vapor co-deposition are discussed. Furthermore, Mössbauer spectroscopy was not the only applied technique, AC- and DC-susceptibility, x-ray diffraction and transmission electron microscopy were used as well.

The structure of this thesis is as follows. The first block deals with the summary and discussion of the physical properties of magnetic nanoparticles, as found from other publications, and covers chapters 1-1.7. The first chapter provides a detailed insight into the physical properties of magnetic nanoparticles, followed by a chapter about the most common experimental methods used for their characterization, drawing a special attention on Mössbauer spectroscopy. The fourth chapter gives a small insight into the different methods of nanoparticle preparation.

In the second block, the experimental results are presented and discussed. In chapter 3, the applications of different models on the Mössbauer spectra of strongly interacting $ZnFe_2O_4$ nanoparticles is presented. Chapter 4 gives details about the formation of magnetic nanoparticles during their preparation with the solvothermal synthesis (a collaboration with the Institut für Partikeltechnik of the TU Braunschweig). The subsequent chapter deals with the interpretation of the low temperature Mössbauer spectra of iron clusters in a silver or ytterbium matrix. A new model for the description of the low temperature Mössbauer data of these samples, is developed and applied and the results are compared to those of established models (a collaboration with the Centro Brasileiro de Pesquisas físicas (CBPF) in Rio de Janeiro, Brasil).

The third block contains the summary, the codes that were used to simulate the models and the bibliography.

Chapter 1

Magnetic dynamics of nanoscale particles

In this chapter, the basics of the magnetic dynamics of nanoscale particles are presented.

1.1 Superparamagnetism

1.1.1 Single domain particles

Macroscopic ferromagnetic samples tend to form domains, in order to reduce stray fields and hence their magnetic potential energy. A domain is a region, in which the spins are aligned ferromagnetically but in another direction than the spins of

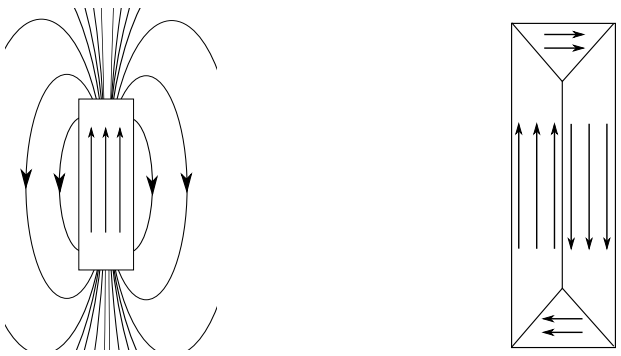

(a) (b)

Figure 1.1: The influence of the formation of domains on the magnetic stray fields. Ferromagnetic material (a) without and (b) with a domain structure and the corresponding magnetic stray fields indicated by the curved lines with the arrowheads. Almost no demagnetization field occurs outside of the sample in case of a formation of domains in the material.

its neighboring domain. The reduction of the stray fields due to the formation of a domain structure is shown schematically in figure 1.1

The domains are separated by a so-called Bloch wall, which can be understood as a region where the spins turn their direction from being parallel to the spins in the first domain to being parallel to the spins in the second domain. In order to reduce the overall energy of the spins within the Bloch wall, it should be infinitely big in a first approach. However, the influence of the magnetocrystalline anisotropy (for more details, see next section), results in a finite thickness of the Bloch wall as the energetically most favorable state.

When the particle radius r decreases, the energy the system needs to form a domain wall (surface energy, scales with r^2) becomes bigger than the energy the system gains through the reduction of the magnetic stray fields (volume energy, scales with r^3). The critical size, where the energy loss through the formation of a domain wall cannot compensate the energy gain through the reduction of the magnetic stray fields, can be estimated by

$$r_{\mathrm{crit}} < \frac{9\sigma_W^{180^\circ}}{\mu_0 M^2}, \tag{1.1}$$

with $\sigma_W^{180^\circ}$ being the energy of a 180° domain wall per unit area [10]. Therewith, the critical radius r_{crit} is $\approx 10^{-7}\,\mathrm{m}$, for the typical values $\sigma_W^{180^\circ} \sim 10^{-2}\,\mathrm{Jm}^{-2}$ and $\mu_0 M^2 \sim 1\,\mathrm{T}$ [10]. Particles with a radius $r < r_{\mathrm{crit}}$ consist of one single domain and hence perfectly aligned (anti-) parallel spins for $T < T_{\mathrm{C}}$. Notably, the actual critical radius differs strongly, for different materials and the value given here should only be understood as a rough approximation.

The direction of the ensemble of parallel spins is defined by the "anisotropy", the spins experience. The most common magnetic anisotropies can be described by an uniaxial potential

$$E_{\mathrm{MC}} = K_1 \sin(\theta)^2 + K_2 \sin(\theta)^4, \tag{1.2}$$

as it is shown in figure 1.2 (a) and discussed in the next section. If the temperature is high enough to allow the magnetic moments of the particles to overcome the energy barrier between the two minima in the uniaxial potential corresponding to different orientations of the magnetic moment of the nanoparticle, a fluctuation between the minima in the $E(\theta)$ potential will take place. These fluctuations are called "overbarrier fluctuations", the particle is now "superparamagnetic". This term is based on the fact, that due to the fluctuations of the spin ensembles, a sample may appear paramagnetic below T_{C}. In contrast to a "normal" paramagnet, where the spins of single atoms fluctuate, the collective of the spins in the particle fluctuates here, while still being parallel to each other. The sample can therefore be understood, as paramagnet with giant magnetic moments, a superparamagnet.

If the temperature is not high enough to allow the particle magnetic moment to

overcome the anisotropy energy barrier, the magnetization direction will fluctuate around a local minimum in the $E(\theta)$ potential. These fluctuations are called "collective excitations" and have frequencies in the order of $10^{10} - 10^{13}\,\mathrm{s}^{-1}$ [11].

The overbarrier fluctuation rate of a single domain particle with a uniaxial anisotropy for $\Delta E \gg kT$, can be estimated using the Néel-Brown expression [12, 13]

$$\tau = \tau_0 \exp\left(\frac{\Delta E}{k_\mathrm{B} T}\right), \tag{1.3}$$

where τ_0 has a value of typically $10^{-9} - 10^{-11}\,\mathrm{s}$ and ΔE is the anisotropy energy barrier, the particle experiences. Different models describing the overbarrier fluctuation rate are presented in section 1.3. This relaxation should not be mistaken with the Brownian relaxation time, which describes the relaxation of the particle magnetic moment due to a motion of the particle in a solution or a liquid.

Only when the relaxation time of the magnetic moments of the particles exceeds the timescale of the technique used, the particle moments appear to be static for this technique. The temperature where this occurs is called blocking temperature T_B. It varies for the different experimental methods due to their different intrinsic timescales. The term superparamagnetism only refers to the magnetic state with $T > T_\mathrm{B}$. Below T_B, the magnetically ordered state is called either superferromagnetic or super-spin glassy (see below).

1.1.2 Magnetic anisotropies experienced by nanoparticles

The easiest model for describing the magnetic behaviour of a superparamagnetic nanoparticle includes uniaxial anisotropy. Equation (1.2), can be further simplified by assuming $K_2 = 0$, since K_2 has almost no influence on the physical properties of the nanoparticles [14]. However, magnetic nanoparticles always experience various types of anisotropies, resulting in a non-uniform potential and different easy axes. The most important types of anisotropies will be discussed in the following.

Magnetocrystalline anisotropy

The origin of the magnetocrystalline anisotropy is spin-orbit interaction. The electronic orbitals of an atom in a material are connected to its well defined crystal axes. Through the spin-orbit interaction, the spin is linked to the oriented orbitals and hence experiences a preferred orientation.

Due to the link between the orbitals and the crystal structure, the magnetocrystalline anisotropy varies for different materials. When the structure possesses a single axis with high symmetry, it can be described by the uniaxial shape given in equation (1.2) and shown in figure 1.2 (a). Magnetite, a very common material used for producing superparamagnetic nanoparticles, has a cubic crystal structure and

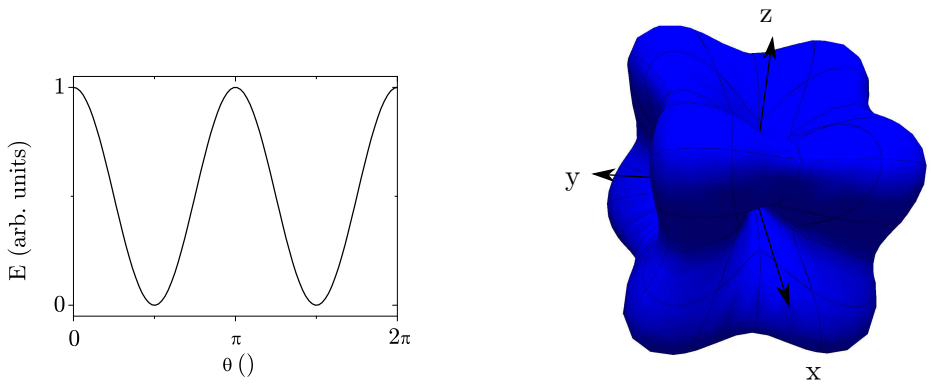

(a) (b)

Figure 1.2: Different scenarios for the magnetocrystalline anisotropy. (a) Uniaxial shape for a crystal with a single axis with high symmetry. (b) Approximate shape for a crystal with a cubic structure with $K_1 > 0$ after equation (1.4).

develops a potential that can be described relative to the three different orientations of the crystal by [15]

$$E_{\mathrm{MAE},(100)} = KV(\cos(\theta)^2\sin(\theta)^2 + \sin(\theta)^4\cos(\phi)^2\sin(\phi)^2 \tag{1.4}$$

$$E_{\mathrm{MAE},(110)} = \frac{KV}{4}(\cos(\theta)^4 + \sin(\theta)^4(\sin(\phi)^4 + \sin(2\phi)^2)) + \frac{KV}{4}\left(\sin(2\theta)^2 \cdot \left(\cos(\phi)^2 - \frac{1}{2}\sin(\theta)^2\right)\right) \tag{1.5}$$

$$E_{\mathrm{MAE},(111)} = KV\left(\frac{1}{3}\cos(\theta)^4 + \frac{1}{4}\sin(\theta)^4\right) - KV\left(\frac{\sqrt{2}}{3}\sin(\theta)^3\cos(\theta)\cos(3\phi)\right). \tag{1.6}$$

A three-dimensional plot of this scenario is shown in figure 1.2 (b). Although this structure shows eight different maxima and six different minima, the path between two neighboring minima via the smallest potential well still looks similar to the uniaxial potential shown in figure 1.2 (a) with the only difference, that a transition between these two maxima would include an angle of only $\pi/4$ and not $\pi/2$.

The shape of the magnetocrystalline anisotropy for other types of crystal structures will not be discussed here and it is referred, e.g., to [16] instead.

Shape anisotropy

Shape anisotropy arises from the demagnetization field in the nanoparticle. It can be expressed by

$$(H_d)_i = -\sum_j N_{ij} M_j, \tag{1.7}$$

where N_{ij} is a tensor of demagnetization factors and M_j the magnetization of the sample. In general, it is very complicated to calculate N_{ij} for a randomly shaped sample. Analytical solutions are only available in the case of an ellipsoid [17]. If the magnetization M lies parallel to one of the principal axes a,b or c of the ellipsoid, $\underline{\underline{N}}$ can be diagonalized [10]. The energy, the system loses through the demagnetization field H_d can finally be calculated by integrating over the whole sample

$$E = -\frac{1}{2} \int \underline{M} \cdot \underline{H}_d \, dV. \tag{1.8}$$

In case of an ellipsoid with $a > b = c$ the energy in dependence of the angle between the magnetization and the a axis is given by [18]

$$E = \frac{1}{2} M^2 (N_{zz} - N_{xx}) \sin(\theta)^2, \tag{1.9}$$

where N_{ii} are the components of the diagonalized $\underline{\underline{N}}$.

Hence, the shape anisotropy forces the magnetization to point along the largest principle axis of an ellipsoidal shaped sample and therefore has an uniaxial character as well. If the particles have a spherical shape, it is zero.

Stress anisotropy

The origin of the stress anisotropy is pressure on the particle that induces strain. Due to the magnetostriction, which is induced by the spin-orbit coupling, the spins in the particle are forced to change their direction in order to minimize the overlap of the orbitals. The direction of this anisotropy depends on the directions of the strain and it has uniaxial character as well.

Surface anisotropy

Due to the strongly increased surface / volume ratio of magnetic nanoparticles compared to bulk materials, their surface properties become important. The physical properties that are present in the core of the particles may change significantly at the surface, for example by a variation of the lattice constants etc. All these phenomena can contribute to the magnetic anisotropy and are summarized under the term ”surface anisotropy” [19].

Dependence on temperature and particle size

In real systems, there will always occur a superposition of the different types of anisotropies. For this reason, the temperature and particle size dependences are very complex and vary for the different materials.

After [20], the magnetocrystalline anisotropy of a bulk material decreases with increasing temperature, following $(1 - T/T_C)^{2.2}$. However, for the nanoparticles discussed in this work, $T_B \ll T_C$, wherefore the influence of the temperature dependence of the magnetocrystalline anisotropy can be neglected.

A theoretical approach on the temperature dependence of the magnetic surface anisotropy has been presented in [19] for different types of anisotropies. The magnetic anisotropy at $T = 0.1\,T_C$ has already decreased by a factor of ≈ 0.1 for uniaxial anisotropies and by a factor of ≈ 0.2 for cubic anisotropies.

As one can find in the following sections, the anisotropy constant K has mostly been defined as temperature independent in the literature, although a temperature dependence is relevant and should be kept in mind.

The dependence of the magnetic anisotropy on the particle size is directly connected to the surface / volume ratio and therewith on the importance of the surface anisotropy compared to the volume dependent magnetic anisotropies (magnetocrystalline, shape and stress ansiotropy). With decreasing particle size, the influence of the first one increases, which results in different values for the magnetic anisotropies for different particle sizes. A phenomenological description of the particle size dependent behavior has been proposed by Bødker *et al.* [21] as

$$K_{\text{eff}}(D) = K_V + \frac{6}{D} K_S, \tag{1.10}$$

where K_V is the anisotropy constant of the volume anisotropy and K_S for the surface anisotropy. This describes the size dependent anisotropy constant of metallic Fe-nanoparticles determined with Mössbauer spectroscopy very well.

Luis *et al.* [22] used the same formula to describe $K_{\text{eff}}(D)$, which follows from a careful analysis of AC- and DC-susceptibility data of Co nanoparticles.

Comment

Almost every model that is used for the description of the physical properties of magnetic nanoparticles in literature is based on an uniaxial potential (see subsequent chapter 2). This is a reasonable assumption, since almost all relevant anisotropies for magnetic nanoparticles have this uniaxial character, except the magnetocrystalline anisotropy in part. Therefore, the anisotropy that is used for the description of non-interacting particles in the following is based on uniaxial anisotropy, as well.

1.2 Interparticle interactions

So far, no magnetic interactions between the particles have been taken into account. They may, however, have a strong influence on the physical properties of the magnetic nanoparticles. Different types of interparticle interactions and their influence on the behavior of the magnetic nanoparticles are discussed in the following.

Furthermore, electric dipole-dipole interactions between the particles exists as well, which are not discussed here.

Dipole-dipole interaction

The magnetic dipole-dipole interaction energy between the spins of the single atoms in a conventional paramagnet lies in the order of $E_{\mathrm{dip}}/k_{\mathrm{B}} \approx 1\,\mathrm{K}$ and is therefore much smaller than other mechanisms that force an ordering of the spins. However, magnetic nanoparticles have a strongly increased magnetic moment compared to the magnetic moments of single atoms and therefore, dipole-dipole interactions become important for such systems.

A special case is a chain of nanoparticles coupled with dipole-dipole interactions, whose magnetic moments arrange parallel to each other along the chain direction (compare to figure 1.3 (a)).

However, the interaction between two neighboring particles forces them to find the best possible orientation which matches their stray magnetic field, as one can see as well from the dipolar energy of two interacting magnetic moments

$$E_{\mathrm{dip}} = \frac{\mu_0}{4\pi r^3}\left(\underline{\mu}_1 \cdot \underline{\mu}_2 - \frac{3}{r^2}(\underline{\mu}_1 \cdot \underline{r})(\underline{\mu}_2 \cdot \underline{r})\right). \tag{1.11}$$

As shown in [18], the influence of a particle with a fixed orientation of its magnetic moment on the orientation of the magnetic moment of another particle at a random site can be described by connecting these two particles with a vector $\underline{r}$. When the magnetic moment of the first particle has an angle of θ with respect to $\underline{r}$, then the magnetic moment of the second particle has an angle of approximately $-\theta$ with respect to $\underline{r}$ (see figure 1.3 (b)).

Hence, multiple particles in close contact coupled through dipole-dipole interaction experience a random distribution of interaction strengths and directions, which is comparable to frustration of individual spins due to competing interactions at their sites, resulting in a spin-glass like state. This scenario is shown in figure 1.3 (c) for three particles. In analogy to the term superparamagnetism, this scenario is called "super-spin glass" [23].

Irrespective of their orientations, dipole-dipole interactions between nanoparticles

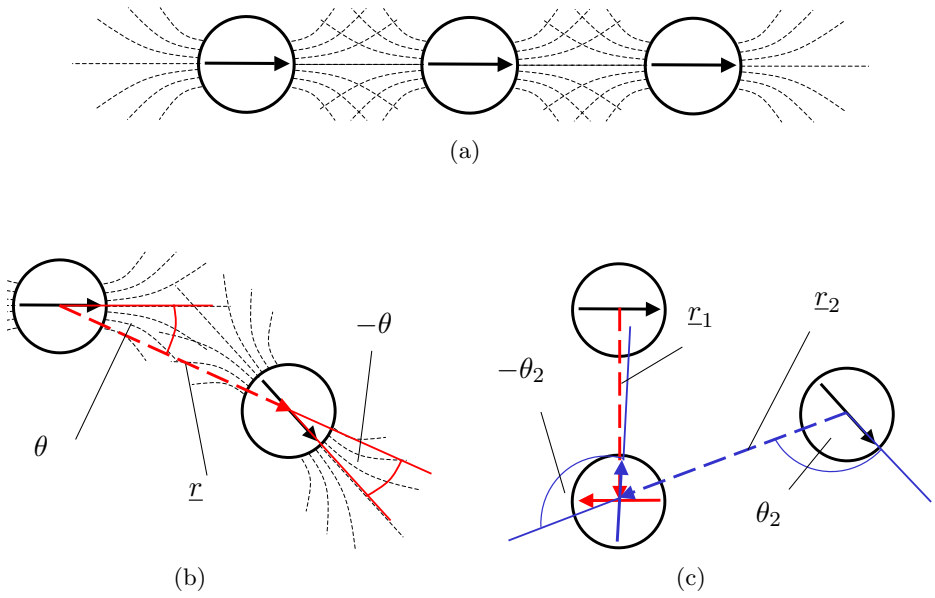

Figure 1.3: Different effects of the dipole dipole interaction on the orientation of the magnetic moments of neighboring particles. The dipolar fields are indicated by broken lines. (a) The magnetic moments in a chain of particles are aligned parallel to each other along the chain direction. (b) Determination of the direction of the magnetic moments of two neighboring particles with the method after [18] as described in the text. (c) Competing interactions on a third particle as a result of the superposition of the interactions described in (b) on the site of the third particle. Here $\underline{r}_1$ and $\underline{r}_2$ are the connecting vectors between the particles $1 \rightarrow 3$ and $2 \rightarrow 3$, respectively. θ_2 is the angle between $\underline{r}_2$ and the direction of the magnetic moment of particle 2, θ_1, has a value of 90°C and is not shown here for reasons of clarity.

always result in a cos()-shaped potential (i.e. there is an easy direction). It can be described by

$$E_{\text{int}} = E_0 \cdot \frac{1}{2}(\cos(\theta) + 1). \tag{1.12}$$

The function has been normalized to values between 0 and 1 in order to act analogous to equation (1.2). A superposition of unidirectional potentials with different phases and strengths, again result in a unidirectional potential. This can be shown by using the concept of a phasor

$$A\cos(x+\theta) = \text{Re}\left(A\exp(i(x+\theta))\right) \tag{1.13}$$

and calculating therewith the superposition

$$\begin{aligned} A_1\cos(x+\theta_1) + A_2\cos(x+\theta_2) &= \text{Re}(A_1\exp(ix)\exp(i\theta_1)) && (1.14)\\ &+ \text{Re}(A_2\exp(ix)\exp(i\theta_2)) && (1.15)\\ &= A_3\cos(x+\theta_3). && (1.16) \end{aligned}$$

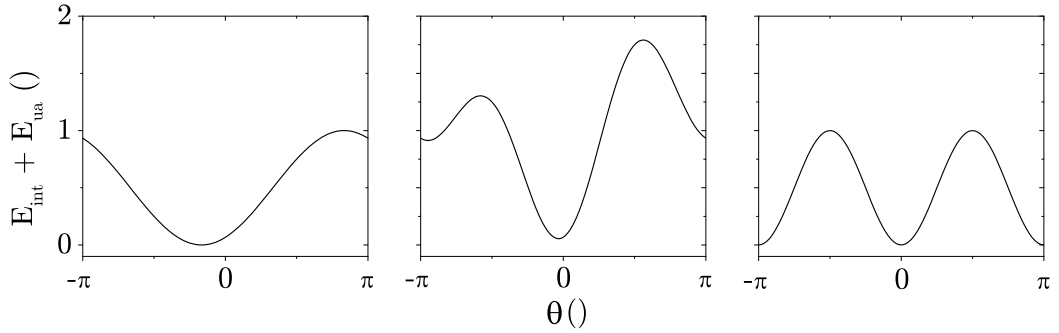

Figure 1.4: Superposition of a uniaxial E_{ua} and unidirectional potential E_{int} after the equation $E_0 \cdot \frac{1}{2}(\sin(\varphi - \pi/3) + 1) + KV \sin(\varphi)^2$ for $KV = 0$, $E_0 = 1$; $KV = 1$, $E_0 = 1$ and $KV = 1$, $E_0 = 0$ (from left to right).

The blocking temperature of the system depends on the interaction energy E_0 and the strength of the anisotropy constant K as well. Since both of them must not necessarily be parallel to each other, complex potentials might occur. Examples are given in figure 1.4 for a fixed phase of $-\pi/3$ and different strengths of the interparticle interactions and the anisotropy energy.

Exchange interaction between nanoparticles in close contact

Next to dipole-dipole interactions, exchange interactions between the surface atoms of particles in close contact play an important role in interparticle interactions, especially for ferrimagnetic or antiferromagnetic particles, whose net magnetic moments and hence the dipole-dipole interaction between them is small compared to ferromagnetic particles. These might be either direct exchange or super exchange interactions. In contrast to the dipole-dipole interactions, exchange interactions tend to align the particle moments parallel to each other, which results in an ordered state, being called "super-ferromagnetism" [23]. The influence of the exchange interactions on the magnetic energy of a particle was found to be well described by a mean field [24]

$$E = -J_{\mathrm{eff}} \underline{M}(T) \cdot \langle \underline{M}(T) \rangle \,. \tag{1.17}$$

Here, $J_{\mathrm{eff}} \langle \underline{M}(T) \rangle$ represents an effective interaction mean field from the neighboring particles, $\underline{M}(T)$ is the sublattice magnetization and $J_{\mathrm{eff}} = \sum_i J_{ij}$ is the effective exchange coupling constant. This interaction has a unidirectional character as well.

However, surface spin canting (described below) is able to influence the effective exchange interactions between the particles (i.e. decrease its strength).

A transition from a super-spin glass to a super-ferromagnetic groundstate has been observed with increasing concentration of Fe clusters in an Ag matrix [25]. When

the concentration of Fe clusters exceeds a critical value, the clusters are in very close contact and form bigger structures of ferromagnetically ordered clusters, due to exchange interactions, resulting in the super-ferromagnetic groundstate of the system.

RKKY-interaction

If the magnetic nanoparticles are embedded in a matrix of a metallic, non-magnetic material, RKKY interactions between the particles via the conduction band of the host material may occur. The interaction between two spherical clusters, whose radius r is much smaller than their distance R, can be described by [26]

$$E = \tilde{J}_0 \frac{\cos(2k_\mathrm{F}R)}{R^3}. \tag{1.18}$$

Here, J_0 is the effective coupling constant and k_F is the Fermi-wave vector. In contrast to dipole-dipole interactions, RKKY-interactions exhibit an oscillatory character, which results in a superspinglass groundstate of a system with randomly distributed magnetic clusters in a non-magnetic host matrix.

Effect on T_B

The effect of the interparticle interactions on the relaxation time depends on the strength of the interactions. It has been shown for weakly interacting maghemite nanoparticles, that the blocking temperature T_B decreases with increasing interaction [27, 11]. This behavior has been explained by calculating the average fluctuation rate for weak interparticle interactions and different angles between the direction of the interparticle interactions and the easy axis (compare to section 1.3.3 and 1.3.4).

If the interparticle interactions are much stronger than the anisotropy energy, the energy barrier, the magnetization direction has to overcome, is increased, relative to the barrier without interparticle interactions and hence the blocking temperature is increased as well.

Freezing behavior

The freezing of the non-interacting particles can be described by the Néel-Brown equation (see equation 1.3 and the next section) and therefore yields different blocking temperatures for different techniques due to the different experimental timescales. In contrast, particles experiencing magnetic interparticle interactions exhibit a collective freezing over a small temperature range, once the interactions become relevant. Hence the blocking temperature is similar for different techniques.

By performing temperature dependent AC-susceptibility measurements for different frequencies of the applied magnetic field, it is possible to gain information about

the presence of interparticle interactions through the different freezing behaviors of interacting and non-interacting particles (see section 2.2.2).

Comment

When interparticle interactions are discussed in the following, they should always be understood as effective average magnetic interparticle interactions. The particles do interact magnetically even in the superparamagnetic regime at temperatures far above the blocking temperature. However, these interactions do basically not affect the magnetic properties of the particles, since they average to zero due to the fast fluctuations of the particles. Therefore, the term "effective" always denotes interparticle interactions, that do not average to zero due to fast fluctuations of the particles. The term "average" accounts for the average value of the distribution of the interparticle interactions in case of a super-spin glass groundstate.

1.3 Relaxation time of magnetic nanoparticles

Various models describing the temperature dependence of the relaxation time of magnetic nanoparticles were proposed in the literature throughout the last decades. The most important approaches will be reviewed in this chapter.

1.3.1 The Néel-Brown expression

The first expression presented is valid for particles with a uniaxial anisotropy, no interparticle interactions, no external magnetic field and for $\Delta E \ll k_{\mathrm{B}}T$. It is the so-called Néel-Brown expression [12, 13]

$$\tau = \tau_0 \exp\left(\frac{\Delta E}{k_{\mathrm{B}}T}\right), \tag{1.19}$$

with

$$\tau_0 = \frac{\sqrt{\pi}}{2}\frac{\mu}{\gamma_0 \Delta E}\sqrt{\frac{kT}{\Delta E}}, \tag{1.20}$$

where ΔE is the energy barrier, μ is the magnetic moment of the particle and γ_0 is the gyromagnetic ratio. It was already presented in the first section of this chapter (equation (1.3)). This equation can still be found in almost every publication on superparamagnetism up to now, despite its limited applicability. The reason is, that it is generally used to explain the features of the particular measurement qualitatively through the variation of the relaxation time τ, typically with temperature. A rough estimation of τ is therefore sufficient in most of the cases. Furthermore, the more detailed models presented in the following are under strong debate up to now and selecting a proper model is therefore hardly possible.

1.3.2 Solutions for any $\Delta E/k_{\mathbf{B}}T$

The limitation $\sigma = \Delta E/k_{\mathrm{B}}T \gg 1$ of the Néel-Brown expression is based on an approximation Brown used in the calculation (see e.g. [28]). An exact solution of this problem for all values of $\Delta E/k_{\mathrm{B}}T$ was presented in [28]. Since this analytical expression is very complex, the approximate expression

$$\tau = \tau_0 \left(\frac{4\sigma}{\exp(\sigma) - 1} \left(\frac{1}{1 + 1/\sigma} \sqrt{\frac{\sigma}{\pi}} + 2^{-\sigma - 1} \right) \right)^{-1}, \tag{1.21}$$

with $\tau_0 \propto VM_s$ [29], has been presented as well [30].

1.3.3 The model after Dormann *et al.*

A model based on the Néel-Brown expression but including interparticle interactions has been presented by Dormann *et al.* [31]. Based on the dipole-dipole interactions between the particles, they calculated the relaxation time for weakly interacting particles to

$$\tau = \tau_0 \exp\left(\frac{\Delta E}{k_{\mathrm{B}}T} + \frac{n_1 \epsilon^2 (3z^2 - 1)^2}{3k_{\mathrm{B}}^2 T^2} \right), \tag{1.22}$$

and for strongly interacting particles to

$$\tau = \tau_0 \exp(-n_1) \exp\left(\frac{\Delta E}{k_{\mathrm{B}}T} + \frac{n_1 \epsilon (3z^2 - 1)}{k_{\mathrm{B}}T} \right), \tag{1.23}$$

with

$$\epsilon = \frac{\mu_0}{4\pi} \frac{\mu_i \mu_j}{r_{ij}^3}, \tag{1.24}$$

originating from the expression of the dipole-dipole interaction between the particles i and j, their respective magnetic moments μ_i and μ_j and the interparticle distance r_{ij}, $\epsilon(3z^2 - 1)$, being the so called interaction parameter and n_1 being the number of nearest neighbors.

After the observation of a decrease of the relaxation time for weak interparticle interactions (see above, section 1.2), this model was extended using [32]

$$\tau_0 = \tau_0(T) \tag{1.25}$$

in order to involve this effect.

1.3.4 The model after Mørup *et al.*

Another model including interparticle interactions was proposed by Mørup and Tronc [11], after calculating the global minimum and maximum of the $E(\theta)$ potential including the influence of the interparticle interactions of the neighboring

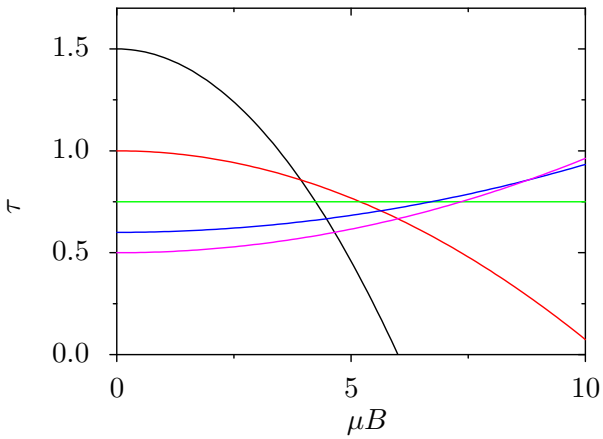

Figure 1.5: The relaxation time τ in dependence of the interaction strength calculated from the model after Mørup *et al.* [11] for the following different values of $KV/k_\mathrm{B}T$; —: 3/2, —: 1, —: 3/4, —: 3/5 and —: 1/2. For more details, see text.

particles, which results in

$$\tau = \tau_0 \exp\left(\frac{\Delta E}{k_\mathrm{B}T} - \frac{\mu^2 \left\langle B_i^2 \right\rangle}{3k_\mathrm{B}^2 T^2}\left(1 - \frac{3}{4}\frac{k_\mathrm{B}T}{\Delta E}\right)\right), \tag{1.26}$$

with $\left\langle B_i^2 \right\rangle$ is the average dipole interaction field, which can be expressed by

$$\left\langle B_i^2 \right\rangle = 2\left(\frac{\mu_0}{4\pi}\right)^2 \mu^2 \sum_j r_{ij}^{-6}. \tag{1.27}$$

The authors claimed, that their model is only valid for $\mu_i B_i \lesssim \Delta E$ [33] and $\mu_i B_i \ll k_\mathrm{B}T$. As it is shown in figure 1.5, the relaxation time decreases with increasing interaction strength $\mu \langle B_i \rangle$ for $k_\mathrm{B}T \lesssim KV$ and increases with increasing $\mu \langle B_i \rangle$ for bigger values of $k_\mathrm{B}T/KV$. Hence, this model includes at least qualitatively the decrease of the relaxation time for weak interparticle interaction strength. However, due to the limitations mentioned above, the graphs shown in figure 1.5 are only valid for small values of μB.

Equations (1.22), (1.23) and (1.26) have the same structure based on the Néel-Brown equation, their only differences are the numerators in the second term in the exp()-function and hence the calculation of the interaction strength.

In a direct comparison of these two models by Hansen and Mørup [34], the model by Dormann *et al.* was criticized and the better validity of the model after [11] was emphasized.

Obviously, both models for the relaxation time for particles including interparticle interactions presented here, have only limited applicability since they are only defined for a very constricted set of parameters. Furthermore, the debate between the two groups came to an abrupt end, with the death of J.-L. Dormann [7]. Therefore, the scientific discussion about the two expressions can be understood as still being open.

1.4 Surface-spin canting

In 1968, a unexpected decrease of the saturation magnetization of maghemite nanoparticles with decreasing particle size has been observed [35]. Mössbauer measurements on the same material suggested surface effects of the particles as the origin [36, 37], while finite size effects have been discussed as well (i.e. a uniform spin canting all over the particle) [38]. However, in the following years, measurements with a huge variety of experimental techniques pointed to surface spin canting as the origin of the decrease in the saturation magnetization [39, 37, 40]. In the latter, evidence for the spin glass structure of the surface layer was found. A numerical calculation of the spin structure in a 25 Å particle can be found in [41]. The thickness of the disordered surface layer was found to be 1.2 nm for $CoFe_2O_4$ particles with an average diameter of 4.3 nm [39], $\approx$ 0.9 nm for $NiFe_2O_4$ with a diameter of 4.2 nm [42], 1 - 2 nm for magnetite particles with an average diameter of 10 nm [43] and 0.4 nm for maghemite nanoparticles [44]. In another publication [45], the surface / volume ratio of iron oxide nanoparticles for different sizes has been determined from Mössbauer spectroscopy. It ranges from 80 % for particles with a diameter of 3 nm to 40 % for particles with a diameter of 10 nm. Hence, surface spin canting plays an important role, even for bigger particles with a diameter of 10 nm and more. The canting of the surface spins, especially in oxides, can be related to broken exchange bonds [46].

It was found from Mössbauer spectroscopy [47], that the fraction of frozen spins increases over a wide temperature range, hence the freezing temperature of the spins in the surface layer, T_{fr}, and the blocking temperature T_{B} are in general not the same. Above T_{fr} the spins are not frozen and hence should align with the strongest anisotropy at their site or fluctuate. Due to the broken exchange bonds, this is not necessarily the exchange interaction between the core and the surface layer, the dipole-dipole interactions between the atoms in the surface shell and the huge magnetic moment of the ordered core may contribute as well. In order to gain more information about this scenario, we performed a simulation. The orientation of the spins in the surface shell can be seen in figure 1.6 (a). In figure 1.6 (b) - (d), the energy of the interaction of the spins in the surface layer with the magnetic moment of a neighboring particle is given. In case of the relative positions in subfigures (b) and (c), the spins in the surface shell lower the energy of the system and hence increase interparticle interactions between the particles (notice the average energy

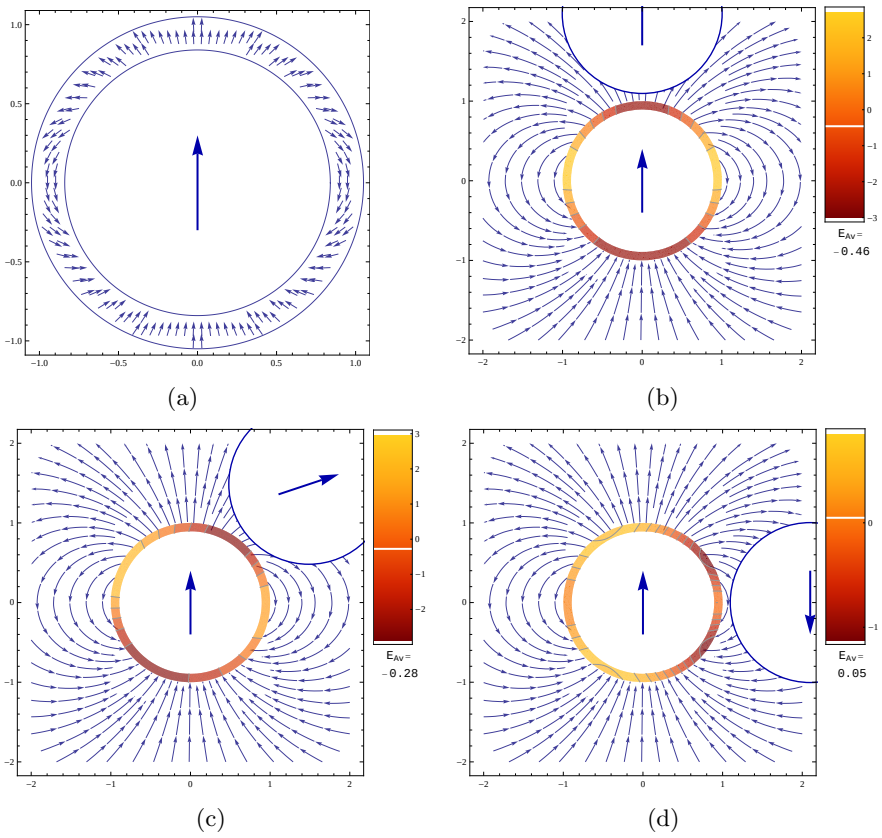

Figure 1.6: (a) Orientation of free magnetic moments in a surface shell coupled to the core by dipole-dipole interaction. (b) - (d) Energy of the interaction of the atoms in the surface shell with an orientation as shown in subfigure (a) with the ordered core of a second particle for different relative positions. The orientation of the second particle is defined by the dipole dipole interaction with the core of the first particle. The legends help to identify the strength of the energy for the different positions in the shell, below the legend, the average energy E_{Av} of the actual positions is given. The thickness of the surface layer is $0.2 \times$ the radius of the whole particle. The core - core distance of both particles is the same for every position, hence the energies are comparable.

E_{Av} below the legends). Only in the scenario in subfigure (d), the energy of the system is increased, however, by a value which is much smaller than the ones in the other two scenarios. As shown with these simulations, a surface shell coupled to the core by dipole-dipole interactions, basically increases the interparticle interaction strength between neighboring particles. Hence a freezing of the spins in the surface layer into random directions at low temperatures would result in a decrease of the strength of the interparticle interactions.

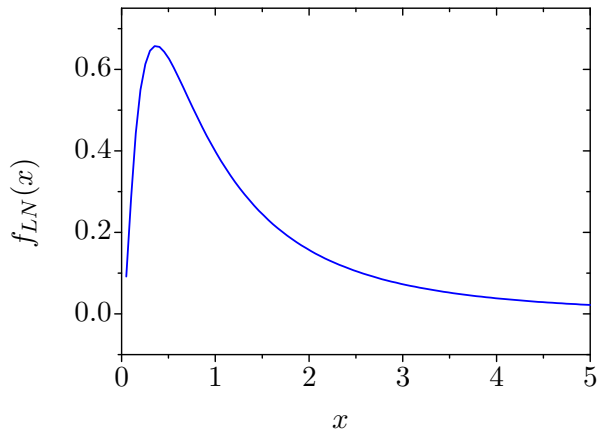

Figure 1.7: Probability density function of a log normal distribution after equation (1.28) with $\sigma = 1$ and $\mu = 0$.

1.5 Particle-size distribution

Real particle systems always have a finite particle-size distribution. The most common function to describe particle size distributions is the probability density function of the log-normal distribution

$$f_{LN} = \frac{1}{x\sigma\sqrt{2\pi}} \exp\left(-\frac{(\ln x - \mu)^2}{2\sigma^2}\right), \quad x > 0, \tag{1.28}$$

where μ is the mean deviation and σ is the standard deviation. The function is plotted in figure 1.7.

For non-interacting particles, a particle-size distribution leads to a distribution of blocking temperatures T_B, since the anisotropy energy barrier scales with the particle volume.

In the case of interacting particles, the particle-size distribution plays a minor role in the freezing process, since the interparticle interactions are averaged over the neighboring particles and hence the particle-size distribution is not relevant (see above).

Experimental methods that help to determine the particle-size distribution are discussed in the next chapter.

1.6 Materials

The most common material used for the production of magnetic nanoparticles is γ-Fe_2O_3 (maghemite). It has been used in numerous studies up to now and will be

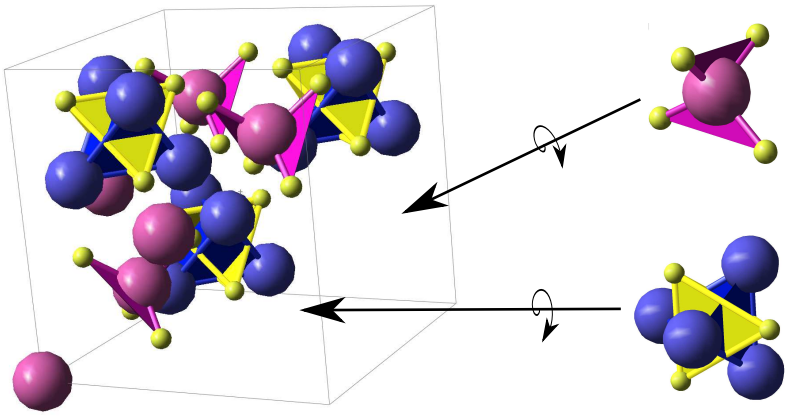

Figure 1.8: Crystal structure of magnetite with a highlighted tetrahedral (up) and octahedral group (down) (extracted and turned). Here, • are the oxygen ions, ● are the A ions and ● are the B ions.

a part of this work as well. However, the crystal structure of maghemite is closely related to the crystal structure of magnetite, Fe_3O_4, which will be described at first.

1.6.1 Magnetite

Magnetite crystallizes in the FD3m space group and can be described by the general formula AB_2O_4, where A are ions at tetrahedral sites and B are ions at octahedral sites. In one unit cell, four octahedral groups and four tetrahedral groups can be found. The first consists of four B ions and four O ions, while the tetrahedral group consists of one A ion and again four O ions. Additional A ions are situated at the corner and the surface of the cube. The complete unit cell and the two groups are shown in figure 1.8. This structure is called normal spinel. An example is bulk $ZnFe_2O_4$, with the divalent Zn^{2+} ions being on the tetrahedral site and the trivalent Fe^{3+} ions being on the octahedral site.

However, it is possible, that the tetrahedral sites are occupied by half of the B ions and the octahedral sites by the remaining A and B ions. This structure is called inverse spinel and can be described by the general formula $B(AB)_2O_4$. In the case of magnetite, the A ions are trivalent iron ions (Fe^{3+}) and the B ions are divalent and trivalent iron ions (Fe^{2+} and Fe^{3+}). Intermediate states between the normal spinel and the inverse spinel are described by introducing the inversion parameter x to the general formula which results in $A_xB_{1-x}(A_{1-x}B_{1+x})_2O_4$, with $x = 0$ resulting in an inverse spinel and $x = 1$ in a normal spinel.

In order to understand the magnetic properties of magnetite, one has to take a closer look on the individual ions. The trivalent Fe^{3+} ions have the electronic configura-

tion $[Ar]4s^23d^5$ while the divalent Fe^{2+} ions have the configuration $[Ar]4s^23d^6$. The Fe^{2+} and Fe^{3+} ions on the octahedral sites are coupled via double exchange, which is a ferromagnetic exchange between ions with a different valence where the additional electron delocalizes between the two ions and hence lowers its energy. The tetrahedral Fe^{3+} ions are coupled to the Fe^{3+} on the octahedral sites by an antiferromagnetic superexchange coupling via an O^{2+} ion. Hence the moments of the Fe^{3+} on the tetrahedral and octahedral sites are aligned antiparallel and compensating themselves and only the magnetic moment of the Fe^{2+} is left. Therefore, magnetite is a ferrimagnet [10].

Bulk Fe_3O_4 undergoes a phase transition at around $T_V \approx 125\,\mathrm{K}$, the so-called Verwey transition, named after its discoverer [48]. At the Verwey transition, electron hopping between Fe^{2+} and Fe^{3+} sets in, leading to a mixed valence state. A change in the conductivity and in the crystal structure occurs at this transition. It has been investigated very well since its discovery, however, its physical origin is still under discussion up to now. A comprehensive review with the historical context has been presented by Walz [49]. T_V strongly depends on the scale of the sample, it decreases and smears out with decreasing particle size. While T_V has still the bulk value for 150 nm particles, it decreases down to $\approx 20\,\mathrm{K}$ for particles with an average diameter of 50 nm and vanishes for smaller particles [50]. However, in another study [51], the Verwey transition has been observed in smaller particles as well. Therefore one can assume, that not only the particle size but also properties like the fraction of defects or the presence of other phases play an important role (e.g. magnetite is frequently accompanied by maghemite, which is hard to distinguish from magnetite with common techniques and does not exhibit a Verwey transition and therefore is capable of reducing the volume of magnetite within the particles).

1.6.2 Maghemite

The structural properties of maghemite (γ-Fe_2O_3) are closely related to those of magnetite. Both exhibit a spinel structure, with the difference, that the octahedral sites in maghemite are not fully occupied and cation vacancies exist instead, which is manifested in the formula $(Fe^{3+})_8[Fe^{3+}_{5/6}\,\square_{1/6}]_{16}O_{32}$. There are different possibilities for vacancies $\square$ at the octahedral sites. A random distribution of the vacancies over the octahedral sites would result in the same space group like magnetite, Fd3m [52, 53]. However, various types of space groups for maghemite have been identified in the past, indicating at least a partially ordering of the vacancies on certain octahedral sites (see for example [54, 55]). In actual publications, ordered vacancies seem to be the exception and it is still not clear, in which cases the vacancies are disordered, as pointed out by [56]. Bastow *et al.* [57] found increasing vacancy disordering with decreasing particle size for ball-milled maghemite nanoparticle from ^{57}Fe-NMR in contrast to [58], where indications for ordered vacancies in particles with an average size of 240 nm × 30 nm were found from powder neutron and X-ray diffraction.

The presence of vacancy order / disorder can in principle be verified by Mössbauer spectroscopy. As pointed out in, [59] the magnetically split spectrum at low temperatures looks asymmetric in case of ordered vacancies and symmetric otherwise. However, the linewidth of spectra measured on magnetic nanoparticles using Mössbauer spectroscopy is typically strongly enhanced, which makes the observation of this effect typically hardly possible.

Maghemite is as well ferrimagnetic and has a Néel-temperature of approximately 950 K and a saturation magnetization of 87.4 emu/g [36].

1.6.3 Distinguishing between magnetite and maghemite

It was found, that magnetite nanoparticles transform to maghemite at a temperature of approximately 473 K [60], which easily leads to the coexistence of both, magnetite and maghemite in one sample e.g. in case of heating during the preparation process. However, due to their similar structural properties, the differentiation between magnetite and maghemite is not very easy, especially in the case of nanoparticles, where the small scales lead to a broadening of the spectral shapes in most spectroscopic methods like Mössbauer spectroscopy and NMR, for example. However, it was discovered, that Raman-spectroscopy is a reliable tool to distinguish between the two materials, even in case of nanoparticles, since the Raman spectra for maghemite and magnetite have a different shape. Examples for the spectra for different iron oxides are presented in [61]. However, one has to be careful when measuring the Raman spectra, since too much laser power and a too small spot size can result in a heating of the sample at the measuring position and hence to a undesired transformation of magnetite to maghemite during the measurement.

A distinction between magnetite and maghemite is also possible from a careful analysis of spectra measured with x-ray photoelectron spectroscopy, as discussed in [62, 63].

1.6.4 Various ferrites

Next to the ferrites containing only iron and oxygen, numerous other types exist. Their physical properties strongly depend on the added material and on the degree of inversion x. Typical examples are $ZnFe_2O_4$ and $CoFe_2O_4$. More details about $ZnFe_2O_4$ can be found in chapter 3.

1.6.5 Other types of iron oxides

Another iron oxide material that plays an important role in nanoparticle research is wustite (FeO). It was found, that a (partial) phase transformation from Fe_3O_4 to FeO may occur for particles with a size of $\gtrsim 15$ nm prepared via decomposition of iron oleate [64, 65].

Goethite (α-$Fe^{3+}O(OH)$) particles are investigated in [23]. This publication will be further discussed in section 2.1.3.

1.6.6 Metallic iron

The treatment of metallic nanoparticles is very difficult. Due to their large surface / volume ratio the particles oxidize easily when they are in contact with oxygen or water. One can distinguish between two types of measurements on metallic iron nanoparticles. On the one hand, in situ measurements on bare metallic nanoparticles in order to avoid the contact of the particles with air [21, 66] and on the other hand measurements on particles embedded into a matrix of another material [67, 68, 69, 70, 71, 72, 73].

Bødker *et al.* performed in situ Mössbauer measurements on bare metallic iron nanoparticles with a diameter of 2 - 4 nm on carbon supports [21, 66]. They found two main components of the magnetic hyperfine field, being connected to atoms in the core of the particles (α-Fe) with a hyperfine field of around 25 T and to atoms on the surface of the particles with a hyperfine field of around 36 - 40 T. In addition, they observed a decrease of the blocking temperature with increasing particle size. Both effects underline the strong influence of surface effects on the physical properties of metallic iron nanoparticles.

The properties of metallic iron nanoparticles embedded in different materials depend on the physical properties of the matrix [67, 68, 69, 70, 71, 72]. Detailed analysis on this topic will be presented in chapter 5 of this work. The study of nanoparticles embedded in a polymer, revealed further specifics of metallic iron nanoparticles, namely an increased magnetic moment per atom of around $2.6\,\mu_B$ compared to the bulk α-Fe value of $2.2\,\mu_B$ [73].

1.7 Preparation routes

A scientific or industrial usage of magnetic nanoparticles demands certain properties of the particles, e.g. a small size distribution, good crystallinity, well defined magnetic state for the whole particle and no agglomeration. Hence it is desirable, that the synthesis route provides particles with these properties and furthermore allows the control over important nanoparticle parameters, e.g. the size, the morphology and the material. In addition, the synthesis should be fast, environmental friendly and not involve too many materials and machines. Many different synthesis routes have been developed so far, matching the above mentioned requirements more or less.

In general, one can distinguish between two different approaches regarding the preparation of magnetic nanoparticles, the bottom-up and the top-down approach. The

latter begins with bigger clusters of the material, which are systematically minimized until the desired size is achieved. A common method that is based on this approach is ball milling. Although this preparation route is environmental friendly and does typically not need too much hardware, it has several disadvantages, e.g. the emergence of defects within the nanoparticles (less crystalline regions) due to the acting mechanical forces as well as a contamination of the particles with the milling material. However, as shown e.g. in [74, 75], different types of materials like mixed ferrites may be prepared by the so-called mechanochemical route.

Bottom-up approaches are based on the nucleation of clusters from monomers within a carrier medium followed by a steady growth of the nuclei to nanoparticles of the desired size. These approaches are able to produce particles of different materials, sizes and morphologies and a good crystallinity, since they do not introduce defects due to mechanical forces. A typical preparation method based on a bottom-up approach is the solvothermal synthesis, which will be discussed in more detail in chapter 4. In this method, $Fe(acac)_3$ is used as a precursor and and mixed with a solvent. The mixture is heated up, which results in the formation of nuclei and a subsequent development and growth of nanoparticles.

Another preparation method, which will be discussed in this work, is vapor co-deposition. Two immiscible materials are vaporized and are accumulating again on a substrate, which results in thin films. The formation of clusters of one of the materials in a matrix of the other material can be achieved by choosing very different vaporization rated for both materials. More details about this method can be found in chapter 5.

Chapter 2

Experimental methods

A wide range of different experimental methods can be used in order to analyze the physical properties of nanosized particles, e.g. AC- and DC-susceptibility, NMR and electron micrographs (TEM). An outstanding role in this context plays Mössbauer spectroscopy, which is an extraordinary helpful tool when studying this type of samples.

However, details of the analysis of the Mössbauer data are still controversially discussed. Mössbauer spectra of nanosized particles exhibit various types of shapes, depending on the material, the interaction between the particles, the fraction of a surface shell with canted spins on the whole particle, etc. Plenty of different models have been proposed in the literature during the last decades, yet none of them involves all the different effects and hence can be used as a universal model. Furthermore, up to now, no detailed overview over the different models has been presented.

In this chapter, the different experimental methods used to examine magnetic nanoparticles with a special focus on Mössbauer spectroscopy will be discussed. At first, a short introduction to Mössbauer spectroscopy will be given, followed by a description of the most important models which can be used for the interpretation of Mössbauer spectra of magnetic nanoparticles. The section is divided in a discussion of models, which allow the simulation of the Mössbauer absorption spectrum itself and a model, that allows the simulation of the temperature dependence of a single Mössbauer parameter (see below). For simplicity reasons, $\hbar = 1$ in the following.

In the subsequent sections, further techniques used in this work to study the properties of magnetic nanoparticles in this work are discussed.

2.1 Mössbauer spectroscopy

2.1.1 Introduction

The experimental technique is based on the Mössbauer effect, discovered by Rudolf L. Mößbauer in 1957 [76]. He examined the nuclear absorption of 129 keV γ-radiation by a natural Ir crystal. A ^{191}Ir source was mounted on a rotating disc, which offered the possibility to regulate the velocity v_{rel} of the source relative to the absorber. Due to the Doppler effect, the energy of the radiation depends on v_{rel}. Hence Mößbauer was able to measure the absorption of the crystal for different energies. This procedure is very similar to the experimental realization of the Mössbauer spectroscopy used nowadays (see below).

However, the most important result of Mössbauer's work was achieved by measuring the temperature dependent cross section of a system where source and absorber are at rest with respect to each other. At that time, it was believed that the emission- and absorption line are not centered around the same energy, since the γ-quantum transfers momentum to its origin ion. Hence it was expected, that the cross section increases with increasing temperature, since the width of the emission- and absorption lines and therewith their overlap increases with temperature as well. However, Mössbauer observed a completely different behavior as expected. He measured an increase of the cross section with decreasing temperature. Mössbauer interpreted this effect with a complete absorption of the momentum of the γ-quantum by the crystal lattice, while the energy of the quantum is not lowered. Since the γ-quantum is able to create a phonon, the fraction of this recoil-less emission is strongly connected to the presence of phonons in the material, which decreases with decreasing temperature. Therefore, the fraction of recoilless emitted γ-quanta increases with decreasing temperature, which results in the observed increase of the absorption. The temperature dependent recoil-less fraction of the radiation can be calculated using the Mössbauer-Lamb factor. The effect of the emission of the γ-radiation without a shift of the energy is called recoilless emission, or Mössbauer effect. For this discovery and its correct interpretation, Mößbauer received the Nobel price in physics in 1961.

For more details about the discovery of the Mössbauer effect, it is referred to [77].

Based on the Mössbauer effect, an experimental method was developed, which uses the particularly small linewidth and well defined energy of the emitted γ-rays, called Mössbauer spectroscopy.

The experimental procedure in modern Mössbauer spectroscopy is based on the measurement of the fraction of absorbed γ-quanta by a sample containing specific probe atoms whose nuclear transitions match the energy of the γ-rays for different values of E_γ around the original value. In this work, the probe atoms are ^{57}Fe.

With this method it is possible, to monitor the transition of the nuclear spin from the ground state to the excited state, $I_g \rightarrow I_e$, in the nucleus of the probe atom. The width of the γ-ray line is small enough to observe changes in the hyperfine structure of the probe atoms and therewith to gain information about their electronic and magnetic properties. In a Mössbauer spectrum, the relative transmission is plotted relative to the excitation energy of the free nucleus (represented here by the Doppler velocity of the source, which is proportional to the energy).

In the following section, static hyperfine interactions and their influence on the Mössbauer spectrum are discussed.

2.1.2 Static hyperfine interactions

Static electric and magnetic interactions between the nucleus and its environment lead to a shifting and / or splitting of the hyperfine patterns. This can be observed in the Mössbauer spectrum. The most important effects are described in this section. More details about the static hyperfine interactions in Mössbauer spectroscopy can be found e.g. in [78] or [79]. The following section is based on both sources.

Isomer shift and quadrupolar interaction

As discussed in [79], in the framework of a point-charge model, the energy arising from the interactions of electric charges (described by their potential at the site of the nucleus $\phi(\underline{r})$) in the surrounding of the nucleus (with a distribution of positive electric charges $\rho(\underline{r})$) can be described by

$$E = \int \rho(\underline{r})\phi(\underline{r})\mathrm{d}^3 r. \tag{2.1}$$

A Taylor series expansion of $\phi(\underline{r})$ gives

$$\begin{aligned} E &= \phi_0 \int \rho(\underline{r}) d^3 r \\ &+ \sum_{\alpha=1}^{3} \left(\frac{\partial \phi}{\partial x_\alpha}\right)_0 \int \rho(\underline{r}) x_\alpha d^3 r \\ &+ \frac{1}{2} \sum_{\alpha,\beta} \left(\frac{\partial^2 \phi}{\partial x_\alpha \partial x_\beta}\right)_0 \int \rho(\underline{r}) x_\alpha x_\beta d^3 r \\ &+ \ldots \end{aligned} \tag{2.2}$$

The first term only describes the Coulomb interaction at the site of the nucleus and can be neglected here. The second term represents the dipole moment of the charges

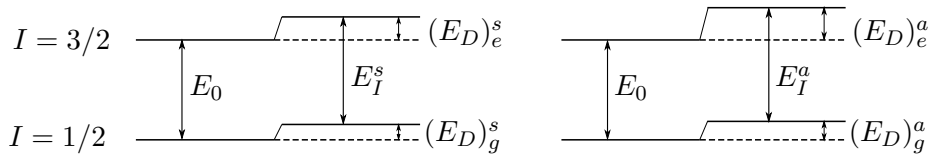

Figure 2.1: Splitting of the energy levels resulting in the isomer shift. The left term scheme represents the source (index s), while the right term scheme represents the sample (absorber) (index a). Note that $E_s \neq E_a$.

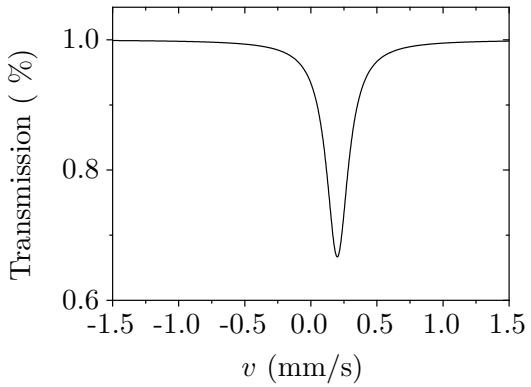

Figure 2.2: Simulation of a single line Mössbauer spectrum made with an isomer shift of +0.2 mm/s.

in the nucleus, which is zero. However, the third term can be rearranged to

$$\frac{1}{2}\sum_{\alpha,\beta}\left(\frac{\partial^2\phi}{\partial x_\alpha \partial x_\beta}\right)_0 \int \rho(\underline{r}) x_\alpha x_\beta d^3r = \frac{1}{6}\sum_{\alpha}\left(\frac{\partial^2\phi}{\partial x_\alpha^2}\right)_0 \int \rho(\underline{r}) r^2 d^3r + \frac{1}{2}\sum_{\alpha}\left(\frac{\partial^2\phi}{\partial x_\alpha^2}\right)_0 \int \rho(\underline{r})\left(x_\alpha - \frac{r^2}{3}\right) d^3r. \tag{2.3}$$

Both terms of this last expression are relevant for Mössbauer spectroscopy.

Using the relation for the average quadratic radius of the nucleus,

$$< r^2 >= \frac{1}{Ze}\int \rho(\underline{r}) r^2 d^3r, \tag{2.4}$$

and

$$(\Delta\phi)_0 = \sum_\alpha \phi_{\alpha\alpha} = \frac{e}{\epsilon_0}\left|\psi(0)\right|^2, \tag{2.5}$$

with $\phi_{\alpha\alpha} = \left(\frac{\partial\phi}{\partial x_\alpha}\right)_0$, which follows from the Poisson-equation, the first term can be rearranged to

$$E_I = \frac{Ze^2}{6\epsilon_0}\left|\psi(0)\right|^2 < r^2 > . \tag{2.6}$$

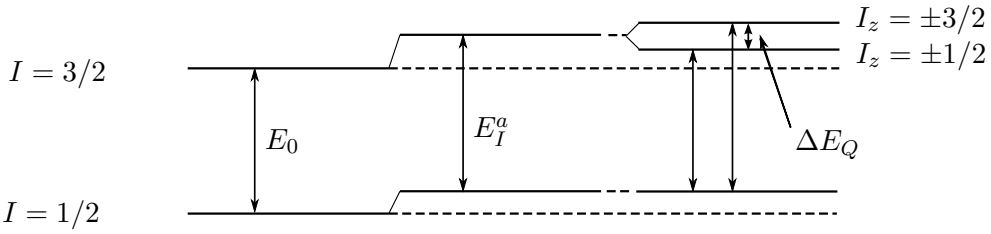

Figure 2.3: Splitting of the $I = 3/2$ level due to the nuclear quadrupolar interaction.

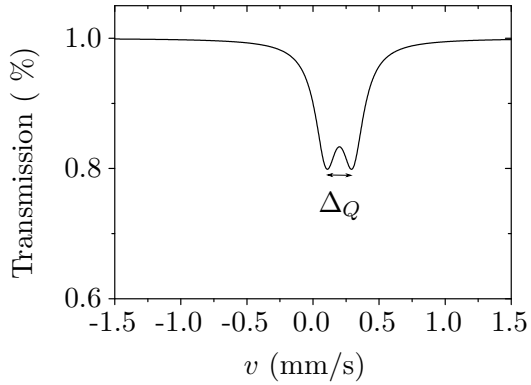

Figure 2.4: Simulation of a Mössbauer spectrum in the presence an isomer shift of $+0.2\,\mathrm{mm/s}$ and a quadrupolar splitting with $\Delta_Q = 0.2\,\mathrm{mm/s}$.

This monopole energy describes a shift of the energy level, which depends on the average quadratic radius of the nucleus, $< r^2 >$, and on the probability of finding an electron at the site of the nucleus, $|\psi(0)|^2$. The difference between the shift of the source E_I^s and the absorber E_I^a, $\delta = E_I^s - E_I^a$ is the isomer shift. It moves the spectrum along the velocity axis, as demonstrated in figure 2.1 and in figure 2.2, respectively.

Since the last integral in equation (2.3) equals the equation for a quadrupole moment for $x_\alpha = z$, the whole term can be summed up to

$$E_Q = \frac{e}{6} \sum_\alpha \phi_{\alpha\alpha} Q_{\alpha\alpha} = \frac{e}{6} \sum_\alpha V_{\alpha\alpha} Q_{\alpha\alpha}, \tag{2.7}$$

describing the interaction of an electric field gradient at the nucleus, V, with its quadrupolar moment, Q. In case of a field gradient with axial symmetry, the quadrupolar energy results in

$$E_Q = \left[3I_z^2 - I(I+1)\right] \frac{eQV_{zz}}{4I(2I-1)}, \tag{2.8}$$

where V_{zz} is the last element in the trace of the matrix describing the electric field gradient at the nucleus. The quadrupolar energy results in a splitting of the $I = 3/2$ level into two sublevels with an energy difference ΔE_Q. This energy difference can be observed as the quadrupolar splitting in the Mössbauer spectrum. One can find from this equation, that a non-vanishing quadrupolar interaction results in a splitting of the Mössbauer line into a doublet, as shown in figure 2.3 and 2.4. A quadrupolar splitting happens when a non-vanishing electric field gradient at the site of the core is present, typically in the case of a non-cubic arrangement of the atoms around the probe atom.

The second order Doppler shift

This effect is based on the thermal motion of the lattice atoms. The relativistic description of the Doppler effect yields a term, where the quadratic average velocity of the lattice atoms is included. This additional term describes a shift of the energy of the γ-rays and therewith a shift of the complete Mössbauer spectrum along the v-axis, similar to the aforementioned isomer shift. The effect depends on the temperature difference between the absorber and the source, ΔT. An estimation of the second order Doppler shift for ^{57}Fe, using Dulong-Petit's law [79] (i.e. in the high T limit for $T > \Theta_D$), gives

$$-\frac{\mathrm{d}\omega}{\mathrm{d}T}\frac{1}{\omega_0} = 2.4 \cdot 10^{-15}\,\mathrm{K}^{-1}. \tag{2.9}$$

For $\Delta T \approx 200\,\mathrm{K}$, one expects a frequency shift which corresponds to a shift of the complete spectrum in the order of magnitude of $0.1\,\mathrm{mm/s}$.

The isomer shift and the second order Doppler shift both result in a shift of the spectrum along the v-axis, which makes a distinction between both effects complicated.

The magnetic hyperfine interaction

The magnetic hyperfine interaction is based on the interaction between the magnetic dipole moment of the nucleus with a magnetic field H at the site of the nucleus. Under the influence of magnetic hyperfine interactions, a Zeeman splitting occurs and the degeneracy of the I_z states is lifted. The selection rule for $M1$ radiation, $\Delta I_z = 0, \pm 1$ results in six possible transitions between the $I = 1/2$ groundstate into the $I = 3/2$ state. The Mössbauer spectrum therefore splits into six different lines, as it can be seen in figure 2.6.

The magnetic hyperfine field is be described by the interaction of the nuclear spin I with the spin of the electronic system $H = \underline{I}\,\underline{\underline{A}}\,\underline{S}$, where $\underline{\underline{A}}$ is the so-called hyperfine tensor. In most cases, this Hamiltonian can be simplified to an effective Zeeman interaction $H = \underline{B}_{\mathrm{eff}}\underline{I}$, with the "effective magnetic hyperfine field", $\underline{B}_{\mathrm{eff}}$. In the

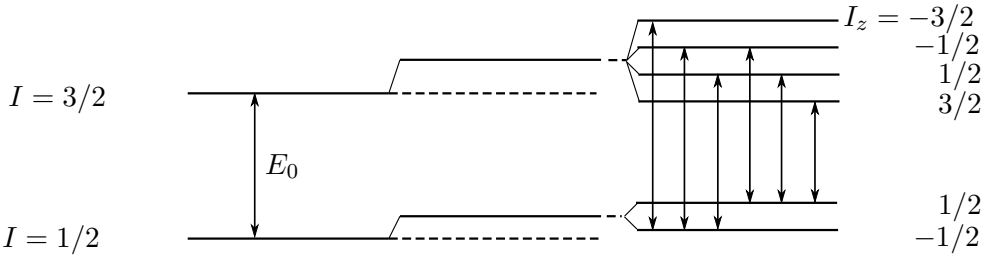

Figure 2.5: Magnetic splitting of the $I = 3/2$ and the $I = 1/2$ level and the corresponding allowed transitions.

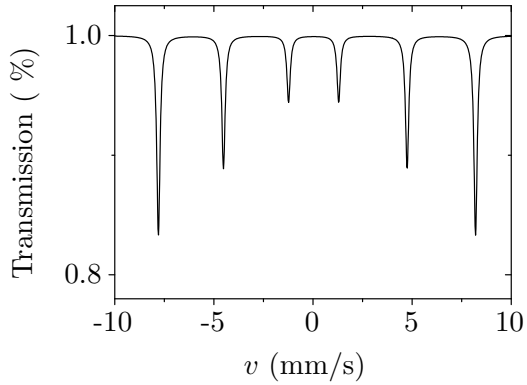

Figure 2.6: Simulation of a Mössbauer spectrum in the presence of an isomer shift of +0.2 mm/s and a magnetic splitting with a value of 16 mm/s between the outer lines. This value corresponds to a magnetic field of about 49.5 T.

following, $\underline{B}_{\mathrm{eff}}$ will be denoted as the magnetic hyperfine field $\underline{B}_{\mathrm{hyp}}$.

The different contributions to $\underline{B}_{\mathrm{hyp}}$ are

$$\underline{B}_{\mathrm{hyp}} = \underline{B}_{\mathrm{el}} + \underline{B}_{\mathrm{ex}}. \tag{2.10}$$

$\underline{B}_{\mathrm{el}}$, which is proportional to the electronic spin $\underline{B}_{\mathrm{el}} \propto \langle S_z \rangle$, denotes the magnetic fields at the nucleus with an electronic origin. It contains a contribution of the orbital angular momentum of the electrons, $\underline{B}_{\mathrm{oam}}$ and a contribution arising from the dipole-dipole interaction between the nucleus and the electrons, $\underline{B}_{\mathrm{dip}}$. However, the main contribution on the local magnetic field at the ^{57}Fe nucleus arises from the Fermi-contact term $\underline{B}_{\mathrm{Fer}}$, which is based on the uncompensated s-electron density in the nucleus. The magnitude of $\underline{B}_{\mathrm{Fer}}$ is of the order of some 10 T.

The influence of an external magnetic field $\underline{B}_{\mathrm{ex}}$ on $\underline{B}_{\mathrm{hyp}}$ contains basically three components. Next to the contribution of the external field itself, $\underline{B}_{\mathrm{ext}}$, the influence of the neighboring atoms due to the polarization, which is the so-called Lorentz-field $\underline{B}_{\mathrm{Lor}} = \frac{4\pi}{3}\mu_0 \underline{M}$ and the demagnetization field $\underline{B}_{\mathrm{DM}} = -\mu_0 D M'$, where D is

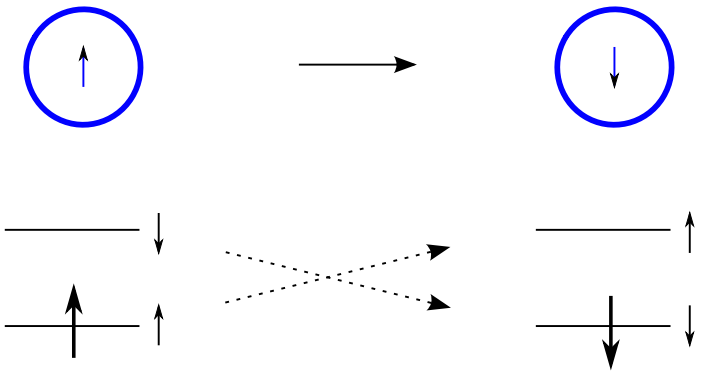

Figure 2.7: Flip of the particle moment in analogy to spin flips within a Kramers doublet with effective spin 1/2.

the geometry dependent demagnetization factor and M' is the magnetic moment per volume. However, the strength of $\underline{B}_{\mathrm{ex}}$ has typically a maximum value of a few hundreds of T and is rather small compared to $\underline{B}_{\mathrm{el}}$.

2.1.3 Magnetic dynamics in Mössbauer spectroscopy

Basics

In this section, the most important models that are used to describe the Mössbauer spectra of fluctuating magnetic fields, are discussed. However, at first, the difference between the thermally activated spin flips of an ordinary paramagnet are compared to the spin flips of a superparamagnetic particle.

In the simplest case, the electronic spin system can be described by a Kramers doublets with effective spin-$\frac{1}{2}$. For a normal paramagnet, the Kramers doublet is degenerate above T_{C}. Below T_{C}, when the magnetic interaction between the atoms sets in, the degeneration of the doublet is lifted, the population of the two states becomes unequal and is determined by Boltzmann statistics. The magnetic moment of the doublet $g \langle S_z \rangle \mu_B$ is increasing with decreasing T due to a stronger population of the energetically lower spin state. Therefore, the magnetic hyperfine field B_{hyp}, which is proportional to $\langle S_z \rangle$ increases with decreasing temperature as well.

A magnetic nanoparticle below T_{C}, is made up of multiple magnetic moments which are coupled through exchange interactions. Therefore, each of these moments can be described by a non-degenerate Kramers doublet. The reason for the non-magnetic Mössbauer pattern for $T_{\mathrm{B}} < T < T_{\mathrm{C}}$ is therefore not a equal population of the two states in the non-degenerate Kramers doublet. In fact, when the magnetic moment of the nanoparticle revolves, the state with the higher energy and the state with the lower energy of the Kramers doublet are changing positions (see figure 2.7). Therefore, the state at the lower level experiences a spin flip, although not being thermally

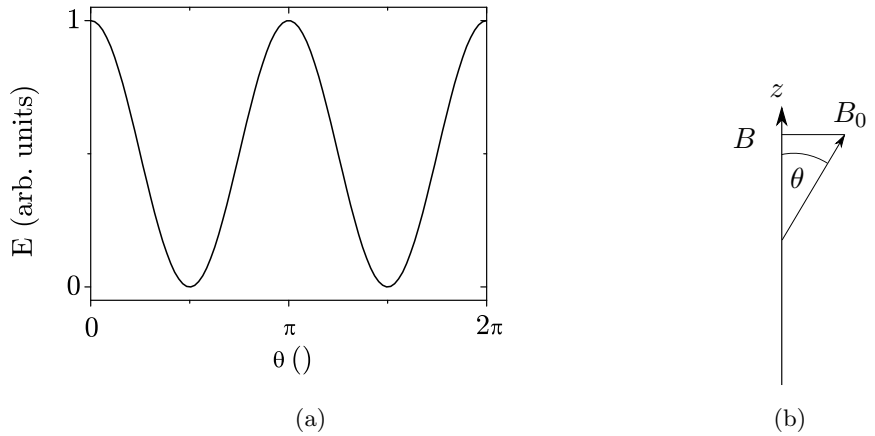

Figure 2.8: (a) Uniaxial anisotropy, the minima are at $\theta = 0$ and $\theta = \pi$, furthermore $KV = 1$. (b) Sketch to illustrate the $B = B_0 \cos(\theta)$ dependence, the z-axis lies parallel to the easy axis.

excited to the higher spin state. At temperatures $T \lesssim T_\mathrm{B}$, the time between these spin flips becomes long enough to allow the observation of a magnetically split Mössbauer pattern.

Hence, the magnetic dynamics of nanoparticles can be divided in two different processes: thermal excitations, which lift the spin in the lower state to the higher state and a change of the upper and lower state due to a revolution of the magnetic moment of the nanoparticle. Both processes occur parallel to each other, but are on different timescales.

Since thermal excitations of the spin in the state with the lowest energy are always present (i.e. $\langle S_z \rangle$ of the individual spins within the particles is a function of temperature), the system is in the fast limit (even if the superparamagnetic relaxation frequency is slow). Therefore, the effective field approximation can be used and the Hamiltonian of the magnetic hyperfine interaction can be written as [80]

$$H = \underline{\underline{A}}\,\underline{S}\,\underline{I} \sim B_\mathrm{hyp}\underline{I}. \tag{2.11}$$

The magnetically split Mössbauer spectrum at $T \lesssim T_\mathrm{B}$ of the nanoparticles presented in this work hence always consists of the familiar six line pattern. The only exception is the $Fe(acac)_3$ dispersed in benzyl alcohol spectrum presented in chapter 4, which will be discussed there.

One can distinguish three regimes with different fluctuation rates of the magnetic moment of the particles, when discussing the influence of magnetic dynamics on the Mössbauer spectrum. In the presence of magnetic hyperfine fields like those

typically observed in this work ($30 - 55\,\mathrm{T}$) the crucial parameter in all three cases is the nuclear Larmor precession frequency $\omega_L = \gamma \cdot B$ ($\approx 10^9\,\mathrm{s}^{-1}$), since it is faster than the inverse timescale of the interaction of the nucleus of the probe atom with the γ-quantum. If

- the timescale of the magnetic dynamics is much faster than that of ω_L, the magnetic hyperfine field fluctuates numerous times during one period of ω_L^{-1} and the observed hyperfine field averages to zero and no magnetic splitting of the Mössbauer spectrum is observed
- the timescale of the magnetic dynamics is much slower than that of ω_L, the magnetic hyperfine field appears to be static and a magnetically completely split Mössbauer spectrum can be observed
- the timescale of the magnetic dynamics is comparable to that of ω_L, complex hyperfine patterns are observed.

During the last decades, numerous models that try to simulate Mössbauer spectra of magnetic nanoparticles over the whole temperature range, from 0 K up to temperatures where the system is far in the superparamagnetic regime, have been published. One can distinguish between two types of models, i.e. those that simulate the Mössbauer spectrum directly and those, that simulate the temperature dependence of certain parameters (here, the average hyperfine field). This chapter begins with the discussion of models of the first type, followed by a discussion of models of the second type.

Two level relaxation model

One of the first attempts to model the effect of magnetic dynamics on the Mössbauer spectrum has been presented by Wickman *et al.* in 1966 [81]. This model is based on the relaxation in a Kramers doublet, but can however be applied to a uniaxially shaped two valley potential. The relaxation occurs between two states with hyperfine fields of the same size but different sign, which are separated by an energy barrier, denoted as KV here (see figure 2.8 (a)). If the z-axis is parallel to the easy axis, the hyperfine field fluctuates from $+B_0$ to $-B_0$, according to figure 2.8 (b). The Wickman model gives a pair of Lorentzians

$$I(\omega) = -\mathrm{Re}\left(\frac{\frac{1}{2}\left(\frac{1}{i(\omega-\omega_0)+\frac{\Gamma}{2}+\gamma}+\frac{1}{i(\omega+\omega_0)+\frac{\Gamma}{2}+\gamma}\right)}{1-\gamma\left(\frac{1}{2}\left(\frac{1}{i(\omega-\omega_0)+\frac{\Gamma}{2}+\gamma}+\frac{1}{i(\omega+\omega_0)+\frac{\Gamma}{2}+\gamma}\right)\right)}\right), \tag{2.12}$$

where ω_0 is the magnitude of the magnetic splitting, Γ is the linewidth and $\gamma \sim 1/\tau$ is the relaxation frequency. Three of those pairs have to be summed up with their corresponding area and splitting in order to simulate a Mössbauer spectrum, like it is shown in figure 2.9.

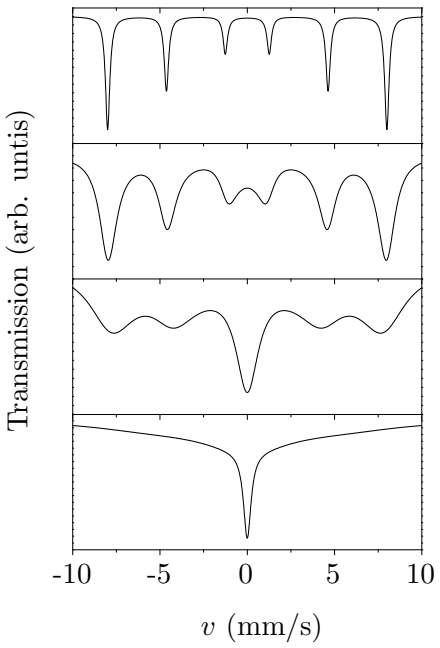

Figure 2.9: Mössbauer spectra calculated by use of the Wickman model [81] for a hyperfine splitting of 8 mm/s, $\Gamma = 0.2$ mm/s, and $\gamma = 1.2 \cdot 10^6$ Hz, $= 1.2 \cdot 10^7$ Hz, $= 3.6 \cdot 10^7$ Hz and $= 1.2 \cdot 10^8$ Hz from top to bottom, respectively.

For high and low frequencies, one can observe a behavior corresponding to the first two cases described in the beginning of this section. However, at intermediate frequencies, the spectrum smears out and finally collapses into a non-magnetic single line structure. The peak in the center of the spectrum in figure 2.9 in the case of $\gamma = 3.6 \cdot 10^7$ Hz (conversion from mm/s to Hz after [82]), is typical for magnetic dynamics with a uniaxial character, as it will be discussed later in this section.

Generalized two level model (GTL)

An expansion of the two level relaxation model, was presented in [83]. In the GTL, the lowest point of the two energy minima (see figure 2.8 (a)) are not at the same energy, but separated by an energy difference $2\Delta E$. This scenario hence describes magnetic nanoparticles in a potential, with a dominant uniaxial character combined with a small unidirectional contribution. This corresponds to the scenario given in figure 1.4 (b) in section 1.2, namely particles under the influence of interparticle interactions, that are weak compared to their uniaxial magnetic anisotropy.

Since dipole-dipole interactions between randomly distributed particles result in an distribution of interparticle interaction strength, Afanas'ev and Chuev included a

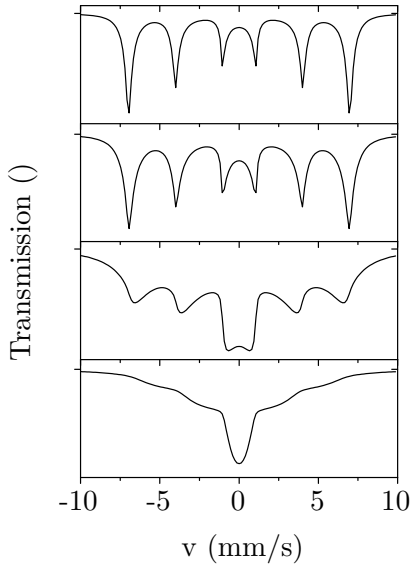

Figure 2.10: Mössbauer spectra calculated by use of the GTL model for $KV/k_{\mathrm{B}}T =$ 5, 4.54, 3.33 and 2.23 and $\tau_0 = 10^{-9}$ s from top to bottom, respectively.

normal distribution of ΔE

$$P(\Delta E, \sigma) = \frac{1}{\sqrt{2\pi}\sigma} \exp\left(-\frac{(\Delta E)^2}{2\sigma^2}\right) \tag{2.13}$$

in the model.

A set of spectra resulting from the GTL for different temperatures is shown in figure 2.10. The temperature dependence of the relaxation rate was calculated with $\tau = \tau_0 \exp(KV/k_{\mathrm{B}}T)$ and $\sigma = 0.2\,KV$.

At intermediate temperatures, asymmetric line broadening is present, which is often observed in Mössbauer spectra of interacting magnetic nanoparticles, as it is demonstrated in chapter 3.

Spherical relaxation

A model for spherical relaxation with a similar formalism has been presented as well [84]. In this case, there is no energy barrier between the different states in the potential landscape and every direction is equally probable. All three pairs of

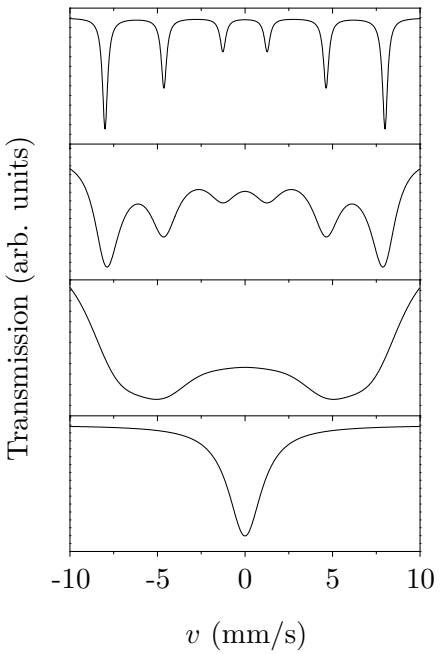

Figure 2.11: Mössbauer spectra resulting calculated on basis of spherical relaxation for $\Gamma = 0.2\,\mathrm{mm/s}$, $\omega_0 \hat{=} 8\,\mathrm{mm/s}$ and $\gamma = 1.2 \cdot 10^7\,\mathrm{Hz}$, $= 1.2 \cdot 10^8\,\mathrm{Hz}$, $= 3.6 \cdot 10^8\,\mathrm{Hz}$ and $= 5.8 \cdot 10^8\,\mathrm{Hz}$ from top to bottom, respectively.

Lorentzians are given by

$$I(\omega) = -\mathrm{Re}\left(\frac{\sum_{i=1}^{6} \frac{I(i)}{i(\omega + a(i)\omega_0) + \frac{\Gamma}{2} + \gamma}}{1 - \frac{1}{4}\gamma\left(\sum_{i=1}^{6} \frac{I(i)}{i(\omega + a(i)\omega_0) + \frac{\Gamma}{2} + \gamma}\right)}\right), \tag{2.14}$$

where $a(i)$ and $I(i)$ are parameters that can be extracted from table 2.1. An example for the simulation of the Mössbauer spectra is shown in figure 2.11. Compared to the model describing uniaxial relaxation, the Mössbauer spectrum of the spherical relaxation is not dominated by a central peak at intermediate relaxation rates, but rather exhibits a uniform collapse.

Table 2.1: Approximate values for $a(i)$ and $I(i)$.

i	1	2	3	4	5	6
$a(i)$	1	0.5790	0.1580	-0.1580	-0.5790	-1
$I(i)$	1	0.66	0.33	0.33	0.66	1

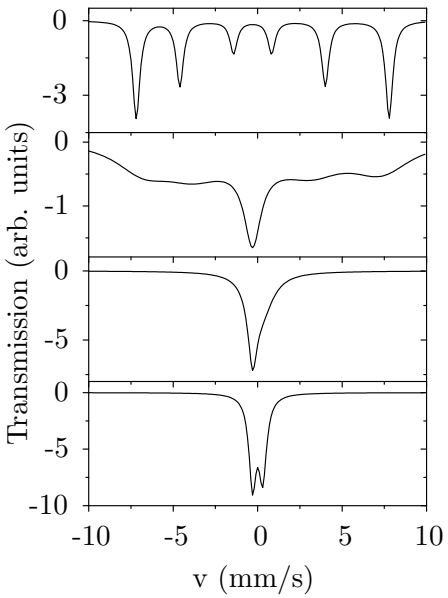

Figure 2.12: Mössbauer spectra in the case of an electrical field gradient oriented perpendicular to the direction of the fluctuating magnetic field. The parameters are: $h = 30\,\mathrm{mm/s}$, $\Gamma = 0.5\,\mathrm{mm/s}$, $Q = 0.15\,\mathrm{mm/s}$; the relaxation rate γ is $5.8 \cdot 10^6\,\mathrm{Hz}$, $2.3 \cdot 10^7\,\mathrm{Hz}$, $5.8 \cdot 10^8\,\mathrm{Hz}$ and $1.2 \cdot 10^{10}\,\mathrm{Hz}$ from top to bottom.

Fluctuating magnetic field in the presence of an electric field gradient

In 1968, M. Blume and J.A. Tjon proposed a model describing the Mössbauer spectra of a randomly fluctuating magnetic hyperfine field between values B_0 and $-B_0$ in the presence of an electric field gradient [85]. This publication includes two different simplified cases, namely the electric field gradient being oriented perpendicular or parallel to the fluctuating magnetic field. The case with the electric field gradient being perpendicular to the magnetic field is more complex, since transitions between the nuclear levels can be induced in this scenario, which is not possible in the other case. However, Blume and Tjon succeeded in finding an analytical expression that describes the Mössbauer spectrum for this scenario. Details about the calculations are not given here, but can be found in [85].

Simulations of this scenario with different fluctuation rates γ can be found in figure 2.12. In the case of slow relaxation rates, the model gives a pattern similar to a superposition of a static magnetic hyperfine field B_{hyp} with an electric quadrupolar interaction q where $B_{\mathrm{hyp}} \gg q$. At intermediate relaxation rates the spectrum begins to collapse. In contrast to the model which describes uniaxial relaxation without a quadrupolar interaction, the main peak is not at $v = 0\,\mathrm{mm/s}$ but appears shifted to negative velocities which can be attributed to the quadrupolar interaction. This scenario can be easily mistaken with the spectrum calculated from the model

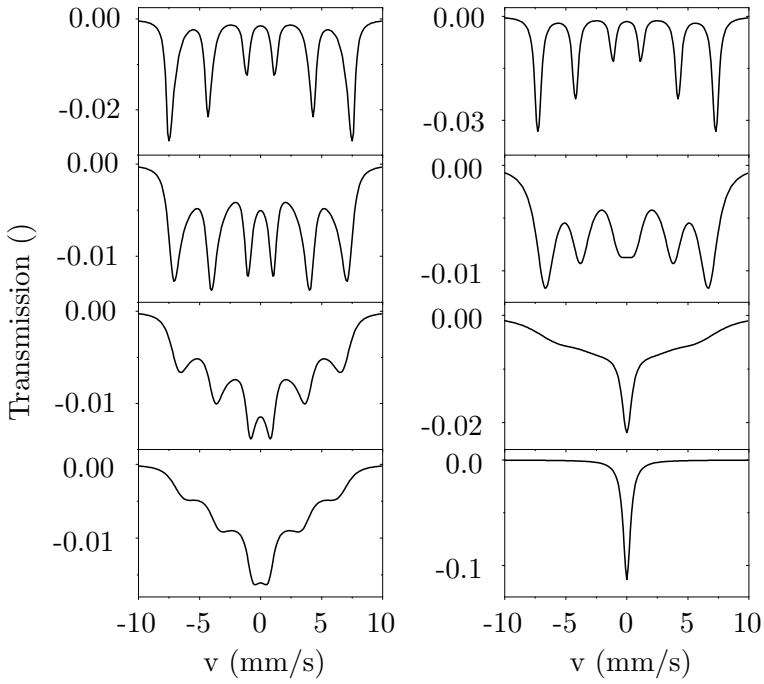

Figure 2.13: Simulations of Mössbauer spectra on the basis of the the MLR model. The simulation includes $n = 35$ steps and $\tau_0 = 10^6$ s for the left panel and $\tau_0 = 10^9$ s for the right panel. The simulation was executed with $KV/k_BT = 10$, 3, 1 and 0.1 from top to bottom for the left panel and $KV/k_BT = 10$, 5, 4 and 1 for the right panel.

with uniaxial relaxation and no quadrupolar interaction at fast frequencies, shown in figure 2.9. In order to prevent a misinterpretation of Mössbauer spectra in this scenario, a careful discussion of the data is necessary.

For fast relaxation rates, the spectrum turns into a doublet.

Multi-level relaxation (MLR) model

So far, the models describing relaxation with an uniaxial character involve only the relaxation between the two lowest states of the potential. This is an oversimplification, since in reality, the direction of the magnetic moment of nanoparticles is able to occupy various positions in the potential landscape. An expansion from the two-level relaxation model to a multi-level relaxation model was introduced by Jones and Srivastava in 1986 [86]. Due to its complexity, it has yet only been used a few times to describe experimental data (see e.g. [29] and [87]).

The model is based on an expansion from the two steps used in the Wickman model

to $n = 2S+1$ steps (details about the calculations can be found in [29]). It has been found, that the number of levels that are necessary in order to describe the spectra properly is about 25 - 36 [29]. The relaxation rate can be calculated by using the equation presented in section 1.3.2. Therewith, the only free parameters next to the typical Mössbauer parameters are the energy barrier height KV and the relaxation time constant τ_0. A particle size distribution can be included by using a distribution of KV.

Simulations of the Mössbauer spectra with different values of the parameters can be found in figure 2.13. The corresponding code can be found in section A.1.2. The character of the collapse of the six line spectra differs for different values of τ_0. For the smaller value presented in figure 2.13, the lines become asymmetric at intermediate KV/k_BT values, until the whole spectrum collapses into a triangular shaped structure (left panel). For larger values of τ_0, the collapse of the spectrum resembles the collapse of the spectra in the framework of the Wickman model.

In the fitting procedure established by Lierop *et al.* [29], the relaxation parameter R is set to zero at low temperatures, since the system is in the collective excitations regime, where no overbarrier fluctuations occur. Only at higher temperatures, $R > 0$ (typically around $T = 0.3\,KV/k_\mathrm{B}$, see [29]). In this scenario, the lowest temperature with $R > 0$, defines the blocking temperature T_B. This definition is only valid for Mössbauer spectroscopy. Since the timescale of Mössbauer spectroscopy ($\approx 10^{-9}\,\mathrm{s}$) is similar to τ_0 in equation 1.3, the temperature where the nanoparticles enter the superparamagnetic regime ($\approx 0.3\,KV$) is similar to the instrumental timescale and is therewith the blocking temperature. However, if $R = 0$, the off-diagonal elements

$$M_{kk\pm1} = -P_{kk\pm1}\left(\exp\left(-\frac{\Delta E}{k_\mathrm{B}T}\right)\right), \tag{2.15}$$

with

$$P_{kk+1} = R[S(S+1) - (k-S-1)(k+S)] \qquad k < (2S+1)/2 \tag{2.16}$$

$$P_{kk-1} = R[S(S+1) - (k-S-1)(k+S-2)] \qquad k \geq (2S+1)/2, \tag{2.17}$$

in the matrix $\underline{\underline{M}}$ that describes the Mössbauer spectrum vanish. Than, the diagonal elements are

$$M_{kk} = i(\omega - \omega_k) + \Gamma. \tag{2.18}$$

In order to calculate the Mössbauer spectrum $I(\omega)$, one has to evaluate the relation

$$I(\omega) = 2\mathrm{Re}(\underline{W}\,\underline{\underline{M}}^{-1}\underline{1}). \tag{2.19}$$

Here, $\underline{W}$ is the occupation probability and $\underline{1}$ is a vector with the dimension of the matrix, that is filled up with 1. The inversion of $\underline{\underline{M}}$ and the multiplication with $\underline{W}$ yields an equations, whose real part is a sum of Lorentzians whose distance to the center depends on the angle θ to the easy axis (see figure 2.8), weighted with

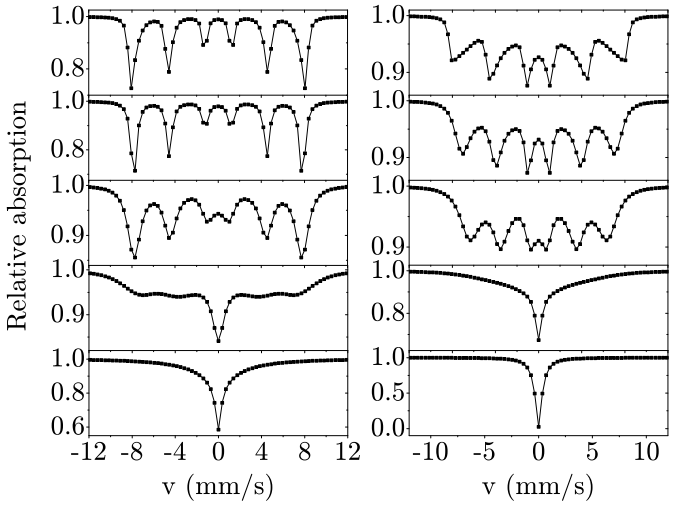

Figure 2.14: MLR spectra from the code used here (see section A.1.2) with the same parameters as those in the simulated spectra in figure 1 in [86] (not shown here). The shape of the spectra presented in this figure and those presented in [86] are the same, demonstrating the correct performance of the code used here.

W_k. This is a distribution of static hyperfine patterns with different splitting and does not take into account any relaxation effects (for more details, see chapter 3). However, the model is able to reproduce the Mössbauer spectra of different types of non- or weakly interacting nanoparticles very well.

The simulated model used in the following, is verified by creating spectra with the same parameters as those used for the simulation of the spectra shown in figure 1 in [86] (see figure 2.14). Both results look very similar, indicating the validity of the code used here. Noticeable, the absorption values presented in the spectra in Ref. [86], is misleading. The collapsed, non-magnetic pattern for high relaxation rates, has the same maximum absorption as the very broad pattern top right. Therefore, the values for the different spectra are not comparable and each spectrum is normalized to a maximum absorption of $\approx 10\%$ and should not be compared to the values of the MLR used here.

The MLR model does not include a quadrupolar interaction. Hence the fitting of experimental spectra including a quadrupolar interaction will always yield some discrepancies, especially when the relaxation rate is fast and a distinct peak in the center in the center of the spectrum appears.

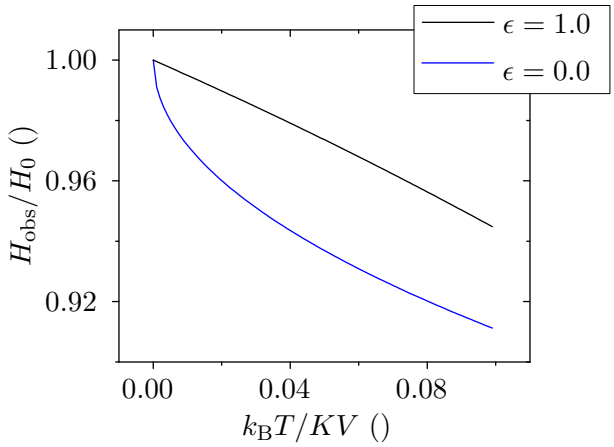

Figure 2.15: Simulation of the temperature dependent development of the normalized average magnetic hyperfine field with $\epsilon = 0$ and $\epsilon = 1$.

An expansion of the MLR including the quadrupolar interaction, has been published by Chuev in 2011 [88]. This model is however even more complex than the MLR presented here and would therefore require even more calculation time. For this reason, and since the quadrupolar splittings of the materials discussed in the following are rather small, only the MLR without a quadrupolar interaction will be used in the following.

A particle size distribution can be implemented, by calculating the spectra for different values of KV and perform a weighted sum afterwards. The corresponding code is given in chapter A.

Temperature dependence of the average hyperfine field

So far, the discussed models always predicted the shape of a Mössbauer spectrum of non-interacting magnetic single-domain nanoparticles under different circumstances. In the 1980's, S. Mørup *et al.* [89] developed models, that predict the temperature dependent behavior of the average hyperfine field of non-interacting magnetic nanoparticles for different potential shapes. The average hyperfine field is determined by fitting the Mössbauer spectrum with a hyperfinefield distribution and calculating its average value.

They showed that, if $k_{\mathrm{B}}T \ll KV$, the normalized magnetic hyperfine field is given by

$$B_{\mathrm{obs}}/B_0 = 1 - \frac{k_{\mathrm{B}}T}{KV}\left(\left(\frac{\partial^2 E}{\partial u_x^2}\right)_0^{-1} + \left(\frac{\partial^2 E}{\partial u_y^2}\right)_0^{-1}\right), \tag{2.20}$$

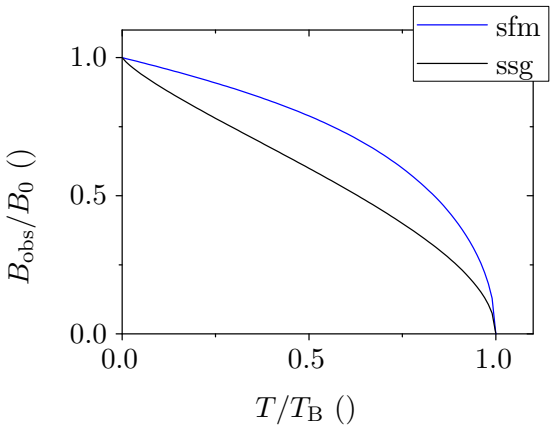

Figure 2.16: Simulation of the temperature dependent development of the normalized average magnetic hyperfine field for $\epsilon = 0$ and $\epsilon = 1$.

where u_i are the direction cosines of the magnetization vectors [89]. They described the potential by

$$E(\theta) = KV[\epsilon \sin(\theta)^2 + (1-\epsilon)\sin(\theta)^4] \tag{2.21}$$

and gave two approximations for $\epsilon = 0$ and $\epsilon = 1$. The results are shown in figure 2.15. Using these models and assuming non-interacting particle, it is possible to estimate the anisotropy constant from low-temperature measurements.

The super-ferromagnetism / super-spin glass models

In the same year and by the same group, further models for interacting particles were developed [23]. They predict the temperature dependence of the magnetic hyperfine field from $T = 0\,\mathrm{K}$ up to T_B for the case of a single value of the exchange coupling constant (this scenario is called "super-ferromagnetism" (SFM)) and a Gaussian distribution of the exchange coupling constant (this is called "super-spin glass" (SSG)) (compare to section 1.2).

Both models are based on a modified Weiss mean field approach [89], after which the average magnetization of a crystallite can be calculated by

$$\langle M \rangle = M_0(T) L\left(\frac{\sum_j K_{ex}^{ij} \langle M \rangle M_0(T)}{k_B T}\right), \tag{2.22}$$

where $\sum_j K_{ex}^{ij}$ is the sum over the different exchange coupling constants between the particles, $L(x)$ is the Langevin function and $M_0(T)$ is the magnetization of the crystallite. This was assumed to be the same as the bulk value of the same material. Further calculations finally led to the expression

$$b(T) = \frac{B_{obs}}{B_0(T)} = L\left(\frac{3T_p}{T}\left[\frac{B_0(T)}{B_0(T_p)}\right]^2 b(T)\right) \tag{2.23}$$

for the SFM scenario and

$$q = \int_{-\infty}^{\infty} \mathrm{d}z (2\pi)^{-1/2} \exp\left(-\frac{z^2}{2}\right) L\left(\frac{3T_\mathrm{p}}{T}\left[\frac{B_0(T)}{B_0(T_\mathrm{p})}\right]^2 \sqrt{q}\, z\right)^2 \tag{2.24}$$

for the SSG scenario. In the last case, $\sqrt{q}$ is used as $b(T)$. T_p is the transition temperature above which the system is superparamagnetic, while it is in the SFM or SSG state below. T_p is the only free parameter. In order to plot the equations, it is necessary to know the temperature dependent magnetization $B_0(T)$ of the corresponding bulk material. However, if $T_\mathrm{p} \ll T_\mathrm{C}$, the magnetization curve becomes approximately static and the influence of $B_0(T)$ almost vanishes. Hence, for the normalized numerical solutions for both cases, which are plotted in figure 2.16, $B_0(T) = 1$ was used. Despite this simplification, the basic trend of the two cases can still be observed.

The two scenarios can be attributed to two different types of interaction between the nanoparticles. A direct exchange interaction between the surface atoms of ideal ferromagnetic particles without a surface spin canting and a negligible dipole-dipole interaction between the particles would result in a coupling constant $K_\mathrm{ex} > 0$ with a small distribution. This scenario can be attributed to the SFM case. Dipole-dipole interactions between particles in close contact with a negligible direct exchange interaction would result in a distribution of coupling constants around $K_\mathrm{ex} = 0$, which can be related to the SSG case. The last scenario is realized e.g. for coated particles with a big magnetic moment, where the surface atoms are not in direct contact. The SFM scenario, however, should rather be observed, for particles with a small net magnetic moment in direct contact with a negligible surface spin canting.

In Ref. [23], the temperature dependence of the average normalized hyperfine field was successfully fitted with the SFM model, the SSG model was not able to describe the data.

The code for the simulation of the SFM / SSG model are shown in chapter A.

The capability of describing the Mössbauer data for different types of nanoparticles of the different models presented in this section, will be discussed in the following chapters.

Qualitative analysis of Mössbauer spectra

The complex shape of the Mössbauer spectra allows a qualitative interpretation of the data, which might already be sufficient in many cases (especially, when a comparison with different samples is not necessary). E.g. the blocking temperature can be estimated with satisfying accuracy from the spectral shape. Furthermore, the presence of interparticle interactions can be identified from the Mössbauer spec-

tra at temperatures near the blocking temperature. If the particles are truly non-interacting, the spectrum is made up of a non-magnetic contribution in its center and an additional broad magnetic structure (see e.g. the spectra resulting from the simulation with the uniaxial Wickman model in figure 2.9). In the case of strong interparticle interaction, the Mössbauer spectra at $T \approx T_B$ typically show a broad structure, indicating a collective collapse of the magnetically split structure into a non-magnetic pattern (similar to the patterns extracted from the MLR for small τ_0, see figure 2.13, left side). For a comparison of the Mössbauer spectra of interacting and non-interacting particles, it is referred to [24].

However, the problem for the application of the models to measurements, is obvious from the description of the models in this section. The first ones only describe a two-level relaxation process, which is sufficient to demonstrate the general behavior of Mössbauer spectra measured on magnetic nanoparticles at different temperatures, but not sufficient for a fitting of measured data. The model for spherical relaxation describes the Mössbauer spectra resulting from particles that undergo a rather uniform relaxation (like e.g. Brownian relaxation of spherical nanoparticles) very well, but is not applicable to processes based on uniaxial relaxation. The MLR is a good expansion of the two-level relaxation models, but is however only designed for non-interacting particles. For this reason, the only applications of this model were performed on Mössbauer measurements on a ferrofluid [29, 87]. The only model that is designed to fit interacting magnetic nanoparticles is the SFM/SSG model, which is however only capable to reveal limited information from the spectra compared to the MLR.

2.2 DC- and AC-susceptibility

Susceptibility measurements are another well-known tool in magnetic nanoparticle research. While DC-susceptibility is mostly used to gain information about the blocking temperature and the surface spin canting, AC-susceptibility provides the possibility to measure the blocking temperature for different time scales, which can be used to quantitatively identify the strength of the interparticle interaction.

Memory effects were observed in both techniques.

In the following, the typical measurement procedures of both techniques, commonly used in nanoparticle research, are shortly discussed.

2.2.1 DC-susceptibility

The DC-susceptibility $\chi = M/H$ measures the magnetization of a sample under the influence of an external magnetic field.

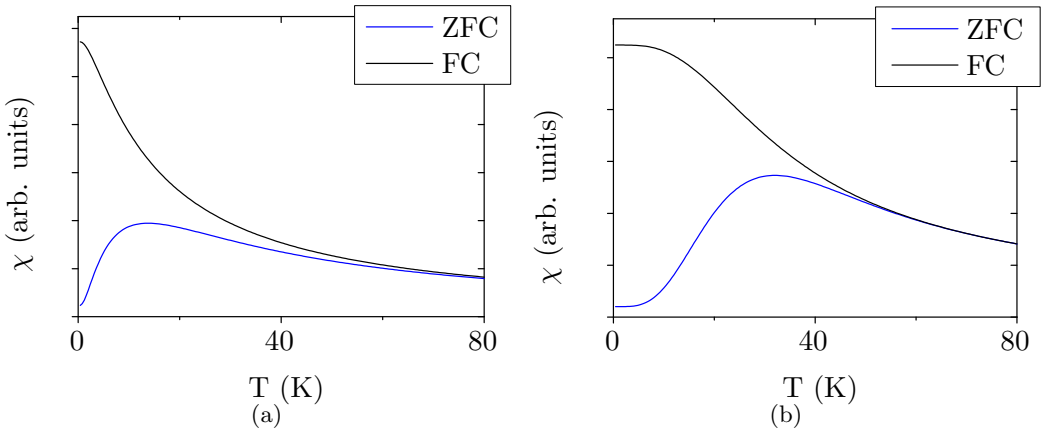

Figure 2.17: Simulations of ZFC/FC curves of non-interacting magnetic nanoparticles with a size distribution after [90] with the parameters $\nu_0 = 10^{10}\,\mathrm{Hz}$, $\nu_T = 2\,\mathrm{K/min}$ and (a) $K_{\mathrm{eff}} = 7\,\mathrm{kJ/m^3}$, $\mu = 1\,\mathrm{nm}$ and $\sigma = 0.33\,\mathrm{nm}$ as well as (b) $K_{\mathrm{eff}} = 20\,\mathrm{kJ/m^3}$, $\mu = 4\,\mathrm{nm}$ and $\sigma = 0.8\,\mathrm{nm}$. μ and σ are the parameters defining the underlying log-normal (a) and normal (b) particle diameter distribution.

Zero-field-cooled (ZFC) and field-cooled (FC) measurements

These types of measurements are commonly used in order to identify T_{B}. In the ZFC case, the sample is placed in the cryostat and cooled down to a low temperature (typically the lowest accessible temperature T_{l}) without an external magnetic field. After reaching T_{l}, the external field is switched on and the sample is heated up again. During the heating up process, the measurement is performed.

The FC procedure is almost the same except that the sample is cooled down to T_{l} in the presence of a high external magnetic field (typically 0.1 T). The external magnetic field applied during the heating-up process must not necessarily be the same.

A model that describes the ZFC/FC curves for magnetic nanoparticles in a uniaxial potential was presented in [90]. Simulations for a realistic set of parameters are shown in figure 2.17 for a log-normal and a normal distribution of the particle diameter. The code for the simulation of the ZFC / FC curves is given in chapter A. Both scenarios show the typical temperature dependent behavior. For the ZFC curve, the susceptibility is small at low temperatures and increases with increasing temperature up to T_{max}. For higher temperatures, it decreases again and finally units with the FC curve. The susceptibility of the FC curve is much higher at low temperatures and it decreases continuously over the whole temperature range.

When the system is cooled down without an external field, the magnetic moments of

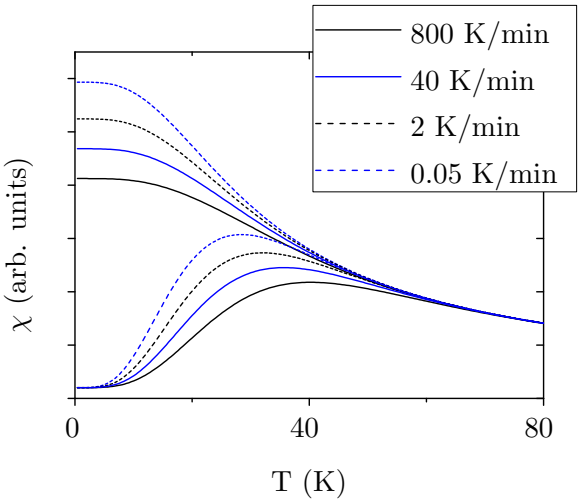

Figure 2.18: Simulation of the ZFC/FC curve for different heating up rates ν_T. $\nu_T = 800\,\mathrm{K/min}$ and $\nu_T = 40\,\mathrm{K/min}$ are certainly not realistic but are displayed as examples.

the individual nanoparticles are oriented in random directions, therefore χ is small at low temperatures in the ZFC case. The external field, that is applied during the heating up process, is not sufficient to align the frozen magnetic moments at low temperatures. With increasing temperature, however, the thermal energy combined with the influence of the external magnetic field is strong enough to change the direction of the magnetic moment of the nanoparticles and achieve an alignment along the direction of the magnetic field. At T_{max}, the maximum number of the particle magnetic moments are aligned. With increasing temperature, the thermal energy becomes bigger, so that the particles become superparamagnetic and χ decreases continuously since the time average of the magnetization decreases.

After cooling the sample in a strong external magnetic field (FC), the magnetic moments of the particles are aligned parallel to the magnetic field, which results in the high value of χ at low temperatures. With increasing temperature, relaxation of the nanoparticles sets in and χ decreases. When the FC and ZFC curve coincide, the influence of the parallel alignment of the nanoparticles at low temperatures has vanished.

The detailed shape of the curves depends on the heating up rate ν_T. Simulations of the curve presented in figure 2.17 (b) for different values of ν_T after [90] are shown in figure 2.18. With increasing ν_T, T_{max} is increasing as well as the point where the two curves merge into each other. The reason for this effect is the time-dependent relaxation of aligned particles (see e.g. [90]).

Since the shape of the curves depends on ν_T and on the applied magnetic field,

$T_{\max}$ cannot be understood as the blocking temperature T_B of the system. A way to calculate the anisotropy energy K_{eff} from $T_{\max}$ and other parameters through

$$K_{\text{eff}} = \frac{\gamma k_B T_{\max}}{V_{\max}} \tag{2.25}$$

with

$$\gamma \approx 0.9609 \cdot \ln\left(\frac{\nu_0 T_{\max}}{\nu_T}\right) - 1.629 \tag{2.26}$$

and

$$V_{\max}^3 = \frac{\gamma}{\gamma - 1} \frac{1}{\rho(V_{\max})} \int_0^{V_{\max}} V^2 \rho(V) \mathrm{d}V \tag{2.27}$$

was presented in [90].

So far, interparticle interactions have not been taken into account. In [91], a study on the development of ZFC/FC curves of Fe_3O_4 nanoparticles mixed with different amounts of SiO_2 nanoparticles in order to increase the average distance between the particles and therefore the interparticle interaction strength, has been presented. While the $\chi(T)$ curves of the nanoparticles with the biggest spacing ($\approx 31.5\,\text{nm}$) show the typical behavior, namely an increase of the FC curve below $T_{\max}$ and could be fitted with a model of non-interacting particles[1], the other curves developed a different behavior. With increasing interparticle interaction strength, the increase below $T_{\max}$ starts to flatten at low temperatures. For the pure magnetite powder, the FC curve is almost constant below $T_{\max}$. Hence the $\chi(T)$ measurements can be used for an estimation of the interparticle interaction strength. One should however keep in mind, that a flattening of the FC curve at low temperatures occurs as well for non-interacting particles with a normal particle size distribution (see figure 2.17). Therefore the observation of a flattened FC curve at low T should only be correlated with interparticle interactions very carefully.

Magnetization versus external field $M(H)$

$M(H)$ measurements are performed at a fixed temperature but with a variation of the external magnetic field (typically in the range from $-5\,\text{T}$ to $5\,\text{T}$). The measurements start at $0\,\text{T}$ and the field is sweeped through the complete range afterwards.

The description of the $M(H)$ curves can be separated into three different regimes (as described e.g. in [93]).

[1] The model they used is the same as in [92], which was blamed to be incorrect in [90]. As described therein, the error results mainly in an underestimation of the influence of the bigger particles. Hence the shape of the simulated curves stays basically the same, but the anisotropy energy constant K is erroneous.

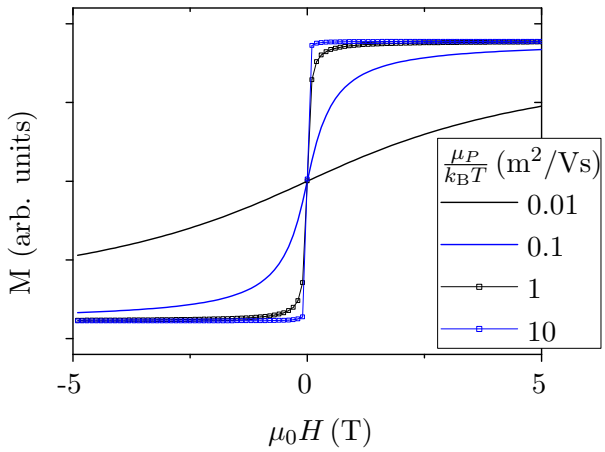

Figure 2.19: Simulation of the $M(H)$ curves after equation (2.28) for different values of $\mu_P/k_\mathrm{B}T$. The particle size distribution is the same as the one used in figure 2.17 (b).

For $T > T_\mathrm{B}$, the curves can be described using the Langevin function

$$M(H,T) = N_p \int_0^\infty \rho(v)\, \mu_p L\left(\frac{v\mu_p H}{k_\mathrm{B}T}\right) \mathrm{d}v \tag{2.28}$$

with

$$L(x) = \frac{1}{\tanh(x)} - \frac{1}{x}, \tag{2.29}$$

being the Langevin function, μ_p being the particle magnetic moment, $\rho(v)$ being the volume distribution of the particles and $v = V/V_\mathrm{max}$. Simulations of the Langevin function for different values of $\mu_P/k_\mathrm{B}T$ are shown in figure 2.19.

The Langevin function arises from the Brillouin function for $J \to \infty$ [10]. Due to the big magnetic moments of the magnetic nanoparticles, it is a good approximation. However, it is only valid at $T \gg T_\mathrm{B}$, since it describes the response of a paramagnetic system without the influence of any anisotropy . When the temperature approaches T_B, anisotropy is not negligible against the thermal energy anymore and hence the Langevin function is not able to describe the measurements anymore.

In this temperature range, the $M(H)$ curves have to be described by the following model. The curves can be calculated using

$$M(H,T) = \int_0^\infty \rho(v) M(H,T,v) \mathrm{d}v \tag{2.30}$$

with

$$M(H,T,v) = N_p k_\mathrm{B} T \frac{1}{2} \int_0^\pi \frac{\partial \ln Z(H,T,\alpha,v)}{\partial H} \mathrm{d}(\cos\alpha) \tag{2.31}$$

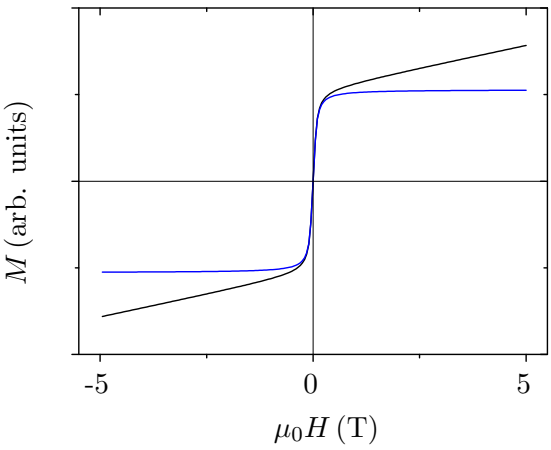

Figure 2.20: Comparison of a simulation of a Langevin curve with (black) and without (blue) an extra paramagnetic contribution due to a distorted layer after equation (2.35). Here, $V = 462\,\mathrm{nm}^3$, $\chi_\mathrm{p} = 0.1$ m·A/V·s, $T = 250\,\mathrm{K}$ and a paramagnetic outer shell of approximately 10% of the overall radius.

and

$$Z(H,T,\alpha,v) = \int_{-\pi}^{0} \exp\left(\frac{v(E_a\cos^2\theta + \mu_m H\cos\alpha\cos\theta)}{k_\mathrm{B}T}\right) \times I_0\left(\frac{v\mu_m H\sin\alpha\sin\theta}{k_\mathrm{B}T}\right)\mathrm{d}(\cos\theta), \tag{2.32}$$

with $I_0(x) = \pi^{-1}\int_0^\pi \exp(x\cos t)\mathrm{d}t$, being a modified Bessel function of the order zero (more details can be found in [93]).

At low temperatures, the particles start to block, which results in hysteresis effects. In order to describe the $M(H)$ curves, it was proposed in the same work to separate the reversible from the irreversible part. Both parts can be calculated by adding and subtracting the part of the hysteresis curve with increasing and decreasing field, respectively, and dividing it by two. The reversible part can be simulated by

$$M_\mathrm{rev}(H,T) = \int_0^{v_T^*(H)} \rho(v)M(H,T,v)\mathrm{d}v, \tag{2.33}$$

with $v_T^*(H) = v_T^*/(1 - H/H_\mathrm{irr}(T))^\beta$. v_T^* is defined by $v_T^* = T/T_0$ (T_0 is the peak in the ZFC measurement). The irreversible part can be simulated by

$$M_\mathrm{irr}(H,T) = M_\mathrm{rem}(0)\int_{v_T^*(H)}^{\infty} \rho(v)\mathrm{d}v, \tag{2.34}$$

for $H < H_\mathrm{irr}(T)$. $M_\mathrm{rem}(0)$ is the remanent magnetization at $T = 0\,\mathrm{K}$.

An important parameter that can be extracted from $M(H)$ curves is the saturation magnetization M_s. However, it has been found in several studies, that M_s of nanoparticles is in general smaller than the corresponding bulk value and decreases with decreasing particle size (see e.g. [35, 94]). The origin of this effect is the non-magnetic surface layer, discussed in the previous chapter. In order to incorporate this, Chen *et al.* [95] proposed a model that includes a paramagnetic layer in combination with the Langevin function and a particle size distribution

$$M(H) = \int_0^\infty \rho(V) \frac{M_\mathrm{s} V_c L(x) + V_s \chi_\mathrm{pm} H}{V} \mathrm{d}V, \tag{2.35}$$

where $\rho(V)$ is the particle volume distribution, V_c is the volume of the magnetic core of the particle, $L(x)$ is the Langevin function, $x = \mu_0 M_\mathrm{s} V_c H / k_\mathrm{B} T$, V_s is the volume of the paramagnetic shell and χ_pm is the paramagnetic susceptibility. Since their model is based on the Langevin function and on a paramagnetic layer, it should be only applicable at $T > T_\mathrm{B}$. A simulation of the $M(H)$ curves with and without a paramagnetic layer after equation (2.35) is shown in figure 2.20. The corresponding code is given in chapter A.

As shown in [96], interparticle interactions lead to an increase of the coercivity. A model that describes the magnetization curves of magnetic nanoparticles in the presence of weak dipole-dipole interaction has been presented in [97].

2.2.2 AC-susceptibility

AC-susceptibility is measured by applying a fluctuating external magnetic field

$$H_\mathrm{ac} = H_0 \exp(-i\omega t) \tag{2.36}$$

to the sample. The susceptibility

$$\chi_\mathrm{ac} = \frac{\partial M}{\partial H_\mathrm{ac}} = \chi'_\mathrm{ac} + i\chi''_\mathrm{ac} \tag{2.37}$$

contains an in-phase component χ'_ac and an out-of phase component χ''_ac, shifted relative to the in-phase component by a phase of $\pi/2$. As described in [98], χ'_ac is the dispersive magnetic response, while χ''_ac is connected to absorptive processes. It is possible to access different timescales by changing the frequency of the applied field.

A rough description of the temperature dependent behavior of non-interacting magnetic nanoparticles can be found in [99]. Above the blocking temperature, $\chi'_\mathrm{ac} = \alpha T^{-1}$ (Curie's law). It is possible to extract information about the average particle volume from α.

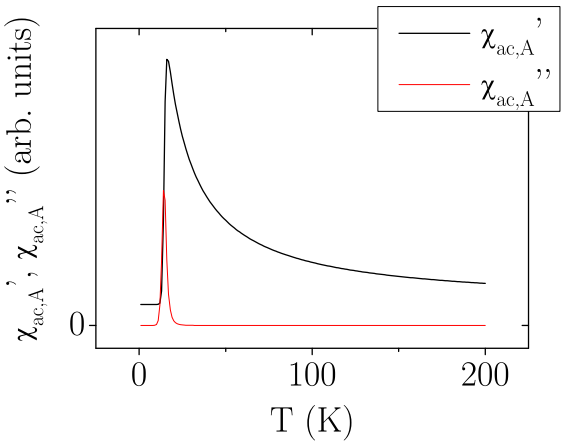

Figure 2.21: Plots of equation (2.38) and (2.39) with $KV/k_\mathrm{B} = 200\,\mathrm{K}$, $\omega = 1000\,\mathrm{Hz}$ and $M_s^2/3K = 0.92$. For the calculation of τ, equation (1.19) was used.

An expression for the simulation of AC-susceptibility curves of magnetic nanoparticles can be found e.g. in [100]. Therein, the experimental curves are described by

$$\chi'_{\mathrm{ac,A}}(\omega, T) = \frac{M_s^2}{3K}\left(1 + \frac{KV}{k_\mathrm{B}T}\frac{1}{1+(\omega\tau)^2}\right) \tag{2.38}$$

$$\chi''_{\mathrm{ac,A}}(\omega, T) = \frac{M_s^2}{3K}\frac{KV}{k_\mathrm{B}T}\frac{\omega\tau}{1+(\omega\tau)^2}. \tag{2.39}$$

The curves are plotted in figure 2.21.

From the temperature that corresponds to the peak, T_p, it is possible to determine the blocking temperature. However, in general $T_\mathrm{p} \neq T_\mathrm{B}$ in presence of a distribution of particle sizes [101]. As discussed therein, a linear dependence

$$T'_\mathrm{p} = \alpha' + \beta' T_\mathrm{B} \tag{2.40}$$

$$T''_\mathrm{p} = \alpha'' + \beta'' T_\mathrm{B} \tag{2.41}$$

can be assumed for χ'_ac and for χ''_ac. Different values for α', α'', β' and β'' are given in the same publication in dependence of the width of the log-normal particle size distribution for antiferromagnetic particles[2]. These calculations are based on non-interacting particles.

Information about the strength of the interparticle interactions can be extracted from the frequency depended shift of T_p, by plotting τ vs. $1/T_\mathrm{p}$ and fitting the

[2]This is considered in the volume dependence of the magnetic moments of the particles $M(V)$. For different types of magnetism, it is necessary to include different $M(V)$ dependences.

result with either an Arrhenius law

$$\tau = \tau_0 \exp\left(-\frac{E_a}{k_\mathrm{B} T_\mathrm{p}}\right) \tag{2.42}$$

or a Vogel-Fulcher law (see [102] for details)

$$\tau = \tau_0 \exp\left(-\frac{E_a}{k_\mathrm{B}(T_\mathrm{p} - T_\mathrm{VF})}\right). \tag{2.43}$$

While the Arrhenius law is only applicable to non-interacting nanoparticles, the Vogel-Fulcher law is able to describe the τ dependence of T_p for interacting nanoparticles. The strength of the interparticle interaction correlates with T_VF.

2.3 Determination of the particle size distribution by transmission electron microscopy

An important parameter regarding the resolution of microscopes based on the scattering of light, is the wavelength λ in combination with the numerical aperture, which limits its maximum value. For typical light-microscopes, the maximum resolution lies in the range of μm, and is hence not sufficient in order to explore the size of nanoparticles.

In a transmission electron microscope (TEM), electrons are used instead of light. The de-Broglie wavelength of electrons in dependence of their kinetic energy is given by [103]

$$\lambda = \frac{12.3}{\sqrt{E}}\,\text{Å}, \tag{2.44}$$

wherein E is measured in eV. The typical accelerating voltage in a TEM lies in the range of a few 100 kV, which gives $\lambda_{100\,\mathrm{kV}} \approx 0.04\,\text{Å}$. However, due to aberration effects, the maximum resolution is not as good (the highest resolution achieved with a TEM lies around 0.5 nm [104]). Hence, the resolution of a microscope using electrons instead of light is in principle good enough to directly observe nanoparticles.

A conventional TEM is made up of three different parts [105]: the illumination stage, the objective and the imaging stage. In the first stage, the electrons are accelerated in an electron gun followed by a parallelization of the electron beam in an electromagnetic lens system. After passing the sample, sufficiently thin to allow the electron beam to pass through, the beam enters the imaging stage, where it is widened and finally falls on a fluorescent screen. This screen converts the electron beam into visible light.

Next to the imaging, a TEM can also be used for different measurement techniques,

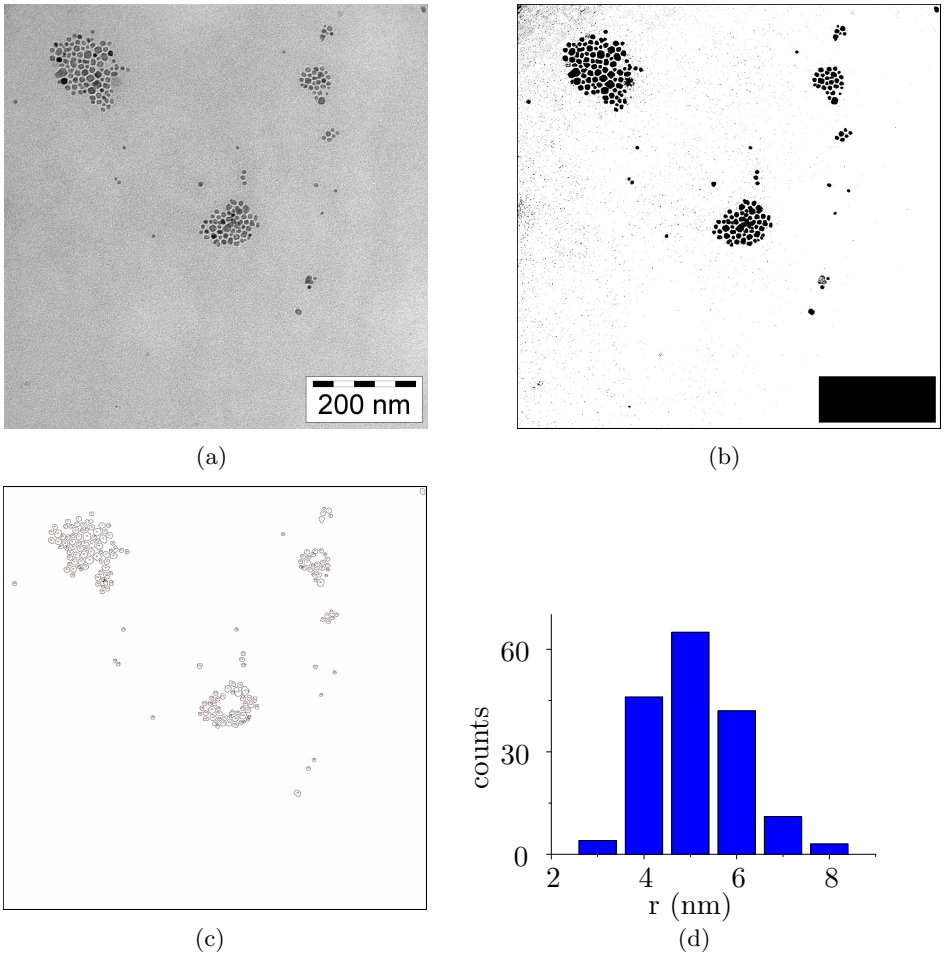

Figure 2.22: (a) Original TEM image of iron-oxide nanoparticles (see section 4). (b) Binarized version of the same image. (c) Resulting image showing the outlines of the detected particles. Note, that the big clusters of overlying particles are not detected. This is due to the manually defined maximum area of the particles, above which all detected particles are neglected. (d) The resulting particle radius distribution assuming spherical particles.

as it is described in [105]. However, since the TEM was only used for imaging in this work, no further explanation of the other methods will be given here.

For the evaluation of the images, IMAGEJ, a freeware software, is used[3]. At first, the images are converted into a binary mode, therefore a good contrast between the particles and the background is desirable. If necessary, overlying and connected particles have to be deleted by hand or neglected by defining a maximal value for the

[3] `http://rsbweb.nih.gov/ij/`

area of the particles. After that, the software searches for any clusters of black color and calculates their areas (and other parameters, if desired). By assuming spherical particles, one can extract the distribution of radii from the distribution of areas. An example for the described procedure is given in figure 2.22.

Chapter 3

Application of the MLR and SFM/SSG model to interacting nanoparticles

The models described in the previous chapter are mostly based on non-interacting magnetic nanoparticles. However, most of the examined particles experience non-negligible interparticle interactions, e.g. dried particles and even particles dispersed in a liquid, in case of agglomeration or a high density of the particles. For this reason, none of the models presented above, except the SFM/SSG model, are applicable to the Mössbauer spectra of most of the examined particles in science and application. In the following, a series of temperature dependent Mössbauer measurements on strongly interacting $ZnFe_2O_4$ nanoparticles is evaluated using the SFM/SSG model and as well the MLR model. While an application of the unmodified MLR to the data gives unreasonable results, it will be demonstrated, that small modifications of the model will allow its application to strongly interacting magnetic nanoparticles.

In the first section, the sample preparation and characterization are presented, followed by a section describing the application of the models. At the end, the results from the application of the models to the Mössbauer measurements are confirmed by DC-susceptibility measurements.

3.1 Sample preparation and characterization

3.1.1 Preparation

The particles were prepared at the Institut für Partikeltechnik of the TU Braunschweig by I.-M. Grabs in the group of G. Garnweitner by a non-aqueous sol-gel method, a procedure presented e.g. in [106] and as well in the following chapter of this work. The only difference to the procedures presented therein is, that next to $Fe(acac)_3$ also $Zn(acac)_{hyd}$ was used as a precursor. In the preparation procedure,

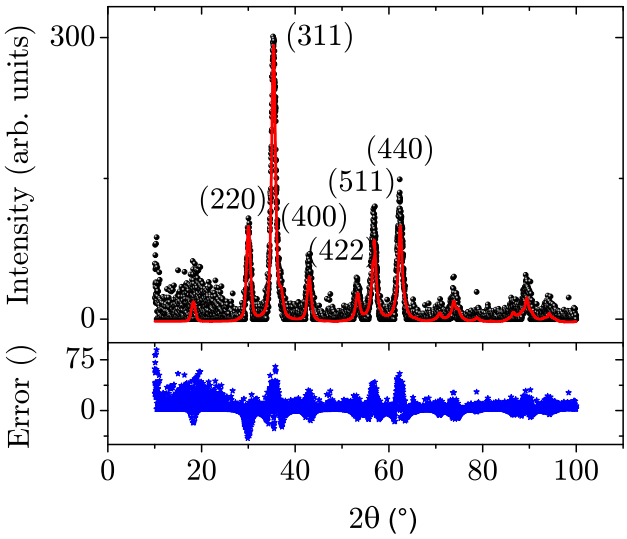

Figure 3.1: XRD pattern of the $ZnFe_2O_4$ particles.

the metal-acetylacetonate is dispersed in benzyl alcohol and heated up to 200°C for several hours. During this time, the particles are formed. Afterwards, the particles are extracted from the solution and dried, which results in a powder of $ZnFe_2O_4$-nanoparticles.

3.1.2 Characterization

In order to characterize the particles, XRD measurements as well as TEM measurements were performed.

$ZnFe_2O_4$ crystallizes in the spinel structure, similar to magnetite. Its detailed structure can be described by $(Zn_{1-x}Fe_x)[Zn_xFe_{2-x}]O_4$, which includes a tetrahedral A site (labeled by ( )) and an octahedral B site (labeled by [ ]). In this formula, x is the inversion parameter. The magnetic properties of $(Zn_{1-x}Fe_x)[Zn_xFe_{2-x}]O_4$ depend strongly on this value as it can be seen in the phase diagram presented in [107] (not shown here). For $x > 0.2$, the material is ferrimagnetic at high temperatures and exhibits a short-range ordered phase at lower temperatures, while for smaller x, the material has a cluster glass and a paramagnetic phase at high temperatures, which turns into a short-range ordered phase below $\approx 30 - 70\,\mathrm{K}$. For $x < 0.1$, a long-range ordered phase at very low temperatures ($T < 15\,\mathrm{K}$) has been observed. A correlation of the inversion parameter with the particle size can be extracted from a comparison of both phase diagrams in the same figure. It shows an increasing inversion parameter with decreasing particle size.

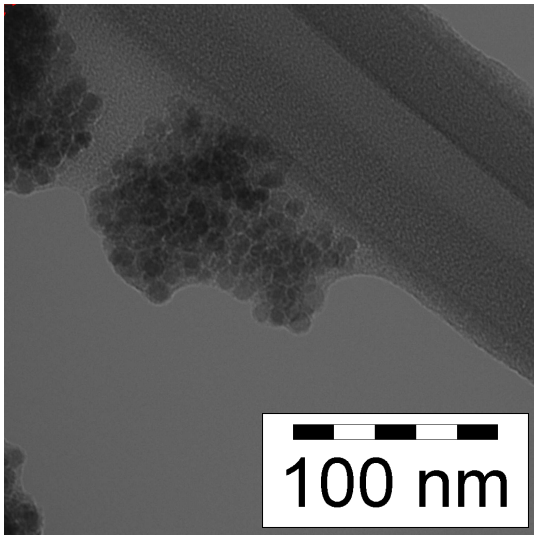

Figure 3.2: TEM image of the $ZnFe_2O_4$ nanoparticles.

The XRD spectrum is displayed in figure 3.1. It is fitted using `FullProf`, a freeware XRD fitting program and a $ZnFe_2O_4$ pattern taken from the ICSD database. The peaks match the typical spinel structure found for these compounds. No indication for undesired phases are found.

Furthermore, TEM measurements were performed on the sample in order to determine the mean particle size and to gain information about the particle morphology. The measurements were performed by L. Hoffmann of the Institut für angewandte Physik of the TU Braunschweig. An example for the TEM images is shown in figure 3.2. It shows spherical particles with an diameter of $10.5 \pm 2\,\mathrm{nm}$[1]. A particle diameter of 10.5 nm indicates, the the particles are in a ferrimagnetic state with a possible short-range ordered state at very low temperatures after the phase diagram presented in [107].

3.2 Mössbauer measurements

Mössbauer measurements were performed between 4 K and 210 K on the dried powder. Representative spectra are shown in figure 3.3. They show a behavior being typical for superparamagnetic nanoparticles, as it is already described in section 2.1.3. At low temperatures, the spectrum shows a well-resolved six line pattern, which collapses into a broad structure at intermediate temperatures (around 70 K) and finally into a sharp doublet. The broad spectrum at intermediate temperatures is typical for interacting magnetic nanoparticles, as discussed section 2.1.3.

[1] These values were roughly estimated from manual measurements of the diameter for random particles, since the image is not suitable for an automated analysis as described in section 2.3.

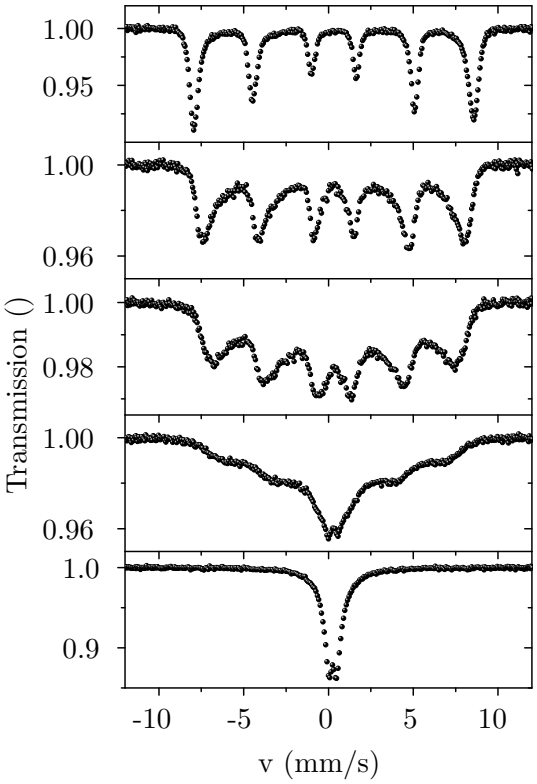

Figure 3.3: A set of representative Mössbauer spectra measured on the $ZnFe_2O_4$ particles for different temperatures. From top to bottom: 4.2 K, 40 K, 70 K, 100 K and 210 K.

The shape of the Mössbauer spectra depends on the inversion parameter x, since the fraction of iron ions occupying A- and B-sites changes with x. Unfortunately, even the spectra at the lowest temperatures are not distinct enough to achieve a definite value for x, due to spin canting at the surface or the interior of the nanoparticles (see section 1.4). However, the Mössbauer spectra can be used as well to estimate x from the phase diagram presented in [107]. Since the spectra show superparamagnetic behavior above 50 K, the particles are still in a ferrimagnetic state in this temperature range. Therefore the inversion parameter can be estimated to be bigger than $x = 0.2$. This agrees well with the findings above, where the magnetic state was estimated from the particle size. Indications for a short range ordered phase at low temperatures cannot be found from the Mössbauer measurements, which however can easily be explained by the expected big error bars in the phase diagram.

In the following subsections, some of the models discussed in the previous section will be used in order to evaluate the Mössbauer spectra. Furthermore, DC-susceptibility

measurements will be presented, in order to underpin the results found from the evaluation of the Mössbauer measurements.

3.2.1 Multi-level relaxation model

The Mössbauer spectra were fitted using two subspectra with an equal area but different isomer shifts, magnetic hyperfine splittings and linewidth, given in table 3.1. The values of the linewidth found from the application of the MLR are relatively high, compared to the values measured on bulk material. The reason for the increased linewidth is most likely a distribution of isomer shifts and quadrupolar interactions due to the increased surface / volume ration of the nanoparticles as well as inhomogeneous broadening. The applications of the MLR to non-interacting nanoparticles by Lierop *et al.* revealed similar values [29]. A quadrupolar interaction is not implemented in the model used here (as discussed in the previous chapter). The effective quadrupolar interaction in the magnetically frozen state of systems being superparamagnetic at higher temperatures is known to be very small [88]. A mismatch between the simulations and our data due to the neglected quadrupolar interaction is therefore only expected at higher temperatures.

The equality of the spectral weights ($x = 1$) is only an approximation, since the exact value of the inversion parameter is not known. However, since different sites are supposed to experience the same magnetic dynamics, both subspectra exhibit the same temperature dependent collapse of the magnetic hyperfine pattern. Therefore, x only has a minor influence on the shape of the spectrum. Furthermore, in this first approach, a particle size distribution is not taken into account. The fits for different temperatures are shown in figure 3.4.

As it can be seen from the fits, the simulations reproduce the data very well at low temperatures. At intermediate temperatures (especially for 100 K), a mismatch between the measurements and the simulations can be observed. At 210 K, the magnetic hyperfine pattern is almost completely collapsed into a quadrupole doublet (blue subspectrum). Only a small fraction of the particles undergoes magnetic relaxation which results in a broadening of the spectrum (green subspectrum).

The parameters which describe the magnetic dynamics within this model are the relaxation parameter R, the height of the anisotropy energy barrier KV, and the onset temperature for overbarrier fluctuations T_B. This temperature corresponds to a blocking temperature, where a transition occurs from collective excitations within the potential well to overbarrier fluctuations.

The relaxation parameter R describes the overbarrier fluctuations. As seen in figure 3.5, it decreases with decreasing temperature and reaches $R = 0$ at T_B [29, 108]. At lower temperatures, no overbarrier fluctuations exist anymore, but collective excitations are present. In the MLR, these are not treated explicitly using a further

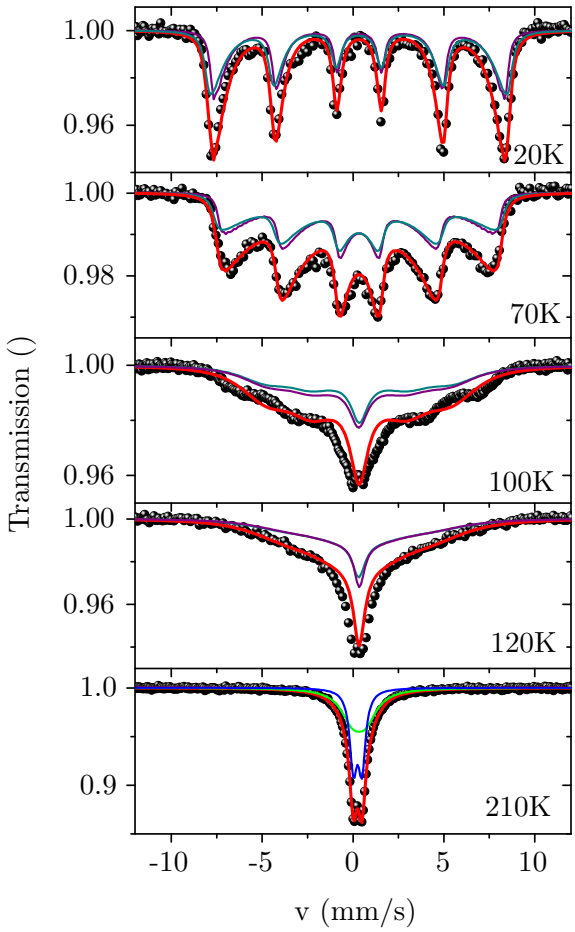

Figure 3.4: Spectra calculated from MLR model adjusted to the measured Mössbauer spectra. For details about the parameters, see text.

relaxation parameter, the spectral shape resulting from these excitations is rather modeled by a distribution of static magnetic hyperfine patterns[2], changing with temperature due to the changing occupation probabilities of the various states within the potential well. Although this treatment is an inadequate description of the spectral shape under collective excitations, it allows a systematic analysis of the parameters within the MLR, as demonstrated in [29].

[2]See [86]: the matrix $\underline{M}$ which defines the Mössbauer spectrum $I(\omega)$ according to equation (3) in [86], is defined by

$$M_{kl} \begin{cases} = 0 & \text{for} \quad k \neq l \\ \in \mathbb{C} & \text{for} \quad k = l \end{cases} \tag{3.1}$$

for $R = 0$ after equation (15) in [86]. This results in a sum of weighted Lorentzians for $I(\omega)$.

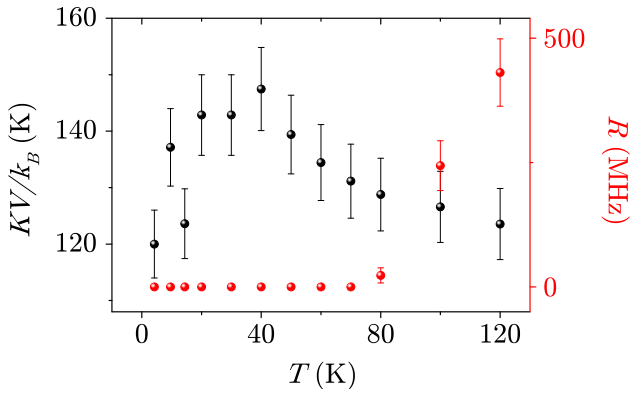

Figure 3.5: Temperature dependence of the anisotropy energy KV (black) and the relaxation parameter (red).

The temperature dependence of the energy barrier KV is plotted in figure 3.5. Its average value is $KV \sim 134\,\mathrm{K} \cdot k_\mathrm{B}$. At higher temperatures, a decreasing tendency is observed. This can again be related to the already above mentioned misfit due to the neglect of quadrupolar interaction and particle size distribution. Furthermore, the decrease of the anisotropy energy with temperature, as it has been discussed in section 1.1.2 can partially contribute to this behavior. Regarding the low temperature behavior, further explanations are needed, which will be given in the course of the further analysis of the measurements.

From simulations of the transition from collective excitations to overbarrier fluctuations [109] one would expect a value of $T_B \sim 0.3 \cdot KV/k_\mathrm{B}$ for the blocking temperature. The value derived from the simulations presented here, is however $T_\mathrm{B} \sim 0.6 \cdot KV/k_\mathrm{B}$ and hence rather big. A possible reason for this increased value are interparticle interactions. Since the MLR uses a uniaxial $E(\theta)$ potential, the unidirectional character of the dipolar interparticle interactions is neglected. A superposition of the interparticle interaction contributions from the neighboring particles with different strength and direction, results again in another unidirectional

Table 3.1: Parameter of the spectra shown in figure 3.4, used for the analysis within the MLR. Isomer shifts δ given here are for the spectrum at 20K relative to Fe metal at RT.

	$B_{0,hyp}$ (T)	δ (mm/s)	W (mm/s)	fraction ()
Site A	52.8 ± 0.8	0.31	0.42	0.5
Site B	51.7 ± 0.8	0.35	0.56	0.5

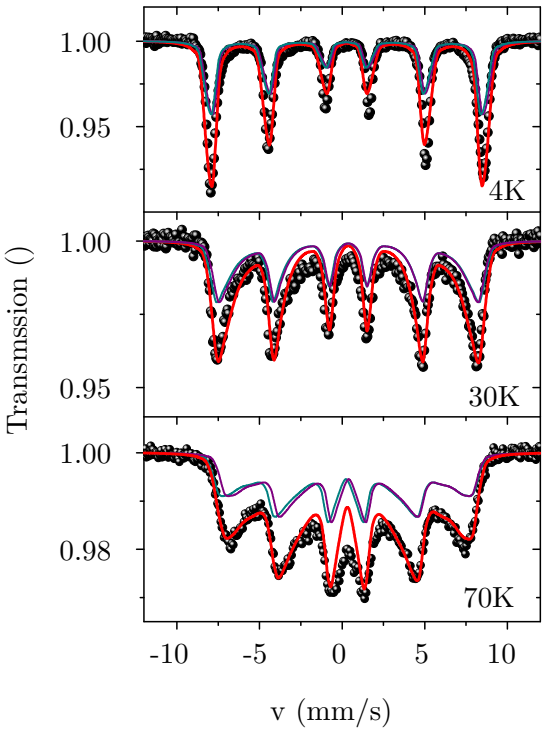

Figure 3.6: Simulation of the modified MLR adjusted to the measurements (see text for more information).

potential (compare to section 1.2). This more adequate $\cos\theta$-shaped potential would increase the transition probability to states far away from the easy direction and result in a faster broadening of the lines with increasing temperature; this means, that the derived value for $k_B T_B/KV$ will decrease. The ratio $k_\mathrm{B}T_\mathrm{B}/KV = \beta$ can therefore be understood as a parameter indicating the strength of the interparticle interactions, with vanishing interaction for $\beta \sim 0.2 - 0.4$ and strong interaction for values around $\beta \sim 0.6$ and bigger. In this way it is possible to gain information about the interparticle interactions from the MLR, although it is not directly implemented in the formalism. From the application of the MLR to weakly interacting particles [29], $\beta \sim 0.22 - 0.32$ can be extracted, which supports the interpretation of β given here.

As shown so far, the fitting of the $ZnFe_2O_4$ nanoparticles using an unmodified MLR is possible, but goes along with several inconsistencies. Their reasons are basically the interparticle interactions as well as the neglected quadrupolar interaction. In the following, the low temperate and high temperature regimes are treated individ-

ually, by a slightly modified MLR as well as a MLR which includes a particle size distribution.

In order to incorporate interparticle interactions, a $\cos\theta$-shaped potential within the framework of the MLR was used. Simulations were performed and adjusted to the measurements (see figure 3.6). The same parameters as in the unmodified MLR, discussed above, were used, except a decreased linewidth ($W = 0.4\,\mathrm{mm/s}$) and a different height of the energy barrier. This parameter is now rather related to the strength of the interparticle interactions than to the anisotropy energy, which is conventionally labeled as KV. Therefore, it will be called E_{int} in the following. The temperature dependence of E_{int} is shown in figure 3.7 (a). Especially at low temperatures, the modified MLR is less sensitive to slight changes in the spectral shape, due to the wide valley of the cos() shaped potential compared to the $\cos()^2$ shaped one, for which reason the decrease of the KV at low temperatures, as found from the unmodified MLR, cannot be observed here. While the low temperature simulations match the spectra very well, a mismatch between the simulation and the spectra in the center of the spectra manifests with increasing temperature. However, the outer lines are reproduced very well.

The temperature dependence of the energy barrier can be explained, if one assumes predominantly dipole-dipole interaction between the particles[3]. This type of interparticle interactions leads to a super-spin glass groundstate with a broad distribution of E_{int} (compare to section 1.2). Due to this distribution of E_{int}, a fraction of the particles experiences only very weak interparticle interaction. Their magnetic relaxation behavior is therefore predominantly determined by their anisotropy energy KV or a superposition of E_{int} and KV, with $E_{\mathrm{int}} \ll KV$. For $T < \beta \cdot KV/k_{\mathrm{B}}$, even the particles that experience hardly no interparticle interactions are frozen, since their anisotropy energy is strong enough to fix the orientation of their magnetic moment. At intermediate temperatures, $T \approx \beta \cdot KV/k_{\mathrm{B}}$, the fraction of particles that are able to overcome the KV dominated energy barriers increases with temperature, for which reason the mismatch between the simulation and the model increases. With the increasing fraction of fluctuating particles, the strength of the average interparticle interactions decreases[4], as it can be seen in figure 3.7 (a). Finally at high temperatures, interparticle interactions break down totally over a small temperature range, when a crucial fraction of the particles has overcome the E_{int} barrier and the fraction of particles contributing to the interparticle interactions is too small.

This reasonable decrease of E_{int} with increasing temperature is the explanation for the decrease of KV found from the application of the unmodified MLR above. It cannot be explained, when interpreting the energy barrier as an anisotropy energy

[3] This type of interaction will be proven to occur in the sample in the next subsection.

[4] The term interparticle interactions discussed here, corresponds to an effective average interparticle interactions (see section 1.2).

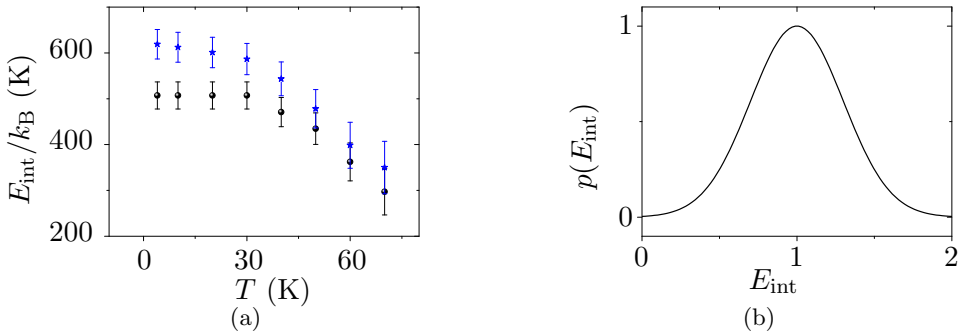

Figure 3.7: (a) Temperature dependence of the interparticle interactions extracted from the simulations of the modified MLR (black) and from the modified MLR which includes a normal distribution of E_{int} (blue). (b) Normalized distribution of E_{int} as it was used in the modified MLR which includes a distribution of E_{int}.

barrier KV in the framework of the unmodified MLR due to the application of a improper model, but in the framework of the modified MLR, where the energy barrier is associated with E_{int}.

A decrease of the interparticle interaction strength E_{int} has been discussed in the literature before [110]. Therein, the T dependence of E_{int} in the (not well defined) scenario when "most of the particles are fluctuating", i.e. not at very low temperatures, can be described by

$$E_{\mathrm{int}} \propto \mathrm{L}\left(E_n/k_{\mathrm{B}}T\right), \tag{3.2}$$

where $\mathrm{L}(x)$ is the Langevin function and E_n is the static interaction per neighbor. The intermediate temperature range between 30 K and 70 K shows a comparable trend.

An accurate modeling, especially of the low and intermediate temperature range including the distribution of E_{int} and KV, is hardly possible, since the easy axis of a particle due to its anisotropy energy and its preferred orientation due to the interparticle interactions are not correlated. The superposition of KV and E_{int} would therefore in general lead to a multiplicity of strongly asymmetric potentials of different shapes that contribute to the shape of the Mössbauer spectrum.

However, a simulation of the low temperature spectra supporting the SSG groundstate that neglects the aforementioned difficulties of the superposition of E_{int} and KV by setting $KV = 0$ can be achieved by simply assuming a normal distribution of E_{int}, centered around a value $E_{\mathrm{int,\,max}} > 0$ (see figure 3.7 (b)). The resulting spectra are shown in figure 3.8. Here, only one subspectrum was used, for simplicity reasons. The simulated spectra are similar to the spectra obtained before, however, the max-

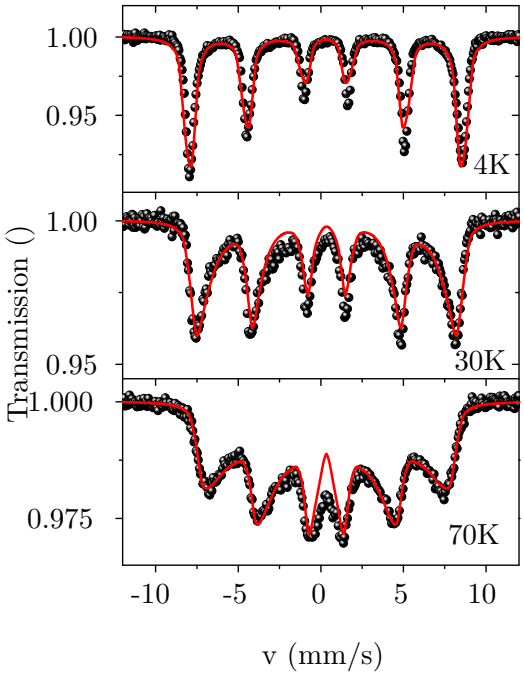

Figure 3.8: Simulation of the modified MLR including a normal distribution of E_{int} adjusted to the measurements (see text for more information).

imum value of the interparticle interaction strength $E_{\mathrm{int,\,max}}$ is slightly increased compared to the E_{int} values obtained before (see figure 3.7 (a)). These simulations show, that the modified MLR without a distribution of E_{int} is a fair approximation. Likewise to the simulations presented above, deviations in the center of the spectra appear with increasing temperature for the same reasons.

The modified MLR presented here, is only an ad hoc approach to demonstrate the influence of interparticle interactions in combination with the MLR. The influence of the asymmetric potentials at low temperatures as well as the increasing fraction of particles overcoming the E_{int} barriers at intermediate temperatures are problems that are not included in the simulations. Furthermore, the strength and direction of the E_{int}, the particles experience, are supposed to be static in this model, since the incorporation of a potential that changes on the same timescale as the Mössbauer timescale, would involve further complications. However, at lower temperatures, this assumption is well justified. These problems contribute to the mismatch between measurement and simulation in the center of the spectra at higher temperatures, already discussed before. Both approaches are, however, sufficient for an estimation of the strength and the temperature dependence of the interparticle interactions.

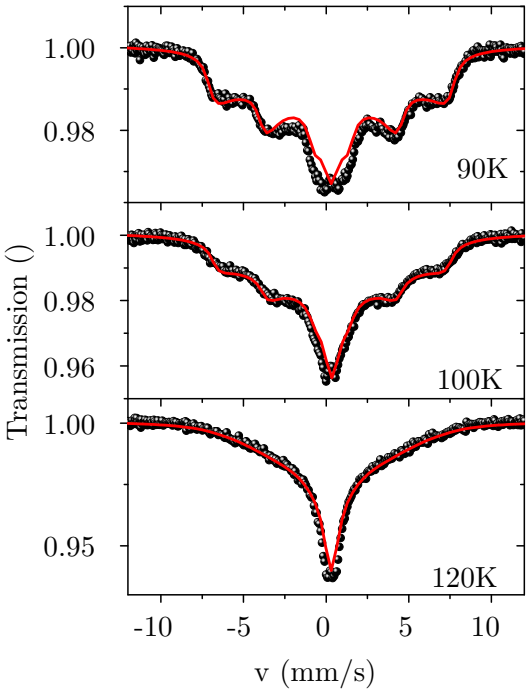

Figure 3.9: Simulation of the high temperature spectra using the MLR with a particle size distribution. Here, only one subspectrum was used.

At high temperatures, where the interparticle interactions have already collapsed, the Mössbauer spectra can be simulated using an unmodified MLR including the particle size distribution (PSD). Since the TEM image of the $ZnFe_2O_4$ nanoparticles presented above is not detailed enough to perform an automated analysis of the PSD, an estimation on basis of the TEM image was used. Within the MLR, a particle size distribution is included through a distribution of energy barriers KV. The resulting distribution of KV, already adjusted to the simulated values, is shown in figure 3.10 (a). The simulations of the Mössbauer spectra are shown in figure 3.9. Only one subspectrum was used here, for simplicity reasons. The simulations of the spectra at 100 K and at 120 K match the data very well, while the simulation of the measurement at 90 K shows a considerable mismatch between the data and the simulation. Furthermore, the distribution of the energy barrier KV was found to be stable for 100 K and 120 K, while a shift to lower values was necessary for the spectrum measured at 90 K (see figure 3.10 (a)). The relaxation rates used for the simulations are shown in figure 3.10 (b). They match the values obtained from Lierop *et al.* very well [29]. The parameter $\beta = 0.43$ and therefore in the expected range for very weak or vanishing interparticle interactions.

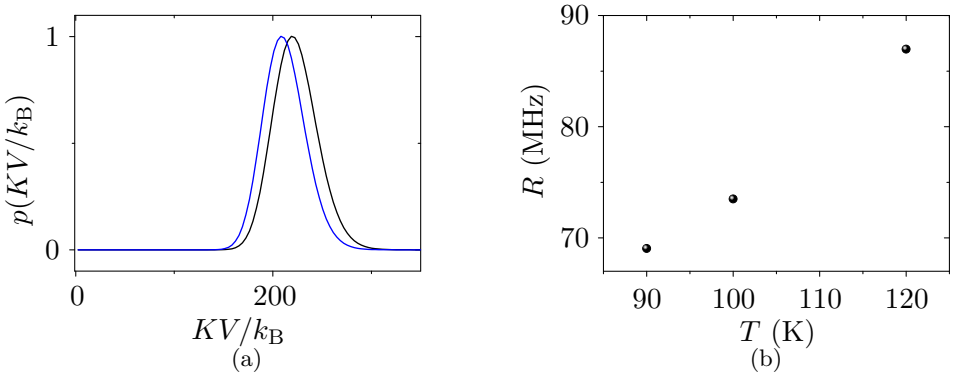

Figure 3.10: (a) Distribution of the energy barrier due to the particle size distribution for 100 K and 120 K (black) and for 90 K (blue). (b) Temperature dependence of the relaxation rate R for the maximum value of KV. A KV dependence of R was implemented by using the model after [30].

From this observation one can conclude, that a unmodified MLR which includes a PSD is able to describe the high temperature data very well, while it starts to fail below 100 K and that the spectra above ≈ 100 K can be described using single particle dynamics.

Using a combination of the modified MLR including a cos()-shaped potential and a unmodified MLR with a PSD, it is possible to reconstruct the spectral shape of strongly interaction magnetic $ZnFe_2O_4$ nanoparticles almost over the complete temperature range, where the magnetic relaxation occurs, beside the temperature range, where the interparticle interactions collapses and a complex superposition of different potential shapes occurs. A combination of the energy barriers found from both approaches gives a good overview over the regions with different magnetic properties (see figure 3.11). At low temperatures, the relaxation of the magnetic moments of the nanoparticles is dominated by the interparticle interactions, whose influence decreases with temperature. At $T \approx 70$ K, the strength of the interparticle interactions E_{int} approaches KV and complex potentials are supposed to occur. A fitting in the intermediate region is not possible. Finally, at 100 K and above, the interparticle interactions breaks down completely and the Mössbauer spectra can be fitted with an unmodified MLR with a particle size distribution.

A similar scenario has been observed from Jonsson *et al.* [111] using magnetization measurements. They investigated a set of interacting particles and came to the conclusion, that the interacting particle system can be described using a spin-glass like groundstate with a broad distribution of energy barriers at low temperatures, which turns over into a single-particle dynamic regime at higher temperatures.

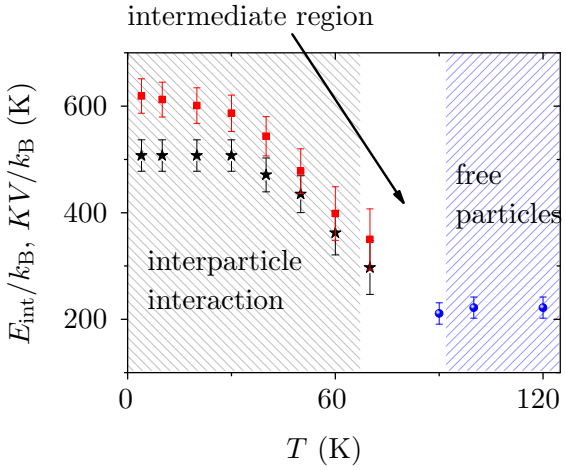

Figure 3.11: Combination of the energy barriers as derived from the modified (from 0 to ≈ 60 K) and unmodified MLR (above 100 K). Here, ★ belongs to the energy barriers without a distribution, and ■ to the maximum value of the energy barrier distribution (both in the framework of the modified MLR).

In summary, using the MLR gives valuable quantitative information about the magnetic properties of the examined nanoparticles, at least after some modifications. The biggest inconsistency of the model is the description of the collective excitations. As described above, these are modeled by assuming a distribution of static hyperfine fields, which assumes the relaxation between the occupied states to be much slower than the nuclear Larmor precession frequency. In fact, the relaxation frequency in the collective excitations regime is much faster than the nuclear Larmor precession frequency. Therefore, the low temperature spectra should rather be modeled using an average hyperfine field instead of a distribution of static hyperfine fields. Nevertheless, this arguable approach is able to describe the Mössbauer spectra at low temperatures very well and provides a reasonable temperature dependence of the different parameters.

The analysis of the Mössbauer spectra using the MLR is, however, very complex. An easier model, was proposed by Mørup *et al.* The application of this model on the obtained data will be presented in the following section.

3.2.2 The super-ferromagnetism / super-spin glass model[5]

In this super-ferromagnetism / super-spin glass model (SFM/SSG) model, the Mössbauer spectrum itself is not simulated, but instead the temperature dependence of the average magnetic hyperfine field $\langle B_{\mathrm{hyp}} \rangle$. This is obtained from a fit of the spec-

[5]Parts of the data presented in this section were obtained in the framework of a co-supervised bachelor thesis of F. Körkemeyer.

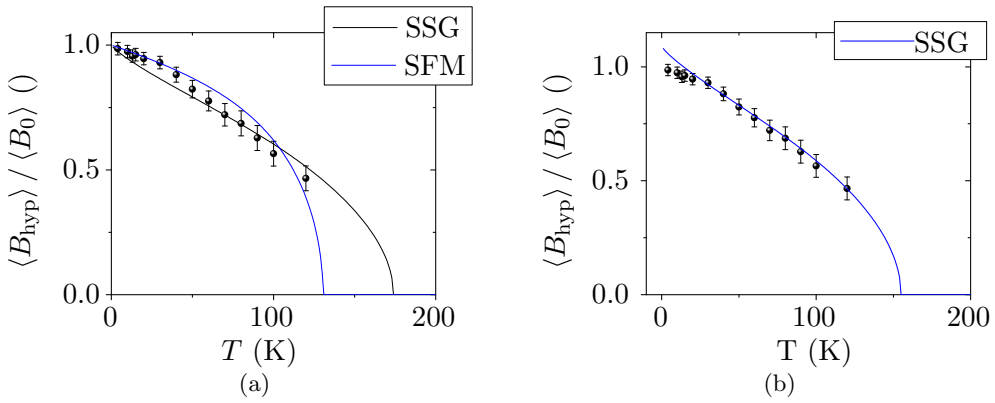

Figure 3.12: (a) The best fits for the SFM model and the SSG model to the experimental data. The transition temperature is $T_{\rm p} = 130\,{\rm K}$ and $T_{\rm p} = 174\,{\rm K}$, respectively. (b) A SSG model multiplied with the factor 1.09 and with a transition temperature of $T_{\rm p} = 155\,{\rm K}$. For further explanations see text.

tra with a hyperfine field distribution [23]. The analysis further requires knowledge of the macroscopic magnetization curve of the bulk material.

The model explicitly includes interparticle interactions resulting in two possible groundstates. In the SFM case, the coupling constant between the particles has one single value, while in the SSG case, it has a Gaussian distribution. A SFM regime is based on direct ferromagnetic exchange interactions between particles, while a SSG regime is typically based on dipole-dipole interactions (see section 1.2). The only free parameter in each of the cases is the temperature T_p, at which the average hyperfine field extrapolates to zero (see figure 3.12).

The magnetization curve for $ZnFe_2O_4$ in the high temperature ferrimagnetic phase was extracted from [107]. However, one should keep in mind that the phase diagram of $(Zn_{1-x}Fe_x)[Zn_xFe_{2-x}]O_4$ is rather complex [107] and especially that T_N depends on the inversion parameter.

The Mössbauer data and the simulations are shown in figure 3.12 (a) and (b). Both, the simulations for the SFM and the SSG model (figure 3.12 (a)) do not match the data very well.

Therefore, a further approach was made, assuming that some fraction of iron spins become randomly frozen in a magnetically canted structure at low temperatures, which reduces the average hyperfine fields, since the magnetic hyperfine field of a frozen surface layer is expected to be smaller than the value for the core of the particles (see i.e. [44] for a comparison of the surface to the bulk hyperfine field

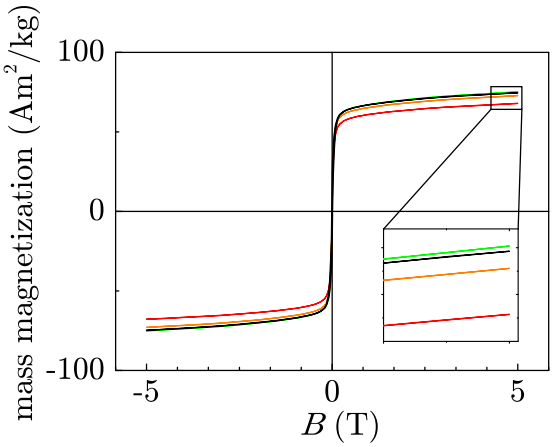

Figure 3.13: M vs. $\mu_0 H$ curves at different temperatures. — 100 K, — 60 K, — 25 K and — 2 K.

for different iron oxides). Whether this canted spin fraction is only restricted to a surface layer can, however, not be proven from these data. Whereas the experimental data represent the average hyperfine field of the entire particles, the values obtained by the SSG model only give those for the non-canted fraction. The values extrapolated from intermediate temperatures using the SSG will therefore overshoot the experimental ones when lowering temperature below the freezing temperature of the spin canted structure.

This scenario demonstrating the effect of a reduced hyperfine field compared to the simulated values from SSG at low temperatures is shown in figure 3.12 (b). The experimental data are very well reproduced down to 30 K when SSG values are scaled by a factor 1.09. This is done since the normalization of experimental data is based on the contribution of the average hyperfine field of the entire particle including the spin canted fraction, as described above. Below 30 K the effect of freezing of a fraction of spins into a canted structure becomes apparent.

Another possibility to explain a reduction from the expected temperature dependence of the magnetic hyperfine field is related to the inversion parameter x. From the phase diagram of $(Zn_{1-x}Fe_x)[Zn_xFe_{2-x}]O_4$ [107] it is well known, that a small change of the degree of inversion can destabilize the ferrimagnetic phase with high Curie temperature in favor of a phase revealing only short-range order at low temperatures. This may occur due to slight changes in stoichiometry of the particle. In consequence, this change of magnetic coupling in the particle may also result in a reduction of the average magnetic hyperfine field.

Taking into account the effect of freezing of a fraction of spins into a canted spin

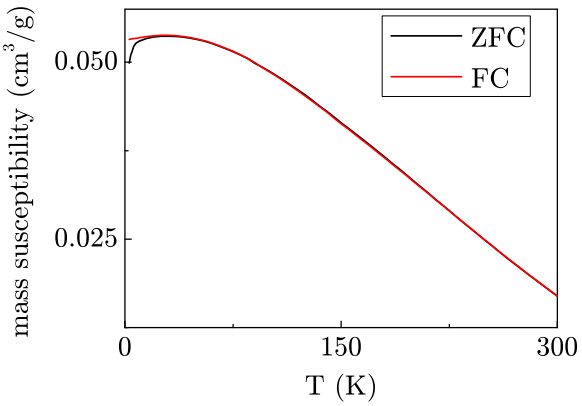

Figure 3.14: ZFC/FC curve measured on the $ZnFe_2O_4$ particles under an external field of 1 T.

structure at low temperatures on the spectral shape, the low temperature behavior of the parameter KV, as found from the data analysis by the unmodified MLR, can now also be explained. The freezing results in an extra contribution to the Mössbauer spectra with a decreased magnetic hyperfine splitting enhancing the asymmetric line shape at low temperatures. This can be compensated in the MLR by a reduced parameter KV at low temperatures (see figure 3.5). Hence the low temperature behavior of KV derived from MLR is not related to a temperature dependent energy barrier but is caused by a fraction of spins freezing into a canted structure.

In summary, the SFM/SSG model reproduces the experimental data, when assuming a canted spin fraction, which is not implemented in the model. Furthermore it supports the assumption, that the sample has a super-spin glass groundstate. Therefore, the dominant interaction between the magnetic nanoparticles is the dipole-dipole interaction. A small organic layer around the particles (a leftover from the preparation) or a layer of canted spins at the particle surface can be the reason for the minor influence of the direct exchange interaction between the particles.

3.3 DC-susceptibility measurements

M vs. H loops were performed at different temperatures and are shown in figure 3.13. They show the typical Langevin-like shape. Details about the values of the saturation magnetization M_s are shown in the inset. M_s increases with decreasing temperature down to 25 K, where it reaches its maximum. The curve measured at 2 K finally shows a decrease of M_s. As described in [112], this behavior is related to spin canting.

The ZFC/FC curves are presented in figure 3.14. From room temperature down to 50 K, both curves increase identically. Below 50 K, the ZFC curve decreases strongly, while the FC curve decreases only slightly. The observed decrease of the FC curve at low temperatures is atypical for superparamagnetic particles. As described in section 2.2.1, a flattening, but no decrease, of the FC curve at low temperatures for strongly interacting particles has been observed. The low temperature behavior of the FC curve can hence not only be explained by strong interparticle interactions. In fact, the spin canting which was found from the M vs. H curves and the application of the SFM/SSG model may explain this behavior. In this scenario, the external field of 1 T is not strong enough to align all the spins frozen into a canted structure below 25 K. When the sample is warmed up again, the frozen spins start to melt and can therefore be aligned in the external field more easily. Therefore the FC curve increases slightly at low temperatures and is not flat.

From $M(H)$ as well as $\chi(T)$, indications for a low temperature spin canting in the $ZnFe_2O_4$ particles have been observed, supporting the findings from the application of the SFM/SSG model. Furthermore, the $\chi(T)$ curve gave indications for interparticle interactions, supporting the findings from the application of the MLR.

3.4 Summary

In this chapter, the application of the MLR to Mössbauer spectra of strongly interacting magnetic nanoparticles has been presented. The unmodified MLR was found to give unphysical results, namely an increase of the parameter $\beta = k_B T_B/KV$ above the expected value and a decrease of KV with temperature above ≈ 30 K. After introducing a unidirectional potential instead of the uniaxial potential and a distribution of interparticle interaction strength due to a SSG groundstate (see below), the low temperature data were reproduced very well. At higher temperatures, a mismatch between the measurements and the simulation in the center of the spectra could be observed. This mismatch was attributed to the onset of fluctuations of particles that experience only weak interparticle interactions. A decrease of the average interparticle interaction strength with temperature goes along with these fluctuations. At intermediate temperatures, the interparticle interactions vanish, since the majority of the particles is fluctuating. In this region, the shape of the potentials of the individual particles are expected to be very complex, since the angle between the orientation of the interparticle interactions and the anisotropy energy are random, and the orientation and the strength of the interparticle interactions are time dependent. Therefore, a fitting in this region is not possible. At higher temperatures, when almost all particles fluctuate very fast, the interparticle interactions average to zero and the Mössbauer spectra can be fitted using the unmodified MLR with a particle size distribution.

The application of the SFM/SSG model revealed the presence of a SSG ground-

state and gave indications for a freezing of a fraction of spins into a canted structure at low temperatures, which can explain the observed low temperature decrease of KV from the MLR. The freezing of a fraction of spins as well as the presence of interparticle interactions have been confirmed by magnetization measurement as well.

Chapter 4

Development of the physical properties of particles during the solvothermal synthesis

In this chapter, the development of the structural and magnetic properties of iron oxide nanoparticles during their preparation with the solvothermal synthesis (see section 1.7) is described. In order to gain information about the properties of the particles during the preparation, not only the final reaction product itself is examined, but also sample material that has been extracted at different times during the synthesis.

Furthermore, this chapter demonstrates the application of the (modified) MLR, as discussed in the previous chapter, to a series of Mössbauer measurements on nanoparticles with different properties. The results are compared with complementary DC-susceptibility measurements on the same samples in order to demonstrate, which kind of information can be drawn from the Mössbauer data.

In the first sections, the basics of nanoparticle preparation in general and earlier measurements on this system are discussed. Further on, the measurements on samples extracted at different times during the reaction, using benzyl alcohol (BnOH) as a solvent, are presented. This section is divided into a part concerning the nucleation phase and into a part, where the following growth of the nanoparticles is described. The presentation of the measurements is followed by a section with a discussion. Afterwards, measurements on a preparation using triethylene glycol (TEG) instead of BnOH are shortly presented and discussed.

Detailed knowledge about the development of the physical and magnetic properties during the synthesis of the particles offers the possibility of improving the synthesis process and allows a tuning of the parameters of the particles.

The research on this topic has been performed in close collaboration with the group of Prof. G. Garnweitner from the Institut of Partikeltechnik at the Technische Universität Braunschweig, especially with I.-C. Masthoff.

The results presented in this section are partially published in [113] and [114].

4.1 Theoretical aspects on the preparation of magnetic nanoparticles

The experimental realization of the preparation of different types of nanoparticles has already been discussed shortly in section 1.7. In the following section, the theoretical aspects of the preparation will be discussed shortly.

Fundamental work on the preparation of nanoparticles was done by LaMer *et al.* in the 50's [115, 116]. Recent introductions to nanoparticle synthesis, based on the work of LaMer, can be found e.g. in [117] and [118]. If not mentioned differently, the following section is based on these sources as well as on private communication with I.-C. Masthoff.

4.1.1 Nucleation

The first step in the formation of nanoparticles is the nucleation, i.e. the formation of a new phase, which arises in the mixture of molecular colloids (monomers) and a solvent (in the case of the solvothermal synthesis presented in this chapter, the monomers are $Fe(acac)_3$ and the solvents are benzyl alcohol (BnOH) or triethylene glycol (TEG)). Nucleation occurs, when the solution is supersaturated, which results in a high Gibbs free energy G. By forming a nucleus within this supersaturated solution the volume part of the Gibbs free energy difference, $\frac{4}{3}\pi r^3 \Delta G_V$, is negative due to a reduced pressure in the solid phase with respect to the liquid pressure. However, the nucleus is only stable, when the reduction of G by $\frac{4}{3}\pi r^3 \Delta G_V$ is not compensated by the surface energy $4\pi r^2 \gamma$, which is positive. Here, γ is the surface energy per unit area. The overall change of Gibbs free energy of the process is hence calculated using a superposition of both terms

$$\Delta G = \frac{4}{3}\pi r^3 \Delta G_V + 4\pi r^2 \gamma. \tag{4.1}$$

The corresponding graph is shown in figure 4.1. For $r < r_c$, the formed nucleus is not stable, since an increase of the radius is energetically unfavorable. The nucleus dissolves again in the solution. However, after reaching the maximum value of ΔG at r_c, the system would have to spend energy in order to overcome the barrier and decrease the size of the nucleus again. Therefore, the size of the nucleus increases further after reaching this point. The radius

$$r_c = -\frac{2\gamma}{\Delta G_v} \tag{4.2}$$

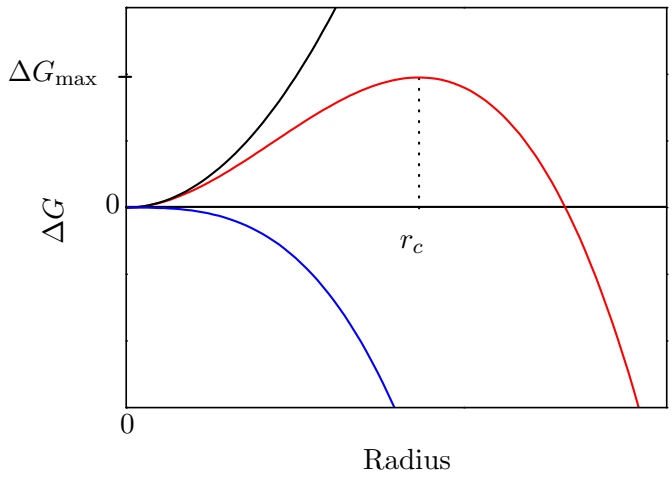

Figure 4.1: Superposition of the surface energy term (black) with the volume energy term (blue) resulting in the ΔG vs. r dependence. For more details, see text.

marks the smallest size, stable nuclei can have. After the formation of a nucleus, the decrease of the surface / volume ratio favors a further growth of this cluster. The particle growth will be discussed in the following section.

A simple diagram, showing the process of nucleation and growth after LaMer is shown in figure 4.2. The concentration of monomers is increased until it reaches the minimum concentration that allows nucleation $C_{\min}$. During the nucleation, the concentration of monomers within the solvent decreases again, which results in a reduction of ΔG. Eventually, after the concentration falls again below $C_{\min}$, no nucleation appears anymore and only the growth of particles takes place, until the equilibrium concentration, C_{eq} is reached.

The nucleation rate can be described by

$$R = \frac{C_0 k_{\text{B}} T}{3\pi d^3 \eta} \exp\left(\frac{-\Delta G}{k_{\text{B}} T}\right), \tag{4.3}$$

where C_0 is the initial concentration of monomers in the solution, d is the diameter of the growth species and η is the viscosity of the solution.

In order to achieve a narrow size distribution, the nucleation should occur in a very small time window, resulting in nuclei with nearly identical size as a starting point for the subsequent growth of the nanoparticles. If the nucleation happens over a larger time window, the nuclei that arose at the beginning are already growing, while further nuclei are still being formed. This results in a considerable particle

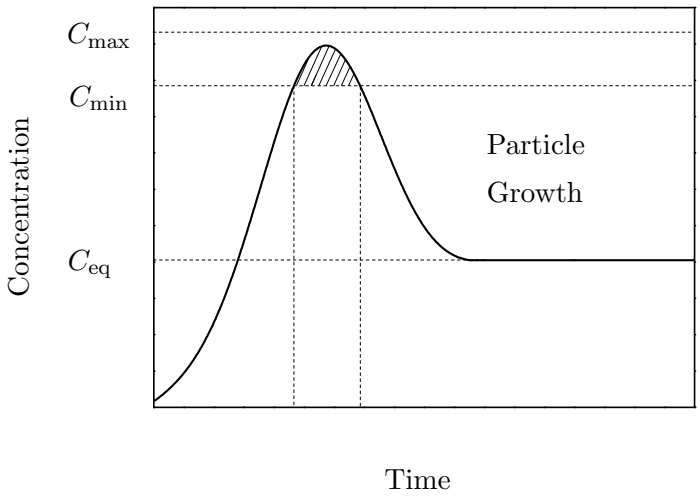

Figure 4.2: Schematic LaMer diagram, showing nucleation and particle growth over time.

size distribution.

4.1.2 Particle growth

As described in [117], the growth of nanoparticles that follows the nucleation step, can be divided into 4 parts. (1) is the formation of growth species, i.e. monomers or small particles / nuclei, that are not energetically favorable with respect to the bigger particles due to their increased surface / volume ratio and resolve in the solution in order to be (2) transported to the surface of the growing particle, (3) adsorption of these species onto the surface of the growing particle and finally (4), irreversible integration of the species onto the particle surface. However, these four steps can be divided in two categories, namely the diffusion of the growth species to the particle surface and the irreversible integration of the species on the particle surface (reaction). The growth of nanoparticles is typically limited by one of these processes, i.e. the slower process determines the growth conditions.

A quantitative description of the particle growth [118], known as the LSW theory, is based on the different concentrations around the particle (concentration of monomers / growth species within the solvent and concentration at the particle surface) and on Fick's first law

$$J = 4\pi x^2 D \frac{\mathrm{d}C(x)}{\mathrm{d}x}. \tag{4.4}$$

Here, J is the flux of growth species passing through a surface with the radius x around the particle, D is the diffusion coefficient and $C(x)$ is the x dependent

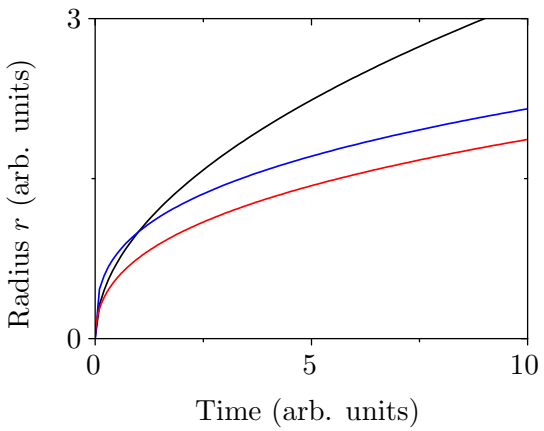

Figure 4.3: Radius versus reaction time for diffusion limited growth (blue), reaction limited growth (black) and a combination of both using $A = 1$, $B = 1$ and $C = 0$ (red).

concentration of monomers / growth species. From this starting point, it is possible to obtain

$$\frac{\mathrm{d}r}{\mathrm{d}t} \propto \frac{1}{1/D + 1/k_D r} \frac{1/r_b - 1/r}{r}. \tag{4.5}$$

Here, k_D is the rate constant of a simple first order deposition reaction and r_B is the critical radius, for which smaller particles decrease in size and bigger particles grow.

Diffusion limited growth

In this scenario, the particle growth is limited by the supply of growth species to the particle surface, i.e. the first three steps described at the beginning of this chapter are much slower than the fourth step. Particle growth, which is controlled by diffusion of growth species, which originate from the surface of smaller particles to the larger particle surface is called Ostwald ripening. Close to the particle surface, a concentration gradient is present, due to the lack of supply with new growth species to the particle surface. This can be described by $D \ll k_D r$ and allows (using other approximations) the simplification of equation (4.5) to

$$\frac{\mathrm{d}r}{\mathrm{d}t} \propto \frac{1}{r^2} \qquad \rightarrow \qquad r^3 - r_0^3 \propto t. \tag{4.6}$$

Reaction limited growth

Here, the irreversible integration of the monomers / growth species onto the surface of the nanoparticle is much slower than the supply with new growth species, i.e.

$D \gg k_D r$. This approximately results in

$$\frac{\mathrm{d}r}{\mathrm{d}t} \propto \frac{1}{r} \qquad \rightarrow \qquad r^2 \propto t. \tag{4.7}$$

Both processes are shown in figure 4.3.

However, in real systems one would expect a superposition of both scenarios. The resulting $t(r)$ behavior can be calculated to

$$t = Ar^3 + Br^2 + C \tag{4.8}$$

and is shown as well in figure 4.3.

4.2 Preparation route

The preparation of the magnetic nanoparticles investigated in this chapter begins with the mixture of 50 g $Fe(acac)_3$ with 1 l of the solvent BnOH or TEG. This mixture is heated up in in a 1.5 L reactor (Polyclave, Typ 3/1 Büchi Glas Uster) to 200°C, where it remains for at least 24 h. A valve at the reactor allows a withdrawal of sample material at any desired time during the preparation without affecting the thermal reaction conditions. The extracted particles are still in solvent. For certain cases, measurements on dried particles were performed as well. The drying process includes two washing procedures using ethyl-acetate, followed by a drying of the particles under vacuum for 48 h.

The reaction taking place during the preparation process can be described by [106, 113]

$$\mathrm{Fe(acac)_3} \xrightarrow{solvolysis} \mathrm{Fe(OH)_{3\text{-}x}(OR)_x} \xrightarrow{condensation} \mathrm{Fe_2O_3}.$$

4.3 Earlier measurements on similar systems

Measurements on similar systems performed at iPAT have been published before [106]. The results of this work are shortly presented in this section.

From UV/Vis measurements, it was found that the concentration of $Fe(acac)_3$ in BnOH and TEG decreases to almost zero within the first one and two hours, respectively.

The formation of the magnetic nanoparticles in the solvents BnOH and TEG are traced using dynamic light scattering (DLS), magnetization measurements and XRD measurements. For the particles dispersed in BnOH system, the DLS measurements revealed an average particle size of 12.5 nm even for the first hours of reaction,

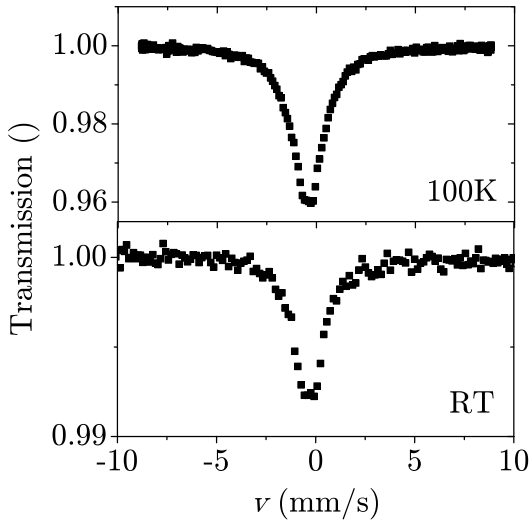

Figure 4.4: Mössbauer spectra measured on $Fe(acac)_3$ powder at the indicated temperatures.

followed by a slight increase of 15 nm with prolonged annealing. This can be understood in two ways. Either, particles already form in the heating-up phase and develop their almost entire size in that small time range, or despite the stabilization of the particles, a considerable amount of agglomerated particles exists within the sample.

The XRD measurements show an improvement of the crystallinity throughout the first four hours of reaction, which has however only been discussed qualitatively.

The saturation magnetization of the particles is very low below 2 h and jumps to a stable, high value afterwards.

When TEG is used as a solvent, the particle size determined from DLS increases from 7 nm within the first hours to 30 nm after 47 h of reaction, indicating that the agglomeration of the particles is less important in this case. The XRD measurements showed, that the crystallinity of the particles increases constantly throughout the first 14 h of reaction and hence over a much bigger timescale, compared to BnOH. Furthermore, the saturation magnetization increases more smoothly within the first 4.5 h and does not saturate.

For the synthesis with both solvents, it is proposed that magnetite is the resulting product. However, since this assumption is based on XRD measurements, a

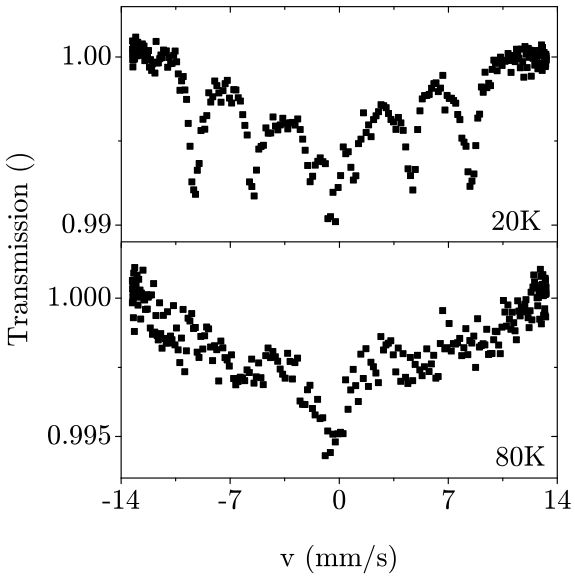

Figure 4.5: Mössbauer spectra measured on $Fe(acac)_3$ mixed with BnOH with the same proportion as the one used for the particle synthesis [113].

certain fraction of maghemite might also be present in the particles.

The measurements presented in the following, are based on these results but are supposed to extend the observations by using other measurement techniques and evaluation methods.

4.4 Experimental observations

In this section, experimental observations are presented and discussed. It is separated into a part about the properties of the initial materials and the heating-up phase, followed by a part about the thermal annealing of the mixture of the particles with BnOH. Afterwards, a short discussion about the Mössbauer measurements on particles dispersed in TEG will follow.

Different methods have been applied in order to investigate the physical properties of the particles during their growth. XRD, XPS and UV/Vis have been performed and evaluated and TEM has been performed by I.-C. Masthoff. ZFC/FC and $M(H)$ measurements have been performed by D. Menzel. Mössbauer measurements in an external magnetic field have been performed by J.A.M. Cagigas in Rio de Janeiro.

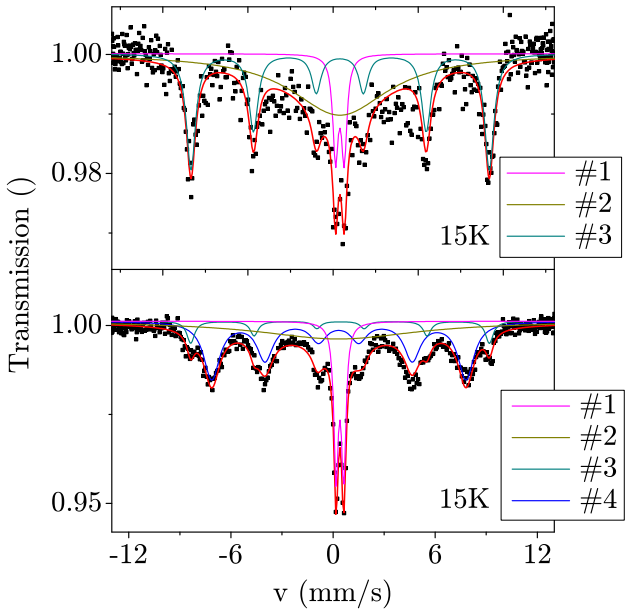

Figure 4.6: Mössbauer spectra measured at 15 K on samples extracted during the sample synthesis after the reactor has reached 160°C (top) and 180°C (bottom) [113].

The preparation of all particles discussed in the following was performed at the iPAT by I.-C. Masthoff using the solvothermal synthesis.

4.4.1 heating-up phase[1]

During the heating-up phase, samples were extracted from the reactor every 20°C and immediately cooled to room temperature afterwards.

As a first step, Mössbauer spectra were taken on $Fe(acac)_3$ powder at 100 K and at room temperature. The spectra are shown in figure 4.4. They show a broad single peak exhibiting a non-Lorentzian lineshape, which is almost temperature independent. Mössbauer measurements on the same material can be found in the literature [119]. The Mössbauer spectra presented therein have a similar shape and show almost no temperature dependence. By ruling out every other mechanism that could lead to a broadening of the Mössbauer lines, the author concluded, that slow spin-spin relaxation between the trivalent iron ions in $Fe(acac)_3$ is the reason for the

[1]Parts of the data presented in this section were obtained in the framework of a co-supervised bachelor thesis of A. Borchers.

broadening of the single line.

In figure 4.5, measurements on the mixture of $Fe(acac)_3$ with BnOH at 20 K and 80 K with the same proportion as the one used for the particle synthesis are presented. At low temperatures, the spectrum is made up of a well resolved sextet pattern, a superimposed broad structure and a non-magnetic single line pattern. At 80 K, the spectrum is severely broadened compared to the low temperature spectrum. At first glance, this temperature dependent behavior might be interpreted as resulting from superparamagnetic relaxation of magnetic nanoparticles emerging from the mixture of $Fe(acac)_3$ with the solvent. However, the magnetic hyperfine splitting of the sextet pattern corresponds to approximately 55 T, which is too big for the typical magnetic hyperfine pattern of iron oxide nanoparticles at low temperatures ($\approx$ 52 T for maghemite, see [120]). Therefore, it can be assumed, that the shape of the Mössbauer spectra is not due to magnetic nanoparticles and that no reaction took yet place. It can rather be explained with the increased distance between the $Fe(acac)_3$ molecules, which leads to a slowing down of spin-spin relaxation and thus is the origin of the magnetically split Mössbauer spectrum. The trivalent iron ions in $Fe(acac)_3$ have a $[Ar]3d^5$ electron configuration resulting in a spin $S = \frac{5}{2}$ groundstate. Due to the missing orbital moment ($L = 0$), spin-lattice relaxation is suppressed. Therefore, spin-spin relaxation is the only relaxation mechanism. When the relaxation time decreases below the characteristic timescale of Mössbauer spec-

Table 4.1: Parameters of the spectra shown in figure 4.6: centershift CS relative to metallic Fe at RT, magnetic hyperfine field B_{hyp}, quadrupole splitting $e^2qQ/2$, linewidth W (HWHM) and the relative spectral area. The site numbers in the first column are given in the same color as the corresponding subspectra. The first three columns contain the parameter of the subspectra for the sample extracted at 160°C, while the last four columns contain the parameter of the subspectra for the sample extracted at 180°C.

#	CS (mm/s)	B_{hyp} (T)	$e^2qQ/2$ (mm/s)	W (mm/s)	Area (%)
1	0.51	0.00	0.50	0.19	9
2	0.51	0.00	0.00	3.58	55
3	0.52	54.3	0.01	0.32	36
1	0.51	0.00	0.45	0.16	16
2	0.44	0.00	0.00	5.68	33
3	0.54	54.4	-0.03	0.27	8
4	0.45	46.3	0.01	0.56	43
	±0.02	±0.8	±0.04	±0.02	±2

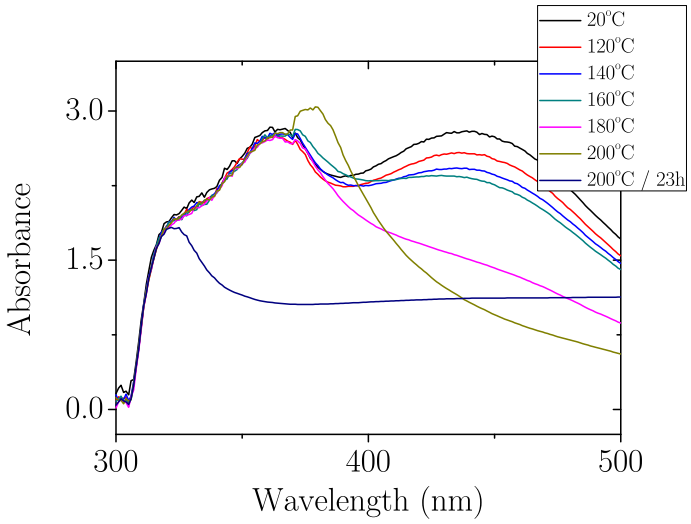

Figure 4.7: UV/Vis spectra taken on samples extracted during the heating-up phase at different temperatures [113].

troscopy, a magnetic hyperfine pattern can be observed. Similar observations were made in [119].

Measurements at 15 K on samples extracted during the heating-up phase of the reactor at 160°C and at 180°C, are presented in figure 4.6. The spectrum of the sample extracted at 160°C looks similar to the low temperature spectrum in figure 4.5, hence no reaction has occurred yet. It is fitted using a sextet pattern, a broad background and a non-magnetic doublet. The parameters can be found in table 4.1, the magnetic hyperfine field of the sextet matches the estimation for the magnetic pattern in figure 4.5 given above. However, the spectrum of the sample extracted at 180°C shows an additional magnetic sextet with a smaller splitting of ≈ 46.3 T. This additional magnetic hyperfine pattern can be attributed to the first nuclei arising in the solution. Its value of 46.3 T is smaller than the expected value for maghemite, which can be explained by a considerable amount of spin canting within the particle, which reduces the observed magnetic hyperfine field.

Therefore, the Mössbauer measurements provide clear indications for a nucleation of the $Fe(acac)_3$ monomers to magnetic nanoparticles / clusters while the temperature of the reactor is between 160°C and 180°C.

In addition, UV/Vis spectra were measured on these samples on a UV-3100PC Spectrophotometer from VWR. The curves are shown in figure 4.7. For $T < 180$°C, the curves show two distinct maxima around 360 nm and 440 nm, being typical for $Fe(acac)_3$ [121]. The second maximum in the curve of the sample extracted at 180°C

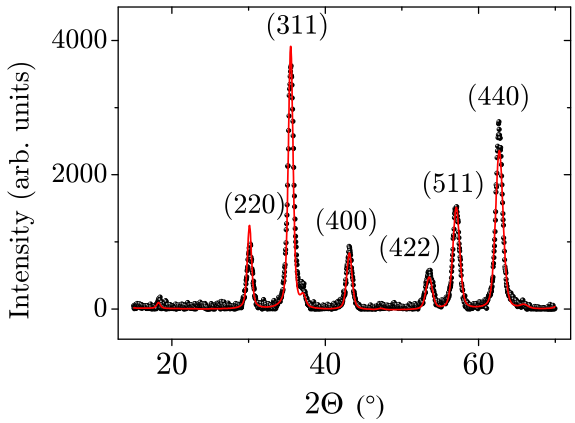

Figure 4.8: XRD spectrum of the sample obtained after 23 h of run #1. The spectrum was fitted using a maghemite powder pattern.

has almost vanished completely, indicating a transformation of $Fe(acac)_3$. The curves of the samples extracted at 200°C and after the reactor stood at 200°C for 23 h, both show a different shape compared to the low temperature spectra as well. Hence, the UV/Vis measurements support the findings from Mössbauer spectroscopy presented above.

Using Mössbauer spectroscopy, it would in principle be possible to quantitatively determine the nucleation rate during the heating-up phase if more samples between 160°C and ≈ 200°C were available. With the exact knowledge of the temperature vs. time dependence during the heating-up phase of the reactor, one could verify equation (4.3). This is, however, not part of this work.

4.4.2 Thermal annealing at 200°C

After the heating-up phase, the temperature of the reaction stays constant at T_R = 200°C until the end of the preparation process. The time of material extraction after the reaction temperature is reached, will be called reaction time t_R in the following.

The measurements presented in the following have been performed on samples obtained from two different preparation runs (#1 and #2) under similar conditions. During run #1, samples were extracted every 30 min for the first 8 h and with bigger intervals of 60 min for increased reaction times. This results in a total extracted volume of ≈ 60 %. As it has been shown before [122], an extraction of too much sample material during the synthesis may shift the equilibrium of the system, which might result in different properties of the particles. Therefore, another preparation run (#2) was performed, where sample material has been extracted every minute

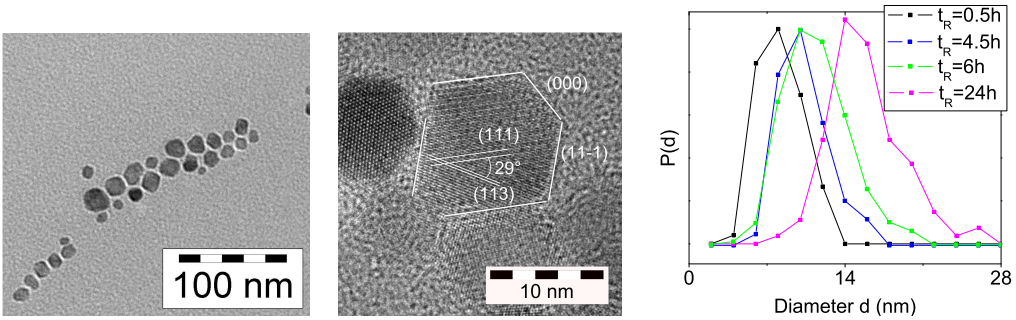

(a) (b) (c)

Figure 4.9: (a) TEM image of the sample with $t_R = 24\,h$. (b) High resolution TEM of the latest sample of run #1. The lattice plains are marked for one of the particles. The borders of this particle are parallel to different lattice plains, which results in the canted shape. (c) Particle size distribution for different values of t_R. From [114].

for the first 15 min, every 2 h for $t_R \leq 8\,h$ and one last time at $t_R = 24\,h$. Less sample material was withdrawn per extraction in run #2, which results in less total extracted volume compared to run #1. For the first 12 h of reaction, the particle size obtained from samples from both runs behaves similar, while at longer reaction times, the particle size of the run #1 increases strongly, compared to the particle size of run #2 (as it will be discussed in the following section). However, since the particle size of both preparation runs behaves similar within the first 12 h of reaction time, it is assumed that the properties of particles from both preparation runs extracted in this t_R region are the same and therefore the discussion of the measurements in the following chapter will be focused on $t_R < 12\,h$. If not otherwise stated, the measurements presented in the following have been performed on run #1.

Structural properties and particle growth

In order to examine the structural properties of the magnetic nanoparticles, XRD and TEM measurements have been applied. The XRD spectrum of the dried sample obtained after $t_R = 24\,h$ is presented in figure 4.8. It is fitted with a pattern expected for maghemite, however, a differentiation between maghemite and magnetite from XRD is hardly possible, since both materials share the same spinel structure. A second phase cannot be observed. The peaks appear rather sharp, which is an indication of the good crystallinity of the particles. A broadening of the diffraction lines of the XRD patterns can be observed for lower t_R (not shown here). By using the Scherrer equation [123], this broadening can be correlated with the size of the crystalline regions within the particles (called "crystallite size" in the following), as shown in figure 4.10.

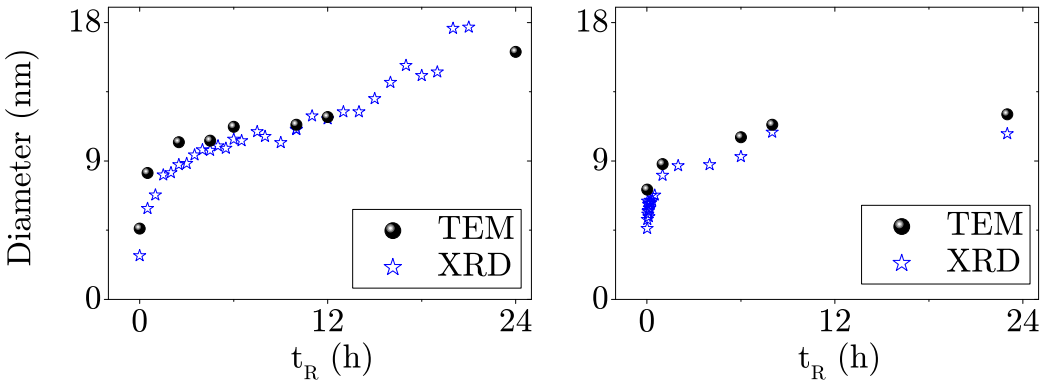

Figure 4.10: Particle diameter obtained from TEM and and crystallite diameter obtained from XRD for run #1 (left) and run #2 (right) (partially adopted from [114]).

TEM and HTEM images are presented in figure 4.9 (a) and (b). The TEM image taken on a sample obtained after 24 h of reaction shows almost spherical particles aligned in a chain structure, which would imply, that the magnetic moments of the particles in this image are well aligned along the chain direction (compare to section 1.2) and hence the system is super-ferromagnetic. However, since the samples have been dried in order to make a TEM image, the chain structure may have developed during the drying process as well. Other TEM images not presented here, show that most of the particles agglomerate in a more random structure. The high-resolution TEM image presented in figure 4.9 (b) shows spherical particles as well as particles with a rather polygonal structure. The lattice plains have been determined for a particle with a polygonal structure. This examination shows, that most of the borders of this particle are parallel to different lattice plains. In figure 4.9 (c), different particle size distributions (PSD's), extracted from the TEM images after the method described in section 2.3, are presented, showing that the average particle diameter increases with t_R and that the width of the particle size distribution increases as well.

The average crystallite / particle diameter determined from both methods for both runs are shown in figure 4.10. The particle diameter for run #1 from TEM measurements has a value of approximately 7 nm for $t_R = 10$ min and increases systematically up to 16 nm for $t_R = 24$ h. The XRD values start with approximately 7 nm and increase up to approximately 18 nm for $t_R = 21$ h. For run #2, TEM and XRD start at approximately 5 nm, for $t_R = 0$ min and increase up to approximately 12 nm for $t_R = 24$ h. Notably, the first value for run #1 was only estimated, since the quality of the TEM image was not good enough to allow an automatic analysis of the par-

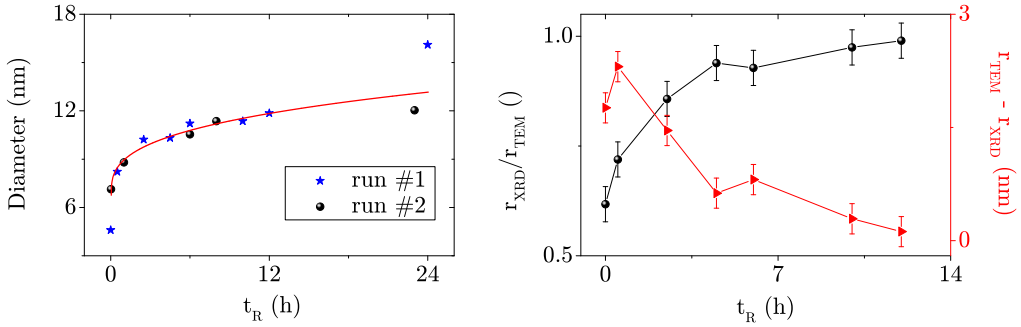

Figure 4.11: Combination of the particle diameter as obtained from TEM for both runs, fitted with a diffusion limited Ostwald ripening model (left). Crystallite radius as obtained from XRD divided by the particle radius as obtained from TEM as a measure for the crystallinity (black) and the radius obtained from XRD subtracted from the radius obtained from TEM (red) (partially adopted from [114]).

ticle size. The first 12 h, the particle diameter obtained for both runs behave very similar, as discussed above (see figure 4.11).

The curve of the t_R dependent particle diameter was fitted using the diffusion limited Ostwald ripening approach (equation (4.6)), which matches the data best. The curve describing the surface controlled growth does not fit the data.

As it can be observed in figure 4.10, the crystallite size obtained from XRD measurements is smaller than the particle size obtained from TEM measurements for $t_R < 12$ h. The reason is, that XRD measurements are limited to well crystalline regions within the particles, while TEM is able to measure the particle size, irrespective of potentially present non-crystalline regions. Therefore, the fraction of the crystallite size obtained from XRD on the particle size obtained from TEM can be understood as a measure for the crystallinity of the particles (compare to [124]). The corresponding plot is shown in figure 4.11 (right in black). Up to $t_R = 4.5$ h, r_{XRD}/r_{TEM} increases strongly and converges afterwards almost to 1, indicating that the crystallinity of the particles for small t_R is rather poor and of similar good quality above $t_R \approx 5$ h. In the same figure, the difference between the radius obtained from TEM and the radius obtained from XRD, $r_{TEM} - r_{XRD}$, is shown (in blue). If the non-crystalline region would have the same size for every t_R and the crystallinity would only improve due to the increasing particle size, this parameter should be the same for every t_R. However, it decreases significantly with temperature throughout the first 14 h. This proves, that the increase of crystallinity is not only due to an increase of the particle size but also to a healing of the non-crystalline regions with prolonged reaction time.

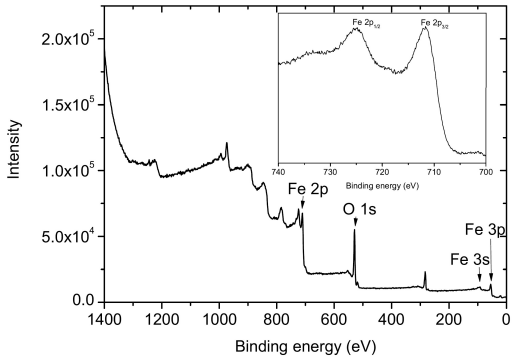

Figure 4.12: XPS spectrum of the sample obtained after 23 h reaction time from [114].

In order to distinguish whether the particles consist of maghemite or magnetite, XPS measurements were performed. The XPS spectrum is shown in figure 4.12. The peak structure indicates, that maghemite is the predominant material, however, the presence of a small fraction of magnetite cannot be excluded from these data. For more details, see [114].

Summing up the results obtained so far, the measurements on structural properties revealed that the examined particles grow continuously throughout the synthesis time up to 16 nm (run #1) and 12 nm (run #2). Their crystallinity increases to an almost optimal value within the first 4.5 h. The particles are spherical like and consist most likely of maghemite with possibly a small fraction of magnetite.

Magnetic properties[2]

The magnetic properties have been investigated using Mössbauer spectroscopy and magnetization measurements. In this section, the measurements are presented, while in the subsequent section the results are discussed.

The Mössbauer spectra of measurements on selected samples, still dispersed in BnOH, are presented in figure 4.13. Since it has to be ensured that the absorber is still in a frozen state, the maximum temperature of the Mössbauer measurements presented here is 200 K. At low temperatures, the spectra are made up of a well resolved quasi-static six line pattern, indicating that the particles are in a blocked state. With increasing temperature, the magnetic six line pattern starts to collapse into a non-magnetic structure due to the fast fluctuations of the magnetic moments of the nanoparticles. This can, however, only be observed for the sample with the

[2]Parts of the data presented in this section were obtained in the framework of a co-supervised bachelor thesis of D. Mauch.

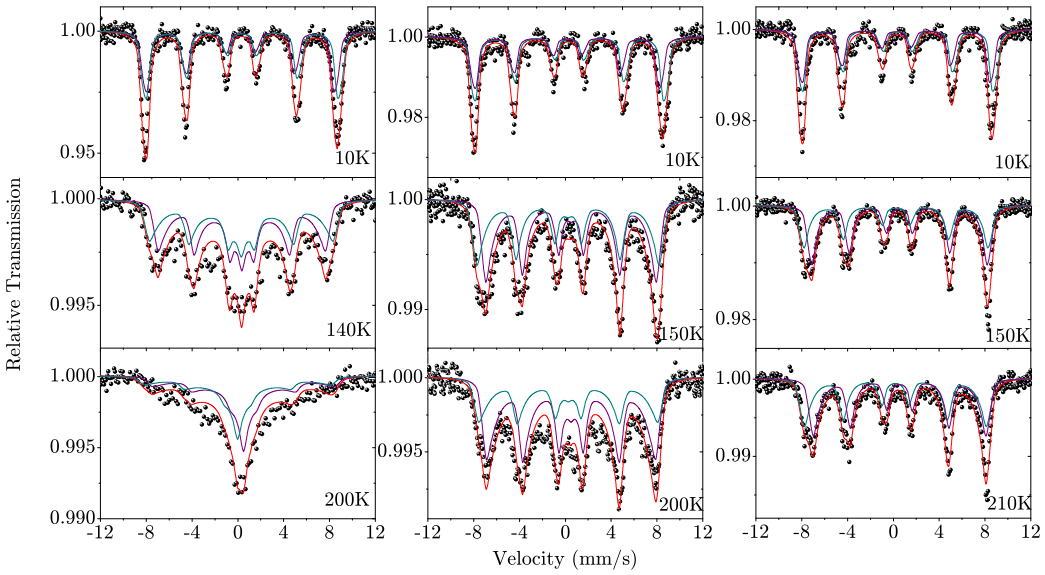

Figure 4.13: Mössbauer spectra measured on samples with $t_R = 1\,h$, $t_R = 4.5\,h$ and $t_R = 23\,h$ (from left to right) at the indicated temperatures [114].

lowest t_R, since the blocking temperature for the particles increases strongly with t_R and is far above 200 K for longer t_R. Notably, the low temperature spectrum at $t_R = 23\,h$ reveals a shoulder between the 2nd and the 3rd line at ca. -3.5 mm/s and the weight of the outer lines changes between 50 K and 200 K from the left one being the predominant line at low temperatures to the right one at higher temperatures. The shoulder is typical for magnetite at low temperatures and the change of weights of the outer lines is an indication for the Verwey transition, occurring only in magnetite and not in maghemite, as discussed in [51]. Therefore, at least a small fraction of magnetite must be present within the particles.

The spectra are fitted using the MLR model which includes the particle size distribution, which is discussed in section 2.1.3. Two subspectra were used, which is the smallest number of subspectra which fits the data. The temperature where overbarrier fluctuations set in, corresponds to $0.6\,KV$ for the samples with a small t_R, which is strongly increased compared to the expected value and indicates the presence of strong interparticle interactions (see previous chapter). It was not necessary to increase the onset temperature of overbarrier fluctuations for samples with $t_R > 4.5\,h$, since the blocking temperatures of these samples in Mössbauer spectroscopy is so high, that the overbarrier fluctuation regime is not reached at the highest mea-

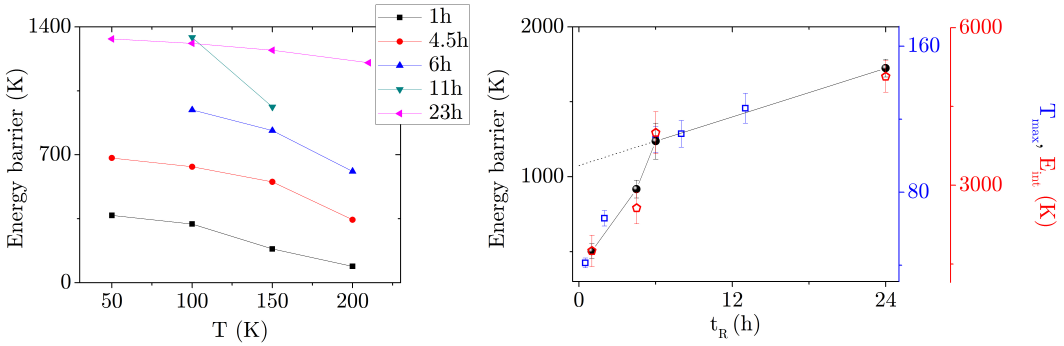

Figure 4.14: Left: temperature dependence of the energy barrier resulting from the fit with the MLR model. Right: t_R dependence of the 50 K values of the energy barrier from the unmodified MLR. The value corresponding to the $t_R = 6$ h sample was extrapolated from higher temperatures (black). E_{int} dependence on t_R resulting from a fit using the modified MLR (red). t_R dependence of the maximum temperature of the ZFC curves (blue). The black line is only a guide to the eyes. The dotted line is an extrapolation of the curves above $t_R = 6$ h. Partially adopted from [114].

surement temperature (200 K), even for the smallest particles of the samples. The temperature dependence of the energy barrier (see figure 4.14 left) is similar to the one presented in the previous chapter (see figure 3.5). It increases with decreasing temperature and converges against a constant value for low temperatures [3]. A plot of the t_R dependence of the 50 K value of the energy barrier extracted from the MLR is shown in figure 4.14 right[4]. The low temperature value was chosen, since the energy barrier for every t_R has roughly stabilized at this temperature. For the first 6 h of reaction, it increases strongly with t_R followed by a less strong rise.

In order to take into account interparticle interactions, the spectra were fitted again, using a modified MLR with a cos()-shaped potential (see previous chapter). An example of the fits is shown in figure 4.15. At lower temperatures, the model matches the measurements very well, while at higher temperatures a mismatch can be observed in the center of the spectrum. This mismatch can be explained by the influence of some fluctuating particles, which experience almost no interparticle interactions due to the super-spin glass groundstate, as discussed in the previous chapter. Moreover, the 200 K spectrum of the sample with $t_R = 1$ h could not be fitted using this model, presumably because it is in the intermediate regime, where interparticle interactions vanish. In the same figure, the temperature dependence of the energy

[3] The 100 K point of the $t_R = 11$ h sample does not match the trend of the other samples. This deviation is interpreted as an artifact.

[4] In cases where no 50 K value was measured, it was extrapolated from the values at higher temperatures, assuming a similar temperature dependent behavior of the energy barrier for all samples.

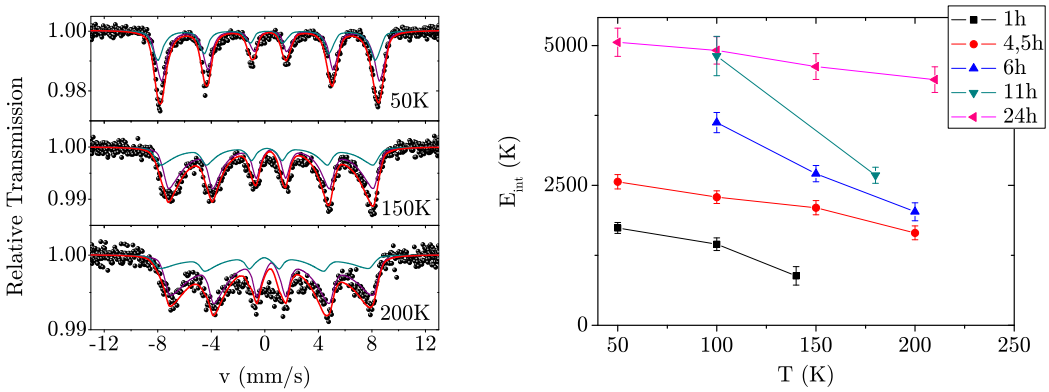

Figure 4.15: Example for a fit with the cos()-shaped potential to the sample with $t_R = 4.5\,h$ (left). Temperature dependence of E_{int} for the different samples (right).

barrier (in this case it can be associated with the interparticle interaction strength E_{int}) is presented. The trend of the temperature dependence looks similar to the temperature dependence of the energy barrier from the unmodified MLR in figure 4.14, left. The reaction time dependence of E_{int} is plotted as well in figure 4.14, right. Although the absolute values of E_{int} are much larger compared to the energy barrier resulting from the fit with the unmodified MLR, the trend of the data is the same. Note, that the different values differ only by a constant factor. The reason for the different absolute values, is the shape of the potential. A collapse of the Mössbauer spectrum within the framework of the unmodified MLR can be achieved by much smaller KV/k_BT values as in the framework of the unmodified MLR, since the relative angle to the easy axis / direction increases much faster in the latter case.

An accurate description of the distribution of interparticle interactions would, however, include not only the super-spin glass groundstate due to the dipole-dipole interactions between the particles but also the distribution of the particles within the solution (including a certain degree of agglomeration, see next section). Since the latter distribution can be hardly estimated, a fit using a distribution of E_{int} is not applied to these measurements.

Magnetization measurements were performed in order to gain complementary information about the magnetic properties of the nanoparticles.

In figure 4.16, the ZFC/FC curves measured on samples with different t_R are presented. The curves are normalized to the low temperature FC value and show two unexpected steps, one around 260 K and one around 200 K for every sample. The step at higher temperatures can be associated with the freezing of BnOH, which results in a turnover from Brownian relaxation to Néel relaxation and therewith a

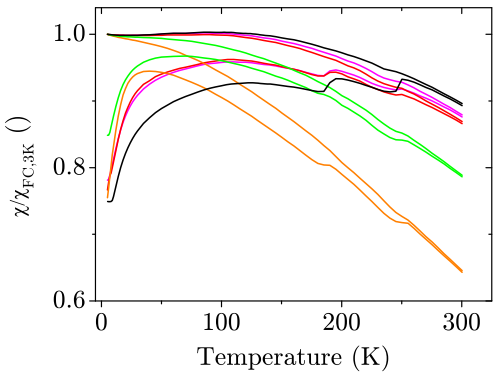

Figure 4.16: ZFC/FC measurements on samples with $t_R = 30\,\text{min}$ (orange), 2 h (green), 6 h (red), 8 h (pink) and 13 h (black), normalized to the value of the FC curve at the lowest temperature [114].

change in the relaxation rate. After a publication where similar anomalies were observed in measurements on a ferrofluid [125], the second anomaly can be associated with the defreezing process of the solution. After [126], the freezing temperature of the solution depends on the density of nanoparticles. When the interparticle interaction strength becomes effective at the freezing temperature of the solvent, agglomeration of particles can occur slightly before the freezing of the solution. While the density of nanoparticles in the region around the agglomerated clusters is very small, particles with a smaller interparticle interaction strength do not agglomerate. In the regions without agglomeration, the density of particles is higher, compared to the first scenario. Therefore, the solution contains regions with almost no nanoparticles and as well regions with a high density of nanoparticles. During the heating-up process, there are mainly two different melting points, due to the two different particle densities, and therefore two anomalies. Whether this explanation can indeed be applied to the samples discussed here, would be the topic of further investigations and can not be conclusively clarified here.

Apart from the step anomalies, the curves show the typical behavior for ZFC/FC curves measured on magnetic nanoparticles. The ZFC curves exhibits a broad maximum. The temperature of the maximum value, T_{max}, is connected to the blocking/freezing temperature of the sample. The FC curve increases from room temperature down to T_{max} for every sample and flattens at lower temperatures more and more for increasing t_R. A flattening of the FC curve at low temperatures can be associated with the presence of interparticle interactions (see section 2.2.1). Therefore, the ZFC/FC measurements support the findings from Mössbauer spectroscopy which indicate an increase of the interparticle interactions with increasing t_R.

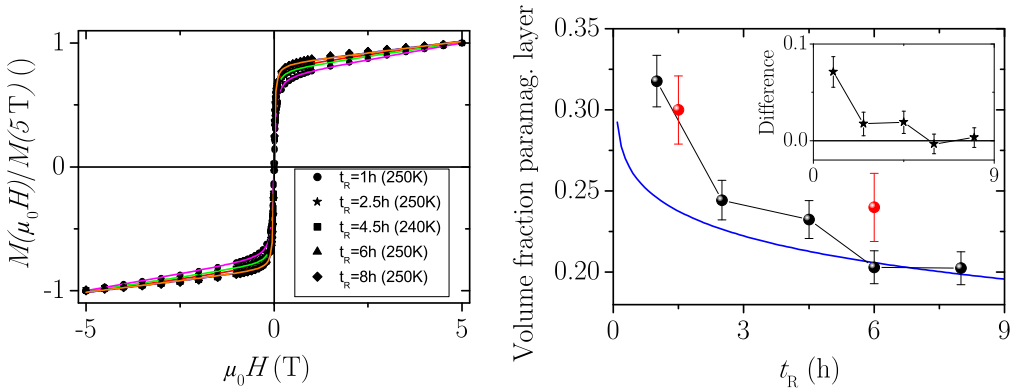

Figure 4.17: $M(H)$ magnetization curves fitted with a model after [95] for different t_R (left). The resulting volume fraction of the paramagnetic layer with the calculated contribution of a particle-size-independent surface shell of 0.4 nm and the difference between the curves in the inset (right). The red data points indicate the volume fraction of the paramagnetic layer as found from Mössbauer measurements in an external magnetic field on samples from an older preparation run. For more details, see text. From [114].

The t_R dependence of T_{max} is presented in figure 4.14. It shows the same trend as the energy barriers extracted from the MLR fits to the Mössbauer spectra. However, the absolute values are again different, which is connected to the different timescales of Mössbauer and susceptibility measurements (which is however less important in the presence of interparticle interactions). Furthermore, T_{max} is on the one hand connected to the blocking / freezing temperature and not to the energy barrier like the results from the MLR and on the other hand, is not exactly the blocking temperature but only a measure for it.

$M(H)$ measurements performed at 250 K are presented in figure 4.17. The curves are normalized to their maximum value, in order to allow a better comparison. Since the measurements were performed on the particles still being in solution, no reliable calculation of the absolute values of the magnetization curves could be performed, due to possible sedimentation, residues of unreacted $Fe(acac)_3$, etc. Therefore, the saturation magnetization of the curves is not discussed in the following. Since the measurement temperature is higher than T_{max} for all samples, the curves can be fitted using the Langevin function (see section 2.2.1). However, in order to allow simulation of the data, a model which combines the Langevin function with a paramagnetic layer (see [95] and section 2.2.1) was used. The fraction of the paramagnetic layer decreases with increasing t_R from 32 % at $t_R = 1$ h to 20 % at $t_R = 6$ h, where it stabilizes (figure 4.17).

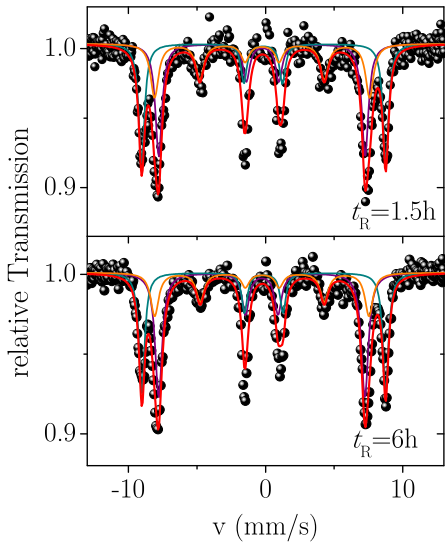

Figure 4.18: Mössbauer measurements on similar samples from an older preparation run (which was not used for other measurements presented in this chapter) in an external magnetic field of 5 T at the indicated reaction times, at 10 K.

As an example for the Mössbauer measurements in an external magnetic field on similar samples, two spectra measured at $t_R = 1.5$ h and $t_R = 6$ h at 10 K are shown in figure 4.18. The spectra were fitted using three subspectra. The dark cyan subspectrum with an increased magnetic hyperfine field of 55.2 T can be attributed to tetrahedral A site, with a moment of $5\,\mu_B$ per unit cell. The purple subspectrum with a decreased magnetic hyperfine field of 46.6 T corresponds to the octahedral B-site, which has a magnetic moment of $9\,\mu_B$ per unit cell. Due to their bigger magnetic moment, the B site moments align parallel to the external field and the magnetic moments on the A site are aligned antiparallel to the external field. Since the magnetic hyperfine field of Fe is negative, this results in a reduction of the hyperfine field of the corresponding subspectrum in the first case and in an increase in the latter case. A preferred orientation of the magnetic moments of the probe atoms parallel to the incoming γ-rays due to the external magnetic field leads to a disappearance of the 2^{nd} and the 5^{th} line in the Mössbauer spectrum (see e.g. [79]). Therefore, in both subspectra, the area of those lines is set to zero, since the corresponding magnetic moments are supposed to be in the magnetically ordered region within the nanoparticle which aligns parallel to the external magnetic field. The third subspectrum has the normal 3:2:1 ratio of the areas of the lines, since this is attributed to the canted spins within the particles, which have no correlation to the incoming γ-rays. From the area of this subspectrum, it is possible to estimate the

volume fraction of the canted spins. Therefore it is possible to get the same information from Mössbauer spectroscopy as the one from the fit with the model after Chen *et al.* [95] to the $M(H)$ curves presented above. The resulting volume fractions are shown in figure 4.17. However, since the samples used for the Mössbauer measurements in an external field presented here originate from an older preparation run, the values obtained here should only be understood as an example for the determination of the volume fraction of the canted spins from Mössbauer spectroscopy. Unfortunately, no measurements in external field on the two preparation runs discussed in this chapter could be performed.

Discussion

While XPS and DC-susceptibility measurements indicated, that the particles consist of maghemite, Mössbauer measurements gave clear indications of a Verwey transition, which only occurs in magnetite. Since all measurements were performed after a similar time after preparation of the particles, a time dependent oxidation of the particles cannot be the explanation for these observations. Furthermore, Mössbauer and DC-susceptibility measurements were both performed on samples still being in solution. Therefore, the presence of a solvent cannot be an explanation of the different results, as well. The only possible interpretation of these results is, that both materials are present in the particles. A typical scenario would be a magnetite core, with an outer layer which is oxidized to maghemite or to an intermediate stage [127].

The fact, that the Verwey transition is only visible in the Mössbauer data and not in the ZFC/FC curves, even though both maghemite and magnetite are expected to be present in the particles, can be explained by a smearing out of the Verwey transition over a larger temperature range for smaller particles [51]. For particles that exist of magnetite and maghemite, the effective volume of the fraction of magnetite within the particles is smaller as the observed particle size i.e. from TEM. Since the temperature of the Verwey transition corresponds roughly to the maximum temperature of the ZFC curve, a broadened transition riding up on the global maximum may be hardly observable.

In earlier studies, the average center shift of the Mössbauer spectra at room temperature was used to differentiate between magnetite and maghemite, since it depends on the fraction of vacancies in the particles (see e.g. [128]). An average center shift of 0.510 mm/s was found for magnetite particles, while an average center shift of 0.314 mm/s was found for maghemite nanoparticles. Since the maximum temperature of the measurements presented here is 200 K and not room temperature, it is not possible to estimate the absolute value of the magnetite / maghemite ratio from these values, due to the temperature dependence of the center shift, but its t_R dependence. The average center shift for different samples measured at 10 K is presented in figure 4.19. The centershift changes within a range of ± 0.01 mm/s for the different t_R, which indicates, that the fraction of the materials stays approximately

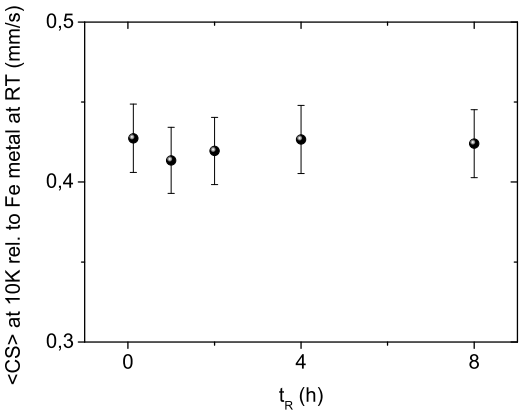

Figure 4.19: t_{R} dependence of the average center shift rel. to Fe metal at RT extracted from the samples measured at 10 K.

constant throughout the first 8 h of the reaction. Therefore, it is rather unlikely, that the particles consist of a shell of maghemite and a core of magnetite, since in this case, the thickness of the maghemite layer would increase with t_{R} by chance exactly in a way, that the ratio of the materials stays the same throughout the preparation. A scenario which is more likely is, that some particles consist of pure magnetite and some particles consist of pure maghemite or that small enclosures of magnetite are distributed within the maghemite particles.

The fitting of the Mössbauer data revealed strong indications for the presence of interparticle interactions, which is supported by the low-temperature behavior of the FC curves. Furthermore, the depth of the step anomaly in the ZFC / FC curves at 200 K increases with t_{R}, which is as well a proof for the increase of interparticle interactions, following the explanation of this anomaly given in the previous section. Both techniques showed a similar reaction time dependence of the energy barrier and the maximum temperature of the ZFC curve, respectively, which is divided into two different regimes. For reaction times below $t_R = 6$ h, both parameters show a strong linear increase, followed by a less strong linear increase for higher temperatures.

In order to verify if the observed linear t_{R} dependence is reasonable, a simple calculation based on randomly distributed particles in the solution without any layer of canted spins being coupled by dipole-dipole interaction, can be used. As a starting point, one has to calculate the average distance in dependence of the particle size. To do this, the concept of the Wigner-Seitz radius r_s is used, which is the radius of a sphere whose volume equals the average space around each particle which does

not touch the space of neighboring particles

$$\frac{4}{3}\pi r_s^3 = \frac{V}{N}. \tag{4.9}$$

The average distance between two neighboring particles can therefore be calculated to

$$d = 2r_s \propto \left(\frac{V}{N}\right)^{1/3}. \tag{4.10}$$

The number of particles within a fixed volume V can be calculated using the mass of all particles within the sphere, m_0. This step however assumes, that no monomers ($Fe(acac)_3$) are left in the solution, that could contribute to the particle growth. With

$$m_0 = \rho_p N V_p, \tag{4.11}$$

where ρ_p is the density of the material of which the particles consist and v_p is the average volume of the particle, the number of particles within V is

$$N = \frac{3m_0}{4\rho_p \pi r_p^3}. \tag{4.12}$$

Therefore, the average distance between the particles in dependence of their radius is

$$d \propto \left(\frac{V\rho_p V_p}{m_0}\right)^{1/3} \propto r_p, \tag{4.13}$$

assuming perfectly spherical particles. The next step includes the calculation of the particle magnetic moment μ_p in dependence of its radius, assuming that the particle consists of perfectly aligned spins without a canted layer. Therefore, μ_p only depends on V_p and magnetic moment per volume, μ, of the particle material

$$\mu_p = \mu\frac{4}{3}\pi r_p^3 \propto r_p^3. \tag{4.14}$$

Since the average dipole-dipole interparticle interaction depends on the square of the particle magnetic moment and the inverse of the third power of distance, it follows

$$\langle E_{\text{int}} \rangle \propto \frac{\mu_p^2}{d^3} \propto r_p^3. \tag{4.15}$$

Using the $r_p \propto t_{\text{R}}^{1/3}$ dependence found from the fit presented in figure 4.11, results in the expected linear t_{R} dependence of the energy barrier

$$\langle E_{\text{int}} \rangle \propto t_{\text{R}}. \tag{4.16}$$

However, a linear dependence of E_{int} on t_{R} can be found in both regimes, above and below $t_{\text{R}} = 6\,\text{h}$. In order to explain the origin of the two different regimes, it is necessary to take a closer look on the t_{R}-dependence of the paramagnetic layer as

found from $M(H)$ measurements presented above.

The volume fraction of the paramagnetic layer, presented in figure 4.17, can be understood as a superposition of the always present fraction of canted surface spins (see e.g. [36]) and a possibly present additional distortion of the magnetic structure within the particles. In order to estimate the t_R dependence of a magnetically distorted surface layer with a constant thickness compared to the overall fraction of the distorted magnetic fraction, a simple calculation was performed, assuming spherical, monosized particles (not discussed here in detail). 0.4 nm was used for the layer thickness, a value found from Mössbauer measurements on γ-Fe_2O_3 particles [44], as already presented in section 1.4. The blue curve shown in figure 4.17, represents the results of the calculation. For higher reaction times, the calculation and the measurements are in very good agreement, but below $t_R = 6\,h$, the difference between the simulation and the measurement increases (compare to the inset in figure 4.17). This is an indication for an additional fraction of a distorted magnetic structure within the particles, that exceeds the expected value of the particle-size-independent surface layer below $t_R \approx 6\,h$.

An increasing fraction of a distorted magnetic structure, as found from the $M(H)$ measurements shown in figure 4.17, can explain the strong decrease of E_{int} and T_{max} below $t_R = 6\,h$, since the average dipole-dipole interaction is proportional to the square of the magnetic moments of the particles, which is decreasing with increasing distorted magnetic structure. Furthermore, a distorted magnetic structure whose magnetic moments are aligned due to the dipole-dipole interaction of the magnetically ordered core of its particle, reduces the interparticle interaction strength not only due to the reduced magnetic moment of the particle but also due to the orientation of the spins within its shell for most of the orientations of the neighboring particles (see section 1.4). The effect of the additional paramagnetic volume below $t_R \approx 6\,h$ on E_{int} can be roughly estimated using $E_{int} \propto \mu^2 \propto V^2$. The volume of the magnetically ordered region within each particle at $t_R = 1\,h$ decreases by additional 15 % due to the increase of the fraction of the additional paramagnetic volume, as shown in the inset in figure 4.17, right. Therefore, the average interparticle interaction strength should decrease by $E_{int} \approx 0.72 E'_{int}$ (assuming no contribution of the distorted magnetic structure to the interparticle interaction), where E'_{int} denotes the exrapolated interaction strength at $t_R = 1\,h$ if the distorted magnetic structure would not be additionally increased at low t_R (and would therefore follow the dotted line at low t_R in figure 4.14, right). The measured E_{int} at $t_R = 1\,h$ is however only half as big as this extrapolated E'_{int} from the high t_R regime. But considering that the estimation of E_{int} is rather rough and the big errorbars, the calculated decrease of E_{int} of 0.72 to its original value due to the additional distorted magnetic structure compared to the extrapolated value, seems reasonable close to the measured decrease by a factor of 0.5. Moreover, at small t_R, the fraction of yet unreacted $Fe(acac)_3$ is presumably bigger compared to higher t_R, which might further contribute to the

decrease of E_{int}.

In this first, simple approach, the reaction time dependence of the energy barrier as well as the maximum temperature of the ZFC curve can be explained very well. However, it is necessary to estimate as well the strength of the interparticle interaction. Therefore, the distance between the particles is calculated, assuming that all $Fe(acac)_3$ monomers contribute to the particle growth and the particles are spherical, monodisperse and monosized. At first, the number of monomers in the initial solution is calculated, using the molecular mass and the overall mass of the solvent and $Fe(acac)_3$ mixture. Afterwards, equation (4.13) is used to calculate the distance between the particles under the assumptions given above. The distance between the particles is found to be approximately 25× their diameter. The magnetic moment of a particle with a diameter of 12 nm (neglecting the influence of a canted surface layer) can be calculated from the magnetic moment of $4\,\mu_B$ per unit cell, which results from the uncompensated Fe^{2+} moments. Using a unit cell volume of $590\,\text{Å}^3$ results in a magnetic moment of $\approx 6000\,\mu_B$ per particle. The interparticle interaction strength for particles with a distance of 300 nm and a magnetic moment of $6000\,\mu_B$ is

$$E_{dip} = \frac{\mu_0}{4\pi}\frac{\mu^2}{d^3} \approx 1 \cdot 10^{-3}\,K \cdot k_{\mathrm{B}} \tag{4.17}$$

and therefore negligible. The interparticle interactions would be stronger if the magnetic moments of the particles would be bigger or if the distances between the particles would be smaller. Since the magnetic moments of the particles depend strongly on their size, which was measured unambiguously via TEM and, due to the surface layer, can only be smaller and not bigger, the only possible explanation is a smaller distance between the particles. This would be the case if they are strongly agglomerated. In fact, a comparison between the t_{R}-dependent particle size on a similar system estimated from DLS presented in [106] with the particle size measured from TEM presented in this work shows, that the values from DLS are bigger than the TEM values, especially for smaller t_{R}. This is another indication for agglomeration of the particles. Since DLS only measures the Brownian motion of the agglomerates of particles in the solution and not that of the single particles, the resulting value is increased.

Even when the particles are agglomerated, the increased fraction of the paramagnetic layer at low reaction times can explain the peculiar t_{R} dependent behavior of the energy barrier, as well as the maximum temperature of the ZFC curve, around $t_{\mathrm{R}} = 6\,\mathrm{h}$ (shown in figure 4.14, right), since the decrease of the magnetically disordered region in the particles increases the interparticle interaction. However, one has to take into account, that the degree of agglomeration and therewith the average particle-particle distance probably changes with t_{R} and can therefore contribute to the reaction time dependence of the energy barrier as well. It increases presumably with t_{R} and especially strongly for $t_{\mathrm{R}} > 6\,\mathrm{h}$, since an increase of the interparticle

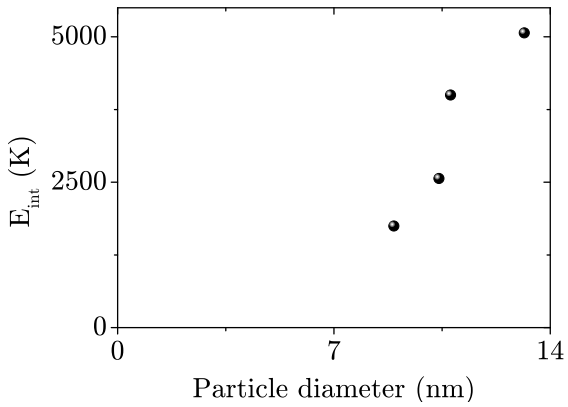

Figure 4.20: interparticle interaction strength E_{int} as found from the fit with the modified MLR to the Mössbauer measurements plotted vs. the particle diameter. In order to calculate the particle diameter for the different t_{R}, the fit presented in figure 4.11 was used.

interactions with the decreasing fraction of the paramagnetic layer also supports the agglomeration of the particles.

The magnetic properties of the nanoparticles develop very similarly to the structural properties. The fraction of the magnetically ordered regions within the particles increases only within the first 6 h of reaction and stabilizes for higher t_{R}, which has been observed for the crystallinity of the particles as well. These observations indicate a close correlation of the structural and the magnetic properties.

In a previous section, slow paramagnetic relaxation due to non interacting $L = 0$ ions was given as an explanation for the Mössbauer spectra measured during the heating-up phase before the first particles were formed. However, the examination presented in this section, indicate a strong magnetic interaction between the particles. In order to extrapolate the interparticle interaction strength E_{int} and to estimate the interparticle interaction strength during the nucleation, it is helpful to plot E_{int} vs. the particle diameter and not vs. t_{R}. This is presented in figure 4.20. The (extrapolated) interparticle interaction strength E_{int} vanishes already for particles with a diameter between 3.5 and 7 nm, indicating that the particles with a size smaller than 3.5 - 7 nm and therefore the nuclei and the initial monomers are non-interacting. This agrees well with the findings of the previous section.

In summary, the examined particles consist predominantly of maghemite with a small fraction of magnetite. Although dispersed in BnOH, the particles experience strong magnetic interactions among each other, which can only be explained with

strong agglomeration of the particles. Their average energy barrier increases with t_R, at first strongly for $t_R < 6\,h$, followed by a less strong linear increase. The origin of these two different regimes, is presumably the t_R dependence of the magnetically ordered fraction within the particles. For very low reaction times, the magnetically disordered region within the particles is much higher than the expected value for the always present surface layer, which results in a smaller interparticle interaction strength compared to particles which have only a magnetically disordered surface layer and otherwise similar properties. However, within the first $t_R = 6\,h$ of reaction, this additional contribution vanishes completely, for which reason the interparticle interaction strength can catch up with the expected value for particles of similar properties but only with the always present magnetically disordered surface structure. This results in the overproportional strong increase for $t_R < 6\,h$. For longer t_R, the magnetically disordered region remains restricted to the surface shell and therefore the interparticle interactions increase less strongly. The origin of the magnetically disordered region within the particles at low t_R can be found in the degree of crystallinity of the particles, which is worse at very low t_R and improves within the first 6 h of reaction, similar to the extra contribution of the magnetically disordered region within the particles. Therefore, the structural and magnetic properties of the particles only improve within the first $t_R = 6\,h$ of reaction time, further annealing at 200°C only results in a slight increase of the particle size and presumably in an increased degree of agglomeration.

Remarkably, all the results on the magnetic properties of the particles discussed in this section (interparticle interactions / surface spin canting / freezing temperatures) can in principle be found using only Mössbauer spectroscopy. However, in order to gain information about these properties from the Mössbauer spectra a fitting with the rather complex (modified) MLR is necessary. With some experience in this topic, a preliminary qualitative interpretation without fitting the data is possible as well. DC-susceptibility measurements are only used as a complementary technique in order to support the Mössbauer measurements here.

4.4.3 TEG as solvent medium

Mössbauer measurements have been performed on a set of samples extracted during the synthesis using TEG as solvent medium. The measurements were performed on samples extracted at $t_R = 0\,h$, 0.75 h, 1.5 h and 10 h and are shown in figure 4.21 and 4.22.

At $t_R = 1.5\,h$ and below, the spectra show the expected six line structure which collapses with increasing temperature superimposed with a non-magnetic pattern. The origin of this non-magnetic pattern is, however, not only superparamagnetic relaxation of small particles but as well a signal resulting from the yet unreacted $Fe(acac)_3$ especially for the first two samples (see figure 1 in [106]). A fit to the spectra using the MLR is hardly possible, since the exact fraction and shape of

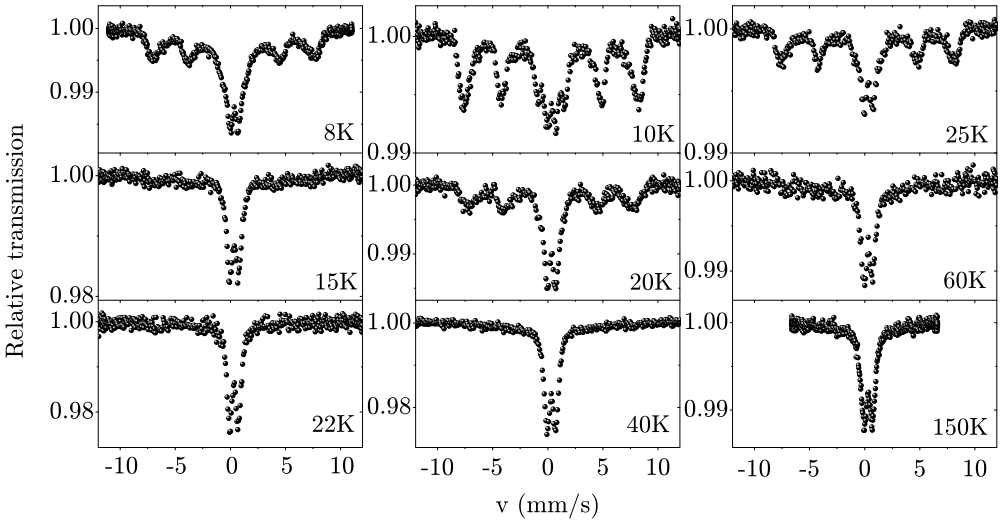

Figure 4.21: Mössbauer measurements on particles extracted during the preparation using TEG as a solvent at $t_R = 0\,h$, $0.75\,h$ and $1.5\,h$ (left to right) and different temperatures.

the signal arising from the $Fe(acac)_3$ molecules is not known and therefore hard to distinguish from the signal of the nanoparticles. Even at $t_R = 1.5\,h$, when almost no unreacted $Fe(acac)_3$ is left, a strong non-magnetic signal, that is superimposed with a well resolved magnetic hyperfine pattern, can be observed at $25\,K$. This is an indication for only weak interparticle interactions in the system. The blocking temperature of the particles increases with increasing t_R, as expected for increasing particle size.

Measurements on samples extracted at $t_R = 10\,h$ are shown in figure 4.22. The spectra on the left side were measured on nanoparticles, still dispersed in TEG, while the spectra on the right side were measured on dried particles. On first glance, the spectra of both samples appear very similar, however, at the highest measured temperature, the shape changes. While the spectrum of the particles in solution shows a less collapsed magnetic hyperfine pattern, superimposed with a non-magnetic structure in its center, the spectrum measured on the dried sample at the same temperature shows a more strongly collapsed hyperfine pattern with only a small contribution of the non-magnetic pattern in the center. In order to quantify this behavior, the spectra were fitted using the unmodified MLR with a particle size distribution resulting from the DLS measurements presented in [106]. As expected, the value of β increases with decreasing interparticle distance from $\beta = 1.1$ for the particles in solution to $\beta = 2.0$ for the dried sample. Noticeable, both values of β are

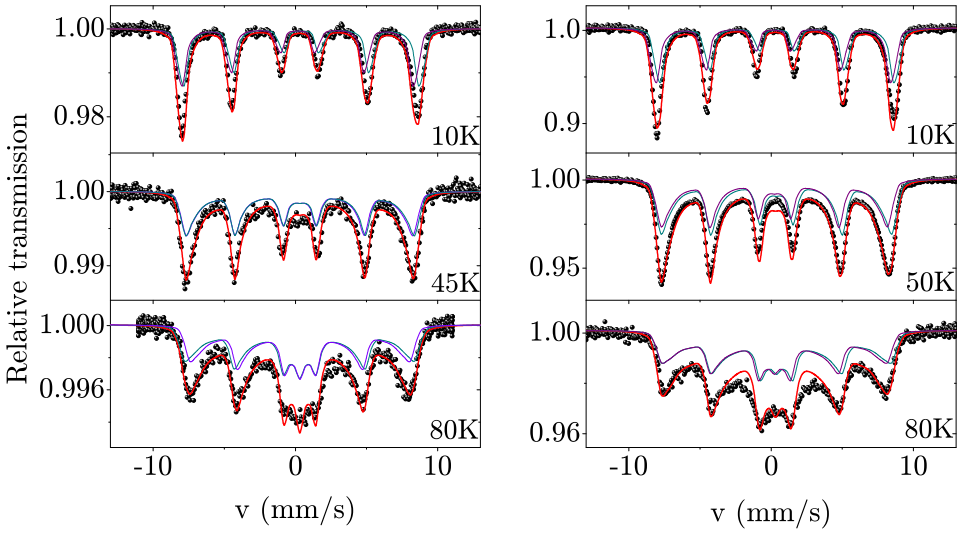

Figure 4.22: Comparison of the measurements on the sample extracted at $t_R = 10\,h$ with the particle dispersed in TEG (left) and the dried sample (right).

strongly enhanced compared to the expected value for non-interacting nanoparticles after [29] and therefore unphysical. This can be explained by considerable interparticle interactions, even for the particles in solution and by the fact, that the utilized particle size distribution was extracted from DLS measurements on another older batch of particles prepared under similar conditions (see [106]). The PSD from DLS might differ considerably from the actual PSD, since this technique is not sensitive to agglomeration of the particles. Furthermore, although prepared under similar conditions, the PSD of the sample measured here must not necessarily be similar to the PSD of the older batch of samples.

The temperature dependence of the energy barrier height for both samples shows a peculiar behavior. While the low temperature value for both samples is the same (at very low temperature, the MLR is very insensitive to slight changes in the energy barrier height and therefore its value is always connected with a large error), at higher temperature, KV of the dried sample is smaller as the corresponding values of the particles in solution (see figure 4.23). The reason for this unexpected KV vs. T dependence is the increased value of β of the dried sample. In order to achieve a collapsed structure like it is presented in the 80 K spectrum, the MLR still has to be in the collective excitation regime and the temperature must be high enough, that the occupation probability of the states far away from the easy axis, and therewith big values of the angle θ, is high. Since the temperature is fixed to 80 K, this scenario can only be achieved by a decrease of the energy barrier. For this reason,

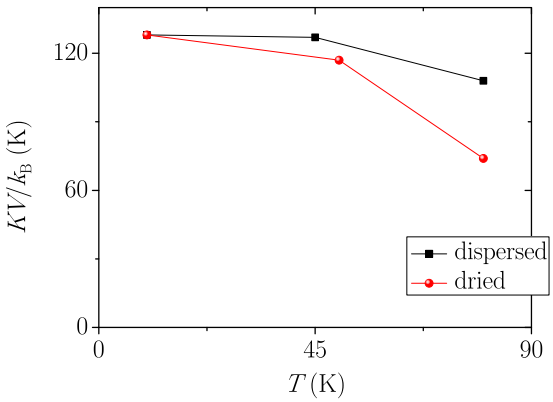

Figure 4.23: Temperature dependence of the energy barrier height resulting from the measurements presented in figure 4.22.

the absolute values of the energy barrier height, resulting from the application of the unmodified MLR can only be taken serious in case of non-interacting particles. However, when the values of β are similar, the resulting values can be used for comparison.

More information about the properties of the nanoparticles synthesized using TEG as a solvent, can be found from older DC-susceptibility measurements on samples synthesized under the same conditions in the iPAT by I.-M. Grabs and performed by D. Menzel in the IPKM in the year 2011, which have not been published yet. The measurements for different reaction times are shown in figure 4.24. From the measurements, it is obvious that no indication for a Verwey transition can be found. Only for the samples with $t_R = 2\,h$ and $4\,h$, very weak indications for an anomaly around $200\,K$ are observable, presumably with the same origin as the anomaly in this temperature region discussed in the previous sections. Furthermore, the curves demonstrate that the interaction between the particles is negligible at low t_R (from the strong increase of the FC curve at low T). With increasing reaction time, E_{int}, however, seems to increase (flattening of the FC curve at low T and small anomalies around $200\,K$). However, the interparticle interaction strength does not get as strong as it is in the particles with BnOH as a solvent, as it can be observed as well from the shape of the Mössbauer spectra.

4.4.4 Origin of the different interparticle interaction strength

The measurements on the particles dispersed in BnOH and TEG gave indication for a decreased interparticle interaction strength for the latter. A possible reason are the different magnetic properties of the solvents. The temperature dependent

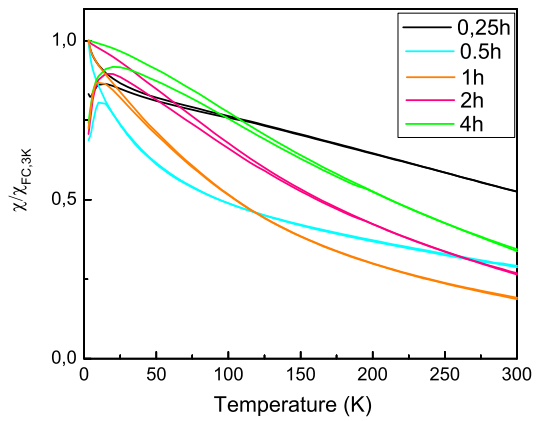

Figure 4.24: ZFC/FC measurements performed on samples prepared in the same way using TEG as a solvent.

ZFC/FC curves on BnOH and TEG is presented in figure 4.25. Both solvents show a diamagnetic susceptibility at higher temperatures. However, the susceptibility of TEG is about one order of magnitude smaller than the susceptibility of BnOH. A diamagnetic matrix around the particles is able to shield their magnetic moments to some extent and therefore to decrease the interparticle interaction strength. In order to estimate the influence of the diamagnetic matrix on the dipolar interparticle interaction, a very simple model is presented in the following.

The model is based on two interacting particles with parallel magnetic moments along their connection line with diamagnetic molecules between them. The interparticle interaction strength of both particles in vacuum is compared to the dipolar energy of the diamagnetic moments of the molecules along the connection line to one of the particles (see figure 4.26).

As a first step, the diamagnetic moment of each of the BnOH and TEG molecules has to be calculated. By using

$$M = \frac{\chi \cdot B_{\text{ext}}}{\mu_0 \cdot (1 + \chi)}, \tag{4.18}$$

the magnetization is calculated from the mass susceptibility and the applied external field (here 0.1 T). The magnetic moment of a single molecule μ can now be calculated from the magnetization by

$$\mu = \frac{M}{n}, \tag{4.19}$$

where n is the number of magnetic moments N in a volume V. This results in $\mu_{\mathrm{BnOH}} = -3.1 \cdot 10^{-7}\mu_{\mathrm{B}}$ and $\mu_{\mathrm{TEG}} = -5.4 \cdot 10^{-6}\mu_{\mathrm{B}}$.

Using the distance between the particles calculated in the previous section, the number of the molecules on the line between the particles is ≈ 600 for BnOH and ≈ 550 for TEG. Now, the absolute values of the dipolar energy of the diamagnetic molecules on the connection line between the particles, and the particle is compared to the dipolar energy between the two particles by

$$(|\sum_i E_{\mathrm{int}}(r_{\mathrm{Mol}_i\text{-Part}}, \mu_{\mathrm{Mol}}, \mu_{\mathrm{Part}})|)/E_{\mathrm{int}}(r_{\mathrm{Part\text{-}Part}}, \mu_{\mathrm{Part}}, \mu_{\mathrm{Part}}). \tag{4.20}$$

This gives a value of 0.005 for BnOH and of 0.07 for TEG. The dipolar energy of the BnOH molecules is two orders of magnitude smaller than the interaction strength between both particles and is therefore negligible. However, the interaction strength of the TEG molecules with the particle is only approximately one order of magnitude smaller than the interaction strength between the two particles and can therefore not be neglected. This observation supports the findings of the decreased interparticle interaction strength in case of TEG. This very simple model may, however, only be used for a very rough estimation for the influence of the diamagnetic solvents.

The calculation presented here does not take into account the agglomeration of the particles, which has been discussed in the previous sections. However, it shows in general, that the magnetic properties of the solvents are able to reduce the magnetic interaction between the particles. A reduction of the interparticle interaction is capable of reducing the degree of agglomeration and is therefore a possible explanation for the different interparticle interaction strength between particles prepared in TEG and BnOH.

It should however be noted, that not only a shielding of the magnetic moments of the particles by the diamagnetic molecules of the solvent contributes to the reduction of agglomeration when TEG is used, but also the structure of the molecules. While the TEG molecule has a rather elongated shape, the benzyl alcohol molecule has a ring structure. Therefore, the TEG molecules are rather able to prevent the particles from agglomerating.

4.5 Summary

The formation of magnetic iron oxide nanoparticles during the solvothermal synthesis has been studied. The main part of the examination has been performed on samples from a preparation path where benzyl alcohol (BnOH) is used as a solvent. Furthermore, measurements on samples from a similar preparation route, using triethylene-glycol (TEG) instead of BnOH as a solvent, were shortly presented and discussed. The preparation process with the solvothermal synthesis can be divided

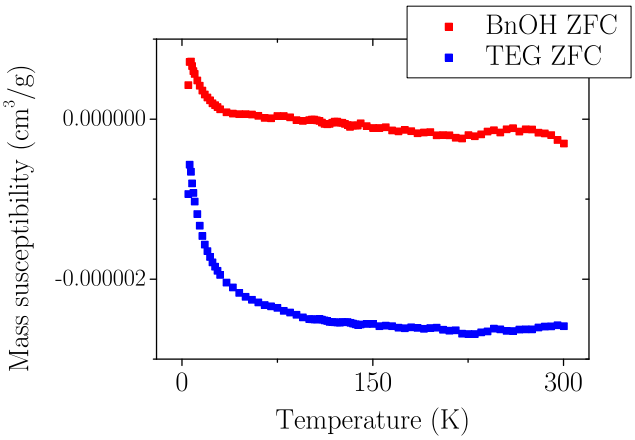

Figure 4.25: Comparison of the ZFC susceptibility curves measured on both solvents. The container where the solvents were stored during the measurement was measured empty before and the resulting signal was subtracted from the measurements of the container with the solvents. Nevertheless, the increase of the signal at low temperatures might be explained by superparamagnetic particles still present in the container, whose magnetic properties (i.e. the interaction with neighboring particles) are modified by the presence of the solvents and therefore give a slightly different signal compared to the signal of the empty box.

into a heating-up phase at the beginning of the synthesis and into an annealing phase, after the reaction temperature T_R is reached.

For the preparation based on BnOH, it was found that the $Fe(acac)_3$ monomers do not react and undergo slow paramagnetic relaxation up to a reaction temperature of $T_R \approx 160°C$, which is an indication of vanishing interaction between the monomers. The nucleation of the nanoparticles from the monomers sets in, when the reaction temperature reaches $\approx 180°C$. The knowledge of the temperature where the nucleation sets in, in principle allows a reduction of the width of the particle size distribution by e.g. heating only the solvent up to the nucleation temperature and injecting the $Fe(acac)_3$ when the temperature is reached. Thus the time interval during which the nucleation takes place (see figure 4.2) should be shortened considerably.

TEM measurements during the annealing phase indicate, that the size of the particles increases continuously up to 12 nm within the first 24 h of reaction. The particles are made up predominantly of maghemite, however, at least a small fraction of magnetite is present. From a comparison of the crystallite and the particle size, as obtained from XRD and TEM, it is concluded that the crystallinity of the particles improves during the first 4.5 h after reaching the reaction temperature and stabilizes

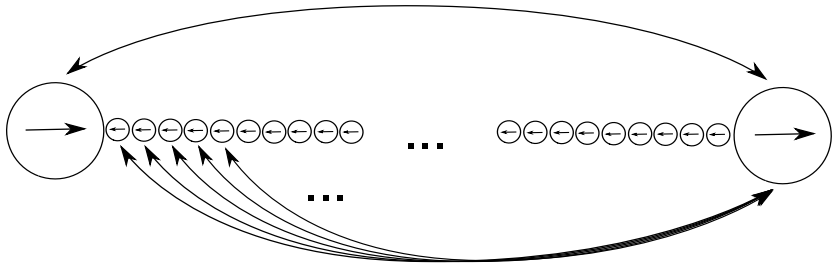

Figure 4.26: Schematic illustration of the model used here to estimate the influence of the diamagnetic matrix.

at a very high value afterwards. The fraction of the magnetically ordered volume within the particles behaves similar to the crystallinity. Within the first 6 h after reaching the reaction temperature, it increases up to $\approx 80\,\%$, which is the expected value when taking into account a disordered surface-shell of 0.4 nm (as determined for maghemite nanoparticles in [44]) for the corresponding particle size. The analogy in the t_{R}-dependence of both parameters is an indication for their close correlation.

Strong interparticle interactions throughout the whole annealing phase were found from Mössbauer and magnetization measurements. Since the expected interaction between randomly distributed particles within the solution is negligible, it is concluded that a strong agglomeration of the particles is present. The interparticle interaction strength E_{int} showed a behavior, which is closely connected to the crystallinity and the fraction of the paramagnetic layer; a strong increase below $t_{\mathrm{R}} = 6\,\mathrm{h}$, followed by a moderate increase at higher t_{R}. The strong increase at low t_{R} is presumably connected to the overproportionally increasing fraction of the magnetically ordered region within the particles and an increase of the degree of agglomeration as well.

Taking all these results for the preparation with BnOH as a solvent into account, one can conclude that after $t_{\mathrm{R}} = 6\,\mathrm{h}$, the particles are fully developed and a further annealing only results in a slight increase of the particle size and does not improve the structural or magnetic properties. On the contrary, the degree of agglomeration is presumably increased thereby.

The knowledge of the reaction time dependent development of the physical properties of the particles, enables one to obtain particles with different properties. By stopping the reaction within the first $t_{\mathrm{R}} = 6\,\mathrm{h}$, it is possible to obtain magnetic nanoparticles with a particle size which ranges from very small particles with an increased fraction of magnetically disordered areas to particles with a bigger size and an almost optimal magnetically ordered fraction. The blocking temperature of the particles can in general be tuned by stopping the reaction at different points as well,

but due to the agglomeration of the particles, further processing of the particles will presumably change the blocking temperature again.

Mössbauer measurements and DC susceptibility have been performed on particles prepared with the same technique but using TEG instead of BnOH as a solvent. ZFC/FC measurements showed no indications for a Verwey transition, wherefore the particles consist presumably basically of maghemite. The shape of the Mössbauer spectra are a superposition of a magnetically split contribution and a non-magnetic pattern in the center of the spectra. This shape is typical for non- or weakly interacting particles. A comparison of the Mössbauer spectra of particles dispersed in TEG and dried particles revealed an increase of the parameter β, which is connected to the interparticle interaction strength (see previous chapter), for the dried particles, supporting the observation that the interparticle interactions for the particles in solution are only weak. ZFC/FC measurements allowed a similar conclusion. The magnetic properties of the solvents BnOH and TEG can be used as an explanation for the different interparticle interaction strength, as demonstrated by a very simple model. While the influence of the diamagnetic BnOH on the interparticle interactions is two orders of magnitude smaller than the interparticle interaction strength, the diamagnetic moments of the TEG molecules are big enough to exhibit a considerable shielding of the particle magnetic moments and therefore reduce the interparticle interaction strength. A shielding of the magnetic moments of the particles reduces as well the agglomeration of particles. By using other even more appropriate solvents, the degree of agglomeration among the nanoparticles can further be controlled. In combination with an interruption of the synthesis at a well-defined reaction time, it might be possible to achieve well-crystalline, non-agglomerated particles. This will, however, be the topic of further studies and cannot be discussed in this work.

The solvothermal synthesis therefore is an easy, environmental friendly, low-energy preparation method for magnetic nanoparticles. It offers the possibility to tune the magnetic and structural properties of the final particles by stopping the synthesis at different reaction times. The knowledge of the temperature where the nucleation sets in, in principle allows a reduction of the width of the particle size distribution. A problem of this preparation method is the agglomeration of the particles already during the preparation. However, it was found that the degree of agglomeration depends on the magnetic properties of the solvent. The usage of a proper solvent might reduce the degree of agglomeration considerably.

Notably, all the results regarding the magnetic properties of the particles presented in this chapter could have been obtained only from a careful analysis of the Mössbauer spectra. Only the quantitative determination of the magnetically disordered fraction within the particles was determined from the $M(H)$ measurements, since no Mössbauer measurements in an external magnetic field were performed on the samples discussed here. Apart from that, the susceptibility measurements discussed in

this chapter do not give additional informations, that could not have been obtained from Mössbauer spectroscopy. Furthermore, informations about the structural properties are obtained from Mössbauer spectroscopy as well, emphasizing its versatile character.

Chapter 5

Fe-nanoclusters in Ag and Yb films prepared by vapor co-deposition

In the previous chapters, the physical properties of magnetic nanoparticles, dried and in a solution, both with a size of mostly around 10 nm, have been discussed. The Mössbauer spectra of those particles were mainly evaluated using the MLR after Jones *et al.* [86].

In order to demonstrate the evaluation of the low temperature Mössbauer spectra of a very different sample type, measurements on iron clusters, distributed in a matrix of Ag and Yb are examined in this chapter. A new approach to evaluate the low temperature Mössbauer spectra is presented, since although the MLR was found to give good results when applied to spectra measured on magnetic nanoparticles, the description of the collective excitation regime in the framework of this model is not physically reasonable, as discussed before (see section 3.2). The reason is, that the relaxation within the potential well is described by a superposition of static magnetic hyperfine patterns, weighted with the occupation probability of the individual states in the potential well at a certain temperature. However, the fluctuation time of the collective excitations is far smaller than the timescale of Mössbauer spectroscopy.

Therefore, a more adequate description of the Mössbauer spectra in this regime should be based on a temperature dependent, average hyperfine field, resulting from the time average of the orientation of the magnetic moment of the particle in the potential landscape. For comparison with the results of the different approaches, the MLR is applied to the Mössbauer spectra as well.

In the 1960s and 1970s, $Au_{1-x}Fe_x$ and $Cu_{1-x}Mn_x$ have been studied extensively, since both systems were proposed as model spin glass systems [129, 130, 131]. A phase diagram for $Au_{1-x}Fe_x$ is presented in [132]. It includes seven different phases,

starting with a transition from a paramagnetic to a spin glass phase for low concentrations, turning over to a paramagnetic to superparamagnetic to a cluster glass phase transition. Beyond a critical concentration (here $\approx 15.5\,\%$), the system turns ferromagnetic up to high temperatures, while a combined ferromagnetic and cluster glass phase is found at lower temperatures. After [25], a super-spin glass groundstate can be expected for the concentration range of Fe in Ag discussed in the following.

As it can be seen from [129, 130, 131, 132], the complex behavior of these materials has already been studied intensively 40 years ago and their different phases have been well understood.

Nowadays, the study of magnetic nanoclusters in different, non-magnetic materials is again of great interest. For small concentrations and therewith very dilute systems, the single-ion Kondo effect has been observed, while bigger clusters, resulting from a higher concentration, are interesting since they may reveal more information about the electronic properties of quantum dots.

Systems ranging between these two regimes are not studied very extensively yet.

Therefore, a series of measurements on Fe diluted in Ag and Yb, using concentrations ranging from $0.3\,\%$ up to $5\,\%$, with different methods, including X-ray diffraction, (magneto-) resistivity, DC- and AC-susceptibility, low-energy μSR and Mössbauer-spectroscopy, was started in the group of E. Baggio Saitovitch at the Centro Brasileiro de Pesquisas físicas (CBPF) in Rio de Janeiro (Brasil). Several of these results have been published [67, 68, 69, 70]. The aim of the measurements on these materials is, to learn more about the formation of magnetic clusters in non-magnetic materials, the magnetic dynamics of the clusters, including the strength and the type of magnetic interaction, and the dependence on different preparation parameters.

The results presented in following chapter come in part from a long-lasting collaboration between the group of E. Baggio-Saitovitch with the IPKM. The aim of the present work is, to gain information about the low-temperature magnetic properties of the clusters, by evaluating the low temperature Mössbauer spectra, measured mainly at CBPF, and by evaluating AC susceptibility measurements on the samples. The AC-susceptibility measurements have been performed by M. Thede at the ETH Zurich. Other work, like e.g. the preparation and characterization of the films and the identification of the cluster types, has been done before in master and PhD theses at CBPF by P. Munayco, W.T. Herrera and C. Rojas-Ayala [133, 68, 72].

In the following sections, the results of earlier measurements on Ag(Fe) are described and a simulation for the low temperature Mössbauer data is presented. This simulation is based on the specific physical properties of the Fe clusters, as found from

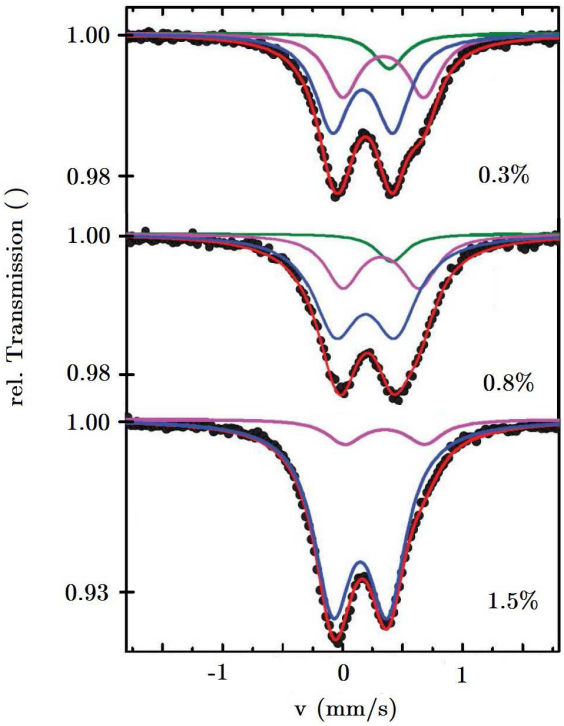

Figure 5.1: Room temperature Mössbauer spectra for the Ag(Fe) films with different concentrations (adopted from [68]).

the earlier measurements. Afterwards, the measurements on Yb(Fe) and their differences to Ag(Fe) are presented and discussed.

The percentage of iron in Ag or Yb films should always be understood as atomic % in this chapter.

5.1 Ag(Fe)

5.1.1 Sample Preparation

The samples were prepared by vapor co-deposition. Simultaneous evaporation of pure iron and silver on a kapton substrate with different evaporation rates leads to thin Ag(Fe) films with adjustable concentrations of Fe (details about the preparation technique can be found in [134, 68, 133]). The thickness of the films is in the range of a few μm. A comparison of different films showed, that the results do not vary for different thicknesses.

The kapton temperature during the preparation was either 285 K or 85 K. The results differ slightly for the two temperatures, which can be explained as a result of the different diffusion behavior of Fe for different temperatures. Since the differences between the Mössbauer patterns in the magnetic regime around helium temperature are minor, only the films prepared at 285 K kapton temperature are considered.

Samples with Fe concentrations ranging between 0.3 % and 1.5 % have been studied.

If not mentioned differently, the results presented in the following section originate from [67].

5.1.2 Measurements

Room Temperature Mössbauer Spectroscopy

The room temperature Mössbauer spectra of the different samples are shown in figure 5.1. The spectra are well described by three non magnetic subspectra, two doublets (DI with bigger quadrupolar interaction and DII with smaller quadrupolar interaction) and one singlet (S), for all concentrations. Earlier measurements had been fitted with one doublet and two singlets [134] but a careful comparison showed, that the present model matches the spectra slightly better.

The spectra can be attributed to different Fe aggregates by taking a closer look at the hyperfine parameters. The concentration dependent variation of the parameters is shown in figure 5.2. The area, the quadrupolar splitting and the isomer shift are varying systematically, which is an evidence for the good quality of the model. A bigger quadrupolar interaction can be correlated with particles with a less symmetric surrounding, for example particles on the surface of a cluster. Therefore, a first idea is to associate DI with particles on the surface of a cluster and DII with particles in the core of a cluster. This can be excluded, since the areas of these two subspectra would imply clusters in the μm range. Clusters with such a size would exhibit a freezing of their magnetic moment at much higher temperatures as observed in the following.

The most likely explanation therefore is, that DII belongs to bigger clusters with a higher symmetry around Fe than those responsible for DI. The remaining singlet S has to be attributed to Fe monomers, since they do not experience any quadrupolar interaction at all in a cubic lattice site of Ag.

With increasing concentration, the fraction of monomers and small clusters decreases. Since this behavior is expected, it supports the interpretation of the different cluster types given here.

Mössbauer measurements under an external magnetic field ranging from $B_{ext} = 0\,\mathrm{T}$

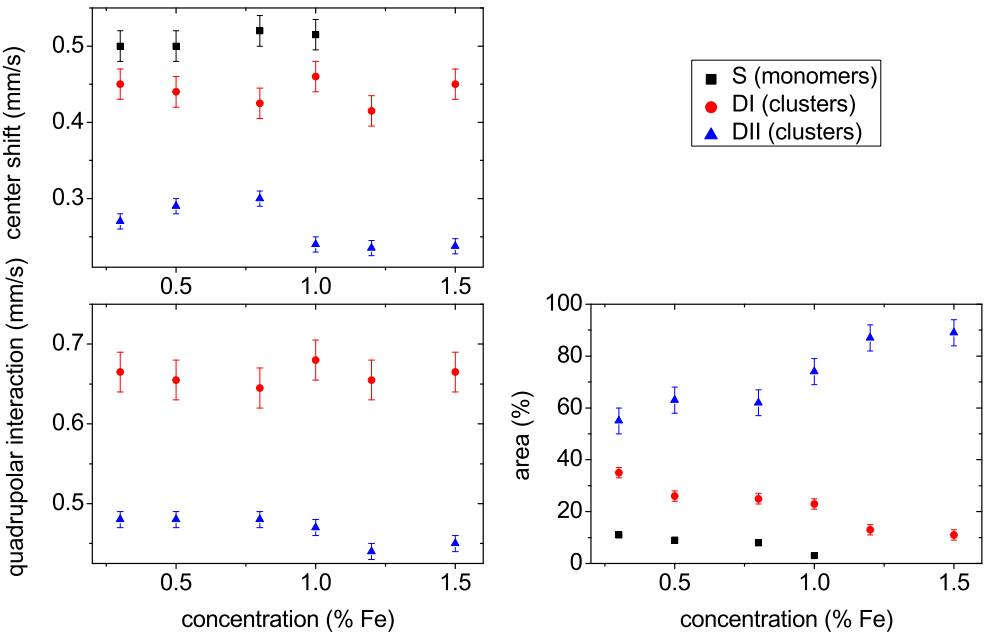

Figure 5.2: Variation of the parameters of the room temperature Mössbauer spectra for different concentration (adopted from [68]).

up to $B_{ext} = 7\,\mathrm{T}$ at $T = 30\,\mathrm{K}$ gave more information about the cluster types. A fit of the dependence of the magnetic hyperfine field on the external magnetic field with a modified Brillouin function after [135] for uniaxial fluctuations yielded an average magnetic moment of $\mu \approx 35\mu_B$ which is a reasonable for small, ferromagnetic clusters. However, this value should just be understood as a rough approximation, since the utilized model does not include interparticle interactions, which are clearly present in this system as it will be shown below.

(Magneto-) Resistance

More information about the magnetism in the Ag(Fe) system can be found from resistivity measurements. The results for different concentrations can be found in [67]. The resistivity for high concentrations shows a decreasing resistance with decreasing temperature for temperatures above 20 K, an area with a smaller slope around $T = 12\,\mathrm{K}$ and a strong decrease around $T = 7\,\mathrm{K}$ down to the lowest temperature. With decreasing Fe concentration, the slope in the region around $T = 12\,\mathrm{K}$ continues decreasing and even turns negative for concentrations below 0.5 %. In the 0.3 % measurement, a minimum around $T = 18\,\mathrm{K}$ is followed by a maximum around

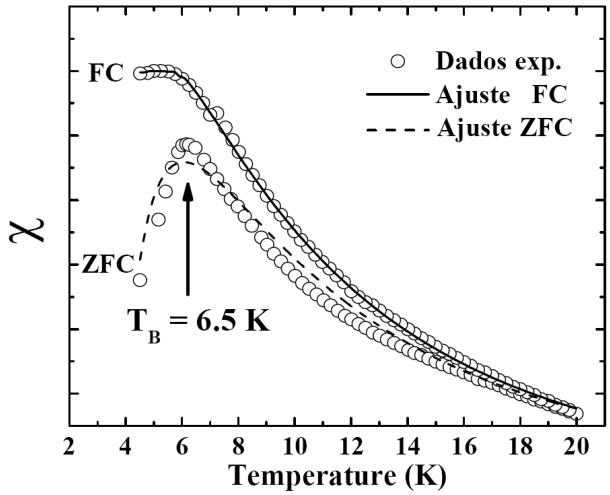

Figure 5.3: DC-susceptibility FC and ZFC curve for a 1 % Ag(Fe) film [133] with $B_{ext} = 20\,\mathrm{Oe}$. The solid lines are fits, which are not discussed in the present work. Instead, it is referred to [133]. Reproduced with the kind permission of P. Munayco.

$T = 6\,\mathrm{K}$, for lower temperatures, the resistance decreases again.

The minimum around $T = 18\,\mathrm{K}$ and the following increase of resistance at lower T are a result of the Kondo-effect, which is due to a polarization of the Ag conduction electrons around the magnetic Fe impurities. The decrease at lower temperatures can be interpreted as the onset of the magnetic coupling between the magnetic Fe clusters via the Ag conduction electrons. They couple through the RKKY interaction, which results in a suppression of the Kondo-effect and, for this reason, the following decrease of the resistivity [136, 137].

For higher concentrations, the magnetic coupling sets in at higher temperatures and hence suppresses the Kondo effect much earlier. Therefore, the distinct structure resulting from the Kondo-effect smears out with increasing concentration.

AC- and DC-susceptibility measurements

AC- and DC-susceptibility measurements were performed in order to gain more information about the magnetic regime, i.e. the blocking temperature and the interparticle interaction.

The ZFC/FC curve, presented in figure 4 in [67], looks atypical. The increase of the FC curve for low temperatures appears to be strongly enhanced, in comparison with similar measurements leaving the physical meaning of this experiment under

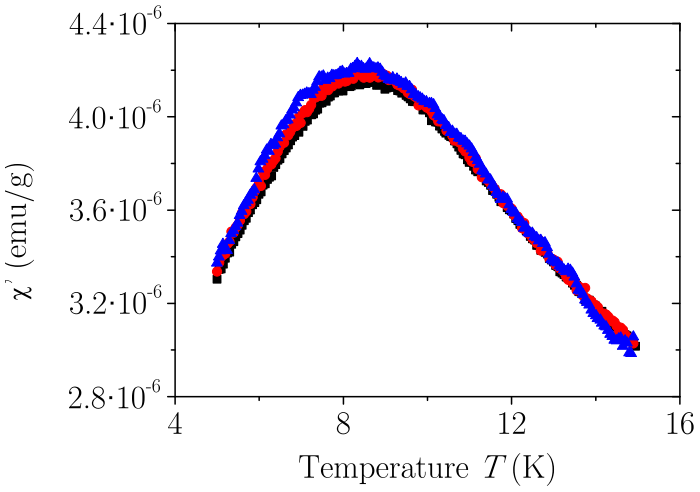

Figure 5.4: AC-susceptibility curves for different frequencies. ■: 550 Hz, ●: 350 Hz and ▲: 150 Hz.

question. Therefore, data from a similar sample of the same concentration is used for further discussion (see figure 5.3).

From the maximum of the ZFC DC-susceptibility curve shown in figure 5.3, it is possible to estimate a blocking temperature of $T_B \approx 6.5\,\mathrm{K}$ since the external magnetic field is only $B_{ext} = 20\,\mathrm{Oe}$ and therefore the difference between the maximum temperature and the blocking temperature is only small. The FC curve is increasing with decreasing temperature and finally flattens around $T = 6\,\mathrm{K}$, which is a clear evidence for interparticle interactions.

To confirm the presence of interparticle interactions in the sample, AC-susceptibility measurements have been performed. The freezing of the particles can be seen as a maximum, which changes its temperature for measurements at different frequencies. This frequency dependent shift gives information about the interparticle interactions in the system.

The AC-susceptibility curve for a 1 % film in [67] shows a peak at around $T = 10\,\mathrm{K}$, which is associated with the blocking temperature. In order to confirm the presence of interparticle interactions, additional AC-susceptibility measurements with different frequencies on another similar 1 % film have been performed at ETH Zürich by M. Thede. Their evaluation was a part of this work. The results are shown in figure 5.4.

With increasing frequency, the maximum shifts to lower temperatures, which is

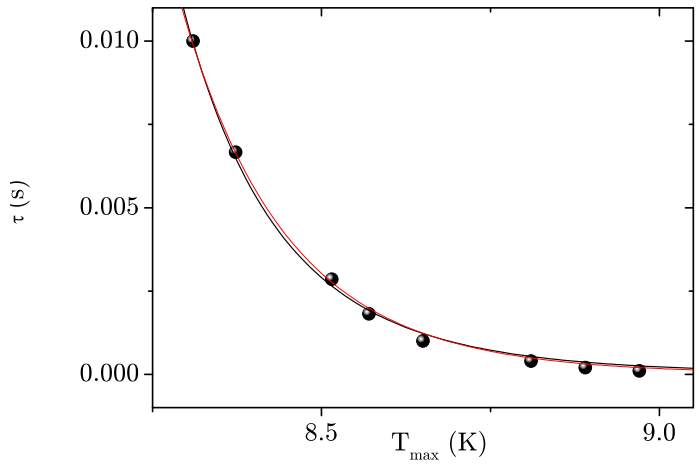

Figure 5.5: Comparison between a fit with the Vogel-Fulcher law (——) and the Arrhenius law (——) to the data from figure 5.4.

shown in figure 5.5. The temperature which corresponds to the maximum value of the real susceptibility χ' has been determined by fitting with a polynomial and solving the extreme value problem. The best fits with an Arrhenius law

$$\tau = \tau_0 \exp\left(\frac{A}{T}\right) \tag{5.1}$$

and a Vogel-Fulcher law

$$\tau = \tau_0 \exp\left(\frac{A}{T - T_{VF}}\right) \tag{5.2}$$

are presented in the same figure. The parameters for the Arrhenius law are $\tau_0 = 1{\cdot}10^{-25}$ s and $A = 440$ K and for the Vogel-Fulcher law are $\tau_0 = 1{\cdot}10^{-10}$ s, $A = 48.8$ K and $T_{VF} = 5.66$ K. They show clearly, that it is necessary to use a Vogel-Fulcher law for an appropriate description of the data, since the values of the parameters derived from the Arrhenius law are physically not reasonable. This is an evidence for considerable interaction between the magnetic clusters (compare for example to [138]). Since the value of $T_{\mathrm{VF}} \approx 0.7 \cdot T_{max}$ is rather big, the interparticle interactions appears to be very strong in this system.

LE-μSR

LE-μSR TF measurements have been performed at the Paul-Scherrer-Institut on a 1 % Ag(Fe) film. The spectra at different temperatures were fitted with a damped

cosine function

$$A(t) = A_0 \cos(\omega \cdot t + \varphi) \cdot \exp\left(-(\lambda t)^{\beta}\right), \tag{5.3}$$

as shown in [70]. From the loss of asymmetry around 18 K, one can clearly define the onset of magnetic order or magnetic freezing, respectively. The strength of the damping of the cosine function is related to the fluctuations of the magnetic moments of the clusters. Between 15 K and 100 K, the damping parameter λ can be described by an Arrhenius law with an activation energy of $E_A = 22\,K \cdot k_B$ for $\beta = 1$ and $E_A \approx 40\,K \cdot k_B$ for $\beta = 1/2$. At higher temperatures, muon diffusion sets in and it is not possible to evaluate the spectra anymore.

The applicability of the Arrhenius law to the data at higher temperatures demonstrates, that no magnetic interaction between the clusters is present in this temperature range. The magnetic interaction only sets in, when the clusters start to freeze. This behavior is similar to the temperature dependence of the interaction strength of the strongly interacting $ZnFe_2O_4$ nanoparticles below the blocking temperature presented and discussed in figure 3.11 in chapter 3. In order to fit the low temperature spectra it was necessary to include strong magnetic interparticle interaction, which however decreases with increasing temperature. At higher temperatures, a fitting of the data with a model that does not include interparticle interactions was possible, indicating a decreasing and finally vanishing interparticle interactions with increasing temperature.

Preliminary summary

So far, the results from the described measurements draw a coherent picture of the magnetic properties of the the Ag(Fe) films.

The Fe ions form three different types of aggregates in the Ag film, i.e. ferromagnetic clusters with two different sizes and monomeric Fe. Their relative fractions depend on the Fe concentration. The clusters are expected to be randomly distributed in the Ag(Fe) film. At low temperatures, they couple through the conduction electron band of Ag by RKKY interaction and hence exhibit a spin glass temperature below which the magnetic clusters are frozen.

The following simulation is based on a random distribution of the clusters in the Ag film. It is, however, not possible to exclude a scenario, where the Fe clusters are located at phase boundaries in the Ag film.

5.1.3 Simulation of the low-T Mössbauer data

In this section, a possible simulation of the low temperature Mössbauer data of the Ag(Fe) films is presented. As discussed in chapter 3, modelling of the collective excitations within the framework of the MLR, is based on a distribution of

magnetic hyperfine fields. Since the fluctuation rate of the collective excitations is much higher than the nuclear Larmor precession frequency, Mössbauer spectra in this regime should, however, rather be modeled using an average hyperfine field instead of a distribution. This approach is used for the development of a model in this section. It is based on the physical properties of the systems found from the measurements described above, namely randomly distributed ferromagnetic Fe clusters coupled via RKKY interaction. In the first step, the simulation of the Mössbauer spectrum resulting from the collective excitations of the Fe clusters that experience strong interparticle interactions and in the second part the simulation of the over-barrier fluctuations are described.

As a comparison, fits to the data using the MLR are presented and discussed afterwards.

The potential

At first, it is necessary to define a potential for a certain cluster. This topic has already been discussed in chapter 1.2, but will be repeated here shortly. Without interparticle interactions, the potential is of uniaxial shape

$$E_{uniaxial}(\theta) = KV \sin(\theta)^2. \tag{5.4}$$

In this case, the particle has one easy axis and it can flip between its two easy directions parallel to this axis. A potential shape like this is mostly generated by one of the two strongest anisotropies, the shape anisotropy or the magnetocrystalline anisotropy. More details about the different anisotropies can be found in chapter 1.1.2 of this work.

The interparticle interaction, however, acts as a molecular field, which results in a different potential, since the particle has only one easy direction and no easy axis anymore. Therefore, the potential has to be described as

$$E_{interaction}(\theta, \varphi) = E_{\mathrm{int}} \cdot 0.5(\sin(\theta + \varphi) + 1). \tag{5.5}$$

E_{int} is the strength of the interparticle interactions (i.e. the superposition of all interparticle interactions contributions of the neighboring particles) at the cluster site and the phase accounts for the different directions of the interparticle interactions relative to the other anisotropies at the cluster site. The calculation of E_{int} is described in the next section.

A complete potential of a particle is described by the superposition of these two shapes

$$E(\theta, \varphi) = E_{uniaxial} + E_{interaction} \tag{5.6}$$

and depends strongly on the magnitude of KV relative to E_{int}.

In general, one can consider three different cases:

1. $KV \gg E_{\mathrm{int}}$: essentially uniaxial character, the anisotropy of the system can be described with equation (5.4)

2. $KV \approx E_{\mathrm{int}}$: potential shape depends strongly on the phase φ; which means the angle between the easy axis and the easy direction, random values of φ result in many different potential shapes and hence presumably broad spectra in Mössbauer spectroscopy

3. $KV \ll E_{\mathrm{int}}$: only one easy direction, potential is described by equation (5.5) and φ can be easily neglected

The interparticle interaction

The fitting model is based on the spin-glass ground state of the nanoscale Fe clusters in the Ag film. One cluster is surrounded by its neighboring clusters, whose spin is pointing into random directions, due to the RKKY interaction between the clusters. Furthermore, the clusters are supposed to be randomly distributed in the sample, which results in a normal-distribution of the cluster - cluster distance around the average distance.

This was realized by summing up the RKKY interaction of one central cluster with its six nearest neighbors for N different clusters.

The starting point of the calculation was the simulation of the distance between the clusters, which was realized by using the inverse errorfunction

$$R = \sqrt{2}\,\mathrm{erf}^{-1}(\Lambda) \cdot \mu \cdot \sigma + \sigma \tag{5.7}$$

with Λ being a random number between -1 and 1 and σ being the average distance between the clusters. By choosing a value of $\mu = 0.4$, the FWHM of the corresponding distribution remains in a reasonable range for every value of μ [1]. The resulting values of R for different Λ give distances, whose probability of occurence is related to a normal distribution of the clusters in the film.

The strength of the interparticle interactions at a certain cluster was than modeled by using the expression for the RKKY interaction between ferromagnetic spherical clusters, whose radius is much smaller than their distance (after [26])

$$E = \frac{J^2 m^* k_{\mathrm{F}}^2 M_{s,1} M_{s,2} K}{(2\pi)^9 \hbar^2} \frac{\pi^2 \cos(2k_{\mathrm{F}}R)}{8k_{\mathrm{F}}^3 R^3}, \tag{5.8}$$

with K being

$$K = (\sin(2k_{\mathrm{F}}r_1) - 2k_{\mathrm{F}}r_1\cos(2k_{\mathrm{F}}r_1))(\sin(2k_{\mathrm{F}}r_2) - 2k_{\mathrm{F}}r_2\cos(2k_{\mathrm{F}}r_2)). \tag{5.9}$$

[1] That means, the height of the corresponding normal distribution at $x = 0$ is less than 5 % of the maximum height.

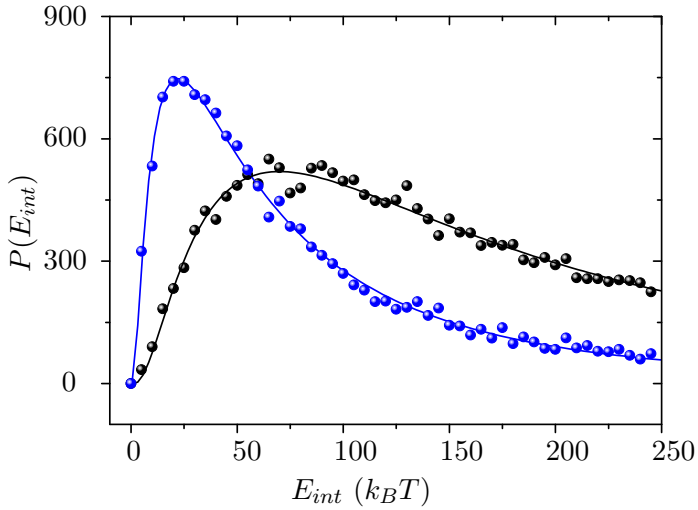

Figure 5.6: Distribution of interparticle interactions for the 0.5 % Fe (◕) and the 1 % Fe (◕) sample. The fits are described in the text.

Here, k_F is the Fermi wave vector, M_s the magnetization of the cluster, R the distance between the clusters and r the radius of the cluster. In the following, all constants except the distance between the clusters will be combined to an effective coupling constant $\tilde{J}_0$, which reduces equation (5.8) to

$$E = \tilde{J}_0 \frac{\cos(2k_\mathrm{F}R)}{R^3}. \tag{5.10}$$

The average distance between iron clusters containing 20 particles in fcc silver with a lattice constant of 4.1 Å [103] and an iron concentration of 1 % is approximately 3.2 nm and the Fermi wave vector for silver is $k_\mathrm{F} = 1.2 \cdot 10^{10}\,\mathrm{m}^{-1}$ [103]. That means, that the average distance corresponds to an angle of approximately 75^o in the cosine function in equation (5.10). In the following, k_F is set to $75/R$ in order to keep the correct length scale of the cosine function, deviations from this calculation due to different concentrations are neglected in the following.

Another distribution is resulting from the spin/cluster glass groundstate of the system, hence the orientation of the neighboring spins is supposed to be random in all three dimension. This was realized by multiplying the interparticle interactions for each neighboring cluster with a three dimensional, normalized vector whose components are random numbers between -1 and $+1$. The complete expression for the interparticle interactions at one cluster site, resulting from its six nearest neighbors is therefore

$$E_\mathrm{int} = \left| \sum_{i=1}^{6} \tilde{J}_0 \frac{\cos(2k_\mathrm{F}R)}{R^3} \cdot \frac{1}{\sqrt{x_i^2 + y_i^2 + z_i^3}} \begin{pmatrix} x_i \\ y_i \\ z_i \end{pmatrix} \right| \tag{5.11}$$

where x_i, y_i and z_i are the random numbers between -1 and 1. It is possible to use only the magnitude of the vector and lose the information about the direction of the interaction, because its only use would be, to know the direction relative to the easy axis of the particle which will be neglected as described below.

Performing this calculation for 20000 different clusters and evaluating the resulting data leads to a distribution of interparticle interactions as shown in figure 5.6 for the 0.5 % and the 1 % sample (these are the results of the best match of the simulation with the Mössbauer data, the parameters will be given below). As expected, the average interparticle interaction energy of the 0.5 % sample is much smaller than that of the 1 % sample. The units of E_{int} cannot be derived from the calculations performed yet, but only from the comparison with the experimental data, which will be done in the subsequent section.

The fits were performed using the log-normal distribution probability density function

$$f(x, \mu, \sigma) = a \cdot \frac{1}{\sqrt{2\pi}\sigma x} \exp\left(\frac{(\ln(x/c) - \mu)^2}{2\sigma^2}\right), \quad x > 0, \tag{5.12}$$

which gives very good results. The only reason to perform these fits is, to use them for the following calculations, which is much easier and faster than using the discrete results from the numerical calculations.

The hyperfine field-distribution

The next step is, to calculate the distribution of hyperfine fields from the distribution of interparticle interactions. A distribution of E_{int} leads to a distribution of the heights of the potentials for interacting clusters described by equation (5.5) as shown in figure 5.7.

The hyperfine field is connected to the angle θ by

$$B_{\mathrm{hyp}} = B_0 \cos(\theta) \tag{5.13}$$

with B_0 being the hyperfine field a $T = 0\,\mathrm{K}$. Hence one needs to find an expression for $P(E_{\mathrm{int}})$ in dependence of θ, which can be converted to the hyperfine field distribution. E_{int} as a function of θ follows from equation (5.6)

$$E_{\mathrm{int}}(\theta) = \frac{E - KV \sin(\theta)^2}{0.5(\sin(\theta + \varphi) + 1)} \tag{5.14}$$

which can be converted to $E_{\mathrm{int}}(B_{\mathrm{hyp}})$ by using

$$\theta(B_{\mathrm{hyp}}) = \arccos\left(\frac{B_{\mathrm{hyp}}}{B_0}\right). \tag{5.15}$$

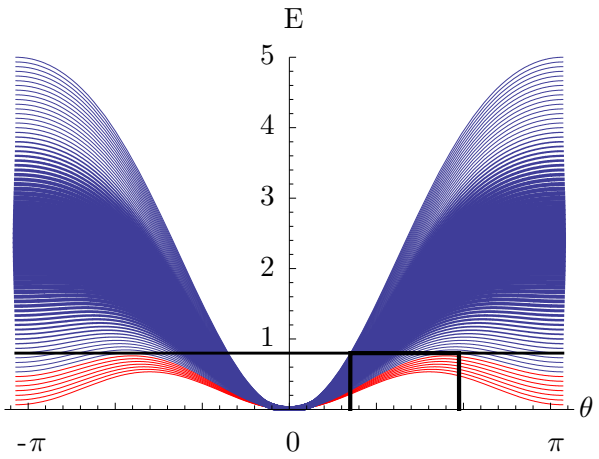

Figure 5.7: Distribution of potentials resulting from the distribution of interparticle interactions. The horizontal black line indicates a certain temperature T_0 while the vertical lines indicate the range of angles θ for this special case. The red lines are already lying below $E = k_\mathrm{B}T_0$ and do not take part in the calculation of the distribution of hyperfine fields anymore. An uniaxial contribution with $KV < E_\mathrm{int}$ can be identified in the increase of the potential at low energies around $+\pi/2$ and $-\pi/2$.

With this equation it is possible to determine the value of E_int that gives a potential shape that results in a hyperfine field of B_hyp at a temperature $k_\mathrm{B}T$. Inserting this E_int as x in the log-normal distribution probability density function (equation (5.12)) results in the probability of a certain value of E_int as a function of the hyperfine field B_hyp

$$P(E_\mathrm{int}(B_\mathrm{hyp})) = P(B_\mathrm{hyp}) = a \cdot \frac{1}{\sqrt{2\pi}\sigma E_\mathrm{int}(B_\mathrm{hyp})} \exp\left(\frac{(\ln(E_\mathrm{int}(B_\mathrm{hyp})/c) - \mu)^2}{2\sigma^2}\right), \tag{5.16}$$

which is the hyperfine field distribution.

The results for the 1 % and the 0.5 % sample are shown in figure 5.8.

The Mössbauer spectrum was derived from the hyperfine field distribution by summing up standard sextets

$$M(v, \Gamma, B_\mathrm{hyp}) = \sum_{i=1}^{6} \frac{1}{\pi} \frac{I(i)\Gamma}{\Gamma^2 + (v - a(i)B_\mathrm{hyp})^2} \tag{5.17}$$

with the hyperfine field distribution

$$M_{dist}(v) = \sum_i P_{B_\mathrm{hyp}/B_0}(i) \cdot M(v, \Gamma, i). \tag{5.18}$$

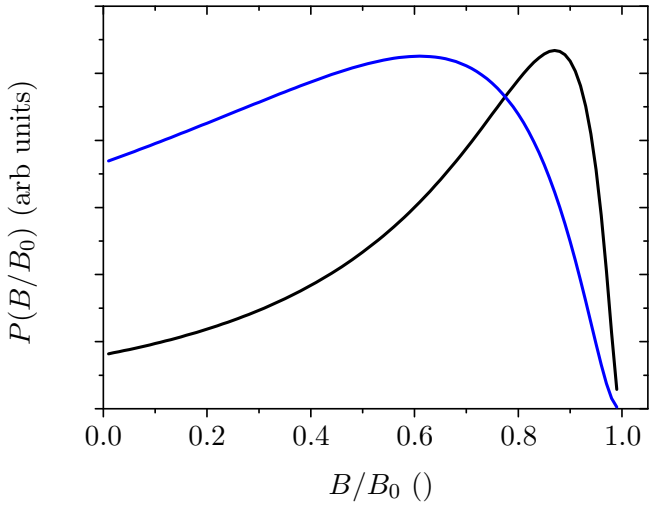

Figure 5.8: Hyperfine field distributions calculated from the distribution of interparticle interactions shown in figure 5.6 for the 1 % sample (——) and the 0.5 % sample (——).

for 50 different nodes. The values for $a(i)$ and $I(i)$ can be found in table 2.1 in section 2.1.3.

In both cases shown in figure 5.8, a significant fraction of the distribution has negative values of B_{hyp}/B_0. This is due to θ exceeding $\pm\pi/2$ which is connected to interparticle interactions with $kT > 0.5 \cdot E_{\mathrm{int}}$. In this region, overbarrier fluctuations set in and the Mössbauer spectrum can no more be described by the collective excitations of the clusters in their potential wells. In the following section, the fraction of clusters that experience overbarrier fluctuations is calculated and the resulting Mössbauer spectrum of these clusters is simulated.

The overbarrier fluctuations

In order to calculate the fraction of clusters experiencing overbarrier fluctuations one has to define a temperature at which the overbarrier fluctuations set in. As discussed before, numerical calculations [109] indicated a strong increase of the overbarrier-fluctuations for a value of $k_{\mathrm{B}}T/E_{\mathrm{int}} = 0.3 - 0.4$. However, in order to prevent a sharp cut off of the hyperfine field distribution, a value of $k_{\mathrm{B}}T/E_{\mathrm{int}} = 0.5$ was chosen here, since this value accompanies a hyperfine field of $B_{\mathrm{hyp}} = 0\,\mathrm{T}$.

The fraction of particles with $k_{\mathrm{B}}T/E_{\mathrm{int}} < 0.5$ was than calculated by fitting the actual hyperfine field distribution with its expected shape and integrating over the

range of $[0, B_0]$ and $[-\infty, B_0]$

$$\delta_{OBF} = 1 - \frac{\int_0^{B_0} F(B_{\mathrm{hyp}})\mathrm{d}B_{\mathrm{hyp}}}{\int_{-\infty}^{B_0} F(B_{\mathrm{hyp}})\mathrm{d}B_{\mathrm{hyp}}}. \tag{5.19}$$

The function $F(B_{\mathrm{hyp}})$, representing the shape of the hyperfine field fluctuations, was derived by generating a hyperfine field distribution with $P(B_{\mathrm{hyp}}) \approx 0$ at $B_{\mathrm{hyp}} = 0\,\mathrm{T}$ and interpolating it afterwards using the interpolation function of MATHEMATICA, which results in the function $f(x)$. Finally, a shift of this derived function was achieved by manipulating it using $F(B_{\mathrm{hyp}}) = a \cdot f(B_{\mathrm{hyp}}/b + c)$, which is able to fit the distributions very well.

The overbarrier fluctuations were simulated by using a model for spherical fluctuations (see section 2.1.3). Uniaxial fluctuations do not make sense here, since the shape of the potential has no uniaxial character.

The fluctuation rate was calculated using

$$\tau = \tau_0 \exp\left(\frac{\Delta E}{k_{\mathrm{B}}T}\right), \tag{5.20}$$

the values of ΔE have not been calculated for every value of the interparticle interaction, since this would increase the time of the calculation too much. Instead, an average value of ΔE was calculated by using the fact, that the average interparticle interactions E_{int} for Ag(Fe) is much bigger than $k_{\mathrm{B}}T$. Hence, $P(E_{\mathrm{int}})$ can be assumed to be linear in this region (small values of E_{int} in figure 5.6) and the average value of E_{int} between 0 and the maximum E_{int} for clusters experiencing overbarrier fluctuation, $E_{int,max}$, which can be defined as

$$E_{int,max} = 2k_{\mathrm{B}}T, \tag{5.21}$$

is found to be

$$\Delta E = \sqrt{2}k_{\mathrm{B}}T. \tag{5.22}$$

This value is independent of the slope of the linear interpolation and hence the value is the same for every concentration.

The number of clusters

For a good reproducibility, it is necessary to perform the calculations for a big number of clusters, which however increases the calculation time. In order to find a good balance between these two parameters, the distribution of interparticle interactions has been calculated for a different number of clusters with the same parameters and their scattering has been compared. An example is shown in figure 5.9.

The distribution for $N = 60000$ has a bigger standard deviation compared to the

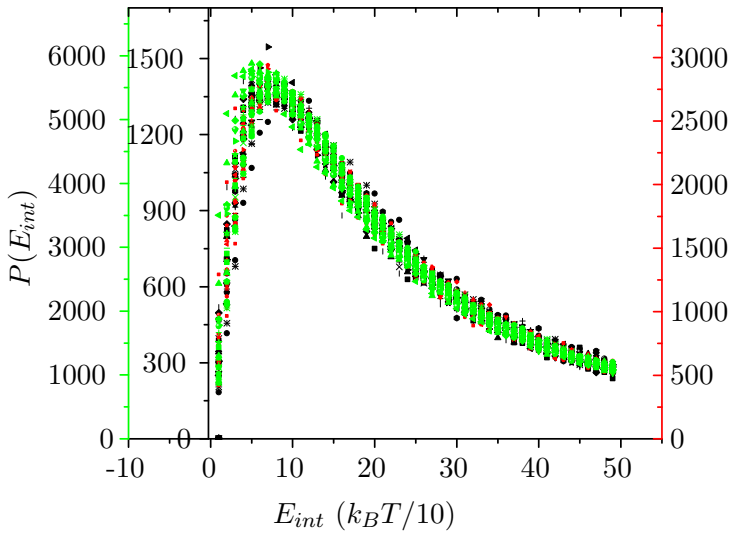

Figure 5.9: Distribution of interparticle interactions for different number of clusters. Here is ●: $N = 60000$, ●: $N = 120000$ and ●: $N = 240000$.

distribution for $N = 120000$ and $N = 240000$. The standard deviation of the latter is quite similar, hence $N = 120000$ was chosen as the number of clusters, which gives a good compromise between calculation time and reproducibility.

The final Mössbauer spectrum

The final Mössbauer spectrum was plotted by adding up the normalized spectra for the collective excitations and the overbarrier fluctuations and weighting them with their fractions. As a starting point, all parameters were set to the expected values and the simulation was compared with the measurements. Some parameters were set to be constant for every concentration (including the temperature $k_\mathrm{B}T$, the height of the barrier resulting from uniaxial anisotropy KV, the relaxation time τ_0 and hence τ as well, the linewidth Γ and the isomer shifts δ), while other parameters changed with the concentration (including the average inter-cluster distance R, the average cluster moment m, the fraction of the subspectra, which was correlated with the room temperature measurements, and the hyperfine field at zero temperature B_0, which was only allowed to vary slightly).

A detailed look on these parameters is presented below.

Since the fraction of the monomeric clusters is only small, they will be neglected in the following and only two subspectra for the two different cluster types will be used.

5.1.4 Comparing the simulation with the measurements

In this section, the resulting Mössbauer spectra from the simulation described above are compared to the measurements. This was not done by a fitting program but by adjusting the values manually until an optimum value was reached, which, however, will be called "fitting" in the following.

The simulations were performed for Ag films containing 0.3 %, 0.5 %, 0.8 %, 1 % and 1.5 % Fe and are shown in figure 5.10 and 5.11.

As it can be seen in these figures, the simulations match the measurements very well. With increasing concentration, the spectra turn over from a less defined broad structure to a distinct sextet which, however, still is considerably influenced by magnetic dynamics as it can be seen in the broad lines. The simulations for the 1 % and the 1.5 % Fe films exhibit a slight mismatch with the measurements at $\approx -5\,\mathrm{mm/s}$ $- -6\,\mathrm{mm/s}$, which will be discussed below.

The parameters

As a first step, the concentration independent parameters and afterwards, the parameters depending on the concentration will be presented.

The value of KV/k_B was chosen to be 0.11 K and has only a minor influence on the simulation, since $k_\mathrm{B}T \gg KV$ (compare to the previous section). The fact that the clusters are supposed to be very small [67] and the interparticle interaction strength was found to be very strong (see section 5.1.2), supports $KV \ll E_\mathrm{int}$. Nevertheless, this value should only be understood as indicating the order of magnitude of KV. For this reason, the value is used for both clusters.

The value of $\tau_0 \approx 5 \cdot 10^{-11}\,\mathrm{s}$ was found, which results in broad, collapsing spectra in Mössbauer spectroscopy (with a conversion factor for mm/s to Hz from [78]).

The Mössbauer linewidth Γ plays a minor role as well, since a hyperfine field distribution is used. Its value was set to 0.28 mm/s, lying in the typical range for the used absorber thickness and the ^{57}Co sources linewidth.

Finally, the isomer shifts used for the fitting were 0.165 mm/s and 0.281 mm/s, for the subspectrum with the smaller and the bigger fraction, respectively. These values have the opposite trend compared to the room temperature measurements. However, due to the spectral resolution, it is possible that simulations with other values match the data comparably well. Therefore, a detailed discussion of the opposite trend compared to the room temperature data is not presented here.

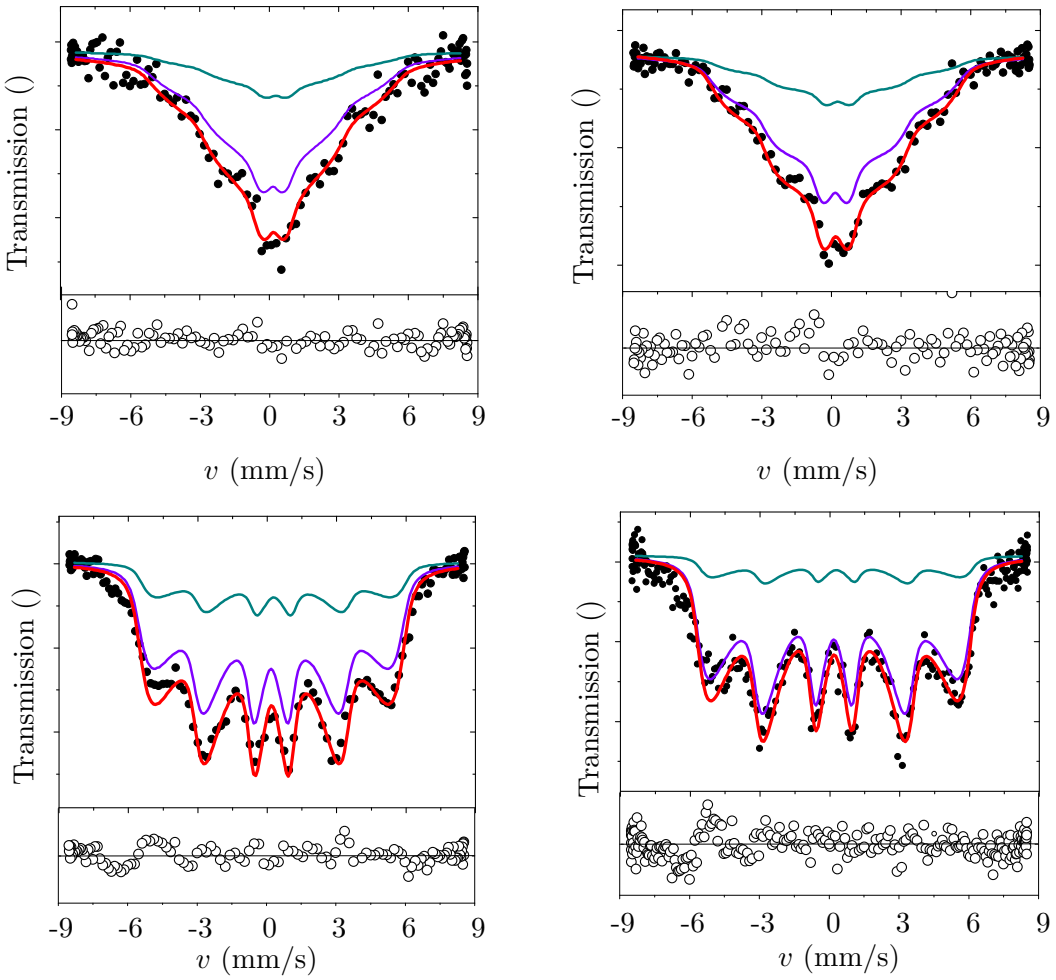

Figure 5.10: Comparison of the simulations and the measurements for the Ag(Fe) films containing 0.5 %, 0.8 %, 1 % and 1.5 % Fe from top left to bottom right.

In figure 5.11, the variation of R and $\tilde{J}$ from equation (5.10) is shown. Their magnitude should not be understood as their absolute values but in dependence of each other, due to the shape of equation (5.10). R decreases and $\tilde{J}$ increases with increasing concentration. With increasing Fe concentration, the distance between the clusters R gets smaller and since the fraction of the bigger clusters increases, the average magnetization M_s of the clusters increases and hence $\tilde{J}$ increases. It is worth to mention, that the variation of $\tilde{J}$ did affect the shape of the simulation much less than the variation of R, since R contributes with a power of 3. In figure 5.12, the Fe concentration dependence of the maximum value of the interparticle interaction strength is presented. It basically increases with increasing Fe concentration, and therefore follows the expected trend.

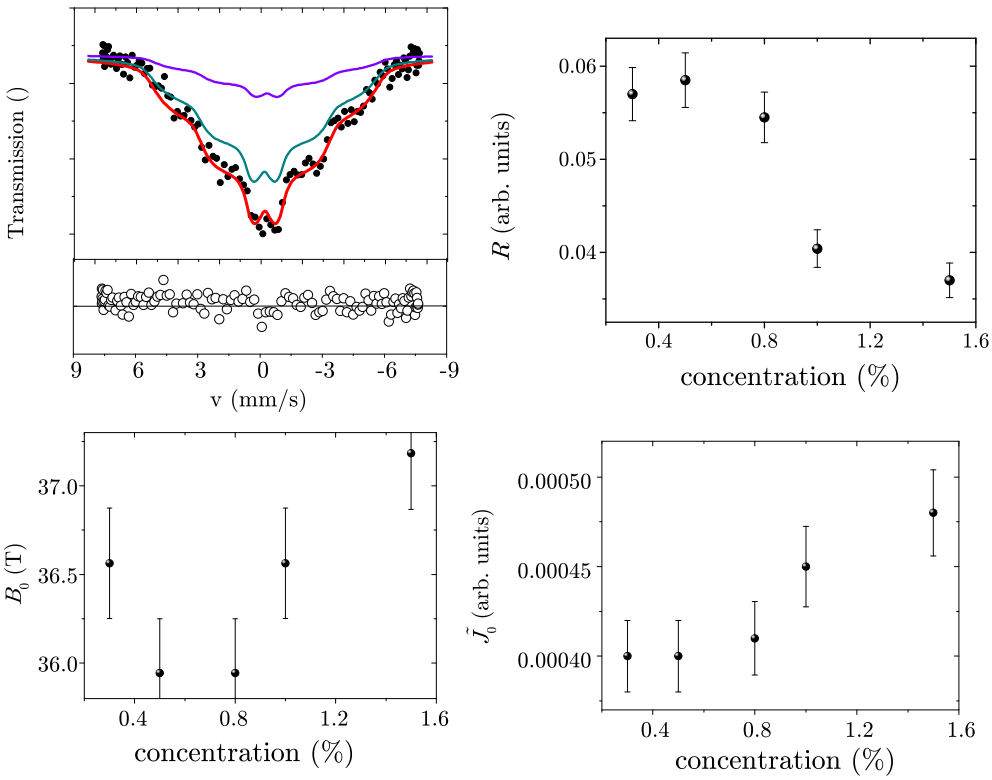

Figure 5.11: Comparison of the simulations and the measurements for the Ag(Fe) films containing 0.3 % Fe and the dependence of the distance R, the coupling strength $\tilde{J}_0$ (as defined in equation (5.10)) and the hyperfine field at zero temperature, B_0, on the Fe concentration.

The spectra and the parameter of the room temperature Mössbauer measurements of the 0.5 % and 0.8 % sample are very similar. In analogy, the low temperature spectra appear very similar as well, for which reason it is not surprising, that the parameter presented in figure 5.11 for these two concentration are rather similar.

The hyperfine field at zero temperature, B_0, has an average value of 36.5 T and hence is bigger than the typical value for magnetic hyperfine fields found for metallic iron. Increasing hyperfine magnetic fields indicate an increase of magnetic moments. Such an increase has been predicted by [139] and was observed by [73], as discussed in section 1.6.6. Furthermore, the hyperfine fields of surface atoms of metallic iron nanoparticles were found to be strongly enhanced compared to the hyperfine fields of atoms in the core [21, 66]. Due to the small size of the clusters, basically all atoms lay in the surface layer, wherefore the measured value matches the enhanced value in of 36 - 40 T very well.

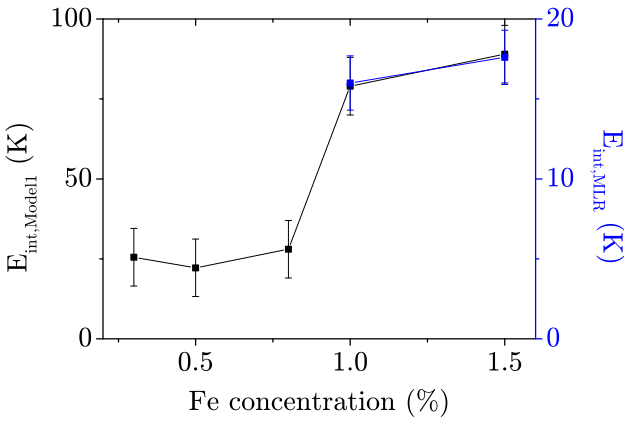

Figure 5.12: Development of the energy barrier height with the Fe concentration from the model presented in this chapter (black), and from the MLR (blue).

Temperature dependence

Temperature dependent measurements on a 1 % sample are taken from another series of preparation of similar samples, performed by P. Munayco in his phd thesis [133]. Presumably due to different preparation parameters, the spectrum at 4 K looks different to the spectrum presented above, the Mössbauer lines are sharper and the six line pattern appears less collapsed.

Nevertheless, the spectra could be simulated using $R = 0.0352$, a linewidth of 0.20 mm/s and a hyperfine field at zero temperature B_0 of 33.5 T. All parameters except $\tilde{J}$ and the temperature T were kept constant in the following. An explanation for the variation of $\tilde{J}$ is the increasing amount of fluctuating neighboring clusters. Since this feature, which decreases the average interparticle interaction, is not implemented in this model it is simulated here by decreasing $\tilde{J}$ for the 8 K measurement from $\tilde{J}_{4\,K,\,6\,K} = 0.0045$ to $\tilde{J}_{8K} = 0.0038$.

When comparing with the parameters presented in figure 5.11, the sample should be located at a concentration between 1 % and 1.5 %.

The results are shown in figure 5.13. The consistency between simulation and measurement is good, but not as good as in the simulations presented above. In particular the 2^{nd} and 5^{th} line are poorly matched. Since this behavior is not observed in before, it is possible to assume sample-specific differences as the origin, e.g. a preferred magnetic orientation of the clusters. This could be induced by structural texture of the films (observed as well in [67]), occurring during the preparation process and resulting in a non isotropic growth of the Fe clusters in the Ag crystal

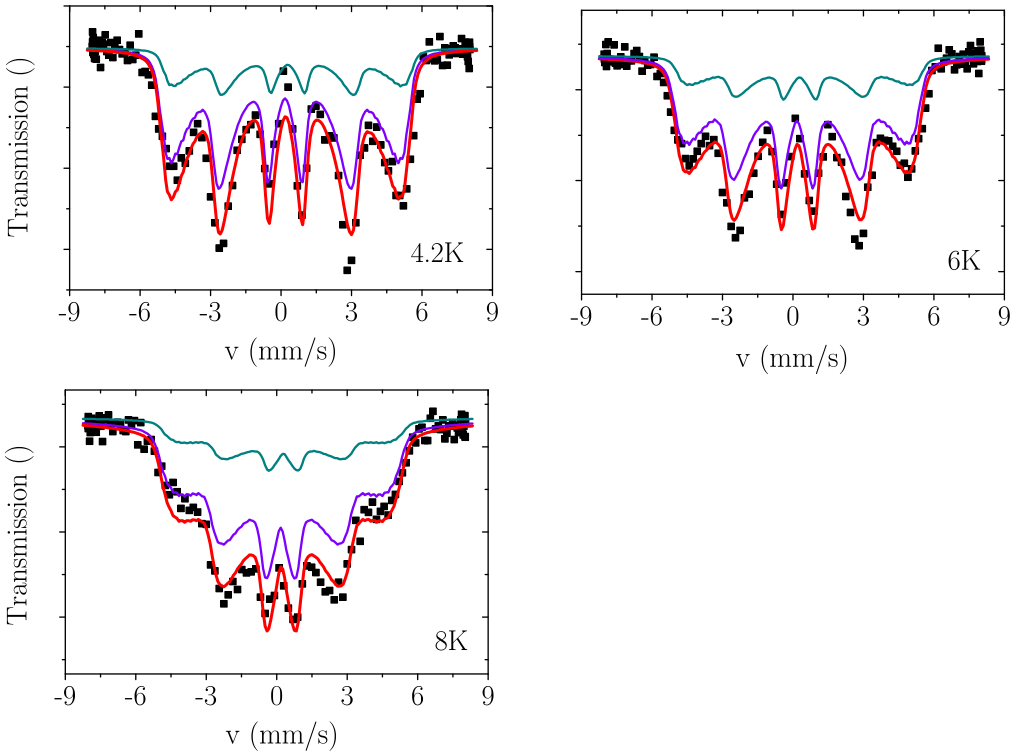

Figure 5.13: Comparison of the simulations and the measurements for the temperature dependent measurements of another 1 % Ag(Fe) film. No polarisation is implemented in the simulation.

lattice. The effect of a preferred magnetic orientation on the spectrum resulting from the model is presented in figure 5.14. The fraction of the area of the lines is in this case not 3:2:1 but 3:2.38:1, which matches the measurements much better. This could also be the explanation for the more distinct structure of the measurement of this sample compared to the 1 % sample presented above. In this scenario, the spin-glass state would not be isotropic anymore and the less strongly bound clusters would experience this polarization and align with it. This would effectively lead to an increase of the interparticle interaction, since these clusters, that produced a random interaction before, give an additional contribution now. However, if the polarization is not too strong, the system still remains in a spin-glass like state. The smaller linewidth could be, at least partially, explained by the polarization as well, since the contribution of inhomogeneous broadening (see below for more details) is reduced and hence the lines are sharper. Since the linewidth may slightly vary for different cryostats and ^{57}Co sources and the measurements on this sample and on the samples presented above were performed at different times and possibly different

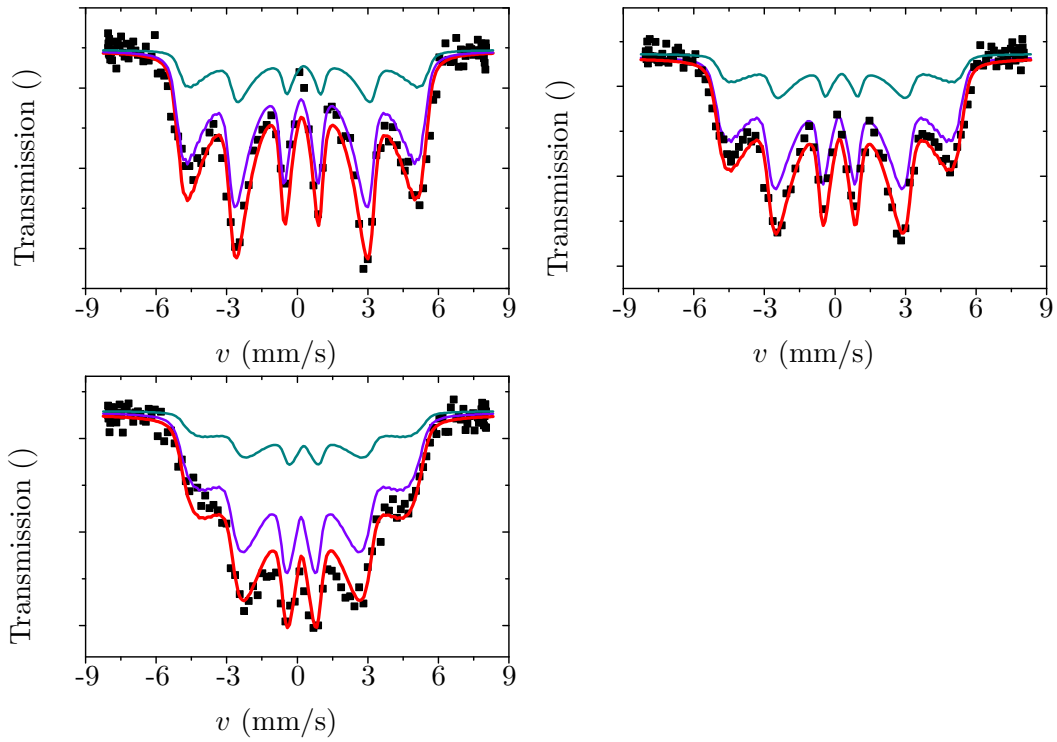

Figure 5.14: The same temperature dependent measurements and simulations as presented in figure 5.13 with an additional polarization (see text).

cryostats, there might be no physical reason for this discrepancy.

The left shoulder

For every sample and temperature, a mismatch between the simulation and the measurements for the left shoulder occurs. The shoulder appears to be smeared out (compare for example to the 1 % Fe sample in figure 5.10), which cannot be explained by introducing an effective quadrupolar interaction.

A possible explanation is a combination of a distribution of the isomer shift and the quadrupolar interaction.

5.1.5 Fitting with the MLR

In order to compare the results of the previous model to the results of an established model, the low temperature data were fitted with the MLR as well. Therefore, the log-normal distribution of interparticle interaction strengths presented in section 5.1.3 is used. Due to the strong interactions between the clusters, the modified MLR with a cos() shaped potential was chosen. The results are presented in figure

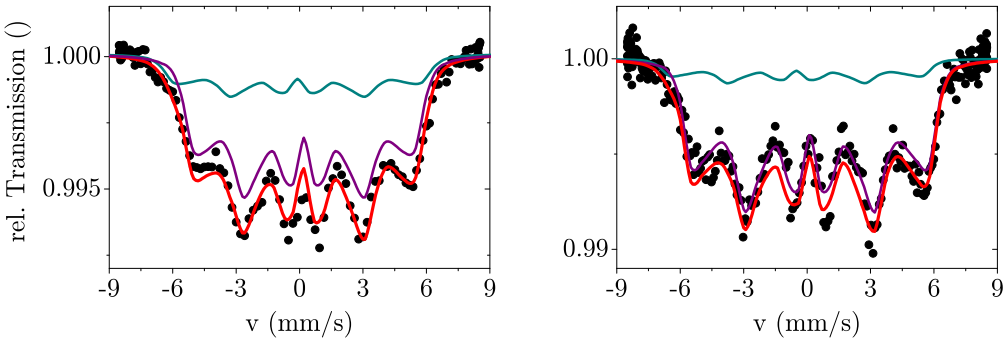

Figure 5.15: Application of the MLR to the films with 1 % Fe (left) and 1.5 % Fe (right).

5.15. A fitting of the data was only possible for the samples containing 1 % and 1.5 % iron. The most likely explanation is, that the freezing temperature of the other samples with a smaller amount of iron is so low, that these samples are at 4 K already in the intermediate regime, where the interparticle interaction strength and the anisotropy energy have a similar strength and the fitting is therefore hardly possible (see chapter 3). That the model presented above gives good fits with reasonable results for the samples that are presumably in the intermediate range, may, however, be due to the different approach for the simulation of the collective excitations. While the hyperfine field distribution used in the MLR is very sensitive to slight changes in the shape of the potentials, the shape of the Mössbauer spectra in the framework of the model presented above is rather dominated by the distribution of interparticle interaction strength. Due to the average angle calculated from the potential, slight changes of the potential shape do not have a strong impact on the spectral shape. However, when the cos shape of the potential turns to a $\cos()^2$ dominated shape, it has to be adjusted, too.

The simulation of the Mössbauer spectra of the samples with 1 % Fe and 1.5 % Fe are shown in figure 5.15, the corresponding maximum value of the interparticle interaction strength distribution is shown in figure 5.12. A comparison with the corresponding value derived from the previous model shows, that the relative values match well, which is however not very significant, when taking into account that only two points are involved into the comparison. The absolute values are however not similar. A collapse of the Mössbauer spectrum in the collective excitation regime within the framework of the MLR (a superposition of a distribution of hyperfine fields weighted by the temperature dependent occupation probability) happens for much higher values of $k_{\mathrm{B}}T/E_{\mathrm{int}}$, than in the model presented above, which uses an average hyperfine field. This example shows, that the absolute values of the potential wells derived from different Mössbauer relaxation models for interacting

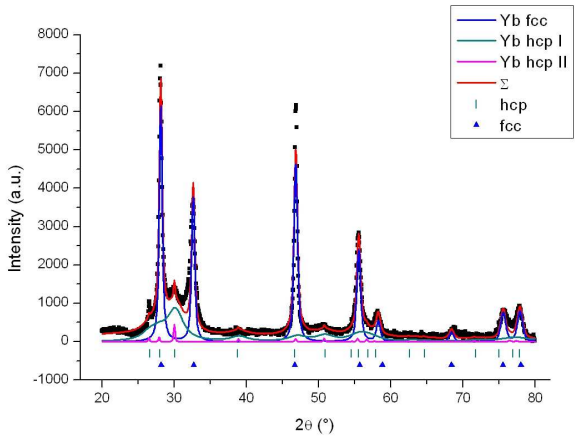

Figure 5.16: XRD measurement of a Yb(Fe) film with 0.6 % Fe. The fitting includes a fcc and two hcp components with different grain sizes (after [69]).

magnetic nanoscale particles should always be treated carefully. However, the relative dependence of the values on certain parameters (here, the concentration of iron in the sample) appears reliable for the different approaches. Furthermore this example shows, that the different models have advantages and disadvantages. While the MLR is not applicable in case of intermediate temperatures (relative to the height of the potential well), the model presented in section 5.1.3 fits the data very well and gives reasonable values. However, it is rather an adhoc approach, combining to extreme cases (the collective excitations as well as the overbarrier fluctuations) and does not present a proper treatment for the transition between the two regimes.

5.2 Yb(Fe)

Films with iron clusters in an ytterbium matrix, were prepared by Chachi Rojas-Ayala using as well vapor co-deposition. The concentrations of Fe lie between 0.3 % and 5 % in different films. In the first part of this section, the room temperature Mössbauer- and other measurements are discussed. In the second part, a closer look will be drawn on the low temperature Mössbauer spectra eventually revealing magnetic relaxation effects.

The films were prepared in the same way as the Ag(Fe) films, discussed above. Since iron is immiscible in ytterbium as well, it is reasonable to assume a formation of Fe clusters, also for this material.

If not mentioned differently, the results presented in the following are based on [69] and [71]. DC-susceptibility measurements and most of the Mössbauer- and XRD

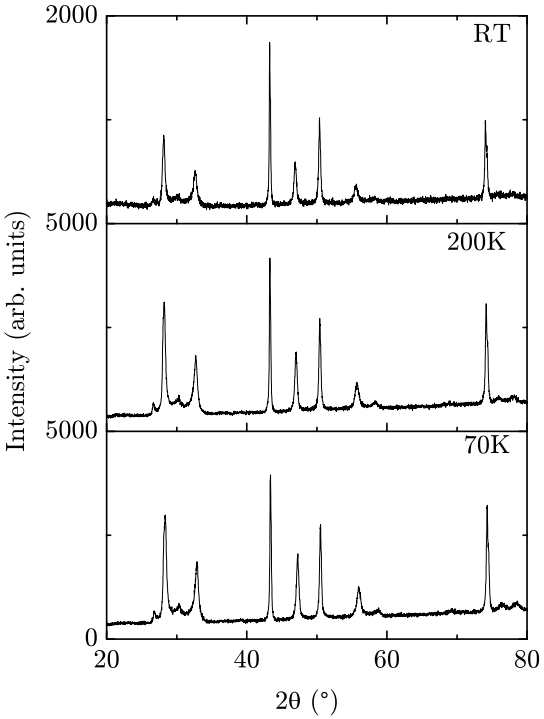

Figure 5.17: XRD measurement on a Yb(Fe) film with 1 % Fe for different temperatures.

measurements have been performed by C. Rojas-Ayala at CBPF. Some Mössbauer and XRD measurements have been performed at the IPKM as well. Furthermore, the low temperature XRD measurement has been performed by T. Woike in Dresden and the AC-susceptibility measurement has been performed by M. Thede in Zurich. The evaluation of the AC-susceptibility-, XRD- and low temperature Mössbauer measurements, as well as the search for a possibility to perform low temperature XRD measurements, was a part of this work.

5.2.1 Measurements

XRD measurements

XRD measurements performed on a film with 0.6 % Fe are shown in figure 5.16. A proper fitting of the data includes one fcc and two hcp phases, which differ in the grain size. Preliminary TEM measurements on a 3.5 % Fe doped Yb film support the findings from the XRD analysis [140]. Ytterbium at room temperature is typically made up of these two different phases, although the transition from fcc at higher

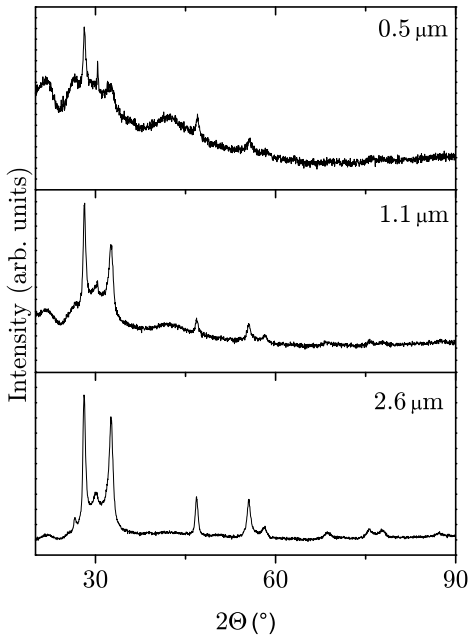

Figure 5.18: XRD spectra on Yb(Fe) films with different thicknesses. The diffraction pattern on the film with the smallest thickness shows an unexpected increase of the intensity at small angles. This effect is presumably a result of the increased linewidth of the diffraction peaks for this thickness and an additional contribution of an enhanced background. Since it only occurs for small thicknesses, this effect will not be further discussed here.

temperatures to hcp at lower temperatures lies at 270 K (see [141]). As pointed out therein, small concentrations of impurities are, however, able to change the ratio of hcp and fcc considerably over a wide temperature range.

A change of the ratio of the hcp and the fcc phase with temperature would involve a temperature dependent movement of the phase boundary, which would presumably affects the properties of the iron clusters (position, orientation, ...). In order to examine this scenario, temperature dependent XRD measurements were performed. The results are presented in figure 5.17. Even for the lowest temperature at 70 K, the shape of the diffraction pattern does not change. Thus it is possible to conclude, that the ratio of fcc and hcp ytterbium stays the same and therefore does not influence the properties of the Fe clusters, at least over this temperature range. It is however possible, that the fraction of hcp to fcc changes at still lower temperatures. However, this scenario will be neglected in the following.

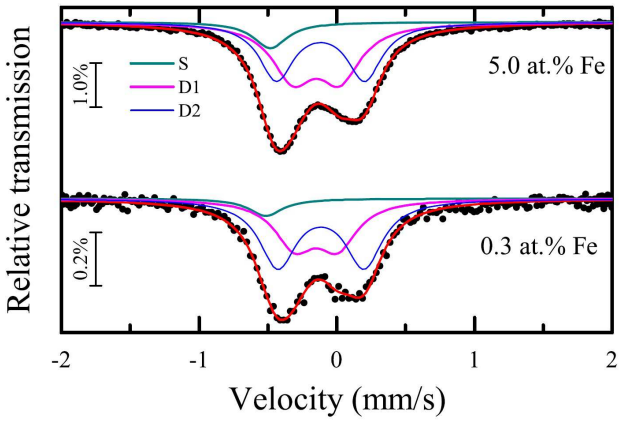

Figure 5.19: Room temperature Mössbauer spectra of Yb(Fe) films with 0.3 % and 5 % Fe but a similar thickness (after [71]).

From the XRD spectrum it is not possible to obtain information about the spatial distribution of the different phases within the film. Since their presence can be closely connected to impurities and defects, it is reasonable to assume, that a major fraction of the hcp phase can be found at the surface of the film. This assumption is supported by the XRD spectra measured on pure Yb films of different thicknesses, shown in figure 5.18. In this figure it can be clearly seen, that the fraction of the hcp phase is much higher for thinner films and decreases with increasing thickness. Furthermore, small grains of the hcp phase are presumably present as well within the film, since defects are expected therein as well.

Room temperature Mössbauer spectroscopy

From previous Mössbauer measurements on Yb(Fe) films measured at room temperature at CBPF, it was not possible to obtain a systematic concentration dependence of the different Mössbauer parameters [69]. Lateron it was found, that the thickness of the films, which had not been kept constant, is a crucial parameter. Only after Yb(Fe) films with a similar thickness around 2.8 μm were used, a systematic concentration dependence of the Mössbauer parameters could be obtained [71]. The spectra are shown in figure 5.19. For the concentration dependence of the Mössbauer parameters, it is referred to [71]. Similar to the Ag(Fe) films presented above, it is possible to obtain systematic fits to the spectra using three different subspectra. They can be attributed to two different types of clusters and a monomeric contribution for the same reasons as the ones presented for Ag(Fe) (see section 5.1.2).

As it can be seen from the data presented in [69], a variation of the film thick-

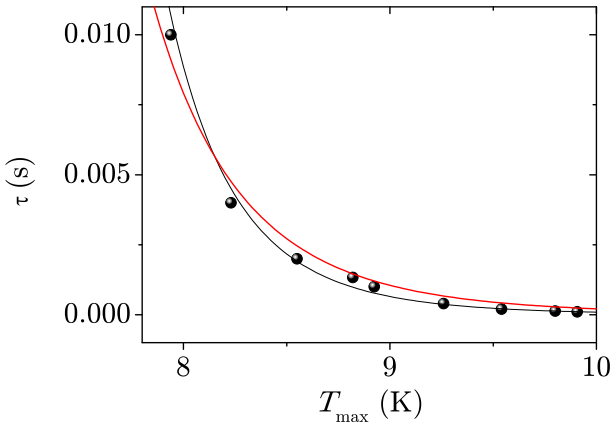

Figure 5.20: Dependence of the temperature at the maximum of χ' on the relaxation time τ from AC susceptibility. The red line is a fit with the Arrhenius law, while the black line is a fit with the Vogel-Fulcher law. For more details, see text.

ness results in a non-systematic behaviour of the Mössbauer parameters. This is an indication that the properties of the clusters within the film are closely connected to the fraction of the two phases, e.g. that the clusters are located at the phase boundaries.

AC-susceptibility measurements

In order to gain information about the presence of interactions between the particles, AC susceptibility measurements were performed on a film which contains 5 % Fe. The timescale dependence of the maximum temperature of χ' is shown in figure 5.20. Analog to the AC susceptibility measurements on the Ag(Fe) film presented above, the data were fitted with an Arrhenius law and a Vogel-Fulcher law. In both cases, $\tau_0 = 10^{-10}$ s. Furthermore, $E_a/k_B = 145.5$ K for the Arrhenius law and $E_a/k_B = 109.8$ K and $T_{VF} = 2$ K for the Vogel-Fulcher law. The fit with the Vogel-Fulcher law matches the data slightly better. However, the fact that $T_{VF} \approx 0.25 \cdot T_{max}$ and that the Arrhenius law with the same value of τ_0 fits the data almost as good, are indications that, in contrast to the interactions strength in the Ag(Fe) films, the interparticle interactions are only very weak if not vanishing in the Yb(Fe) films.

5.2.2 The low temperature Mössbauer data

Examples for the Mössbauer spectra measured on Yb(Fe) at low temperatures are presented in figure 5.21. As it can be seen there, the shape of the spectra is considerably different compared to the Ag(Fe) spectra. Even for the highest concentration of Fe, the shape of the spectrum appears more collapsed than the spectrum with

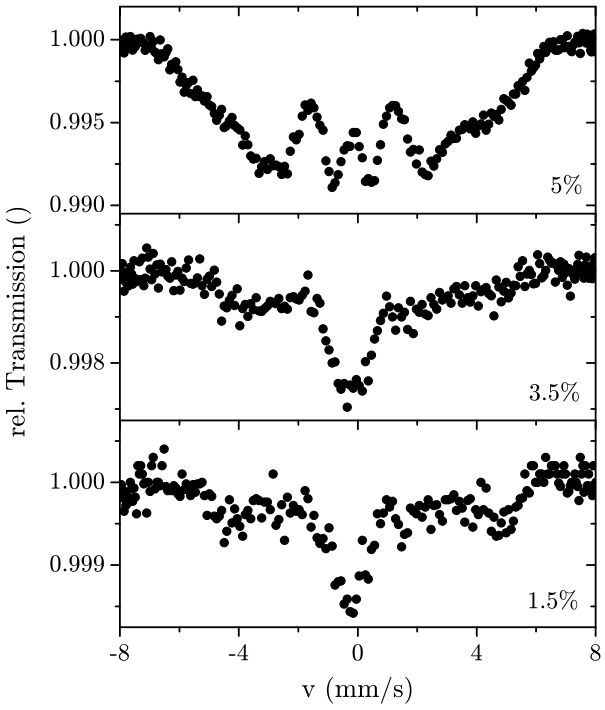

Figure 5.21: Mössbauer spectra of Yb(Fe) films with the depicted concentrations of Fe ions measured at 4.2 K.

the highest Fe concentration in the Ag(Fe) films (see figure 5.10). Therefore, the blocking temperature[2] of the Fe clusters dispersed in Yb films is considerably lower than the freezing temperature of Fe clusters dispersed in Ag films with the same concentration. Therefore, the average height of the magnetic potential of the clusters in the Yb(Fe) films is lower than the height of the potential experienced by the clusters in the Ag(Fe) films with a corresponding concentration. Whereas the main contribution to the potential height, the clusters in the Ag(Fe) films experience, is due to the strong interparticle interaction, a reduced interparticle interaction strength between the clusters in the Yb(Fe) films can explain the reduced potential height. Indeed, the shape of the low temperature Mössbauer spectra supports this assumption. In contrast to the spectra measured at low temperature on the Ag(Fe)

[2]Since the interparticle interactions is very weak in the Yb(Fe) films, as found from the AC-susceptibility measurements presented above, this temperature can be understood as a blocking temperature and not a freezing temperature like it is the case for the spin-glass like behavior in the Ag(Fe) films, which results from the strong interparticle interactions therein.

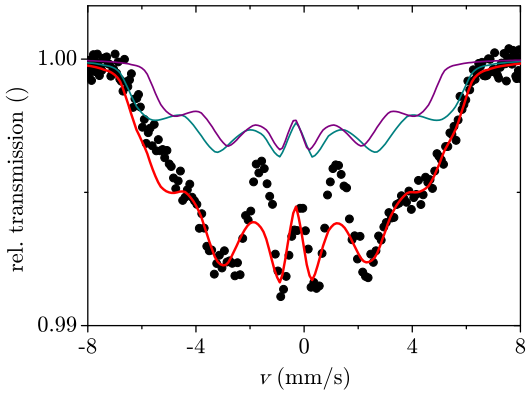

Figure 5.22: Attempt of a fit of the Mössbauer spectrum of a 5 % Fe film measured at 4.2 K.

films, which exhibit a uniform collapse, the spectra measured on the Yb(Fe) films show a non-magnetic contribution in their center and a broad, magnetic structure. As described in section 2.1.3, a collapse of the Mössbauer spectra like this is an indication for weak or vanishing interparticle interactions. This is in agreement with the conclusions drawn from the AC-susceptibility measurements presented above.

A fitting of the spectra presented in figure 5.21, however, was not possible. An alternative model for fitting the spectra involves inhomogeneous broadening (IB). In case of IB, the magnetic hyperfine field is normally distributed, even at the lowest temperature. This effect is not due to relaxation of the magnetic moments but e.g. to different magnetic environments of the probe atoms. The normal distribution of the magnetic hyperfine field results in a six line pattern of Voigt profiles (a convolution of a Gaussian and a Lorentzian distribution). The broadening of the outer lines is stronger than that of the inner ones, due to the field distribution. Some minor IB is in principle present in all kind of Mössbauer spectra. However, the shape of the Mössbauer spectra measured on the Yb(Fe) films at low temperatures, indicates the presence of strong IB (presumably due to the influence of the quadrupolar interaction on the low temperature patterns and to the different properties of the particles on the phase boundaries). A fit that includes a combination of the MLR and IB is not reasonable, since a distinction between these two types of broadening is hardly possible. The only possible approach would be a measurements at still lower temperatures, where the influence of magnetic relaxation is negligible and therefore only the influence of IB can be estimated. Such data are, however, not available for this sample. Therefore, the discussion of the low temperature Mössbauer spectra measured on Yb(Fe) films presented in this work is only qualitative.

A careful analysis of temperature dependent measurements on an Yb(Fe) film should reveal two different blocking temperatures for the two cluster types, if the interparticle interaction strength is indeed zero.

Two possible explanations for a considerably weaker interparticle interactions for Yb(Fe) compared to Ag(Fe) are discussed in the following. The first one, is a reduction of the RKKY interaction strength due to the different electronic properties of Yb compared to Ag. The strength of the RKKY interaction at a certain distance r to its origin, depends on the effective mass m^* and the Fermi-wave vector k_F of the host material (see equation (5.8)). For an estimation of the RKKY interaction strength, it is necessary to know k_F as well as the effective mass of the conduction electrons of Yb and Ag. Using the coefficient γ of the linear part of a fit to the specific heat of a pure ytterbium sample (which is therefore an average value over fcc and hcp Yb), which is proportional to m^*, $\gamma = \alpha m^*$, after [142], the Fermi energy of Yb after [143] and the corresponding values for silver [103] (compare to table 5.1), allows an estimation of the RKKY interaction strength by using

$$\tilde{J}_0 \propto \frac{m^*}{k_\mathrm{F}} = \frac{m^*}{\sqrt{2m^* \cdot E_\mathrm{F}/\hbar}} = \frac{\alpha \cdot \gamma}{\sqrt{2\alpha \cdot \gamma \cdot E_\mathrm{F}/\hbar}} \propto \frac{\gamma}{\sqrt{\gamma \cdot E_\mathrm{F}}}. \tag{5.23}$$

Although this expression only gives a value which is proportional to $\tilde{J}_0$, it is sufficient to compare this value for both materials, resulting in $\tilde{J}_{0,\mathrm{Yb}} \approx 2\tilde{J}_{0,\mathrm{Ag}}$, which means, that the RKKY interaction between the clusters is even stronger in the Yb films compared to the Ag films. The measurements presented in this chapter, however, gave the opposite result, indicating that this is not the correct explanation for the reduced interparticle interaction strength observed in the Yb(Fe) compared to the Ag(Fe) film.

The second possible explanation is based on the location of the Fe clusters at the phase boundaries (see figure 5.23). Assuming that the major fraction of the hcp phase is a layer at the surface and the bottom of the Yb film and that the Fe clusters are basically located at the phase boundaries, then the Fe clusters form a 2D arrangement within the film. Although their average distance is therewith considerably smaller, compared to their distance if they were distributed randomly within the film, the direct connection between two neighboring clusters presumably crosses

Table 5.1: Values for the prefactor of the linear part of the specific heat, γ, and for the Fermi energy, E_F, after [103, 142, 143].

	γ (mJ/(mol·K))	E_F (eV)
Ag	0.6	5.5
Yb	2.9	6.0

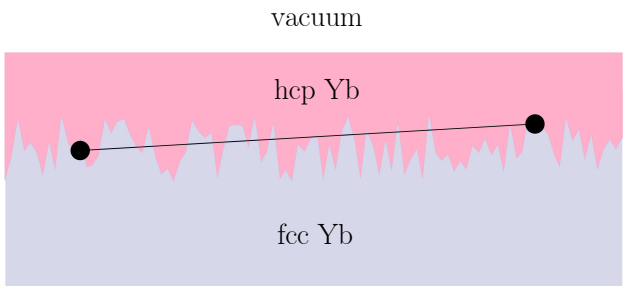

Figure 5.23: Schematic illustration of the connection between two clusters being located at the phase boundary between hcp and fcc Yb at the top of the film (not to scale).

the phase boundary several times or is directly within the phase boundary. The effect of the phase boundary on the RKKY interaction is unclear, but a disturbance if not a vanishing of the RKKY interaction when it crosses a phase boundary is very likely, which can explain the weak interparticle interactions in the Yb(Fe) films.

For further analysis and measurements on Yb(Fe) films, being predominantly not focused on magnetic relaxation, (e.g. Mössbauer measurements in external magnetic fields, etc), it is referred to [72].

5.3 Summary

In this chapter, Fe-clusters embedded in a silver or ytterbium matrix were examined. Samples with different concentrations of Fe were prepared at CBPF in Rio de Janeiro, Brasil, by vapor co-deposition. While the identification of the different cluster types and further analysis on their magnetic properties are the subject of PhD-theses by P. Munayco, W.T. Herrera and C. Rojas-Ayala, this work is mainly focused on the evaluation of the low temperature Mössbauer spectra. In this temperature range, the freezing process of the magnetic moments of the clusters has already set in and the magnetic relaxation of the clusters is slow enough to influence the Mössbauer spectrum. Furthermore, this work includes the evaluation of complementary AC-susceptibility data, from which it is possible to gain information about the interparticle interaction strength.

The low temperature Mössbauer data measured on Ag(Fe) films were evaluated using a model, which was specifically developed for this type of sample. The collective excitations regime in this model is described using an average value of the hyperfine field, which is physically more reasonable than the distribution of static hyperfine fields resulting from the MLR (see chapter 3). It includes a random distribution of Fe clusters within the films, coupled through RKKY interaction via the

conduction electrons of the host matrix. The spectra resulting from the model fit the measurements very well and the parameters show the expected trend, namely a strong interparticle interaction, which increases with increasing Fe concentration and a decrease of the average distance among the particles with increasing concentration. Furthermore, the two spectra with the highest Fe concentration were fitted with the modified MLR model (see chapter 3). The low temperature spectra of films with a lower concentration could not be fitted with the MLR, presumably since they are in the intermediate range, where interparticle interaction strength and the anisotropy energy barrier have a comparable height (see chapter 3). Fortunately, the model used in the first part of this chapter is capable of fitting these spectra as well. Although the trend of the interparticle interaction strength with concentration resulting from the application of the MLR is similar to the one of the first model, the absolute values of the energy barriers are considerable different. This indicates, that the models used to evaluate the Mössbauer spectra should in general rather be used in order to compare different samples with each other, than to extract absolute values for parameters like the energy barrier. The evaluation of AC-susceptibility measurements supports the presence of strong interparticle interactions found from the application of the two models to the low temperature Mössbauer spectra.

A fit with the first model to a set of measurements on a 1 % Fe film at different temperatures, works satisfactorily well. However, the introduction of a preferred orientation of the clusters magnetic moment improves the quality of the fits considerably. Since this preferred orientation was not necessary to fit the other spectra, it can be interpreted as an artifact and may be related to structural texture of the films [67].

While the room temperature Mössbauer measurements on the Yb(Fe) films could be interpreted similar to the corresponding spectra on the Ag(Fe) films, the low temperature Mössbauer spectra differ significantly from them. Up to a concentration of 3.5 % Fe, the spectra consist of a non-magnetic contribution, which is superimposed with a broad magnetic background. As discussed in section 2.1.3, this type of spectra is an indication for vanishing interparticle interactions. Therefore, the magnetic moments of the clusters exhibit rather a blocking than a freezing process at low temperatures. Only the spectrum measured on a film with 5 % Fe is completely collapsed and hence comparable with the 1 % Fe spectra of the Ag(Fe) films. Therefore, the blocking temperature of the Yb(Fe) films is considerably lower compared to the one in comparable Ag(Fe) films. The vanishing interparticle interactions can explain this reduced blocking temperature.

A fitting of the low temperature Mössbauer spectra was however not possible. The best attempt of a fit with a unmodified MLR still shows a strong mismatch with the data. This can be explained with the presence of strong inhomogeneous broadening in the sample. A simulation of a Mössbauer spectrum that includes the relaxation

of the magnetic moments of the clusters and inhomogeneous broadening is not helpful, since it is hardly possible to distinguish between these two effect, which both basically cause a broadening of the Mössbauer lines.

Two different approaches that may explain the weaker interparticle interaction strength for Yb(Fe) were discussed. The first one is based on the different properties of the host matrix, that might change the interaction strength, which depends on the effective mass and the Fermi wave vector of the conduction electrons. However, an estimation of the RKKY interaction strength for Ag and Yb revealed, that the it is even stronger in the Yb films than in the Ag films and that this explanation is therefore not the correct one. The second approach is based on the fact, that the Yb films are made up of a mixture of a hcp and a fcc phases. XRD measurements on Yb(Fe) films of different thicknesses gave indications, that the Fe clusters are predominantly located at the phase boundary between these two phases. Therefore, the direct connection between two neighboring clusters would cross the phase boundary several times, which presumably has a strong influence on the RKKY interaction strength. A further discussion of this effect is however beyond the scope this work.

The evaluation of the low temperature Mössbauer data and comprehensive AC-susceptibility data on the Ag(Fe) and Yb(Fe) films therefore supports the picture of the Fe clusters distributed in the host matrix in case of the Ag(Fe) films. Furthermore, strong interparticle interactions were found for this sample, which increase with increasing Fe concentration. In case of Yb(Fe) films, a quantitative analysis of the Mössbauer data was not possible, but a qualitative analysis revealed that the interparticle interactions are only very weak, if not vanishing, which is presumably due to the location of the Fe clusters at hcp/fcc boundaries in the Yb matrix.

Conclusion

Mössbauer spectroscopy is one of the most frequently used techniques when Fe based magnetic nanoparticles are investigated. Nevertheless, the interpretation of the Mössbauer spectra on this type of samples is commonly incomplete or even inaccurate. The prime reason is a lack of theoretical models, that are able to fully describe the influence of the complex physics of magnetic nanoparticles on the Mössbauer spectra (relaxation effects / interparticle interaction / surface spin canting / particle size distributions / ...). The most promising models, the so-called multi level relaxation model (MLR), originally established in the mid-80's [86] and the so-called superferromagnetism / super-spin glass model (SFM/SSG), originally established in the early 80's [23], have only very rarely been used [23, 29, 87]. Nevertheless, the constantly growing interest on magnetic nanoparticles throughout the last decades due to their interesting physical properties and applications emphasizes the necessity of a workable model that is able to give an adequate description of the Mössbauer patterns measured on magnetic nanoparticles.

The present thesis is dealing with this problem and comprises two main subjects.

The first one is, to review models that are found in literature and claim to be applicable to Mössbauer measurements on magnetic nanoparticles and to apply them on a model system. This includes a modification of an existing model or the development of a new model, if necessary.

The second subject is the detailed examination of different types of nanoscale particles or clusters. Amongst other techniques, the study on these samples involves as well the modified or new Mössbauer models in order to determine their significance and practicability when working on scientifically interesting subjects.

The first two chapters give an introduction into the complex research on magnetic nanoparticles. The **first chapter** deals with the physical properties of magnetic single-domain nanoparticles the timely fluctuation of their magnetic moments and gives a short overview over the different preparation methods for magnetic nanoparticles. In the **second chapter**, the experimental methods, commonly used to examine magnetic nanoparticles, are reviewed. An overview over the different relaxation

models for describing the fluctuation of magnetic nanoparticles as seen from Mössbauer spectroscopy is presented.

Chapter three is the first one, that deals intensively with one of the main subjects of this thesis. The Mössbauer spectra measured on $ZnFe_2O_4$ nanoparticles are evaluated using a multi-level relaxation model (MLR) and a superferromagnetism / super-spin glass model (SFM/SSG). These two models are the most promising candidates for a successful application to real systems. In order to confirm the results found from the evaluation of the Mössbauer measurements, complementary DC-susceptibility measurements were performed. Simulations with the initial MLR model describe the Mössbauer patterns at different temperatures very well. However, the temperature, where the system turns into the overbarrier fluctuation regime,T_{OB}, is unphysically high. This is attributed to the presence of strong magnetic interparticle interactions, which influence the shape of the angle dependent $E(\theta)$ potential, that the magnetic moments of the particles experience. Therefore, an increase of T_{OB} relative to the height of the energy barrier, $\beta = k_{\mathrm{B}}T_{\mathrm{OB}}/KV$, against the expected value, can be understood as an indicator for the presence of interparticle interactions.

A modified version of the MLR, using a more adequate unidirectional potential instead of the uniaxial one was developed and applied to the measurements. It was found, that this model is able to describe the low temperature data very well, but fails at higher temperatures. Next to the presence of only weakly and non-interacting particles due to the assumed super-spin glass ground state of the sample, a breakdown of the interparticle interactions at higher temperatures was found as an explanation. Spectra measured in the temperature range where the breakdown of interparticle interactions happens, could not be fitted satisfactorily, probably because anisotropy and interparticle interactions both influence the shape of the $E(\theta)$ potential, resulting in complex, random shapes. Finally, at even higher temperatures, the spectra can be fitted again with the unmodified MLR which includes a particle size distribution, indicating the presence of single particle dynamics after the breakdown of interparticle interactions. Therefore, a first, almost coherent description of a set of scientifically interacting magnetic nanoparticles with the (modified) MLR is presented in this chapter. Furthermore, the SFM/SSG model is applied, confirming the presence of a spin glass groundstate and indicating the presence of surface spin canting at very low temperatures. The observation of interparticle interactions and surface spin canting is supported as well by DC-susceptibility measurements.

In the next **chapter**, number **four**, which emerges from a close collaboration with the Institut für Partikeltechnik of the TU Braunschweig, the formation of nanoparticles during their preparation, using the so-called solvothermal synthesis, is discussed. In this preparation method, $Fe(acac)_3$ is mixed with a solvent (in the first part benzyl alcohol) and heated up in a reactor to 200°C, where it stays for several hours. The preparation facility offers the possibility of withdrawing sample material at any

time during the preparation process. Extraction of sample material was performed systematically throughout the preparation process, beginning already during the heating-up phase. The latest extraction was performed after a reaction time of 24 h. The nucleation of the particles was found to happen early in the beginning of the preparation from Mössbauer spectroscopy and UV/Vis measurements. The subsequent growth of the particles and the development of their physical properties was traced using DC-susceptibility, TEM, XRD and Mössbauer spectroscopy. The size of the particle grows systematically throughout the reaction and the crystallinity improves strongly within the first 6 h of the reaction and stabilizes afterwards. Closely connected to the crystallinity is the fraction of the magnetically disordered volume within the particles. While it is restricted to the expected surface spin canting value for long reaction times, an additional contribution arises below ≈ 5 h, as found from $M(H)$ measurements. The application of the MLR gave indications for the presence of interparticle interactions again, although the particles are in a solution. This observation was supported by DC-susceptibility measurements. Furthermore, the development of the interparticle interaction strength with reaction time shows a peculiar behavior: it increases strongly within the first 6 h of reaction and considerably less strong for longer reaction times. This behavior is explained by the presence of an additional fraction of a magnetically disordered region in the particles for short reaction times. However, the presence of interparticle interactions reveal, that agglomeration of the particles in the solution occurs.

From these observations, it is possible to improve the properties of the particles prepared in this way, e.g. by injecting the particles only when the solvent has reached the nucleation temperature, which should reduce the width of the particle size distribution and by stopping the reaction after 6 h, when the properties of the particles have fully improved, which should reduce the degree of agglomeration between the particles. An application of these improvements is however not a part of this work, but will be performed in the future.

In the last part of this chapter, samples from a similar preparation using triethylene glycol instead of benzyl alcohol as a solvent are examined. The Mössbauer measurements revealed, that the interparticle interactions in these samples, and therefore the degree of agglomeration, are significantly reduced compared to samples, where benzyl alcohol is used. This is attributed to the diamagnetic properties of the different solvents. Furthermore, the structure of the molecules might contribute to the different agglomeration behavior.

Notably, all the information on the magnetic properties found in this chapter, could have been determined in principle only from the application of the MLR to the Mössbauer spectra. For further investigating spin canting within the particles in more detail, a series of Mössbauer measurements in an external magnetic field should be performed. An example for the evaluation of Mössbauer measurements in an exter-

nal magnetic field on samples obtained from an older preparation run is presented as well.

Up to this point, the Mössbauer models were only applied to iron oxide nanoparticles, that are either dried or in solution. In the **last chapter**, the evaluation of the low temperature Mössbauer data of a whole different system is discussed: small clusters of metallic iron, dispersed in a matrix of non-magnetic silver or ytterbium. While the present work only focuses on the evaluation of the low temperature Mössbauer spectra and AC-susceptibility data, earlier work, like the identification of the different cluster types for both sample types and the observation of Kondo-effect and RKKY interactions in Ag(Fe) films was done in the group of E. Baggio Saitovitch at the Centro Brasileiro de Pesquisas Físicas in Rio de Janeiro, Brasil. In the present work, a new model was developed, that is based particularly on the physical properties of the samples as found from the earlier measurements and that provides a physically more adequate description of the low temperature behavior of the magnetic nanoparticles compared to the MLR. It is able to reproduce the Mössbauer spectra very well, which supports the findings from the earlier measurements. Furthermore, it reveals an increase of the interparticle interactions strength with increasing iron concentration. For a comparison, the MLR was attributed to the spectra as well, but it was not able to reproduce all of them. AC-susceptibility data was evaluated as well, which support the findings of strong interparticle interactions.

The low temperature Mössbauer data of the Yb(Fe) films could not be fitted with the different models. A qualitative analysis of the spectra indicates that the interactions between the clusters are only weak. This is supported by AC-susceptibility measurements. A superposition of interparticle interactions and magnetic anisotropies of similar strength makes a fitting of the spectra hardly possible, as already found in chapter four. However, the electronic properties of the host matrix favor an increase of the strength of the RKKY interactions between the clusters. The observed weak interaction can therefore only be explained, by an aggregation of the clusters at phase boundaries within the films, which weakens the RKKY interactions.

Next to the results discussed in the individual chapters, this thesis demonstrates, that a careful analysis of Mössbauer data measured on nanoscale magnetic particles or clusters with an adequate model (primarily the MLR), is able to give reliable information on many significant parameters of the particles (e.g. the blocking temperature, interparticle interactions, surface spin canting etc.), whose determination would usually involve different types of techniques. This information cannot be obtained only from the imprecise or even inaccurate evaluation of the data, as it can be observed frequently in literature.

The biggest issue of the results arising from the application of the different models are the different absolute values of the energy barriers. However, as demonstrated

in chapter 4, the values of the energy barrier for different reaction times resulting from the application of the unmodified and modified MLR models are proportional to each other. This observation indicates, that only the absolute values of the energy barriers should be treated with caution. Their dependence on certain parameters is a reliable information.

In summary, the application of the rather complex models for the evaluation of the Mössbauer data is very beneficial. However, with some experience in this field, it is possible to gain information about some of the essential parameters even from a qualitative analysis of the Mössbauer spectra, as well. In any case, a careful interpretation of the Mössbauer data measured on magnetic nanoparticles / -clusters is worth the effort. Next to the information that is obtained from the application of a local probe technique like Mössbauer spectroscopy (like e.g. the cation distribution, the valence and the symmetry of the local probe atoms etc.), it very likely reveals as well properties of the dynamic behavior of the magnetic moments of the samples, that are usually only detected using additional techniques.

These observations underline and strengthen the outstanding status of Mössbauer spectroscopy in this field of research.

Acknowledgements

Writing a doctoral thesis can be a long and difficult task, from time to time, but the help and support of colleagues, friends and family made it as comfortable as possible for me.

My first and biggest "thank you" goes to my supervisor, Prof. Dr. F. J. Litterst for giving me the opportunity to work on this interesting and challenging topic, for having an open ear for all of my, from time to time rather stupid, questions and for giving me the chance to spend overall 14 weeks in Rio de Janeiro, one of the most fascinating cities in the world. His immense knowledge and experience in Mössbauer spectroscopy, magnetism, physics in general as well as history of science and philosophy left me marveling multiple times. Although his door was always open for discussing any kind of issues I had, he gave me as well the freedom that is necessary to develop own approaches. I cannot imagine any better supervisor.

I am grateful for financial support via the project VWZN2672+2747 of Nds. Ministerium für Wissenschaft und Kultur and Stiftung Volkswagenwerk.

Furthermore I would like thank Prof. Dr. M. Schilling for taking over the job of the second referee of this thesis and Prof. Dr. A. Hangleiter for being the chairman of the examination board.

Prof. Dr. E. Baggio Saitovitch of the Centro Brasileiro de Pesquisas Físicas welcomed me three times in her work group and offered me the possibility to use their experimental installations during these times. I am very grateful for that. Furthermore I appreciate the financial support of DAAD for the stays at Rio de Janeiro.

I would like to thank Dr. D. Baabe for his support and the good atmosphere in the lab as well as for the helpful discussions on physical and other problems.

The other members of the IPKM have a huge influence on the great working atmosphere in the institute and therewith as well on the completion of this thesis. Furthermore, they offer the possibility to join different "side-projects", which are necessary from time to time, when a little break from the work on the thesis was

needed, a special thanks to D. Schulze-Grachtrup at this point, lighten up long days at conferences and offer an insight into other fields of physics. These are in particular Prof. Dr. S. Süllow, Dr. D. Menzel (special thanks for the rapid, uncomplicated and frequent DC-susceptibility measurements), Dr. A. Awada, D. Rauch, J. Engelke, T. Henning, E. Sadrollahi and Dr. B. Willenberg.

The different topics of this thesis result from collaborations with different institutes and work groups. For their friendship and support during my stay in Rio de Janeiro, journey to Manaus and afterwards, I am deeply thankful to I.C. Souza and F. Dinóla Neto as well as J.A.M. Cagigas, W.T. Herrera and C. Rojas-Ayala from the Centro Brasileiro de Pesquisas Físicas. The great cooperation with I.-C. Masthoff and Prof. Dr. G. Garnweitner from the Institut für Partikeltechnik was a real pleasure for me. Furthermore, thanks to I.-M. Grabs, who prepared the samples that are discussed in chapter 3. I appreciate very much, that M. Thede from the ETH Zurich performed the AC-susceptibility measurements on the Ag(Fe) and Yb(Fe) films presented in chapter 5, that L. Hoffmann from the Institut für angewandte Physik of the TU Braunschweig, performed the TEM measurements on the $ZnFe_2O_4$ particles, presented in chapter 3 and that T. Woike from the TU Dresden performed the low temperature XRD measurements on the Yb(Fe) films, presented in chapter 5.

Ms. Bosse, Ms. Schnettler, Ms. Zeising and Neele from the secretariat supported me, when it came to bureaucracy, e.g. travel costs, renewal of the contract etc. Their help was very necessary and is highly appreciated.

I had the pleasure to work together with several bachelor and master students during their theses, which were partially closely connected to my actual work (A. Borchers, F. Körkemeyer and D. Mauch). With them, and other people, I shared the office during the past three and a half years. We had mostly a great atmosphere here, which I really appreciated.

The guys from the workshop helped me by preparing multiple sample boxes for the Mössbauer measurements and different spare parts. The supply with liquid helium, offered by F. Werner and his team at the helium workshop, was always reliable and friendly. Thank you for that.

I would like to thank as well those good old friends from our bachelor and master study time who, although some of them have left the town, are still somehow around and open for discussions or complaints regarding physics or other topics, in particular M. Hensen, M. Schäpers and R. Weidling.

The private environment plays a significant role for the completion of the thesis. Therefore I would like to thank my friends and family very much, especially my

parents, whose education is the foundation of every further study, for their support during the study and doctoral years and my girlfriend Sinja-Christin for her love and support. With the words of Babylon Bombs: ”I owe it all to you”.

Appendix A

Codes

The program codes presented in the following are written for Mathematica. Since the calculation of the final spectrum takes up to several minutes, they are only designed in order to simulate the spectrum and not to fit the actual measurement. The different parameters have to be adjusted manually in order to achieve the best possible match between the simulated spectrum and the measured data.

They are presented as a screenshot of the printed version of the mathematica files.

A.1 Mössbauer models

A.1.1 MLR with one subspectrum

```
(Debug) In[1]:= Off[Set::"partw"]
               Off[InterpolatingFunction::dmval]
               Off[Solve::ratnz]
               Off[Set::write]

(Debug) In[204]:= Nω = 80;                    (* Number of data points (has to be even) *)
                  Spek = Table[0, {i, Nω + 1}, {j, 2}]; (* Table which will contain the spectrum *)


                  (* Definition of Mössbauer parameter *)
                  KV = 1;                     (* Energy barrier (relative to kT) *)
                  kT = 0.5;                   (* Temperature (relative to KV) *)
                  ABs = 0.1;                  (* Absorption depth *)
                  Γ = 0.2;                    (* Linewidth (mm/s) *)
                  δ = 7.5;                    (* Magnetic hyperfine splitting (mm/s) *)
                  beta = 0 * KV;
                  (* Onset temperature of overbarrier fluctuations relative to KV *)
                  Iso = 1;                    (* Isomer shift (mm/s) *)
                  Bl = 1;                     (* Baseline *)
                  R = 1;                      (* Relaxation rate (mm/s) *)


                  (* Further parameter *)

                  NN = 55;                    (* Number of sites in the potential well *)
                  S = (NN - 1) / 2;
                  ω0 = -14;
                  (* Maximum/minimum velocity of the calculated spectrum (mm/s) *)
                  ωmax = -ω0;
                  Δω = 2 * ωmax / Nω;
                  (* Velocity steps between the simulation points (mm/s) *)



                  (* Definition of the tables,
                  which will contain the two lines of the sextett at a time *)

                  Spek1 = Table[0, {i, Nω + 1}, {j, 2}];
                  Spek2 = Table[0, {i, Nω + 1}, {j, 2}];
                  Spek3 = Table[0, {i, Nω + 1}, {j, 2}];


                  zp = 0;                     (* Counting parameter *)


                  (* Definition of the functions after Jones et al. and Lierop et al. *)
                  ThetaII[k_] := ArcCos[(k - S - 1) / S];
                  En[k_] := -KV * (Cos[ThetaII[k]])^2;
                  W[k_, kT_] := Exp[-En[k] / kT];

                  ΔEPl[k_] := En[k + 1] - En[k];
                  ΔEMi[k_] := En[k - 1] - En[k];
```

```
Ppl[k_, R_] :=
  If[k < (2 S + 1)/2, R (S (S + 1) - (k - S - 1) (k - S)), R (S (S + 1) - (k - S - 1) (k - S))];
Pmi[k_, R_] := If[k ≥ (2 S + 1)/2, R (S (S + 1) - (k - S - 1) (k - S - 2)),
   R (S (S + 1) - (k - S - 1) (k - S - 2))];

Mpl[k_, R_, kT_] := If[ΔEPl[k] > 0, -Ppl[k, R] * (Exp[-ΔEPl[k]/kT]), -Ppl[k, R]];
Mmi[k_, R_, kT_] := If[ΔEMi[k] > 0, -Pmi[k, R] * (Exp[-ΔEMi[k]/kT]), -Pmi[k, R]];

MMPl[ω_, δ_, k_, R_, kT_] := ⅈ (ω - (S - k + 1) * δ/S) + Γ - Mpl[k, R, kT];
MMMi[ω_, δ_, k_, R_, kT_] := ⅈ (ω - (S - k + 1) * δ/S) + Γ - Mmi[k, R, kT];

MM[ω_, δ_, k_, R_, kT_] := ⅈ (ω - (S - k + 1) * δ/S) + Γ - Mmi[k, R, kT] - Mpl[k, R, kT];

(* Calculation of the spectral shape for two lines at a time only for the part
 of the spectrum with negative velocities for calculation time reasons *)
For[ω = ω0, ω ≤ -0 + Δω, ω = ω + Δω,
 zp = zp + 1;

 MMat = Table[0, {i, NN}, {j, NN}];
 WW = Table[0, {i, NN}];
 Eins = Table[1, {i, NN}];
 For[i = 1, i < NN + 1, i++,
  WW[[i]] = W[i, kT];
  For[j = 1, j < NN + 1, j++,
   If[i == j, MMat[[i, j]] = MM[ω, δ, i, R, kT], 0];
   If[i == j - 1, MMat[[i, j]] = Mpl[i, R, kT], 0];
   If[i == j + 1, MMat[[i, j]] = Mmi[i, R, kT], 0]]];
 MMat[[1, 1]] = MMPl[ω, δ, 1, R, kT];
 MMat[[NN, NN]] = MMMi[ω, δ, NN, R, kT];
 MatrInv := Inverse[MMat];
 Spek1[[zp, 1]] = ω;
 Spek1[[zp, 2]] = N[2 * Re[1/(∑_{i=1}^{2*S+1} W[i, kT]) WW.MatrInv.Eins]]]

zp = 0;
δ = δ * 0.5790;

For[ω = ω0, ω ≤ -0 + Δω, ω = ω + Δω,
 zp = zp + 1;

 MMat = Table[0, {i, NN}, {j, NN}];
 WW = Table[0, {i, NN}];
 Eins = Table[1, {i, NN}];
 For[i = 1, i < NN + 1, i++,
```

```
  WW[[i]] = W[i, kT];
  For[j = 1, j < NN + 1, j++,
   If[i == j, MMat[[i, j]] = MM[ω, δ, i, R, kT], 0];
   If[i == j - 1, MMat[[i, j]] = Mpl[i, R, kT], 0];
   If[i == j + 1, MMat[[i, j]] = Mmi[i, R, kT], 0]]];
 MMat[[1, 1]] = MMPl[ω, δ, 1, R, kT];
 MMat[[NN, NN]] = MMMi[ω, δ, NN, R, kT];
 MatrInv := Inverse[MMat];
 Spek2[[zp, 1]] = ω;
 Spek2[[zp, 2]] = 2 / 3 * N[2 * Re[1 / ∑_{i=1}^{2*S+1} W[i, kT] WW.MatrInv.Eins]]]

zp = 0;
δ = δ * 1 / 0.579 * 0.1580;

For[ω = ω0, ω ≤ -0 + Δω, ω = ω + Δω,
 zp = zp + 1;

 MMat = Table[0, {i, NN}, {j, NN}];
 WW = Table[0, {i, NN}];
 Eins = Table[1, {i, NN}];
 For[i = 1, i < NN + 1, i++,
  WW[[i]] = W[i, kT];
  For[j = 1, j < NN + 1, j++,
   If[i == j, MMat[[i, j]] = MM[ω, δ, i, R, kT], 0];
   If[i == j - 1, MMat[[i, j]] = Mpl[i, R, kT], 0];
   If[i == j + 1, MMat[[i, j]] = Mmi[i, R, kT], 0]]];
 MMat[[1, 1]] = MMPl[ω, δ, 1, R, kT];
 MMat[[NN, NN]] = MMMi[ω, δ, NN, R, kT];
 MatrInv := Inverse[MMat];
 Spek3[[zp, 1]] = ω;
 Spek3[[zp, 2]] = 1 / 3 * N[2 * Re[1 / ∑_{i=1}^{2*S+1} W[i, kT] WW.MatrInv.Eins]]]

(* Mirroring of the other half of the spectrum *)
zp = Nω / 2;
For[ω = 0 + Δω, ω ≤ -ω0, ω = ω + Δω,
  Spek1[[zp + 2, 1]] = -Spek1[[zp - 2 * (zp - Nω / 2), 1]];
  Spek2[[zp + 2, 1]] = -Spek1[[zp - 2 * (zp - Nω / 2), 1]];
  Spek3[[zp + 2, 1]] = -Spek1[[zp - 2 * (zp - Nω / 2), 1]];
  Spek1[[zp + 2, 2]] = Spek1[[zp - 2 * (zp - Nω / 2), 2]];
  Spek2[[zp + 2, 2]] = Spek2[[zp - 2 * (zp - Nω / 2), 2]];
  Spek3[[zp + 2, 2]] = Spek3[[zp - 2 * (zp - Nω / 2), 2]];
  zp = zp + 1;];

(* Summing up of the three supparts to a full spectrum *)
zp = 0;
For[ω = ω0, ω ≤ -ω0, ω = ω + Δω,
  zp = zp + 1;
  Spek[[zp, 1]] = Spek1[[zp, 1]] + Iso;
  Spek[[zp, 2]] = Bl - ABs * (Spek1[[zp, 2]] + Spek2[[zp, 2]] + Spek3[[zp, 2]])];

(* Plots a table with the parameters *)
```

```
Grid[
 {{"Iso (mm/s)", "Γ (mm/s)", "R (MHz)", "B_hyp (T)", "KV ()", "k_BT ()", "β (KV)" },
  {Iso, Γ, R * 806.5 * 14.4 * 1000 / 10^6, δ * 1 / 0.1580 * 33 / 5.375, KV, kT, kTB}}, Frame → All]

(* Interpolation of the resulting
 datapoints in order to achieve a smooth function *)
Spectrum = Interpolation[Spek];

(* Plot of the datapoints and the interpolated function *)
Show[Plot[Spectrum[x], {x, -14, 14}],
 ListPlot[Spek], AxesLabel → {"v (mm/s)", "Absorption  ()"}]
```

(Debug) Out[234]=

Iso (mm/s)	Γ (mm/s)	R (MHz)	B_{hyp} (T)	KV ()	k_BT ()	β (KV)
1	0.2	11.6136	46.0465	1	0.5	0

(Debug) Out[236]=

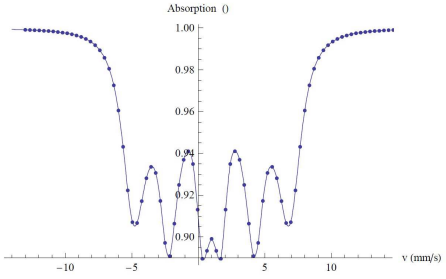

A.1.2 MLR with Particle-size distribution

```
(Debug) In[1]:= Off[Set::"partw"]
Off[InterpolatingFunction::dmval]
Off[Solve::ratnz]
Off[Set::write]

(* Definition of the distribution function
 (here log-normal distribution) and the steps were a spectrum is calculated *)
LN[μ_, σ_, x_] := PDF[LogNormalDistribution[μ, σ],
  ∛(3 x / (4 π)) * 2]                                   (* Log normal distribution *)

MaxxLN[μ_, σ_] := x /. Solve[∂x PDF[LogNormalDistribution[μμ, σσ], ∛(3 x / (4 π)) * 2] == 0, x][[
   2]]        (* Maximum of the distribution *)
MaxLN[μ_, σ_] := PDF[LogNormalDistribution[μμ, σσ],
  ∛(3 MaxxLN[μμ, σσ] / (4 π)) * 2]                      (* Corresponding x value *)
Δi[x_, y_] :=
 MaxxLN[x, y] / 50
(* Stepwidth to determine the start and the stop value *)

Star[μ_, σ_] :=
 First[Module[{x = μ, y = σ},
   (* First value, where a spectrum is calculated *)
   For[i = 0.00001, i < MaxxLN[x, y],
     i = i + Δi[x, y],                                  (* Here,
     where the y value has fallen below 1/20 of the maximum value *)
     If[LN[x, y, i] > MaxLN[x, y] / 20, j = i, 0]
      If[LN[x, y, i] > MaxLN[x, y] / 20, i = MaxxLN[x, y], 0]]
    j]]
Stop[μ_, σ_] :=
 First[Module[{x = μ, y = σ},
   (* Last value, where a spectrum is calculated *)
   For[i = MaxxLN[x, y], i < 30 * MaxxLN[x, y], i = i + 10,
     If[LN[x, y, i] < MaxLN[x, y] / 20, jj = i, 0]
      If[LN[x, y, i] < MaxLN[x, y] / 20, i = 30 * MaxxLN[x, y] + 1, 0]]
    jj]]

ΔStütz[μ_, σ_] :=
 (Stop[μ, σ] - Star[μ, σ]) / 15
(* Distance between the PSD values, for which a spectrum calculated *)
```

(Debug) In[12]:=
```
FakmmsHz = 8.065 * 10^2 * 14.4 *
    10^3;                                                    (* mm/
  s --> Hz *)
FakHzmms = 1.24 * 10^-3 *
     1
  ---------- ;
  14.4 * 10^3
(* Hz in mm/s *)
```

(Debug) In[14]:=
```
μμ = 1.75;

(* Values of the particle DIAMETER (!) distribtuion in nm *)
σσ = 0.2;
```

(Debug) In[16]:=
```
Plot[LN[μμ, σσ, x], {x, 0, 2000}, PlotRange → Full, AxesLabel → {"V (nm³)", "p(V)"}]
```

(Debug) Out[16]=

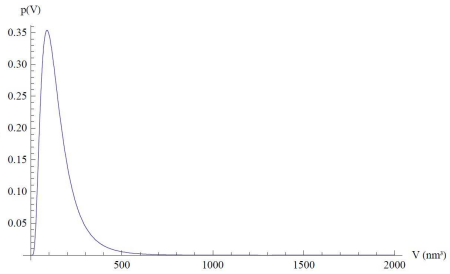

(Debug) In[17]:=
```
Kk = 0.000004;

(* Anisotropy constant in kg*nm²/s² / nm³ *)


Stü = ΔStütz[μμ, σσ];
Stopp = Stop[μμ, σσ];


      Stopp - Star[μμ, σσ]
KVav = -------------------- ;
             2

(* Average value of the energy barrier height *)

jjmax =
  15;
(* Number of subspectra for the different values in the PSD *)

Nω = 80;
Spek = Table[0, {i, Nω + 1},
   {j, jjmax + 1}];
(* Definition of different tables *)
SpekVert1 = Table[0, {i, Nω + 1}, {j, 2}];
SpekVertBL = Table[0, {i, Nω + 1}, {j, 2}];
```

```
For[jj = 1, jj < jjmax + 1,
 jj++,
 (* Caculation of the subspectra corresponding to certain values of KV *)
 m = jj - 8;

 KV = Kk * (KVav + m * Stü);
 ABSav = 0.01;
 ABs = ABSav * LN[μμ, σσ, (KVav + m * Stü)];



 NN = 55;

 (* Mössbauer parameter (compare to program code in previous section) *)
 S = (NN - 1)/2;
 Γ = 0.2;
 k_B = 1.38 *
   10^-5;
 (* in kg nm²/(s^2*K) *)
 kT = k_B * 10;
 δ = 7.5;
 kTB = 0.3 * KV;
 Iso = 0;
 (* Bl=(Σ_{i=1}^{40} NAMESPECTRUM[[i,2]])/40; *)
 Bl = 1;


 Print[ListPlot[Table[{KVav + (kk - 8) * Stü, ABSav * LN[μμ, σσ, KVav + (kk - 8) * Stü]},
    {kk, 0, jj}], Filling → Axis, PlotStyle → PointSize[0.02],
   PlotRange → {{0, Stopp}, All}, AxesLabel → {"V (nm³)", "p(V)"}]];

     (* Plotting of the actual value of KV within the PVD,
 for which the spectrum is calculated *)

 ω0 = -14;
 ωmax = -ω0;
 Δω = (2 * ωmax)/Nω;



 (* Relaxation rate for every value
  of KV after Coffey et al. (see eq. (1.25)) *)
 τ0 = 1/(1 * 10^9 * FakHzmms);
```

```
Coff[KV_, kT_, τ0_] := 1/(τ0 1/(4 * KV/kT) * 1/((KV/kT)/(KV/kT + 1) Sqrt[(KV/kT)/π] + 2^(-KV/kT - 1)) (Exp[KV/kT] - 1));
R = If[kT < kTB, 0, Coff[KV, kT, τ0]];


Spek1 = Table[0, {i, Nω + 1}, {j, 2}];
Spek2 = Table[0, {i, Nω + 1}, {j, 2}];
Spek3 = Table[0, {i, Nω + 1}, {j, 2}];


zp = 0;

ThetaII[k_] := ArcCos[(k - S - 1)/S];
En[k_] := -KV * (Cos[ThetaII[k]])^2;
W[k_, kT_] := Exp[-En[k]/kT];

ΔEPl[k_] := En[k + 1] - En[k];
ΔEMi[k_] := En[k - 1] - En[k];

Ppl[k_, R_] :=
 If[k < (2 S + 1)/2, R (S (S + 1) - (k - S - 1) (k - S)), R (S (S + 1) - (k - S - 1) (k - S))];
Pmi[k_, R_] := If[k ≥ (2 S + 1)/2, R (S (S + 1) - (k - S - 1) (k - S - 2)),
  R (S (S + 1) - (k - S - 1) (k - S - 2))];

Mpl[k_, R_, kT_] := If[ΔEPl[k] > 0, -Ppl[k, R] * (Exp[-ΔEPl[k]/kT]), -Ppl[k, R]];
Mmi[k_, R_, kT_] := If[ΔEMi[k] > 0, -Pmi[k, R] * (Exp[-ΔEMi[k]/kT]), -Pmi[k, R]];

MMPl[ω_, δ_, k_, R_, kT_] := i (ω - (S - k + 1) * δ/S) + Γ - Mpl[k, R, kT];
MMMi[ω_, δ_, k_, R_, kT_] := i (ω - (S - k + 1) * δ/S) + Γ - Mmi[k, R, kT];

MM[ω_, δ_, k_, R_, kT_] := i (ω - (S - k + 1) * δ/S) + Γ - Mmi[k, R, kT] - Mpl[k, R, kT];

For[ω = ω0, ω ≤ -0 + Δω, ω = ω + Δω,
  zp = zp + 1;

  MMat = Table[0, {i, NN}, {j, NN}];
  WW = Table[0, {i, NN}];
  Eins = Table[1, {i, NN}];
```

```
  For[i = 1, i < NN + 1, i++,
   WW[[i]] = W[i, kT];
   For[j = 1, j < NN + 1, j++,
    If[i == j, MMat[[i, j]] = MM[ω, δ, i, R, kT], 0];
    If[i == j - 1, MMat[[i, j]] = Mpl[i, R, kT], 0];
    If[i == j + 1, MMat[[i, j]] = Mmi[i, R, kT], 0]]];
  MMat[[1, 1]] = MMPl[ω, δ, 1, R, kT];
  MMat[[NN, NN]] = MMMi[ω, δ, NN, R, kT];
  MatrInv := Inverse[MMat];
  Spek1[[zp, 1]] = ω;
  Spek1[[zp, 2]] = N[2 * Re[1/(∑_{i=1}^{2*S+1} W[i, kT]) WW.MatrInv.Eins]]]

 zp = 0;
δ = δ * 0.5790;

For[ω = ω0, ω ≤ -0 + Δω, ω = ω + Δω,
  zp = zp + 1;

  MMat = Table[0, {i, NN}, {j, NN}];
  WW = Table[0, {i, NN}];
  Eins = Table[1, {i, NN}];
  For[i = 1, i < NN + 1, i++,
   WW[[i]] = W[i, kT];
   For[j = 1, j < NN + 1, j++,
    If[i == j, MMat[[i, j]] = MM[ω, δ, i, R, kT], 0];
    If[i == j - 1, MMat[[i, j]] = Mpl[i, R, kT], 0];
    If[i == j + 1, MMat[[i, j]] = Mmi[i, R, kT], 0]]];
  MMat[[1, 1]] = MMPl[ω, δ, 1, R, kT];
  MMat[[NN, NN]] = MMMi[ω, δ, NN, R, kT];
  MatrInv := Inverse[MMat];
  Spek2[[zp, 1]] = ω;
  Spek2[[zp, 2]] = 2 / 3 * N[2 * Re[1/(∑_{i=1}^{2*S+1} W[i, kT]) WW.MatrInv.Eins]]]

 zp = 0;
δ = δ * 1/0.579 * 0.1580;

For[ω = ω0, ω ≤ -0 + Δω, ω = ω + Δω,
  zp = zp + 1;

  MMat = Table[0, {i, NN}, {j, NN}];
  WW = Table[0, {i, NN}];
  Eins = Table[1, {i, NN}];
  For[i = 1, i < NN + 1, i++,
   WW[[i]] = W[i, kT];
   For[j = 1, j < NN + 1, j++,
    If[i == j, MMat[[i, j]] = MM[ω, δ, i, R, kT], 0];
    If[i == j - 1, MMat[[i, j]] = Mpl[i, R, kT], 0];
    If[i == j + 1, MMat[[i, j]] = Mmi[i, R, kT], 0]]];
  MMat[[1, 1]] = MMPl[ω, δ, 1, R, kT];
  MMat[[NN, NN]] = MMMi[ω, δ, NN, R, kT];
  MatrInv := Inverse[MMat];
```

```
   Spek3[[zp, 1]] = ω;
   Spek3[[zp, 2]] = 1 / 3 * N[2 * Re[1 / Σ_{i=1}^{2*S+1} W[i, kT] WW.MatrInv.Eins]]]

  zp = Nω / 2;
 For[ω = 0 + Δω, ω ≤ -ω0, ω = ω + Δω,
  Spek1[[zp + 2, 1]] = -Spek1[[zp - 2 * (zp - Nω / 2), 1]];
  Spek2[[zp + 2, 1]] = -Spek1[[zp - 2 * (zp - Nω / 2), 1]];
  Spek3[[zp + 2, 1]] = -Spek1[[zp - 2 * (zp - Nω / 2), 1]];
  Spek1[[zp + 2, 2]] = Spek1[[zp - 2 * (zp - Nω / 2), 2]];
  Spek2[[zp + 2, 2]] = Spek2[[zp - 2 * (zp - Nω / 2), 2]];
  Spek3[[zp + 2, 2]] = Spek3[[zp - 2 * (zp - Nω / 2), 2]];
  zp = zp + 1;];


 zp = 0;
 For[ω = ω0, ω ≤ -ω0, ω = ω + Δω,
  zp = zp + 1;
  Spek[[zp, 1]] = Spek1[[zp, 1]] + Iso;
  Spek[[zp, jj + 1]] = Bl - ABs * (Spek1[[zp, 2]] + Spek2[[zp, 2]] + Spek3[[zp, 2]])];



 SpekPlot = Table[0, {i, Nω}, {j, 2}];
 zp = 0;
 For[ω = ω0, ω ≤ -ω0 - Δω, ω = ω + Δω,
    zp = zp + 1;
    SpekPlot[[zp, 1]] = Spek1[[zp, 1]] + Iso;
    SpekPlot[[zp, 2]] = Bl - ABs * (Spek1[[zp, 2]] + Spek2[[zp, 2]] + Spek3[[zp, 2]])]

  Print[ListLinePlot[SpekPlot,
     AxesLabel → {"v (mm/s)", "Absorption"}, PlotRange → Full, Mesh → All]]

]



(* Summing up the individual spectra *)

For[k = 2, k < jjmax + 1, k++,
 For[h = 1, h < Nω + 2, h++,
  SpekVert1[[h, 1]] = Spek[[h, 1]];
  SpekVert1[[h, 2]] = SpekVert1[[h, 2]] + Spek[[h, k]] * 1 / (jjmax - 1)]
]



(* Finding of Baseline, if not predefined *)

BL = Bl;
```

```
ListPlot[SpekVert1, PlotRange → Full, Joined → True, Mesh → Full,
 InterpolationOrder → 1, PlotStyle → Red, AxesLabel → {"v (mm/s)", "Absorption"}]
```

```
SpekInt1 = Interpolation[SpekVert1];
SpekInt11[x_] := SpekInt1[x] * 1 / SpekVert1[[1, 2]];
```

```
Area1 = 1;
```

```
Manipulate[Show[Plot[
   (AbsorpFinal1 * ((((SpekInt11[x/b1 - Iso1])/Area1)/((SpekInt11[-12])/Area1)) - 1) + AbsorpFinal2 * ((((SpekInt11[x/b2 - Iso2])/Area1)/((SpekInt11[-12])/Area1)) - 1)) + Bl,
   {x, -13.3, 13.3}, PlotStyle → {Red, Thick}, PlotRange → Full],
  Plot[(AbsorpFinal1 * ((((SpekInt11[x/b1 - Iso1])/Area1)/((SpekInt11[-12])/Area1)) - 1)) + Bl,
   {x, -13.3, 13.3}, PlotStyle → Purple, PlotRange → Full],
  Plot[AbsorpFinal2 * ((((SpekInt11[x/b2 - Iso2])/Area1)/((SpekInt11[-12])/Area1)) - 1) + Bl, {x, -13.3, 13.3}, PlotStyle → Blue,
   PlotRange → Full], AxesOrigin → {0, 1}, AxesLabel → {"v (mm/s)", "Absorption"}],
 {{AbsorpFinal1, 50 000}, 50 000, 100 000}, {{AbsorpFinal2, 50 000}, 50 000, 100 000},
 {{Iso1, 0.296}, -0.7, 0.7}, {{Iso2, 0.218}, -0.7, 0.7},
 {{b1, 1.082`}, 0.8, 1.2}, {{b2, 1.083}, 0.8, 1.2}]
```

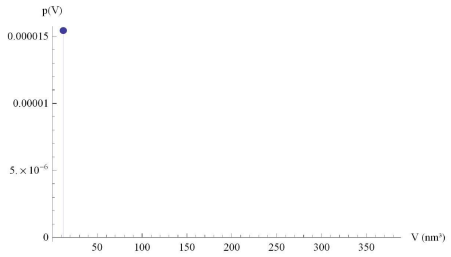

8 | MLR_PSD.nb

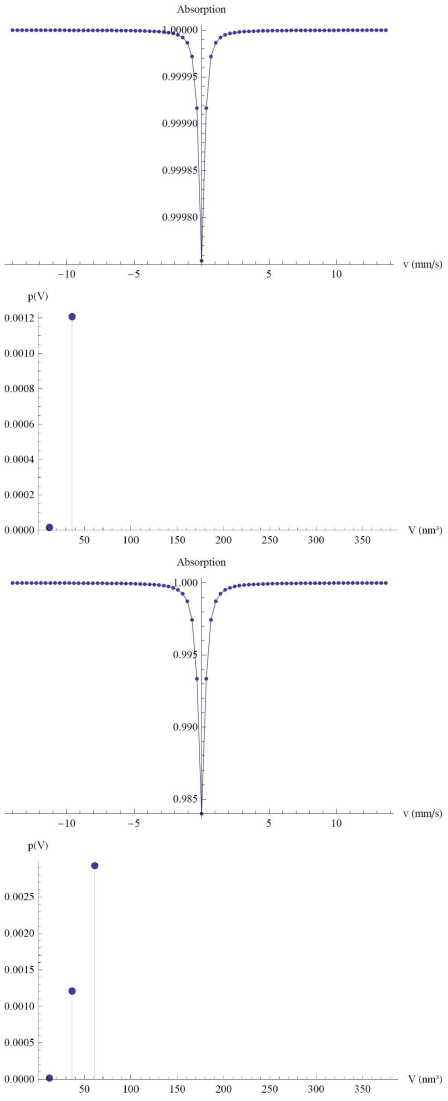
Absorption
1.00000
0.99995
0.99990
0.99985
0.99980
−10
−5
5
10
v (mm/s)
p(V)
0.0012
0.0010
0.0008
0.0006
0.0004
0.0002
0.0000
50
100
150
200
250
300
350
V (nm³)
Absorption
1.000
0.995
0.990
0.985
−10
−5
5
10
v (mm/s)
p(V)
0.0025
0.0020
0.0015
0.0010
0.0005
0.0000
50
100
150
200
250
300
350
V (nm³)

14 | *MLR_PSD.nb*

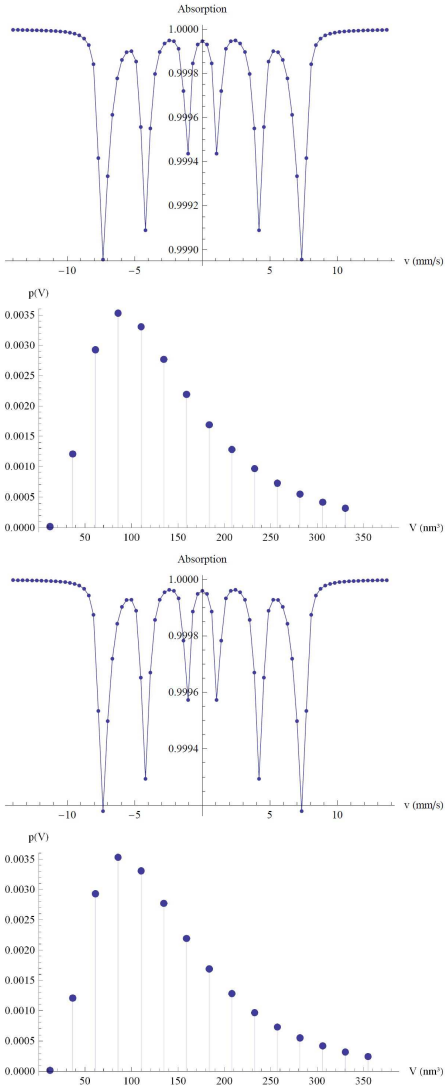
Absorption
1.0000
0.9998
0.9996
0.9994
0.9992
0.9990
−10
−5
5
10
v (mm/s)
p(V)
0.0035
0.0030
0.0025
0.0020
0.0015
0.0010
0.0005
0.0000
50
100
150
200
250
300
350
V (nm³)
Absorption
1.0000
0.9998
0.9996
0.9994
−10
−5
5
10
v (mm/s)
p(V)
0.0035
0.0030
0.0025
0.0020
0.0015
0.0010
0.0005
0.0000
50
100
150
200
250
300
350
V (nm³)

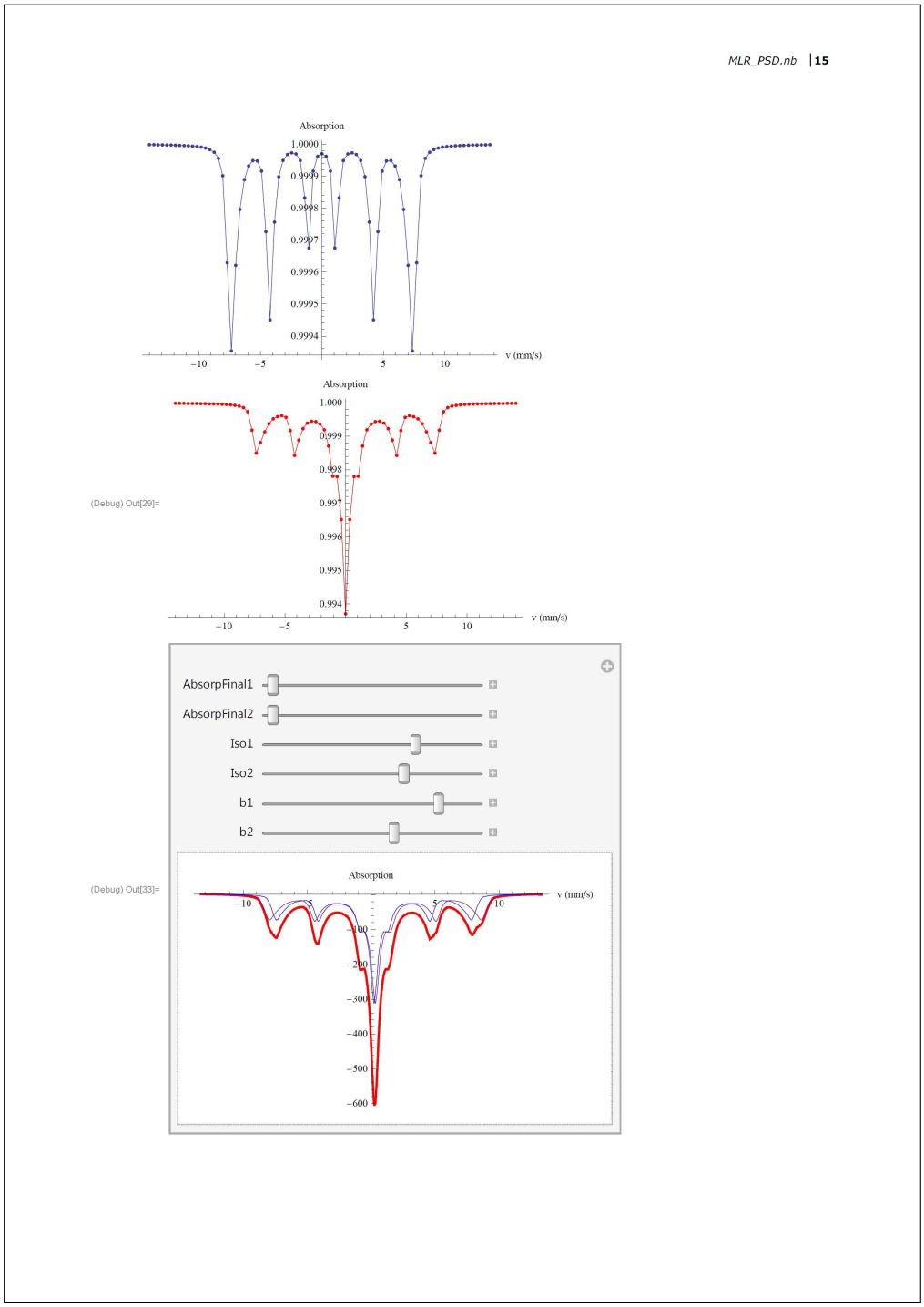

In this code, the middle pages 9 - 13 are not shown, since they display only the Mössbauer spectra with increasing KV. The final result is a graphic, in which it is

possible to adjust the width of the subspectra, the absorption of the subspectra and the isomer shifts of the spectra, without recalculating the whole spectrum. However, when doing so, one has to recalculate the absolute values of the modified parameters, therefore no table with their values is shown in this code.

It is possible to include a measured Mössbauer spectrum by performing only slight changes. If the baseline and the absorption values are determined correctly, than the simulation and the data can be presented in one graph and the simulation can be adjusted to the measurements.

A.1.3 SFM/SSG

In the following, the codes that give a simulation of the super ferromagnetism and the super spin-glass model after [23] are presented. For a correct application, the bulk magnetization curve has to be included in the function $B0[x]$.

SFM

```
(Debug) In[10]:= B0[x_] := 1;    (* define bulk magnetization curve here *)
(Debug) In[11]:=

          (* Superferromagnetism *)
(Debug) In[12]:= L[x_] := Coth[x] - 1/x
          qq1[q_?NumericQ] := q
          qssg1[Tp_?NumericQ, q_?NumericQ, T_?NumericQ] := L[3 * Tp/T (B0[T]/B0[Tp])^2 * q]
          qqq1[TT_, TTp_] := If[TT ≤ TTp, Last[Last[With[{T = TT, Tp = TTp},
                FindRoot[qssg1[Tp, q, T] == qq1[q], {q, 0.01, 1}, Evaluated → False]]]], 0]
        VTp1 = 1;
        VFrac1 = 1;
        Plot[{VFrac1 * qqq1[x, VTp1]}, {x, 0, 1.05},  AxesLabel → {"T(K)", "b(T)"},
         PlotPoints → 45, MaxRecursion → 2, PlotRange → {0, 1.05}, AxesLabel → {"T (K)", "b(T)"}]
```

(Debug) Out[18]=

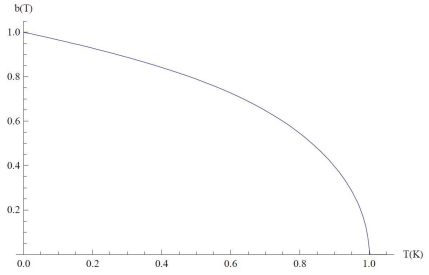

SSG

```
(Debug) In[19]:= B0[x_] := 1;    (* define bulk magnetization curve here *)
(Debug) In[20]:=

                 (* Superspinglass *)
(Debug) In[21]:= L[x_] := Coth[x] - 1/x          (* Definition of the functions *)
                 qq[q_?NumericQ] := q
                 qssg[Tp_?NumericQ, q_?NumericQ, T_?NumericQ] := NIntegrate[
                   1/Sqrt[2 π] * Exp[-z^2/2] * (L[3 * Tp/T (B0[T]/B0[Tp])^2 * Sqrt[q] * z])^2, {z, -∞, ∞}, MaxRecursion → 100]
                 qqq[TT_, TTp_] := If[TT ≤ TTp, Last[Last[With[{T = TT, Tp = TTp},
                     FindRoot[qssg[Tp, q, T] == qq[q], {q, 0.01, 1}, Evaluated → False]]]], 0]
(Debug) In[25]:= VTP = 1;                        (* Plotting of the
                  function for selectable values of T_p and the maximum av. B_hyp *)
                 VFrac = 1;
                 Plot[VFrac * Sqrt[qqq[x, VTP]], {x, 0, 1.050}, PlotRange → {0, 1.15},
                  PlotStyle → Purple, AxesLabel → {"T (K)", "b(T)"}]
```

(Debug) Out[27]=

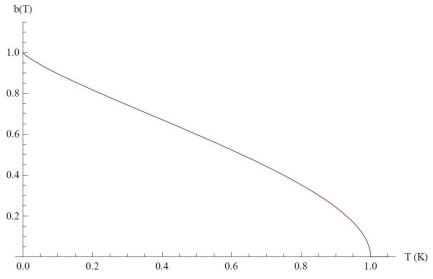

A.1.4 The Ag(Fe)-model

In the following, the code for the model used for the simulation of the Ag(Fe)-low temperature measurements is presented. Is is necessary to define a table that contains the measured spectrum as ”F922” before running the simulation.

(Debug) In[96]:=

```
NN = 10 000; (* number of steps *)
Mom = 0.00048; (* magnetic moment of the particles *)
R = 0.037; (* average distance among the clusters *)
kF = 75/R; (* see chapter 5 *)
Z = 0.4; (* centering of the inverse errorfunction (see equation (5.7)) *)
RR = Table[0, {i, 18}]; (* Random numbers between -1 and 1 (see equation (5.7)) *)
For[i = 1, i < 19, i++,
 RR[[i]] = First[RandomReal[-1, 1]]]
ΔEE = Table[0, {i, NN}, {j, 1}];
RI[Z_, R_] := Sqrt[2] InverseErf[(2 RandomReal[{0, 1}] - 1)] * R * Z + R;
(* equation (5.7) *)
For[i = 1, i < NN + 1, i++,
 (* equation (5.11) *)
 ΔEE[[i]] = 1/1 Norm[Mom * Cos[kF * RI[Z, R]]/(RI[Z, R])^3 * 1(*Normierung*)/Sqrt[RR[[1]]^2 + RR[[2]]^2 + RR[[3]]^2] * {{RR[[1]]}, {RR[[2]]}, {RR[[3]]}} +
     Mom * Cos[kF * RI[Z, R]]/(RI[Z, R])^3 * 1(*Normierung*)/Sqrt[RR[[4]]^2 + RR[[5]]^2 + RR[[6]]^2] * {{RR[[4]]}, {RR[[5]]}, {RR[[6]]}} +
     Mom * Cos[kF * RI[Z, R]]/(RI[Z, R])^3 * 1(*Normierung*)/Sqrt[RR[[7]]^2 + RR[[8]]^2 + RR[[9]]^2] * {{RR[[7]]}, {RR[[8]]}, {RR[[9]]}} +
   Mom * Cos[kF * RI[Z, R]]/(RI[Z, R])^3 * 1(*Normierung*)/Sqrt[RR[[10]]^2 + RR[[11]]^2 + RR[[12]]^2] * {{RR[[10]]}, {RR[[11]]}, {RR[[12]]}} +
   Mom * Cos[kF * RI[Z, R]]/(RI[Z, R])^3 * 1(*Normierung*)/Sqrt[RR[[13]]^2 + RR[[14]]^2 + RR[[15]]^2] * {{RR[[13]]}, {RR[[14]]}, {RR[[15]]}} +
   Mom * Cos[kF * RI[Z, R]]/(RI[Z, R])^3 * 1(*Normierung*)/Sqrt[RR[[16]]^2 + RR[[17]]^2 + RR[[18]]^2] * {{RR[[16]]}, {RR[[17]]}, {RR[[18]]}}]]

hn = BinCounts[ΔEE, {0, 50, 1}];
xhn = Table[0 + i * 1, {i, 0, Length[hn] - 1}];

EintDist = Transpose[{xhn, hn}];
(* the resulting ditribution of interparticle interaction strength *)

EintDist[[1, 1]] = 0.00001;
EintDist[[1, 2]] = 0.00001;

FF1 = FindFit[EintDist, {d * PDF[LogNormalDistribution[a, b], x/c],
   {0.002 < a < 0.11, 0.1 < b < 2, 20 < c < 50, d > 40}}, {a, b, c, d}, {x}];
(* Fitting with a Log-Normal Distribution *)Show[ListPlot[EintDist],
 Plot[d * PDF[LogNormalDistribution[a, b], x/c] /. FF1, {x, 0, 50}, PlotRange → Full]]
```

2 | AgFe.nb

(Debug) Out[111]=

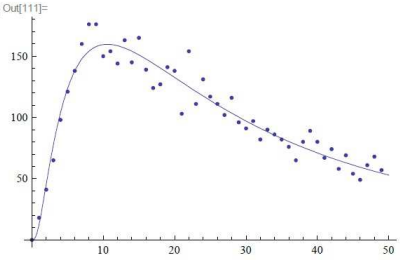


```
kKV1 = 0.01;
kKV2 = 0.01;      (* Definition of Parameters *)
kkT = 0.40;
ΔEint[S_, Sz_, KV_, Ea_] :=
 d * PDF[LogNormalDistribution[a, b], 2 * (Ea - KV * Sin[ArcCos[Sz/S] - π]^2) / (Cos[ArcCos[Sz/S] - π] + 1.000001) / c] /. FF1
ΔEintx[x_] := d * PDF[LogNormalDistribution[a, b], x/c] /. FF1
Eint[θ_, KV_, Ea_] := 2 * (Ea - KV * If[-π/4 < θ - π < π/4, Sin[θ - π]^2, 1]) / (Cos[θ - π] + 1);
(* equation (5.16) *)

(* exemplaric hyperfine field distribution for the determination
 of the fraction of overbarrier fluctuations (see equation (5.19): *)

EintIntt = {{1/100, 2.375614901330802`}, {1/50, 2.450269313872323`},
   {3/100, 2.527814515041478`}, {1/25, 2.6083831203401635`}, {1/20, 2.6921147990466556`},
   {3/50, 2.7791567023913233`}, {7/100, 2.869663921010482`}, {2/25, 2.9637999739079133`},
   {9/100, 3.061737331340637`}, {1/10, 3.163657974249702`}, {11/100, 3.2697539930798936`},
   {3/25, 3.380228290757213`}, {13/100, 3.495294961407656`}, {7/50, 3.6151806437740355`},
   {3/20, 3.7401246944428927`}, {4/25, 3.870380344047569`}, {17/100, 4.006215545832553`},
   {9/50, 4.147913953465874`}, {19/100, 4.295775971994719`}, {1/5, 4.450119888026129`},
   {21/100, 4.6112830857697436`}, {11/50, 4.7796233561889485`}, {23/100, 4.955520307177187`},
   {6/25, 5.139376883413096`}, {1/4, 5.3316210053590325`}, {13/50, 5.532707337760586`},
```

```
{3/10, 6.435615441529535`}, {31/100, 6.688811475997041`}, {8/25, 6.954257791561546`},
{33/100, 7.232659338226325`}, {17/50, 7.524768239172187`}, {7/20, 7.8313873915578505`},
{9/25, 8.153374375056126`}, {37/100, 8.491645696975986`}, {19/50, 8.847181405709557`},
{39/100, 9.221030107428234`}, {2/5, 9.614314424461433`}, {41/100, 10.028236937653622`},
{21/50, 10.464086659243316`}, {43/100, 10.923246087469494`}, {11/25, 11.407198899222603`},
{9/20, 11.917538342642786`}, {23/50, 12.455976397660429`}, {47/100, 13.024353779088244`},
{12/25, 13.624650864025948`}, {49/100, 14.258999633023516`}, {1/2, 14.929696722644293`},
{51/100, 15.639217695721849`}, {13/25, 16.390232644619335`}, {53/100, 17.18562325202223`},
{27/50, 18.02850144298911`}, {11/20, 18.92222977080092`}, {14/25, 19.87044368708228`},
{57/100, 20.877075853001255`}, {29/50, 21.946382652081482`}, {59/100, 23.08297306487373`},
{3/5, 24.291840059492127`}, {61/100, 25.57839463712914`}, {31/50, 26.94850264443102`},
{63/100, 28.408524419940235`}, {16/25, 29.96535727269913`}, {13/20, 31.626480687925202`},
{33/50, 33.40000400413228`}, {67/100, 35.29471608987072`}, {17/25, 37.32013624102599`},
{69/100, 39.48656508615354`}, {7/10, 41.80513367859586`}, {71/100, 44.287848101525675`},
{18/25, 46.94762571919644`}, {73/100, 49.79831753842296`}, {37/50, 52.85470880536664`},
{3/4, 56.13248667796512`}, {19/25, 59.64815918695731`}, {77/100, 63.4189031540953`},
{39/50, 67.46230943766979`}, {79/100, 71.79598059347329`}, {4/5, 76.43691695384234`},
{81/100, 81.40059952221065`}, {41/50, 86.69963786765858`}, {83/100, 92.3417921790141`},
{21/25, 98.32709130888003`}, {17/20, 104.6436383755684`}, {43/50, 111.26149962185494`},
{87/100, 118.12377552257266`}, {22/25, 125.13350103054859`}, {89/100, 132.13433114313924`},
{9/10, 138.88191684853226`}, {91/100, 145.0013049693384`}, {23/25, 149.9234600789209`},
{93/100, 152.79125234137175`}, {47/50, 152.32349827181613`}, {19/20, 146.63192069161678`},
{24/25, 133.0290653844613`}, {97/100, 108.06393394791505`}, {49/50, 68.89035980672992`},
{99/100, 20.847492983134718`}, {1, 1.9520847163767778`*^-28}};
EintInt = Interpolation[EintIntt];
EintFun1[O_] := If[0.01 < O < 0.99, EintInt[O], 0]
```

```
EintIntt2 = Table[0, {i, 100}, {j, 2}];
For[i = 1, i < 101, i++,
 EintIntt2[[i, 1]] = i / 100;
 EintIntt2[[i, 2]] = ΔEint[1, i / 100, kKV1, kkT]]

FF2 = FindFit[EintIntt2, { EintFun1[x / c + b] * a, {0.5 < a < 19.8},
    {0.05 < b < 0.8}, {1 < c < 4.9}}, {a, b, c}, x]                    (* Fitting *)

Show[ListPlot[EintIntt2], Plot[EintFun1[x / c + b] * a /. FF2, {x, 0, 1}]]

FracCollExc = NIntegrate[EintFun1[x / c + b] * a /. FF2, {x, 0, 1}] /
              NIntegrate[EintFun1[x / c + b] * a /. FF2, {x, -1000, 1}]
```

(Debug) Out[123]=

```
{a → 1.03369, b → 0.249946, c → 1.34303}
```

(Debug) Out[124]=

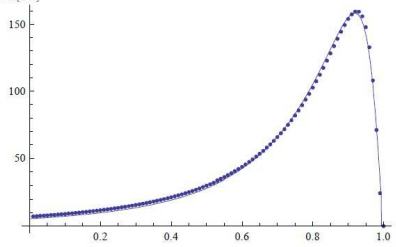

NIntegrate::slwcon :

Numerical integration converging too slowly; suspect one of the following: singularity, value of the integration is 0, highly oscillatory integrand, or WorkingPrecision too small. ≫

(Debug) Out[125]=

```
0.975898
```

(Debug) In[126]=

```
f[x_, s_, t_] := 1/π * s / (s^2 + (x - t)^2)

MS[x_, s_, t_, q_] :=
 -(f[x, s, t + q] + f[x, s, -t + q] + 2/3 f[x, s, 0.579 * (t - q)] + 2/3 f[x, s, -0.579 * (t - q)] +
    1/3 f[x, s, 0.158 * (t - q)] + 1/3 f[x, s, -0.158 * (t - q)])

(* standard Mössbauer spectrum *)

MSV[x_] := Sum[MS[x, 0.35, i / 3, 0] * ΔEint[9, i / 3, 0.6, 0.1], {i, 33}]

τ[τ0_, Eb_, kT_] := τ0 * Exp[Eb / kT]

SphRel[τ0_, Eb_, kT_, Γ_, ω1_, ω_] :=
 -Re[(0.25 (1 / (i * (ω + ω1) + Γ/2 + 1/τ[τ0, Eb, kT]) + 0.66 / (i * (ω + 0.5790 * ω1) + Γ/2 + 1/τ[τ0, Eb, kT]) +
    0.33 / (i * (ω + 0.1580 * ω1) + Γ/2 + 1/τ[τ0, Eb, kT]) + 0.33 / (i * (ω - 0.1580 * ω1) + Γ/2 + 1/τ[τ0, Eb, kT]) +
```

$$\frac{0.66}{\dot{\imath}*(\omega-0.5790*\omega 1)+\frac{\Gamma}{2}+\frac{1}{\tau[\tau 0,Eb,kT]}}+\frac{1}{\dot{\imath}*(\omega-\omega 1)+\frac{\Gamma}{2}+\frac{1}{\tau[\tau 0,Eb,kT]}}\Bigg)\Bigg)\Bigg/$$

$$\left(1-\frac{1}{\tau[\tau 0,\,Eb,\,kT]}*0.25*\left(\frac{1}{\dot{\imath}*(\omega+\omega 1)+\frac{\Gamma}{2}+\frac{1}{\tau[\tau 0,Eb,kT]}}+\frac{0.66}{\dot{\imath}*(\omega+0.5790*\omega 1)+\frac{\Gamma}{2}+\frac{1}{\tau[\tau 0,Eb,kT]}}+\right.\right.$$

$$\frac{0.33}{\dot{\imath}*(\omega+0.1580*\omega 1)+\frac{\Gamma}{2}+\frac{1}{\tau[\tau 0,Eb,kT]}}+\frac{0.33}{\dot{\imath}*(\omega-0.1580*\omega 1)+\frac{\Gamma}{2}+\frac{1}{\tau[\tau 0,Eb,kT]}}+$$

$$\left.\left.\frac{0.66}{\dot{\imath}*(\omega-0.5790*\omega 1)+\frac{\Gamma}{2}+\frac{1}{\tau[\tau 0,Eb,kT]}}+\frac{1}{\dot{\imath}*(\omega-\omega 1)+\frac{\Gamma}{2}+\frac{1}{\tau[\tau 0,Eb,kT]}}\right)\right)\Bigg]$$

```
SphRelVert[τ0_, kT_, KV_, Γ_, ω1_, ω_] := OBF/(OBF + 0.000001) * SphRel[τ0, KV, kT, Γ, ω1, ω] +
  OBF/(OBF + 0.000001) * NIntegrate[ΔEintx[x] * SphRel[τ0, x, kT, Γ, ω1, ω],
    {x, KV + 0.0001, kT - 0.0001}] (* spuerical relaxation *)

ττ0 = 0.0005;
ΔE = 0.56;          (* Further parameters *)
q = 0;

(* Combining the different two contribution *)


SphRelVertMW[τ0_, kT_, ΔE_, Γ_, ω1_, ω_] := SphRel[τ0, ΔE, kT, Γ, ω1, ω]

SpekGes[τ0_, kT_, KV_, Γ_, ω1_, ω_, q_] :=
 (1 - OBF) (Sum[(MS[ω, Γ, i / 4.16, q] * ΔEint[ω1, i / 4.16, KV, kT]), {i, 1, 50}]) +
  OBF * SphRelVertMW[τ0, kT, KV, Γ, ω1, ω]
SpekGes1[τ0_, kT_, KV_, Γ_, ω1_, ω_, q_] :=
 (Sum[(MS[ω, Γ, i / 4.16, q] * ΔEint[ω1, i / 4.16, KV, kT]), {i, 1, 50}])
SpekGes2[τ0_, kT_, KV_, Γ_, ω1_, ω_] := SphRelVertMW[τ0, kT, KV, Γ / 2, ω1, ω]
Frac1 = 0.8;
Frac2 = 1 - Frac1;

OBF = 1 - FracCollExc;


PlotSpekF = Table[0, {i, 200}, {j, 2}];
PlotSpekF1 = Table[0, {i, 200}, {j, 2}];
PlotSpekF2 = Table[0, {i, 200}, {j, 2}];

PlotSpekFF = Table[0, {i, 200}, {j, 2}];
PlotSpekFF1 = Table[0, {i, 200}, {j, 2}];
PlotSpekFF2 = Table[0, {i, 200}, {j, 2}];

PlotSpekFFF = Table[0, {i, 200}, {j, 2}];

For[i = 1, i < 201, i++,
```

6 | AgFe.nb

```
 PlotSpekF[[i, 1]] = (i - 100)/12.0;
 PlotSpekF1[[i, 1]] = PlotSpekF[[i, 1]];
 PlotSpekF2[[i, 1]] = PlotSpekF[[i, 1]];
 PlotSpekFF[[i, 1]] = PlotSpekF[[i, 1]];
 PlotSpekFF1[[i, 1]] = PlotSpekF[[i, 1]];
 PlotSpekFF2[[i, 1]] = PlotSpekF[[i, 1]];
 PlotSpekFFF[[i, 1]] = PlotSpekF[[i, 1]];
]

For[i = 1, i < 201, i++,
 PlotSpekF1[[i, 2]] = SpekGes1[rr0, kkT, kKV1, 0.24, 6, (i - 100)/12.0 + 0.0965, q];
 PlotSpekF2[[i, 2]] = SpekGes2[rr0, kkT, ΔE, 0.24, 6, (i - 100)/12.0 + 0.0965];
]

For[i = 1, i < 201, i++,
 PlotSpekFF1[[i, 2]] = SpekGes1[rr0, kkT, kKV2, 0.24, 6.55, (i - 100)/12.0 - 0.09081, q];
 PlotSpekFF2[[i, 2]] = SpekGes2[rr0, kkT, ΔE, 0.24, 6.55, (i - 100)/12.0 - 0.09081];
]

VorFak1 = Σ_{i=1}^{200} PlotSpekF1[[i, 2]] / Σ_{i=1}^{200} (PlotSpekF1[[i, 2]] + PlotSpekFF1[[i, 2]]);

VorFak2 = Σ_{i=1}^{200} PlotSpekF2[[i, 2]] / Σ_{i=1}^{200} (PlotSpekF1[[i, 2]] + PlotSpekFF1[[i, 2]]);

Effect = 0.00000775;

For[i = 1, i < 201, i++,
 PlotSpekF1[[i, 2]] = (1/VorFak1 * (1 - OBF) * PlotSpekF1[[i, 2]]) * Effect + Σ_{i=1}^{10} F922[[i, 2]]/10;
 PlotSpekF2[[i, 2]] = (1/VorFak2 * (OBF) * PlotSpekF2[[i, 2]]) * Effect + Σ_{i=1}^{10} F922[[i, 2]]/10;
 PlotSpekF[[i, 2]] =
  Frac1 * ((PlotSpekF1[[i, 2]] + PlotSpekF2[[i, 2]] - 2 * Σ_{i=1}^{10} F922[[i, 2]]/10)) + Σ_{i=1}^{10} F922[[i, 2]]/10;
]

For[i = 1, i < 201, i++,
 PlotSpekFF1[[i, 2]] = (1/VorFak1 * (1 - OBF) * PlotSpekFF1[[i, 2]]) * Effect + Σ_{i=1}^{10} F922[[i, 2]]/10;
 PlotSpekFF2[[i, 2]] = (1/VorFak2 * (OBF) * PlotSpekFF2[[i, 2]]) * Effect + Σ_{i=1}^{10} F922[[i, 2]]/10;
 PlotSpekFF[[i, 2]] = Frac2 *
```

```
    ((PlotSpekFF1[[i, 2]] + PlotSpekFF2[[i, 2]] - 2 * Sum_{i=1}^{10} F922[[i, 2]]/10)) + Sum_{i=1}^{10} F922[[i, 2]]/10;
]

For[i = 1, i < 201, i++,
 PlotSpekFFF[[i, 2]] = PlotSpekFF[[i, 2]] + PlotSpekF[[i, 2]] - Sum_{i=1}^{10} F922[[i, 2]]/10;
]

GraphicsGrid[
 {{Show[ListPlot[F922, AxesLabel → {"v (mm/s)", "Absorption"}, PlotLabel → {kKV1, kKV2 ,
       Frac1, τt0, kkT, R, Mom}], ListPlot[{PlotSpekFFF, PlotSpekF, PlotSpekFF},
     PlotRange → Full , AxesLabel → {"v (mm/s)", "Absorption"},
     Joined → {True, True, True, False}, PlotStyle → {{Darker[Blue, 0.25], Thick},
       Darker[Magenta, 0.5], Darker[Magenta, 0.5], Black}]]},
  {Plot[ΔEint[1, x, kKV1, kkT], {x, 0, 1}, AxesLabel → {"B_hyp (normiert)", "ΔB_hyp"},
    PlotRange → Full]}}]
```

(Debug) Out[158]=

{0.01, 0.01, 0.8, 0.0005, 0.4, 0.037, 0.00048}

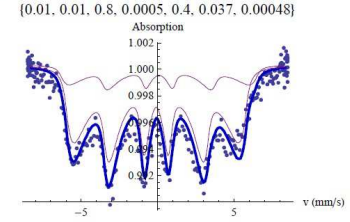

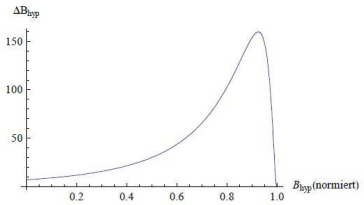

A.2 DC-susceptibility

A.2.1 ZFC/FC curves

This is a simulation after a model of Tournus *et al.* [90].

```
(Debug) In[176]:= (* after equation (1) and (5) Tournus and Tamion, JMMM 323 (2011) *)

(Debug) In[177]:= (* the PSD is given in nm and not in m,
                  since the calculated values get too small for Mathematica otherwise *)
                  (* all other parameters have to be adjusted with m --> nm *)

(Debug) In[178]:= (* PSD: *)

(Debug) In[179]:= ρD[μ_, σ_, D_] := PDF[NormalDistribution[μ, σ], D]
                  (* Plot[ρD[4,0.8,x],{x,0,10}] *)

(Debug) In[180]:= (* PVD: *)

(Debug) In[181]:= μμ = 4;
                  σσ = 0.8;
                  ρV1 = Table[0, {i, 1000}, {j, 2}];
                  For[i = 1, i < 1001, i++,
                   ρV1[[i, 1]] = 4/3 π * (i / 200)^3;
                   ρV1[[i, 2]] = ρD[μμ, σσ, i / 100]]
                  FF = FindFit[ρV1, a * PDF[NormalDistribution[μ, σ], 3/(4 π) ∛x], {a, μ, σ}, x];
                  (* Show[ListPlot[ρV1, PlotRange→Full],
                   Plot[a*PDF[NormalDistribution[μ,σ], 3/(4π) ∛x]/.FF,
                    {x,0,3000}, PlotRange→Full, PlotStyle→{Thick, Red}]] *)
                  ρV[x_] := a * PDF[NormalDistribution[μ, σ], 3/(4 π) ∛x] /. FF

(Debug) In[187]:= (* Definition of parameters and the equations *)

(Debug) In[188]:= kB = 1.3 * 10^-5; (* m → nm *)
                  μ0 = 4 * π * 10^2;  (* m → nm *)
                  ϒ[ν0_, νT_, T_] := 0.9609 * Log[ν0 * T / νT] - 1.629
                  Vlim[ν0_, νT_, Keff_, T_] := ϒ[ν0, νT, T] * kB * T / Keff
                  Vav1[μ_, σ_] := Exp[μ - σ^2]
                  α[ν0_, Keff_, νT_, μ_, σ_] := 0.9283 * Log[ν0 * Keff * Vav1[μ, σ] / (kB * νT)] - 3.69
                  MFC[HMs_, Keff_, ν0_, νT_, μ_, σ_, T_] :=
                   μ0 * HMs / (3 * kB * T) NIntegrate[V^2 * ρV[V], {V, 0, Vlim[ν0, νT, Keff, T]}, MaxRecursion → 12] +
                    μ0 * HMs / (3 * Keff) NIntegrate[α[ν0, Keff, νT, μ, σ] * V * ρV[V],
                      {V, Vlim[ν0, νT, Keff, T], 1 000 000}, MaxRecursion → 12]
                  MZFC[HMs_, Keff_, ν0_, νT_, μ_, σ_, T_] :=
                   μ0 * HMs / (3 * kB * T) NIntegrate[V^2 * ρV[V], {V, 0, Vlim[ν0, νT, Keff, T]}, MaxRecursion → 12] +
                    μ0 * HMs / (3 * Keff) NIntegrate[V * ρV[V], {V, Vlim[ν0, νT, Keff, T], 1 000 000}, MaxRecursion → 12]
```

2 | Code_ZFC_FC_Tournus et al.nb

(Debug) In[195]:=
```
(* Plot parameter, SI units *)
KeffSI = 20; (* kJ/nm³*)
vTSI1 = 0.05; (* K/min *)
v0 = 10^10;(* Hz *)

(* Conversion factors *)
UFakJeV = 1/(1.6022 * 10^(-19));   (* J in eV *)
UFakmnm = 10^9;  (* m in nm *)
UFakms = 60;  (* min in s *)

Keff = KeffSI * 1000 * UFakJeV / UFakmnm^3;

vT = vTSI * 1/UFakms;
```

(Debug) In[198]:=
```
Plot[{MFC[1, Keff, v0, vT, 4, 0.8, T], MZFC[1, Keff, v0, vT, 4, 0.8, T]}, {T, 0, 80},
 PlotRange → {0, All}, Frame → True, FrameLabel → {"T(K)", "χ (arb. units)"}]
```

(Debug) Out[198]=

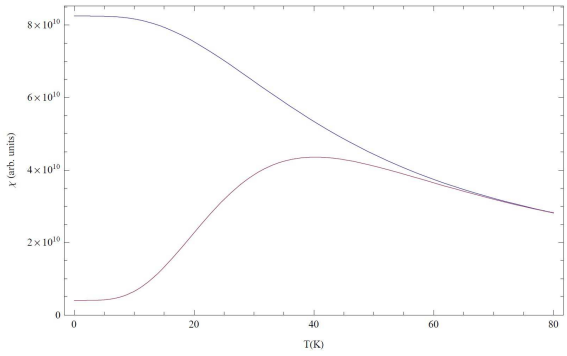

A.2.2 $M(H)$ curves of particles with a paramagnetic shell

The following code is based on Chen *et al.* [95].

```
(Debug) In[54]:= Off[Solve::ratnz]

(Debug) In[55]:= (* Volume of core and shell (δ is the thickness of the shell) *)
                 Vc[V_?NumericQ, δ_?NumericQ] :=
                  N[If[∛(3/(4 π)) * V * 2 < 2 * δ, 0, (π * (∛(3/(4 π)) * V * 2 - 2 * δ)^3)/6]]
                 Vs[V_?NumericQ, δ_?NumericQ] := V - Vc[V, δ]
                 L[x_] := 1/Tanh[x] - 1/x

(Debug) In[58]:= (* 1. model of Chen et al, JAP 105 (2009);
                 the sum below the integral has to be split,
                 otherwise Mathematica can't solve it. *)

(Debug) In[59]:= M[M0_, μ0_, Ms_, δ_, H_, χp_, kBT_] :=
                  M0 * (NIntegrate[ρV[V] (Ms * Vc[V, δ]/V * L[(Ms * Vc[V, δ] * H)/kBT]),
                      {V, 0, 100 000}, MaxRecursion → 120] +
                    NIntegrate[(ρV[V] * (Vs[V, δ]/V * χp))/μ0 * H, {V, 0, 100 000}, MaxRecursion → 120])

(Debug) In[60]:= σσ = 0.261;
                 μμ = 1.447;
                 ρr[r_] := PDF[LogNormalDistribution[μμ, σσ], r];
                 ρV[V_] := ρr[∛(3/(4 π)) * (V)]

(Debug) In[64]:= (* Plot[{ρr[V],ρV[V]},{V,0,100}, PlotRange→Full] *)

(Debug) In[65]:= (* maximum of distribution *)

(Debug) In[66]:= Vm = Last[Last[Last[Solve[∂_V ρV[V] == 0, V]]]]

(Debug) Out[66]= 262.185

(Debug) In[67]:= (* parameter in units of nm *)
                 χp = 0.09;
                 μ0 = 4 * π * 10^2;
                 Ms = 0.4 / μ0;
                 kB = 1.38 * 10^-5;
                 kBT = kB * 250;
                 δ = 0.475;
                 Plot[1 * M[1, μ0, Ms, χp, x, δ, kBT]/M[1, μ0, Ms, χp, 5, δ, kBT], {x, -5, 5}, PlotStyle → {Red, Thick},
                  Frame → True, FrameLabel → {"H (T)", "M (arb. units)"}]
```

2 | Code_Chen_etal.nb

(Debug) Out[73]=

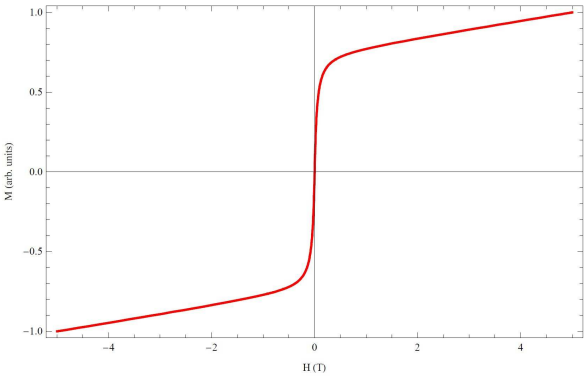

Bibliography

[1] http://www.britishmuseum.org/explore/highlights/highlight_objects/pe_mla/t/the_lycurgus_cup.aspx. 08.01.2014.

[2] M. F. Ashby, P. J. Ferreira, D. L. Schodek. Nanomaterials, Nanotechnologies and Design: An Introduction for Engineers and Architects. Butterworth-Heinemann. See p. 30 (2009).

[3] M. Faraday. The Bakerian Lecture: Experimental Relations of Gold (and Other Metals) to Light. Philosophical Transactions of the Royal Society of London **147**, 145181 (1857).

[4] J. Frenkel, J. Dorfman. Spontaneous and induced magnetisation in ferromagnetic bodies. Nature **126**, 274275 (1930).

[5] S. Nie, *et al.* Nanotechnology Applications in Cancer. Annual Review of Biomedical Engineering **9**, 257288 (2007).

[6] L. Brannon-Peppas, J. O. Blanchette. Nanoparticle and targeted systems for cancer therapy. Advanced Drug Delivery Reviews **64**, 206212 (2012).

[7] J. Dormann, *et al.* From pure superparamagnetism to glass collective state in γ-Fe_2O_3 nanoparticle assemblies. Journal of Magnetism and Magnetic Materials **203**, 2327 (1999).

[8] G. F. Goya. Handling the particle size and distribution of Fe_3O_4 nanoparticles through ball milling. Solid State Communications **130**, 783787 (2004).

[9] G. F. Goya, E. R. Leite. Ferrimagnetism and spin canting of $Zn^{57}Fe_2O_4$ nanoparticles embedded in ZnO matrix. Journal of Physics: Condensed Matter **15**, 641 (2003).

[10] S. Blundell. Magnetism in Condensed Matter. Oxford University Press (2008).

[11] S. Mørup, E. Tronc. Superparamagnetic relaxation of weakly interacting particles. Physical Review B **72**, 32783281 (1994).

[12] L. Néel. Théorie du traînage magnétique des ferromagnétiques en grains fins avec applications aux terres cuites. Annales de géophysique **5**, 99136 (1949).

[13] W. F. Brown. Thermal Fluctuations of a Single-Domain Particle. Physical Review **130**, 16771686 (1963).

[14] N. A. Frey. Surface and interface magnetism in nanostructures and thin films. Graduate School Theses and Dissertations. (2008).

[15] G. Gubbiotti, G. Carlotti, B. Hillebrands. Spin waves and magnetic anisotropy in ultrathin (111)-oriented cubic films. Journal of Physics: Condensed Matter **10**, 2171 (1998).

[16] L. Landau, E. Lifshitz, L. Pitaevski. Electrodynamics of Continuous Media. Elsevier (1984).

[17] J. Osborn. Demagnetizing Factors of the General Ellipsoid. Physical Review **67**, 351357 (1945).

[18] S. Mørup, J. A. Dumesic, H. Topsoe. Applications of Mössbauer Spectroscopy Vol. II. Academic Press (1980).

[19] R. Yanes, *et al.* Temperature dependence of the effective anisotropies in magnetic nanoparticles with Néel surface anisotropy. Journal of Physics D: Applied Physics **43**, 474009 (2010).

[20] B. M. Moskowitz. Hitchhiker's Guide to Magnetism. Environmental Magnetism Workshop. `http://www.irm.umn.edu/hg2m/hg2m_c/hg2m_c.html` (1991).

[21] F. Bødker, S. Mørup, S. Linderoth. Surface effects in metallic iron nanoparticles. Physical Review Letters **72**, 282285 (1994).

[22] F. Luis, *et al.* Enhancement of the magnetic anisotropy of nanometer-sized Co clusters: Influence of the surface and of interparticle interactions. Physical Review B **65**, 094409 (2002).

[23] S. Mørup, *et al.* A new interpretation of Mössbauer spectra of microcrystalline goethite: "Super-ferromagnetism" or "super-spin-glass" behaviour? Journal of Magnetism and Magnetic Materials **40**, 163174 (1983).

[24] M. F. Hansen, C. B. Koch, S. Mørup. Magnetic dynamics of weakly and strongly interacting hematite nanoparticles. Physical Review B **62**, 11241135 (2000).

[25] J. Alonso, *et al.* Crossover from superspin glass to superferromagnet in Fe_xAg_{100-x} nanostructured thin films ($20 \leq x \leq 50$). Physical Review B **82**, 054406 (2010).

[26] G. M. Genkin, M. V. Sapozhnikov. Ruderman-Kittel-Kasuya-Yosida interaction between zero-dimensional and one-dimensional ferromagnetic inclusions in a matrix of nonmagnetic metal. Applied Physics Letters **64**, 794796 (1994).

[27] P. Prene, *et al.* Magnetic properties of isolated γ-Fe_2O_3 particles. IEEE Transactions on Magnetics **29**, 26582660 (1993).

[28] W. T. Coffey, *et al.* Exact analytic formula for the correlation time of a single-domain ferromagnetic particle. Physical Review E **49**, 18691882 (1994).

[29] J. van Lierop, D. H. Ryan. Mössbauer spectra of single-domain fine particle systems described using a multiple-level relaxation model for superparamagnets. Physical Review B **63**, 064406 (2001).

[30] W. Coffey, *et al.* Simple approximate formulae for the magnetic relaxation time of single domain ferromagnetic particles with uniaxial anisotropy. Journal of Magnetism and Magnetic Materials **131**, 301303 (1994).

[31] J. L. Dormann, L. Bessais, D. Fiorani. A dynamic study of small interacting particles: superparamagnetic model and spin-glass laws. Journal of Physics C: Solid State Physics **21**, 2015 (1988).

[32] J. L. Dormann, *et al.* Thermal variation of the relaxation time of the magnetic moment of γ-Fe_2O_3 nanoparticles with interparticle interactions of various strengths. Physical Review B **53**, 1429114297 (1996).

[33] J. Jiang, *et al.* Effect of inter-particle interactions on the superparamagnetic relaxation time in ferrofluids. Proceedings of the ICAME'95 529 (1995).

[34] M. Hansen, S. Mørup. Models for the dynamics of interacting magnetic nanoparticles. Journal of Magnetism and Magnetic Materials **184**, 262274 (1998).

[35] A. E. Berkowitz, W. J. Schuele, P. J. Flanders. Influence of Crystallite Size on the Magnetic Properties of Acicular γ-Fe_2O_3 Particles. Journal of Applied Physics **39**, 12611263 (1968).

[36] J. M. D. Coey. Noncollinear Spin Arrangement in Ultrafine Ferrimagnetic Crystallites. Physical Review Letters **27**, 11401142 (1971).

[37] A. J. Morrish, K. Haneda, P. Schurer. Surface magnetic structure of small γ-Fe_2O_3 particles. Journal Physiques Colloques **37**, 301305 (1976).

[38] F. T. Parker, *et al.* Spin canting, surface magnetization, and finite-size effects in γ-Fe_2O_3 particles. Physical Review B **47**, 78857891 (1993).

[39] D. Lin, *et al.* Polarized neutron study of the magnetization density distribution within a $CoFe_2O_4$ colloidal particle II. Journal of Magnetism and Magnetic Materials **145**, 343348 (1995).

[40] B. Martínez, *et al.* Low Temperature Surface Spin-Glass Transition in γ-Fe_2O_3 Nanoparticles. Physical Review Letters **80**, 181184 (1998).

[41] R. H. Kodama, *et al.* Surface spin disorder in ferrite nanoparticles (invited). Journal of Applied Physics **81**, 55525557 (1997).

[42] M. Sousa, *et al.* $NiFe_2O_4$ nanoparticles in ferrofluids: evidence of spin disorder in the surface layer. Journal of Magnetism and Magnetic Materials **242-245**, 572574 (2002).

[43] T. Kim, M. Shima. Reduced magnetization in magnetic oxide nanoparticles. Journal of Applied Physics **101**, 09M516 (2007).

[44] A. Morrish, K. Haneda. Surface magnetic properties of fine particles. Journal of Magnetism and Magnetic Materials **35**, 105113 (1983).

[45] M. Darbandi, *et al.* Nanoscale size effect on surface spin canting in iron oxide nanoparticles synthesized by the microemulsion method. Journal of Physics D: Applied Physics **45**, 195001 (2012).

[46] R. H. Kodama, A. E. Berkowitz. Atomic-scale magnetic modeling of oxide nanoparticles. Physical Review B **59**, 63216336 (1999).

[47] E. Tronc, *et al.* Surface-related properties of γ-Fe_2O_3 nanoparticles. Journal of Magnetism and Magnetic Materials **221**, 6379 (2000).

[48] E. J. W. Verwey. Electronic Conduction of Magnetite (Fe_3O_4) and its Transition Point at Low Temperatures. Nature **144**, 327328 (1939).

[49] F. Walz. The Verwey transition - a topical review. Journal of Physics: Condensed Matter **14**, 285 (2002).

[50] G. F. Goya, *et al.* Static and dynamic magnetic properties of spherical magnetite nanoparticles. Journal of Applied Physics **94**, 35203528 (2003).

[51] I. Dezsi, *et al.* Phase transition in nanomagnetite. Journal of Applied Physics **103**, 104312104315 (2008).

[52] E. Verwey. The crystal structure of γ-Fe_2O_3 and γ-Al_2O_3. Zeitschrift für Kristallographie **91**, 65 (1935).

[53] G. Hägg, G. Söderholm. Die Kristallstrukturen von Mg-Al-Spinellen mit Al_2O_3-Überschuss und γ-Al_2O_3. Zeitschrift für physikalische Chemie **29**, 95 (1935).

[54] R. Haul, T. Schoon. Zur Struktur des ferromagnetischen Eisen (III)-Oxyds γ-Fe_2O_3. Zeitschrift für physikalische Chemie **44**, 216 (1939).

[55] P. Braun. A Superstructure in Spinels. Nature **170**, 1123 (1952).

[56] R. Grau-Crespo, *et al.* Vacancy ordering and electronic structure of γ-Fe_2O_3 (maghemite): a theoretical investigation. Journal of Physics: Condensed Matter **22**, 255401 (2010).

[57] T. Bastow, *et al.* Vacancy ordering in γ-Fe_2O_3 nanocrystals observed by ^{57}Fe NMR. Journal of Magnetism and Magnetic Materials **321**, 26772681 (2009).

[58] Z. Somogyváari, *et al.* Vacancy ordering in nanosized maghemite from neutron and X-ray powder diffraction. Applied Physics A **74**, 10771079 (2002).

[59] K. Spiers, *et al.* The Mössbauer Spectrum of Maghemite with Ordered Vacancies. 28th Annual Condensed Matter and Materials Meeting (2004).

[60] K. Haneda, A. H. Morrish. Magnetite to maghemite transoformation in ultrafine particles. Journal Physiques Colloques **38**, 321323 (1977).

[61] D. L. A. de Faria, S. Venâncio Silva, M. T. de Oliveira. Raman microspectroscopy of some iron oxides and oxyhydroxides. Journal of Raman Spectroscopy **28**, 873878 (1997).

[62] K.-C. Kim, *et al.* Characterization of magnetic nanoparticles synthesized by sonomechanical method. Nanotechnology Materials and Devices Conference **1**, 600601 (2006).

[63] L. Minati, *et al.* Application of factor analysis to {XPS} valence band of superparamagnetic iron oxide nanoparticles. Applied Surface Science **257**, 1086310868 (2011).

[64] A. Lak, *et al.* Highly stable monodisperse PEGylated iron oxide nanoparticle aqueous suspensions: a nontoxic tracer for homogeneous magnetic bioassays. Nanoscale **5**, 1144711455 (2013).

[65] A. Lak, *et al.* Size dependent structural and magnetic properties of FeO-Fe_3O_4 nanoparticles. Nanoscale **5**, 1228612295 (2013).

[66] F. Bodker, *et al.* Mossbauer studies of ultrafine iron-containing particles on a carbon support. Journal of Physics: Condensed Matter **4**, 6555 (1992).

[67] W. T. Herrera, *et al.* Kondo effect and spin-glass behavior of dilute iron clusters in silver films. Physical Review B **84**, 014430 (2011).

[68] W. T. Herrera. Nanoclusters magnéticos em Filmes Metálicos não Magnéticos (Fe/Ag) e Supercondutores (Co/Bi). Ph.D. thesis, Centro Brasileira de Pesquisas Físicas (2011).

[69] W. Herrera, *et al.* Aggregates of iron in ytterbium films. Hyperfine Interactions **203**, 143147 (2011).

[70] W. Herrera, *et al.* Magnetic dynamics of dilute iron nano-clusters in silver films from Mössbauer spectroscopy and muon spin rotation. Hyperfine Interactions **203**, 149153 (2011).

[71] C. Rojas-Ayala, *et al.* Iron nano-clusters in ytterbium films: a ^{57}Fe Mössbauer spectroscopic study. Hyperfine Interactions **224** (2013).

[72] C. Rojas-Ayala. tba. Ph.D. thesis, CBPF, Rio de Janeiro, Brasil. In preparation (2013).

[73] O. Margeat, *et al.* Ultrafine metallic Fe nanoparticles: synthesis, structure and magnetism. Beilstein Journal of Nanotechnology **1**, 108118 (2010).

[74] V. Šepelák, *et al.* Nanocrystalline Nickel Ferrite, $NiFe_2O_4$: Mechanosynthesis, Nonequilibrium Cation Distribution, Canted Spin Arrangement, and Magnetic Behavior. The Journal of Physical Chemistry C **111**, 50265033 (2007).

[75] V. Šepelák, *et al.* A One-Step Mechanochemical Route to Core-Shell Ca_2SnO_4 Nanoparticles Followed by ^{119}Sn MAS NMR and ^{119}Sn Mössbauer Spectroscopy. Chemistry of Materials **21**, 25182524 (2009).

[76] R. L. Mössbauer. Kernresonanzfluoreszenz von Gammastrahlung in Ir^{191}. Zeitschrift für Physik **151** (1958).

[77] M. Kalvius, P. Kienle, editors. The Rudolf Mössbauer story. Springer (2012).

[78] D. Barb. Grundlagen und Anwendungen der Mössbauerspektroskopie. Akademie-Verlag (1980).

[79] G. Schatz, A. Weidinger, M. Deicher. Nukleare Festkörperphysik. Vieweg+Teubner (2010).

[80] S. Ofer, I. Nowik, S. Cohen. Chemical applications of Mössbauer spectroscopy. Academic Press (1968).

[81] H. Wickman, M. Klein, D. Shirley. Paramagnetic Hyperfine Structure and Relaxation Effects in Mössbauer Spectra: ^{57}Fe in Ferrichrome A†*. Physical Review **152**, 345357 (1966).

[82] D. Barb. Grundlagen und Anwendungen der Mössbauerspektroskopie. Akademie-Verlag Berlin (1980).

[83] A. Afanas'ev, M. Chuev. New relaxation model for superparamagnetic particles in Mössbauer spectroscopy. Journal of Experimental and Theoretical Physics Letters **74**, 107110 (2001).

[84] S. Dattagupta. Study of time-dependent hyperfine interactions by PAC, Mössbauer effect, μSR and NMR: A review of stochastic models. Hyperfine Interactions **11**, 77126 (1981).

[85] M. Blume, J. A. Tjon. Mössbauer Spectra in a Fluctuating Environment. Physical Review **165**, 446456 (1968).

[86] D. H. Jones, K. K. P. Srivastava. Many-state relaxation model for the Mössbauer spectra of superparamagnets. Physical Review B **34**, 75427548 (1986).

[87] A. Amulevicius, *et al.* A study of the magnetic properties of mixed ferrite nanoparticles in ferrofluids. Journal of Molecular Liquids **133**, 152158 (2007).

[88] M. A. Chuev. Multi-level relaxation model for describing the Mössbauer spectra of single-domain particles in the presence of quadrupolar hyperfine interaction. Journal of Physics: Condensed Matter **23**, 426003 (2011).

[89] S. Mørup. Magnetic hyperfine splitting in mössbauer spectra of microcrystals. Journal of Magnetism and Magnetic Materials **37**, 3950 (1983).

[90] F. Tournus, A. Tamion. Magnetic susceptibility curves of a nanoparticle assembly II. Simulation and analysis of ZFC/FC curves in the case of a magnetic anisotropy energy distribution. Journal of Magnetism and Magnetic Materials **323**, 11181127 (2011).

[91] H. T. Yang, *et al.* Achieving a noninteracting magnetic nanoparticle system through direct control of interparticle spacing. Applied Physics Letters **94**, 013103 (2009).

[92] R. Chantrell, M. El-Hilo, K. O'Grady. Spin-glass behavior in a fine particle system. IEEE Transactions on Magnetics **27**, 35703578 (1991).

[93] F. Wiekhorst, *et al.* Anisotropic superparamagnetism of monodispersive cobalt-platinum nanocrystals. Physical Review B **67**, 224416 (2003).

[94] H. M. Lu, W. T. Zheng, Q. Jiang. Saturation magnetization of ferromagnetic and ferrimagnetic nanocrystals at room temperature. Journal of Physics D: Applied Physics **40**, 320 (2007).

[95] D.-X. Chen, *et al.* Size determination of superparamagnetic nanoparticles from magnetization curve. Journal of Applied Physics **105**, 083924 (2009).

[96] M. M. Can, T. Firat, S. Özcan. Interparticle interaction effects on magnetic behaviors of hematite (α-Fe_2O_3) nanoparticles. Physica B: Condensed Matter **406**, 24832487 (2011).

[97] R. Ali-Zade. Magnetization of magnetite nanoparticles mediums with weak magnetic dipole-dipole interaction. Journal of Nanoscience and Nanotechnology **11**, 24962500 (2011).

[98] F. Canepa, M. Solzi. Condensed Matter: New Research. Nova Science Publishers (2007).

[99] D. Martien. Introduction to AC susceptibility. `http://www.qdusa.com/sitedocs/appNotes/ppms/1078-201.pdf` (2011).

[100] J.-O. Andersson, *et al.* Monte Carlo studies of the dynamics of an interacting monodispersive magnetic-particle system. Physical Review B **56**, 1398313988 (1997).

[101] D. E. Madsen, M. F. Hansen, S. Mørup. The correlation between superparamagnetic blocking temperatures and peak temperatures obtained from ac magnetization measurements. Journal of Physics: Condensed Matter **20**, 345209 (2008).

[102] S. Shtrikman, E. Wohlfarth. The theory of the Vogel-Fulcher law of spin glasses. Physics Letters A **85**, 467470 (1981).

[103] N. Ashcroft, N. Mermin. Festkörperphysik. Oldenbourgh (2005).

[104] `http://investor.fei.com/releasedetail.cfm?ReleaseID=262968`. 08.01.2014.

[105] Introduction to TEM, `micron.ucr.edu/public/manuals/Tem-intro.pdf`. 27.10.2013.

[106] I. M. Grabs, *et al.* Formation mechanisms of iron oxide nanoparticles in different nonaqueous media. Crystal Growth and Design **12**, 14691475 (2012).

[107] M. Hofmann, *et al.* The magnetic behaviour of nanostructured zinc ferrite. Journal of Materials Science **39**, 50575065 (2004).

[108] J. van Lierop, D. H. Ryan. Dynamics in fine particle magnets. Physical Review B **65**, 104402 (2002).

[109] J. L. García-Palacios, F. J. Lázaro. Langevin-dynamics study of the dynamical properties of small magnetic particles. Physical Review B **58**, 1493714958 (1998).

[110] E. Tronc, J. Jolivet. Dispersions of γ-Fe_2O_3 Nanoparticles. Mössbauer spectroscopic studies of the superparamagnetic relaxation. Materials Science Forum **235-238**, 659668 (1997).

[111] T. Jonsson, P. Nordblad, P. Svedlindh. Dynamic study of dipole-dipole interaction effects in a magnetic nanoparticle system. Physical Review B **57**, 497504 (1998).

[112] H. Jacobsen, *et al.* Temperature dependence of the magnetization of canted spin structures. Journal of Magnetism and Magnetic Materials **324**, 32183222 (2012).

[113] M. Kraken, *et al.* Formation of magnetic nanoparticles studied during the initial synthesis stage. Hyperfine Interactions **224**, 5763 (2013).

[114] I.-C. Masthoff, *et al.* Study of the growth process of magnetic nanoparticles obtained via the non-aqueous sol-gel method. Journal of Materials Science **49**, 47054714 (2014).

[115] V. K. LaMer, R. H. Dinegar. Theory, Production and Mechanism of Formation of Monodispersed Hydrosols. Journal of the American Chemical Society **72**, 48474854 (1950).

[116] V. K. LaMer. Nucleation in Phase Transitions. Industrial & Engineering Chemistry **44**, 12701277 (1952).

[117] Y. W. Guozhong Cao. Nanostructures and Nanomaterials: Synthesis, Properties, and Applications, 2nd Edition. World Scientific (2011).

[118] D. S. R. Viswanatha. Nanomaterials Chemistry: Recent Developments and New Directions. Wiley-VCH (2007).

[119] J. W. G. Wignall. Mössbauer Line Broadening in Trivalent Iron Compounds. The Journal of Chemical Physics **44**, 24622467 (1966).

[120] C. Serna, *et al.* Spin frustration in maghemite nanoparticles. Solid State Commun. **118**, 437440 (2001).

[121] A. Muhammad. Lewis Acidity of Tris(acetylacetonate) iron (III) Interactions with some Phosphine Derivative in Methylene Chloride Solution. Jour. Chem. Soc. Pak. **14**, 8891 (1992).

[122] M. Zimmermann, G. Garnweitner. Spontaneous water release inducing nucleation during the nonaqueous synthesis of TiO2 nanoparticles. CrystEngComm **24**, 85628568 (2012).

[123] P. Scherrer. Bestimmung der Größe und der inneren Struktur von Kolloidteilchen mittels Röntgenstrahlen. Nachrichten von der Gesellschaft der Wissenschaften zu Göttingen, Mathematisch-Physikalische Klasse **1918**, 98100 (1918).

[124] G. Schmid, editor. Nanoparticles: From theory to application. Wiley-VCH (2010).

[125] G. Schinteie, *et al.* Volume fraction dependent magnetic behaviour of ferrofluids for rotating seal applications. Journal of Physics D: Applied Physics **46**, 395501 (2013).

[126] V. Kuncser. Private communication (2013).

[127] J. Santoyo Salazar, *et al.* Magnetic Iron Oxide Nanoparticles in 10-40 nm Range: Composition in Terms of Magnetite/Maghemite Ratio and Effect on the Magnetic Properties. Chemistry of Materials **23**, 13791386 (2011).

[128] A. Ahniyaz, *et al.* Preparation of iron oxide nanocrystals by surfactant-free or oleic acid-assisted thermal decomposition of a Fe(III) alkoxide. Journal of Magnetism and Magnetic Materials **320**, 781787 (2008).

[129] C. E. Violet, R. J. Borg. Magnetic Ordering in Dilute Solid Solutions of Iron in Gold. I. Physical Review **149**, 540551 (1966).

[130] C. E. Violet, R. J. Borg. Magnetic Ordering in Dilute Solid Solutions of Iron in Gold. II. Electric Hyperfine Interactions. Physical Review **162**, 608615 (1967).

[131] W. Marshall, *et al.* Magnetism of Dilute Alloys. Review of Modern Physics **36**, 399406 (1964).

[132] B. R. Coles, B. V. B. Sarkissian, R. H. Taylor. The role of finite magnetic clusters in Au-Fe alloys near the percolation concentration. Philosophical Magazine Part B **37**, 489498 (1978).

[133] P. Munayco. Nanopartículas de Fe em filmes de metais não magnéticos Ag, Cd e Zn. Ph.D. thesis, Centro Brasileira de Pesquisas Físicas (2006).

[134] M. A. Morales, E. C. Passamani, E. Baggio-Saitovitch. ^{57}Fe diluted in a Ag film prepared by vapor quenching: Nanostructure formation and magnetic behavior. Physical Review B **66**, 144422 (2002).

[135] P. Cregg, L. Bessais. Series expansions for the magnetisation of a solid superparamagnetic system of non-interacting particles with anisotropy. Journal of Magnetism and Magnetic Materials **202**, 554564 (1999).

[136] U. Larsen. Resistance maximum in spin glasses. Physical Review B **14**, 43564367 (1976).

[137] M. G. Vavilov, L. I. Glazman, A. I. Larkin. Electron transport and energy relaxation in dilute magnetic alloys. Physical Review B **68**, 075119 (2003).

[138] A. Kumar, R. P. Tandon, V. P. S. Awana. Study of spin glass and cluster ferromagnetism in $RuSr_2Eu_{1.4}Ce_{0.6}Cu_2O_{10-\delta}$ magneto superconductor. Journal of Applied Physics **110**, 043926 (2011).

[139] G. Rollmann, P. Entel, S. Sahoo. Competing structural and magnetic effects in small iron clusters. Computational Materials Science **35**, 275278 (2006).

[140] C. Rojas-Ayala, *et al.* Structural properties of the pure and Fe-doped Yb films prepared by vapor condensation. to be published (2014).

[141] F. X. Kayser. Diffraction evidence for the existence of an F.C.C. to H.C.P. transformation in Yb. Physica Status Solidi (a) **8**, 233241 (1971).

[142] O. Lounasmaa. Specific Heat of Gadolinium and Ytterbium Metals between 0.4 and 4K. Physical Review **129**, 24602465 (1963).

[143] D. Andrae, B. Paulus. The Crystal Structure of the Close-Packed Polymorphs of Ytterbium: A Quantum Chemical Study. Proceedings of the 34th Annual Condensed Matter and Materials Meeting (2010).